

Aspects of Synthesis, Structure and Catalytic Performance of Alumina Supported NiMo Hydrotreating Catalysts

Citation for published version (APA):

Li, M. (2023). *Aspects of Synthesis, Structure and Catalytic Performance of Alumina Supported NiMo Hydrotreating Catalysts*. [Phd Thesis 1 (Research TU/e / Graduation TU/e), Chemical Engineering and Chemistry]. Eindhoven University of Technology.

Document status and date:

Published: 29/03/2023

Document Version:

Publisher's PDF, also known as Version of Record (includes final page, issue and volume numbers)

Please check the document version of this publication:

- A submitted manuscript is the version of the article upon submission and before peer-review. There can be important differences between the submitted version and the official published version of record. People interested in the research are advised to contact the author for the final version of the publication, or visit the DOI to the publisher's website.
- The final author version and the galley proof are versions of the publication after peer review.
- The final published version features the final layout of the paper including the volume, issue and page numbers.

[Link to publication](#)

General rights

Copyright and moral rights for the publications made accessible in the public portal are retained by the authors and/or other copyright owners and it is a condition of accessing publications that users recognise and abide by the legal requirements associated with these rights.

- Users may download and print one copy of any publication from the public portal for the purpose of private study or research.
- You may not further distribute the material or use it for any profit-making activity or commercial gain
- You may freely distribute the URL identifying the publication in the public portal.

If the publication is distributed under the terms of Article 25fa of the Dutch Copyright Act, indicated by the "Taverne" license above, please follow below link for the End User Agreement:

www.tue.nl/taverne

Take down policy

If you believe that this document breaches copyright please contact us at:

openaccess@tue.nl

providing details and we will investigate your claim.

Aspects of Synthesis, Structure and Catalytic Performance of Alumina Supported NiMo Hydrotreating Catalysts

PROEFSCHRIFT

ter verkrijging van de graad van doctor aan de Technische Universiteit Eindhoven, op gezag van de rector magnificus prof.dr.ir. F.P.T. Baaijens, voor een commissie aangewezen door het College voor Promoties, in het openbaar te verdedigen op woensdag 29 maart 2023 om 11:00 uur

door

Mengyan Li

geboren te Xi'an, China

Dit proefschrift is goedgekeurd door de promotoren en de samenstelling van de promotiecommissie is als volgt:

voorzitter:	prof.dr. D.C. Nijmeijer
1 ^e promotor:	prof.dr. Th. Weber
2 ^e promotor:	prof.dr. E.J.M. Hensen
leden:	prof.dr. E.T.C. Vogt (Utrecht University)
	prof.dr. J.V. Lauritsen (Aarhus University)
	prof.dr. J.A.M. Kuipers
	prof.dr. J.A. van Bokhoven (ETH Zürich)
	prof.dr. J. van der Schaaf

Het onderzoek of ontwerp dat in dit wordt beschreven is uitgevoerd in overeenstemming met de TU/e Gedragcode Wetenschapsbeoefening.

To my family

Mengyan Li

Aspects of Synthesis, Structure and Catalytic Performance of Alumina Supported NiMo Hydrotreating Catalysts

A catalogue record is available from the Eindhoven University of Technology Library

ISBN: 978-90-386-5700-4

Copyright © 2023 by Mengyan Li



INORGANIC MATERIALS & CATALYSIS



The work described in this thesis has been carried out at the Laboratory of Inorganic Materials Chemistry, Eindhoven University of Technology, The Netherlands. We acknowledge financial support from Shell.

Cover design: Mengyan Li

Printed by: ProefschriftMaken

Table of contents

Chapter 1	Introduction and Scope	- 1 -
Chapter 2	Methods	- 11 -
Chapter 3	Catalysts Composition vs. Catalysts Activity	- 27 -
Chapter 4	Alumina Supported NiMo Hydrotreating Catalysts – Aspects of 3D Structure, Synthesis and Activity	- 63 -
Chapter 5	Predicting Catalytic Activity from Oxidic Precursor Properties	- 97 -
Chapter 6	A Non-boehmite Derived γ -Alumina and Its Utilization in HDS Catalysis	- 119 -
Chapter 7	Summary and Outlook	- 143 -
	Acknowledgements	- 147 -
	List of Publications	- 150 -
	Curriculum Vitae	- 151 -

Chapter 1

Introduction and Scope

Global warming and air pollution are the most important technical challenges in environmental catalysis research nowadays, which increases the urgency to change the energy structure dominated by fossil energy and reduce the carbon footprint. Nevertheless, fossil feedstocks and products derived from them, such as transportation fuels or bulk chemicals, will remain indispensable in the coming decades (Figure 1.1) [1]. As the harmful gases, NO_x and SO_x , emit into the air during the combustion of fossil fuels and induce acid rain, legislative regulations have prompted restraining the sulfur level of the fuel. Currently, the maximum sulfur level for ultralow-sulfur diesel (ULSD) oil is 10 ppm (Euro V standard, October 2016) [2]. Besides air pollution, the sulfur in oil also affects the performance of downstream unit operations, catalysts, or even engines. Hence, refineries must remove the impurities from the crude oil that contains a significant amount of sulfur and nitrogen before further processing or use.

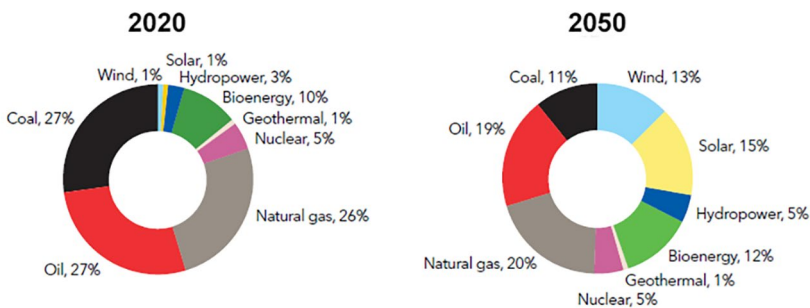


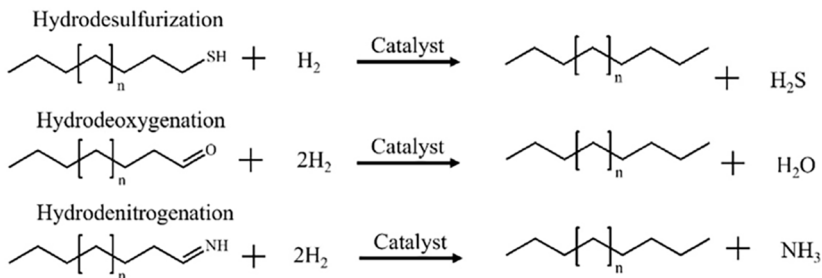
Figure 1.1. World primary energy supply by source, adapted from [1].

1.1. Hydrotreating

Hydrotreating is a well-established process to refine crude oil and produce clean transportation fuels. During hydrotreating, crude oil cuts are selectively reacted with hydrogen in the presence of a catalyst at relatively high temperatures and moderate pressures to remove the undesired impurities (e.g., S, N, O, metals), convert the undesirable aromatics, olefins into stabilized products, and enhances the quality of various fuels (e.g., diesel and gasoline) by increasing the cetane number. The catalytic reactions used to remove S, N, and

Chapter 1

O are hydrodesulfurization (HDS), hydrodenitrogenation (HDN), and hydrodeoxygenation (HDO), respectively [3, 4], formally described as follows:



1.2. Hydrodesulfurization

Sulfur is the vast and most harmful pollutant among various impurities, which makes HDS essential in oil refining. During HDS, sulfur atoms in the organosulfur compounds can be removed by reacting with hydrogen at elevated temperature and pressure in the presence of the catalyst. HDS reaction mainly proceeds via two parallel pathways, the direct desulfurization (DDS) pathway and the hydrogenation (HYD) pathway. Figure 1.2 shows the HDS of thiophene, the C-S bond cleavages directly without hydrogenating C=C bonds in the DDS pathway. While in the HYD route, before substituting a sulfur atom from thiophene, the aromatic ring containing sulfur is hydrogenated. Generally, these two pathways occur simultaneously in the HDS process. The predominant reaction pathway varies according to the nature of the sulfur compounds, the reaction conditions, and the catalyst used.

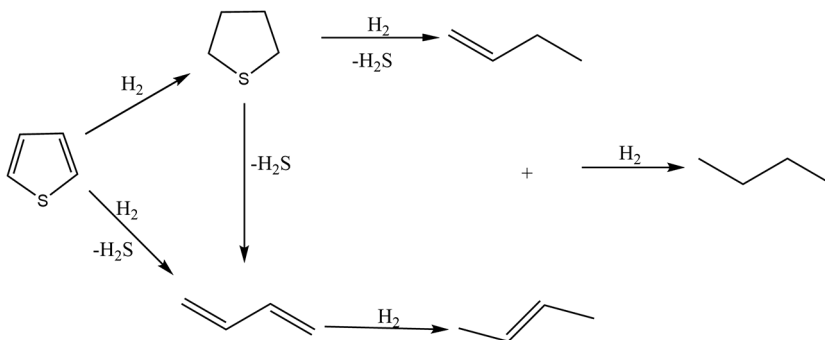


Figure 1.2. Reaction pathways for thiophene HDS.

There is a wide variety of organic sulfur compounds in various petroleum fractions, such as aliphatic sulfur compounds (e.g., mercaptans, sulfides, and disulfides) and thiophene derivatives (e.g., thiophene, benzothiophenes, and dibenzothiophenes). Due to the molecular size and the structure of sulfur-containing molecules, it is more challenging to remove sulfur from thiophene derivatives than aliphatic sulfur compounds. Among thiophene derivatives,

the refractory sulfur-containing species, as illustrated in Figure 1.3, are the most difficult to desulfurize. The reactivity of several thiophene compounds decreases with increasing aromaticity and steric constraints, and the desulfurizing of the refractory sulfur-containing molecules is the so-called deep HDS. As there is always competition between the HDN and HDS of the refractory nitrogen and sulfur-containing species during the deep removal, deep HDS always occurs along with HDN.

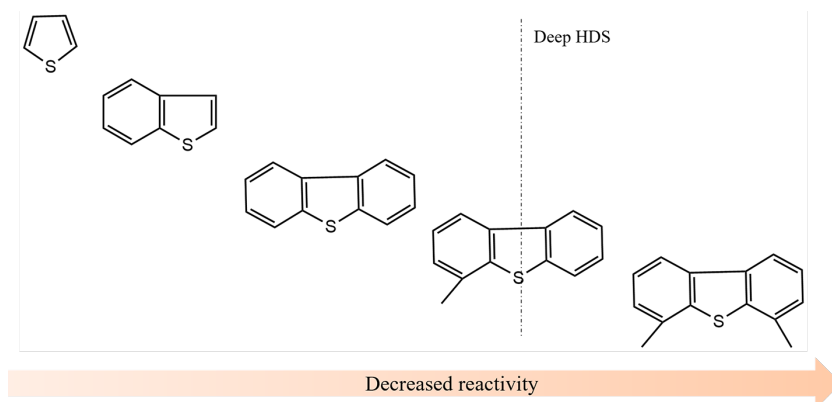


Figure 1.3. Decrease the reactivity of different sulfur-containing compounds in diesel feed.

The scarcity of low-sulfur crude oil and the existence of least reactive refractory sulfur-containing species are the key challenges for refineries. To address this challenge of changing feed quality while meeting the strengthened restrictions on the sulfur content in fuels, more effective catalysts are needed.

1.3. Hydrodesulfurization catalysts

Industrial HDS catalysts are commonly composed of Mo-based or W-based sulfides with Ni or Co sulfides as promoters supported on the high-surface-area γ - Al_2O_3 . γ - Al_2O_3 is the most advanced support in the balance of the surface area, pore size, mechanical strength, and cost, and it is usually prepared by decomposing boehmite ($\text{AlO}(\text{OH})$) at a temperature between 400 °C and 700 °C [5]. Ni/Co promoters can significantly improve catalyst activity by forming the so-called Co(Ni)MoS active structures [6] combining Mo/W with Ni/Co. The most common bimetallic catalysts used in refineries are sulfided Co-promoted MoS_2 (CoMoS), Ni-promoted MoS_2 (NiMoS), or Ni-promoted WS_2 (NiWS) catalysts supported on γ - Al_2O_3 [7]. These three types of HDS catalysts have been well studied, in which CoMoS catalysts are very efficient in the HDS process, but they are less efficient for HDN. The most favorable operation conditions for CoMoS catalysts are approximately 15 – 40 bar. While NiMoS catalysts show better HDN activity and are more effective in hydrogenation than CoMoS catalysts. NiMoS catalysts are preferred when there is an appreciable amount of

Chapter 1

nitrogen in the feed [8, 9]. As for NiWS, though it has the strongest hydrogenation properties [10], high-pressure (≥ 60 bar) is generally required during HDS applications. Among these catalysts, the focus of this thesis is the NiMo/ γ -Al₂O₃ catalysts, and it will be discussed as a representative HDS catalyst hereafter.

NiMo/Al₂O₃ HDS catalysts are commonly prepared by impregnating γ -Al₂O₃ with aqueous solutions containing suitable Mo and Ni compounds, followed by drying and calcination. After calcination, the MoO_x species are highly dispersed over the Al₂O₃ surface, where Mo exists as two coordination structures, a tetrahedral and octahedral coordinated structure. It is well-studied that the tetrahedral MoO_x species are strongly connected to the alumina surface via the formed Mo-O-Al linkages [11]. The octahedral MoO_x species, however, is weakly connected with the alumina surface via the van der Waals force. The oxide catalysts are then activated in an H₂S/H₂ flow (gas phase) [12] or in a flowing feedstock containing/spiked with organic sulfur compounds in the presence of H₂ (liquid phase) [13] at ca. 400 °C to transform into the active sulfided catalysts.

The surface structure model of the sulfided NiMo/Al₂O₃ is illustrated in Figure 1.4 according to the CoMoS model proposed by Topsøe et al. [6]. The MoO_x particles are mainly transferred to MoS₂ particles with single or multiple layers depending on the metal-support interaction in the sample. Such a layered structure composed of one plane of Mo atoms in between two closely packed planes of S atoms. Sulfur and molybdenum in these layers are held together by covalent bonds. In the crystalline state, multiple MoS₂ layers are stacked upon each other and held together only by weaker van der Waals forces. Ni, after sulfidation, exists in three different states, yet two of them are undesirable. Ni₃S₂ and a spinel-type NiAl₂O₄ particle form inevitably due to their high thermodynamic stability; however, either particle contributes effectively to catalytic activity. Phases of interest are the NiMoS particles, in which Ni atoms are dispersed on the edge of MoS₂ particles forming the active sites in the HDS reaction [14]. There are two types of NiMoS phases with different intrinsic activities; Type I is formed in case of strong metal-support interactions in the precursor state, making these structures difficult to sulfide into the active form. Retaining Mo-O-Al bonds favor the formation of single layers, with a distinct orientation relative to the support surface and lower intrinsic activity than Type II catalysts. Type II forms as consequences of weak metal-support interactions, such interactions enhance the formation of fully sulfided particles, which can occur in different degrees of stacking. As high metal dispersion and weak metal-support interaction are the preconditions of forming a highly active catalyst, different strategies were applied to decrease metal-support interactions and to disperse Mo and Ni, such as adjusting the Ni/Mo atomic ratio [15, 16], changing preparation procedures and conditions [17], using additives [18], and varying supports [19-21].

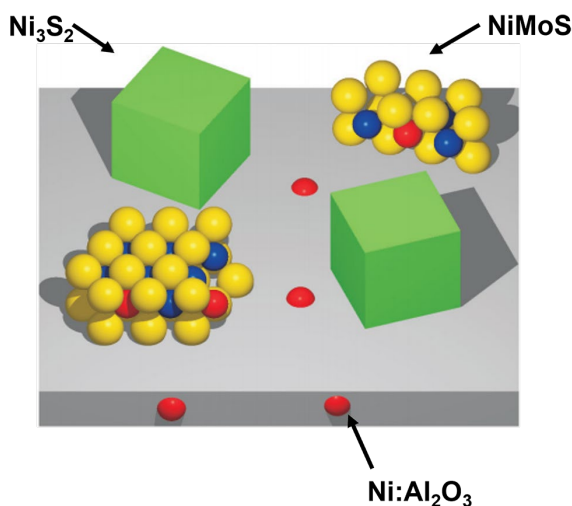


Figure 1.4. A surface structure model of NiMo/Al₂O₃ catalysts.

Besides the conventional incipient wetness impregnation method, hydrothermal deposition [22] or sol-gel synthesis [23, 24] is also used in HDS catalyst preparation. In recent years, preparing supported catalysts via a one-step preparation route has also attracted considerable interest [25]. Compared to the other preparation method, the one-step preparation route, which relates to incorporating metal precursor during the preparation of support, is favorable for evenly dispersing metallic species and is easy to operate.

1.4. Remaining challenges

As introduced in the last section, different strategies can be employed to prepare highly active HDS catalysts. Changing preparation conditions, such as using additives, or adjusting promoter content, as discussed in Chapter 3, is the commonly used one. However, the influence of starting materials (chemical sources) on catalyst structure and performance is barely discussed. As van Veen et al. proposed [26], the Ni-Mo-O structure is the precursor of the active Ni-Mo-S structure in the sulfided NiMo/Al₂O₃ catalysts and the structural properties of oxidic precursors are essential to the final states of the sulfided catalysts. However, the correlation between the structural properties of the oxidic precursors and the catalytic activity still needs to be determined. It would be a significant advantage if this correlation could be revealed, as it would provide us with a structural basis for highly active catalyst preparation.

The structure of the sulfided HDS catalysts, e.g., morphology (particle size and layers) [27] and atomic structure (metal coordination), has been studied theoretically and experimentally [28, 29] over the years based on the Co-Mo-S model structure. Nevertheless, these studies

Chapter 1

are mainly focused on the sulfided active phases. The discussion regarding the metal distribution and coordination situation on γ -Al₂O₃ is missing. The impact of the textural properties of γ -Al₂O₃, such as the porosity, pore distribution, and pore size on catalyst structure and performance, is barely studied. As we introduced in the last section, the metal-support interaction is important in supported HDS catalysts, as it influences the states of the formed active phase. Therefore, to have a comprehensive acknowledgement of supported HDS catalysts and to bridge the gap between the model catalyst and the industrial-like catalyst, a detailed study of alumina structure is needed.

1.5. Scope of the thesis

This thesis aims to understand the influence of the preparation conditions, including additives, calcination, and chemical sources, on catalyst structure and catalytic activity, and to reveal the correlation between the structural properties of the oxidic precursors and the catalytic activity of sulfided catalysts. To tackle these questions, a deep understanding of the structural properties of industrial-type NiMo/Al₂O₃ catalysts, such as the distribution of active phase and promoters on the alumina, and the influence of the porosity of alumina on metal depositions, is needed. For that purpose, two series of NiMo/Al₂O₃ catalysts, varied in formulation and preparation conditions, are studied in the first part of this thesis (**Chapters 3-5**). Based on the above understanding, in the second part of this thesis (**Chapter 6**), the influence of different preparation workflows on catalyst structure and HDS performance was explored.

The influence of the content of the promotor (Ni) is studied in **Chapter 3** to explore the optimal Ni/Mo molar ratio. Besides, **Chapter 3** reports the preparation of two series of NiMo/Al₂O₃ catalysts, prepared from two sets of chemical sources, i.e., (NH₄)₆Mo₇O₂₄/Ni(NO₃)₂ and MoO₃/NiCO₃. In each series of catalysts, different organic additives (citric acid (CA), ethylene glycol (EG), nitrilotriacetic acid (NTA), and malic acid (MA)) are used. The structure of the oxidic precursors and active sulfided samples of these catalysts are characterized. The catalytic activity of catalysts is evaluated in the hydrodesulfurization of thiophene, dibenzothiophene, and gas oil. The influence of preparation conditions on catalyst structure and HDS performance is discussed.

Chapter 4 aims to study the influence of chemical sources on catalysts structure and performance from a more in-depth perspective. A detailed structural characterization of two catalysts prepared respectively from (NH₄)₆Mo₇O₂₄/Ni(NO₃)₂ and MoO₃/NiCO₃ with identical formulation, using malic acid (MA) as an additive, is conducted. A novel technique – ptychographic X-ray computed tomography (PXCT), is used to describe the structural

difference in a three-dimensions (3D) way. Combined with scanning transmission electron microscopy (STEM) and energy dispersive X-ray analysis (EDX), the author want to understand better the actual metal deposition situation on the alumina surface.

Chapter 5 explores the correlation between the structural and physical properties of the oxide NiMo/Al₂O₃ catalyst and the HDS activity of the sulfided catalyst. The structure of oxidic precursors is described using the absorption edge energy (E_g) extracted from ultraviolet–visible diffuse reflectance spectroscopy (UV-vis DRS) and the temperature of the main reduction peak (T_m) extracted from temperature-programmed reduction (TPR). The catalyst HDS activity was evaluated in dibenzothiophene (DBT) HDS.

In **chapter 6**, an alternative method, thermal decomposition of NH₄Al(OH)₂CO₃, is employed to prepare an alumina carrier (Al₂O₃(self-made)). Two NiMo/Al₂O₃ catalysts with the same formulation are prepared on two different alumina, Al₂O₃(self-made) and Al₂O₃(commercial). Taking advantage of this alumina synthesis method, a NiMo/Al₂O₃ catalyst is prepared by incorporating the Mo and Ni in situ during the preparation of alumina (co-grinding). For comparison, a catalyst with identical formulations is prepared using incipient wetness impregnation. Two more catalysts with higher metal loadings are prepared via a two-step impregnation method. By comparing catalyst structure and activity, the influence of metal loading and different preparation workflow on catalyst structure and performance will be discussed.

1.6. References

- [1] D. AS, Energy transition outlook 2022, in, www.dnv.com, 2022.
- [2] A. Tanimu, K. Alhooshani, Advanced hydrodesulfurization catalysts: a review of design and synthesis, *Energy & Fuels*, 33 (2019) 2810-2838.
- [3] A. Stanislaus, A. Marafi, M.S. Rana, Recent advances in the science and technology of ultra low sulfur diesel (ULSD) production, *Catal. Today*, 153 (2010) 1-68.
- [4] C. Song, An overview of new approaches to deep desulfurization for ultra-clean gasoline, diesel fuel and jet fuel, *Catal. Today*, 86 (2003) 211-263.
- [5] S.J. Wilson, The dehydration of boehmite, γ -AlOOH, to γ -Al₂O₃, *J. Solid State Chem.*, 30 (1979) 247-255.
- [6] H. Topsøe, B.S. Clausen, R. Candia, C. Wivel, S. Mørup, In situ Mössbauer emission spectroscopy studies of unsupported and supported sulfided Co–Mo hydrodesulfurization catalysts: Evidence for and nature of a Co-Mo-S phase, *J. Catal.*, 68 (1981) 433-452.
- [7] L. van Haandel, Alumina supported MoS₂-based hydrodesulfurization catalysts: structure and performance in relation to catalyst preparation and activation, (2016).
- [8] Y. Zhao, R. Prins, Mechanisms of hydrodenitrogenation of alkylamines and hydrodesulfurization of alkanethiols on NiMo/Al₂O₃, CoMo/Al₂O₃, and Mo/Al₂O₃, *J. Catal.*, 229 (2005) 213-226.
- [9] S. Bezergianni, A. Dimitriadis, G. Meletidis, Effectiveness of CoMo and NiMo catalysts on co-hydroprocessing of heavy atmospheric gas oil–waste cooking oil mixtures, *Fuel*, 125 (2014) 129-136.

Chapter 1

- [10] C.J. Song, C. Kwak, S.H. Moon, Effect of fluorine addition on the formation of active species and hydrotreating activity of NiWS/Al₂O₃ catalysts, *Catal. Today*, 74 (2002) 193-200.
- [11] B. Scheffer, P. Arnoldy, J.A. Moulijn, Sulfidability and hydrodesulfurization activity of Mo catalysts supported on alumina, silica, and carbon, *J. Catal.*, 112 (1988) 516-527.
- [12] E.J.M. Hensen, P.J. Kooyman, Y. van der Meer, A.M. van der Kraan, V.H.J. de Beer, J.A.R. van Veen, R.A. van Santen, The relation between morphology and hydrotreating activity for supported MoS₂ particles, *J. Catal.*, 199 (2001) 224-235.
- [13] L. van Haandel, G.M. Bremmer, E.J.M. Hensen, Th. Weber, Influence of sulfiding agent and pressure on structure and performance of CoMo/Al₂O₃ hydrodesulfurization catalysts, *J. Catal.*, 342 (2016) 27-39.
- [14] S. Houssenbay, S. Kasztelan, H. Toulhoat, J. Bonnelle, J. Grimblot, Nature of the different nickel species in sulfided bulk and alumina-supported nickel-molybdenum hydrotreating catalysts, *J. Phys. Chem.*, 93 (1989) 7176-7180.
- [15] A.D. Gandubert, C. Legens, D. Guillaume, S. Rebours, E. Payen, X-ray photoelectron spectroscopy surface quantification of sulfided CoMoP catalysts – Relation between activity and promoted sites – Part I: influence of the Co/Mo ratio, *Oil & Gas Sci. Technol.*, 62 (2007) 79-89.
- [16] L. Zhang, Z. Chen, S. Zheng, G. Cai, W. Fu, T. Tang, M. He, Effect of the Co/Mo ratio on the morphology and activity of the CoMo catalyst supported on MgO nanosheets in dibenzothiophene hydrodesulfurization, *Ind. Eng. Chem. Res.*, 59 (2020) 12338-12351.
- [17] T. Huang, J. Chang, S. He, C. Wen, Y. Fan, Efficient hydrodesulfurization of 4, 6-dimethyldibenzothiophene via Ni₄Mo₁₂/Al₂O₃ catalysts prepared by a one-step hydrothermal polyoxometalate dispersion method, *Energy & Fuels*, 33 (2018) 135-147.
- [18] L. Oliviero, F. Maugé, P. Afanasiev, C. Pedraza-Parra, C. Geantet, Organic additives for hydrotreating catalysts: a review of main families and action mechanisms, *Catal. Today*, 377 (2021) 3-16.
- [19] L. Chen, Y. Xu, B. Wang, J. Yun, F. Dehghani, Y. Xie, X. Liang, Mg-modified CoMo/Al₂O₃ with enhanced catalytic activity for the hydrodesulfurization of 4, 6-dimethyldibenzothiophene, *Catal. Commun.*, 155 (2021) 106316.
- [20] W. Zhou, A. Zhou, Y. Zhang, C. Zhang, Z. Chen, L. Liu, Y. Zhou, Q. Wei, X. Tao, Hydrodesulfurization of 4, 6-dimethyldibenzothiophene over NiMo supported on Ga-modified Y zeolites catalysts, *J. Catal.*, 374 (2019) 345-359.
- [21] G.M. Dhar, B.N. Srinivas, M.S. Rana, M. Kumar, S.K. Maity, Mixed oxide supported hydrodesulfurization catalysts – a review, *Catal. Today*, 86 (2003) 45-60.
- [22] Y. Fan, H. Xiao, G. Shi, H. Liu, Y. Qian, T. Wang, G. Gong, X. Bao, Citric acid-assisted hydrothermal method for preparing NiW/USY–Al₂O₃ ultradeep hydrodesulfurization catalysts, *J. Catal.*, 279 (2011) 27-35.
- [23] R. Iwamoto, J. Grimblot, Genesis, characterizations and HDS activity of Mo-P-aluminabased hydrotreating catalysts prepared by a sol-gel method, in, *Studies in Surface Science and Catalysis*, Elsevier, 1997, pp. 195-210.
- [24] F. Dumeignil, K. Sato, M. Imamura, N. Matsubayashi, E. Payen, H. Shimada, Characterization and hydrodesulfurization activity of CoMo catalysts supported on boron-doped sol-gel alumina, *Appl. Catal. A: Gen.*, 315 (2006) 18-28.
- [25] L. van Haandel, J.W. Geus, Th. Weber, Direct synthesis of TiO₂-supported MoS₂ nanoparticles by reductive coprecipitation, *ChemCatChem*, 8 (2016) 1367-1372.
- [26] J.A.R. van Veen, E. Gerkema, A.M. van der Kraan, P.A.J.M. Hendriks, H. Beens, A ⁵⁷Co Mössbauer emission spectrometric study of some supported CoMo hydrodesulfurization catalysts, *J. Catal.*, 133 (1992) 112-123.

Introduction and Scope

[27] S. Eijsbouts, L.C.A. van den Oetelaar, R.R. van Puijenbroek, MoS₂ morphology and promoter segregation in commercial Type 2 Ni-Mo/Al₂O₃ and Co-Mo/Al₂O₃ hydroprocessing catalysts, *J. Catal.*, 229 (2005) 352-364.

[28] S.S. Grønberg, N. Salazar, A. Bruix, J. Rodríguez-Fernández, S.D. Thomsen, B. Hammer, J.V. Lauritsen, Visualizing hydrogen-induced reshaping and edge activation in MoS₂ and Co-promoted MoS₂ catalyst clusters, *Nat. Commun.*, 9 (2018) 2211.

[29] N. Salazar, S.B. Schmidt, J.V. Lauritsen, Adsorption of nitrogenous inhibitor molecules on MoS₂ and CoMoS hydrodesulfurization catalysts particles investigated by scanning tunneling microscopy, *J. Catal.*, 370 (2019) 232-240.

Chapter 1

Chapter 2

Methods

2.1. Materials

Ammonium heptamolybdate tetrahydrate ($(\text{NH}_4)_6\text{Mo}_7\text{O}_{24}\cdot 4\text{H}_2\text{O}$, 99%), nickel carbonate (NiCO_3 , 48 – 50%), phosphoric acid (H_3PO_4 , 85 wt% in H_2O), aluminum nitrate nonahydrate ($\text{Al}(\text{NO}_3)_3\cdot 9\text{H}_2\text{O}$, $\geq 98\%$), ammonium bicarbonate (NH_4HCO_3 , $\geq 99.5\%$), citric acid ($\text{C}_6\text{H}_8\text{O}_7$, 99.5%), ethylene glycol ($\text{C}_2\text{H}_6\text{O}_2$, anhydrous, 99.8%), DL-malic acid ($\text{C}_4\text{H}_6\text{O}_5$, 98%), nitrilotriacetic acid ($\text{C}_6\text{H}_9\text{NO}_6$, $\geq 99\%$), triethylene glycol ($\text{C}_6\text{H}_{14}\text{O}_4$, 99%), D-gluconic acid ($\text{C}_6\text{H}_{12}\text{O}_7$, 49 – 53 wt% in H_2O), thiophene ($\text{C}_4\text{H}_4\text{S}$, 99%), adamantane ($\text{C}_{10}\text{H}_{16}$, 99%) and dibenzothiophene ($\text{C}_{12}\text{H}_8\text{S}$, 98%) were purchased from Sigma-Aldrich. Molybdenum trioxide (MoO_3 , 99.9%) was purchased from Climax. Nickel nitrate hexahydrate ($\text{Ni}(\text{NO}_3)_2\cdot 6\text{H}_2\text{O}$, 98%), ammonium hydroxide ($\text{NH}_3\cdot \text{H}_2\text{O}$, 28%) and n-hexadecane ($\text{C}_{16}\text{H}_{34}$, 99%) were purchased from Alfa Aesar. Polyethylene glycol 400 ($\text{HO}(\text{C}_2\text{H}_4\text{O})_n\text{H}$, for synthesis) was purchased from Merck. All chemicals were used without further purification.

2.2. Characterization technique

2.2.1. Inductively coupled plasma-optical emission spectrometry (ICP-OES)

ICP-OES is commonly used to determine catalyst elemental composition [1]. Due to technical advances in multi-element analysis and high throughput operation at high reliability, it is widely applied in routine research [2]. The elemental composition of the catalyst in this work was collected on an AMETEK Spectroblue FME16 spectrometer. The sample solution was prepared by dissolving 35 mg catalyst in acid solvents; sulfuric acid (diluted with water, 1:1 (vol/vol)) and aqua regia were used for oxide samples and sulfided/spent samples separately.

2.2.2. Temperature programmed reduction (TPR)

TPR is widely used in heterogeneous catalysis to examine the surface chemistry of catalysts [3] and to explore the most efficient reduction conditions [4, 5]. In this work, the reduction property of catalysts was monitored by means of TPR. In detail, the H_2 -TPR experiment was performed on a Micromeritics Autochem II 2920 instrument; ca. 50 mg of

Chapter 2

sample materials were loaded into a U-tube reactor and pretreated at 200 °C in a 50 mL/min He flows for 1 h to desorb the impurities. The temperature was then increased to 900 °C in an H₂/He (5/95 vol%) flow at 5 °C/min and kept at these conditions for 1 h. Meanwhile, the H₂ consumption was monitored using a thermal conductivity detector (TCD). In the end, a TPR profile, a plot of the H₂ consumption against temperature, can be obtained [6].

2.2.3. Ultraviolet–visible diffuse reflectance spectroscopy (UV-vis DRS)

UV-vis DRS can provide the coordination and aggregation states of metal species in a non-destructive way [7, 8]. Generally, a UV-vis spectrum shows the amount of light absorbed by the sample as a function of wavelength. Using the Kubelka-Munk equation [9, 10] (equation 1), the absorption edge energy (E_g) can be extracted by finding the intercept of the straight line for the low-energy rise of a plot of $[F(R_\infty)h\nu]^2$ against $h\nu$ [11].

$$[F(R_\infty)h\nu]^2 = C_2(h\nu - E_g) \quad (1)$$

Where $F(R_\infty)$ is Kubelka-Munk function, $h\nu$ = photon energy. The coordination states of Mo and Ni in the oxide precursors were estimated using UV-vis spectroscopy. By plotting E_g and catalyst HDS activity, a direct correlation between the structural and physical properties of oxidic precursors and the activity of sulfided catalysts was meant to be proposed. UV-vis DRS spectra of the oxide catalysts (75 – 125 μm) in this work were collected on a Shimadzu UV-2401PC spectrophotometer equipped with an integrating sphere coated with BaSO₄ (act as white standard) at room temperature. Samples diluted with BaSO₄ were used for measurement.

2.2.4. Raman spectroscopy

Information on structure, crystallinity and the coordination of metal oxides can be collected using Raman spectroscopy [12]. In this work, the coordination states of Mo and Ni in the impregnation solution and in the oxide catalysts were characterized by means of Raman. The spectra were acquired on a confocal Witec alpha 300 R microscope equipped with a 532 nm diode excitation source, a 1200 lines/mm grating (BLZ = 500 nm), and a charge-coupled device (CCD) detector. A Zeiss LD EC Epiplan-Neofluar Dic 50 \times /0.55 objective was used. The presented spectra of powders were the result of 360 accumulations with an acquisition time of 5 s per accumulation; the spectra of liquids were collected as the results of 10 accumulations with an acquisition time of 30 s per accumulation.

2.2.5. X-ray photoelectron spectroscopy (XPS)

XPS is a surface-sensitive (probing depth is 2 – 10 nm) quantitative spectroscopic technique [13]. In this work, XPS was conducted to reveal the oxidation state of Mo and Ni in NiMo/Al₂O₃ catalysts and the dispersion of Mo and Ni on the alumina surface. The spectra were collected on a Thermo Scientific K-Alpha spectrometer equipped with a monochromatic small-spot X-ray source (Al K α) operating at 72 W and a spot size of 400 μ m. The preparation of sulfided and spent samples for measurement was carried out in an N₂-filled glovebox (H₂O < 1 ppm, O₂ < 1 ppm) to avoid contact with air. The sample was dispersed on a carbon tape-covered alumina holder in the glovebox and was then transferred into the XPS apparatus via an airtight transport vessel. The background pressure prior to measurement was 2×10^{-9} mbar, the survey and region scans were collected using a constant pass energy of 160 eV and 40 eV, respectively. CasaXPS software with a Shirley background subtraction and Gaussian-Lorentzian (30 %/70 %) fitting procedure was used. The C1s signal served as a reference and was set at 284.8 eV.

The quantification of metallic atoms was obtained by measuring the corresponding peak area A_i and using the relative sensitivity factors S_i (equation 2). To approach the effective atomic surface concentrations, all atoms detected on the surface, i.e., Al 2p, S 2p, Mo 3d, O 1s, and Ni 2p (except the contamination carbon), were counted. XPS decomposition enables the absolute quantification of each species.

$$C(i)_T(\%) = \frac{A_i/S_i}{\sum_{i=1...t} A_i/S_i} \times 100 \quad (2)$$

The dispersion of Mo and Ni on alumina was evaluated via equation 3.

$$\frac{Mo(Ni)}{Al} = \frac{A_{Mo(Ni)}/S_{Mo(Ni)}}{A_{Al}/S_{Al}} \quad (3)$$

The relative concentration of each species, e.g., NiS_x, NiMoS, NiO_x, Mo⁶⁺, Mo⁵⁺, and Mo⁴⁺, can be obtained via equation 4. For example, the relative amount of NiMoS was determined:

$$[NiMoS](\%) = \frac{A_{NiMoS}}{A_{NiMoS} + A_{NiO_x} + A_{NiS_x}} \times 100 \quad (4)$$

The effective Ni content in the NiMoS phase was determined using equation 5.

$$C_{NiMoS} = [NiMoS] \times C(Ni)_T \quad (5)$$

Where $C(Ni)_T$ is the effective concentration of Ni determined by XPS (wt%). Equation 6 was used to determine the promoter ratio in the NiMoS phase.

$$\left(\frac{Ni}{Mo}\right)_{slab} = \frac{C_{NiMoS}}{C_{MoS_2}} \quad (6)$$

Where C_{NiMoS} and C_{MoS_2} are the absolute concentration of Ni and Mo in NiMoS and MoS₂ (at%). The promoter ratio in the slab edge of NiMoS was calculated as follows.

Chapter 2

$$\left(\frac{Ni}{Mo}\right)_{edge} = \frac{(Ni/Mo)_{slab}}{D} \quad (7)$$

Where D is the dispersion of NiMoS obtained from TEM data using equation 10.

2.2.6. X-ray diffraction (XRD)

XRD is one of the most frequently applied techniques in catalyst characterization. It can identify crystalline phases inside catalysts and indicate particle size. XRD patterns in this work were recorded on a Bruker D2 Phaser powder diffractometer using Cu K α radiation with a time per step of 0.5 s and a step size of 0.01° in the 2 θ range of 20 – 70°.

2.2.7. Electron microscopy

Electron microscopy is used to determine the size of supported particles and reveal the composition and internal structure of the catalyst due to the atomic resolution. Figure 2.1 illustrates the signals generated when the primary beam hits the sample.

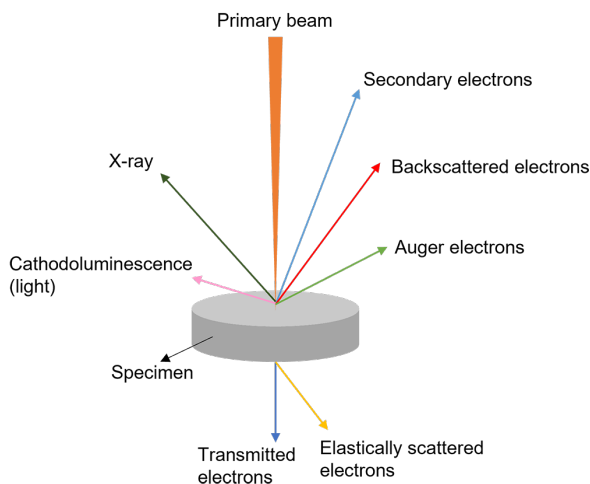


Figure 2.1. The interaction between the primary electron beam and sample in an electron microscopy leads to several detectable signals.

2.2.7.1. Transmission electron microscopy (TEM)

In a TEM, primary electron beams of high energy and high intensity pass through a condenser to produce parallel rays and interact with a specimen to form images. As the attenuation of the beam depends on the density and thickness of the sample, the transmitted electrons form a 2D projection of sample mass, which is subsequently magnified by the electron optics to produce the so-called bright-field (BF) image. The dark-field (DF) image is obtained from the diffracted electron beams, which are slightly off-angle from the transmitted beam.

The morphology information, e.g., particle size and stacking degree of MoS₂ particles in sulfided NiMo/Al₂O₃ catalysts, was extracted from TEM images. The BF-TEM images were collected on a Tecnai 20 electron microscope with an accelerating voltage of 200 kV. The sample suspensions were prepared in a glovebox by dispersing ~5 mg catalyst samples in n-hexane, a few droplets were placed on a microgrid carbon film supported on a Cu grid, and the grid was then transported to TEM. For each catalyst, 10 – 15 representative micrographs were obtained, and the length of > 300 slabs was measured. The mean size of individual MoS₂ platelets (L) and the average number of layers per particle (stacking degree, \bar{N}) were calculated using ImageJ from the acquired TEM images. L was determined by fitting a log-normal function to the slab size distribution, and \bar{N} was calculated according to equation 9.

$$L = 3.2 (2n_i - 1)\text{\AA} \quad (8)$$

$$\bar{N} = \frac{\sum_{i=1...t} n_i N_i}{\sum_{i=1...t} n} \quad (9)$$

Where N_i is the number of MoS₂ platelets in the stacks, and n_i is the amount of individual MoS₂ platelets counted for a given stacking number N_i .

To measure the dispersion of NiMoS particles (D), the average fraction of Mo at the MoS₂ edge was calculated, assuming that MoS₂ slabs were perfect hexagons [14-17]. D is statistically evaluated by dividing the total number of Mo atoms at the edge (Mo_e), including corner sites (Mo_c), by the total number of Mo atoms (Mo_T) using the slab sizes (L) (Equation 10).

$$D = \frac{Mo_e + Mo_c}{Mo_T} = \frac{\sum_{i=1...t} 6n_i - 6}{\sum_{i=1...t} 3n_i^2 - 3n_i + 1} \quad (10)$$

Where n_i is the number of Mo atoms along one side of the MoS₂ slab, and t is the total number of slabs in TEM micrographs.

2.2.7.2. Scanning transmission electron microscopy (STEM)/Energy dispersive X-ray analysis (EDX)

STEM combines the TEM and SEM (scanning electron microscope) modes of operation. In STEM, the electron beam, focused onto a fine spot (0.05 – 0.2 nm), is scanned over the sample in a raster illumination system constructed, so that the sample is illuminated at each point with the beam parallel to the optical axis to form the images. STEM suits analytical techniques like EDX (energy dispersive X-ray analysis) and Z-contrast annular dark-field imaging. EDX is commonly used for elemental analysis [18, 19], and its system is generally attached to a TEM or SEM instrument.

Chapter 2

The morphology of MoS₂ particles and the dispersion of Mo and Ni on the alumina surface were revealed by means of STEM and EDX. HAADF (high-angle annular dark field) STEM images and EDX mapping images of the sulfided and spent catalysts presented in Chapter 4 were collected on a probe-corrected JEOL ARM 200F transmission electron microscope. The sample preparation and image analysis methods are the same as in Section 2.2.7.1.

2.2.8. Ptychographic X-ray computed tomography (PXCT)

PXCT is a coherent X-ray-based technique, which, combined with tomography, enables to obtain 3D electron density maps of the specimen in a non-destructive way [20-22]. With several keV photon energies, PXCT has the potential to bridge the resolution gap between the traditional X-ray imaging methods and electron microscopy, imaging in the spatial resolution range approaching 10 nm in high-contrast samples with a thickness of tens of microns [23].

Coherent diffractive imaging (CDI) is a lensless technique for 2D or 3D reconstruction of the image of nanoscale structures. In CDI, highly coherent X-rays, electrons, or photon illuminates the sample, and the beam scattered by the sample produces a diffraction pattern downstream collected by a detector [24]. The recorded pattern is used to reconstruct an image via the iterative reconstruction algorithm [25-28]. The software in CDI is the replacement of the objective lens in a typical microscope and is used to convert the reciprocal space diffraction pattern into a real space image. The advantage of using no lenses is that the final image is aberration free, so resolution is only diffraction and dose limited. Ptychography is a potent modality of the CDI technique [29, 30]; it shares the same imaging principle with CDI. In ptychography, a 3D dataset consists of acquiring 2D projections of a sample along different sample angular orientations with respect to the incident beam propagation. To facilitate the ptychographic shift-invariance constraint, these illumination regions must partially overlap. With computed tomography algorithms, a 3D map of electron density, of which the provided contrast is quantitative [31], can be reconstructed.

The achievable resolution in ptychography is determined by the accuracy of scanning position, the stability of the measurement system, and the angular extent of the X-ray scattering of the sample, which in turn is determined by sample composition, exposure time, and the detection system. To have a high-resolution 3D image, the ptychographic projections have to provide the required resolution and be distortion-free, meaning that short-range precision of neighboring scanning positions needs to be accurate and long-range precision between extreme scanning points. The latter puts strong requirements on

thermal drift during the scan and position distortions caused by angular error motions of scanning stages or by a slight rotation or skewing between the scanning axes and the image pixels. To ensure the position accuracy, a setup named tomography Nano crYo (OMNY) stage [21, 32-35] was developed by Holler et al., as schematically displayed in Figure 2.2. This setup consists of two mechanical units: sample stages and optics stages. The sample stage is equipped with a rotation axis for tomography and allows precise movement for sample scanning. On the stage, a sample pin [36] is directly mounted on a reference mirror used for the interferometric measurements of sample position. The optics stage is used to provide an X-ray illumination of a few microns in diameter. A diffractive X-ray lens [37] consisting of a central stop (CS), a Fresnel zone plate (FZP), and an order sorting aperture (OSA) is mounted on the optics stage. The reason for using FZP optics is that they do not require angular alignment, and the interferometric measurement of the optics position is simple. Positions (Δx , Δy) and angular measurement (θ_z), measured with differential laser interferometry, are used to calculate and correct the sample position, which can be further utilized in ptychographic reconstructions.

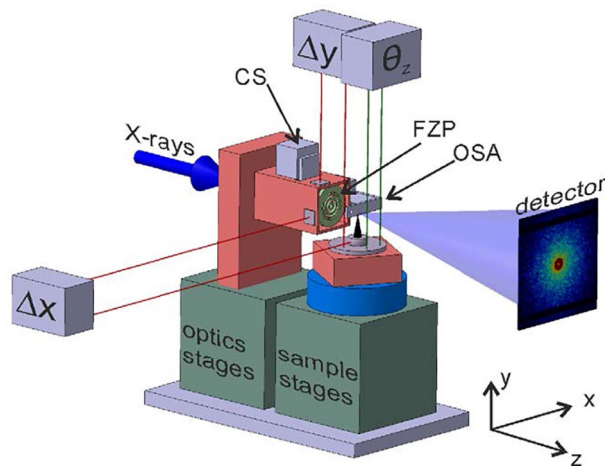


Figure 2.2. Tomography setup, composed of X-ray optics and sample stage units [32].

A sample in a cylinder shape with a diameter and height equal to or marginally larger than the field of view (FOV) is preferred for PXCT measurement. Since the cylinder can minimize the amount of material external to the FOV that is not characterized but which the X-rays must still pass through, i.e., attenuation of the beam, and maximize the volume of sample that can be analyzed, thus improving the statistical representation. To obtain a cylinder shape, the sample extrudates were first mechanically fractured, the central piece of which was then mounted on a tomography pin [36] and was further pre-shaped using a micro-lathe [38] to a diameter of 50 – 80 μm before being reduced to $< 25 \mu\text{m}$ in diameter using focused ion-beam (FIB) milling [39], see Figure 2.3 for the SEM image of one of the

Chapter 2

prepared pillars. To avoid contact with air and the moisture contamination, the shaped cylinder samples were stored in evacuated desiccators prior to measurement.

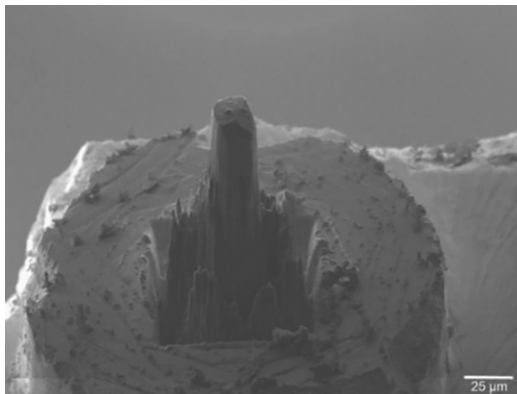


Figure 2.3. SEM image of one of the examined NiMo catalyst pillars.

PXCT in this work was carried out at the cSAXS beamline of the Swiss Light Source (SLS) at 6.2 keV photon energy at room temperature in N_2 atmosphere using OMNY. The pin was introduced into OMNY chamber, enabling sample cryocooling [40] before measurement to reduce X-ray radiation damage. A double-crystal Si(111) monochromator was used as photon energy. An FZP with a 200 μm diameter outermost zone width of 60 nm, and locally displaced zones to provide perturbations of the illumination wavefront, was used [41]. The sample was placed ~ 1.5 mm downstream of the zone plate's focal point. Coherent diffraction patterns were acquired with an in-vacuum 1.5k Eiger detector with a 75 μm pixel size approximately 7.2 m downstream of the sample [42, 43]. An evacuated flight tube was positioned between the sample and detector to reduce air scattering and absorption.

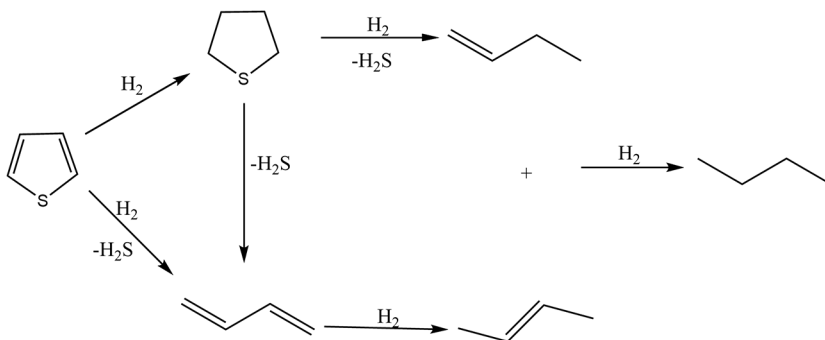
The scanning positions for each tomographic projection were set using a Fermat spiral scanning grid with an average step size of 1 μm [44]. The total FOV covered in a projection was at the maximum of 30×15 μm . Depending on the sample diameter and apparent achievable resolution, 650 – 1423 projections were acquired and later used for tomographic reconstruction based on the Fourier ring correlation of tomographic projections. The acquisition time per scanning point in a single projection was 0.025 s. From each of these diffraction patterns, a region of 600×600 detector pixels was used for the ptychographic reconstructions. The projection reconstructions were obtained with 300 iterations of the difference map algorithm followed by 500 iterations of maximum likelihood refinement using the PtychoShelves package [45]. Projections were acquired, aligned, and a complex-valued 3D index of refraction was computed using a filtered back-projection (FBP) algorithm as described in [46]. The resulting tomograms possess a voxel size of (23.26

nm)³. The obtained quantitative electron density tomograms possess, on average, a half-period spatial resolution of 40 nm. The actual resolution and repeatability of the measurement can be estimated using Fourier shell correlation (FSC) with the ½-bit threshold criteria [47]. The X-ray dose imparted to the imaged samples during tomogram acquisition was estimated to be on the order of $\sim 5e^{10}$ Gy. This was computed using the surface-dose formula in [54], using the area flux density during each ptychographic scan and the mass density of the sample into consideration [48]. In our catalysts system, the sample was assumed to consist of alumina. Detailed tomogram analysis will be further explained in Chapter 4.

2.3. Catalytic activity

2.3.1. Thiophene hydrodesulfurization (HDS)

Thiophene is a model compound used to evaluate catalyst HDS activity. As shown in Scheme 2.1, there are two alternative reaction pathways for thiophene HDS with H₂S and butane as products [49]. In the hydrogenation (HYD) pathway, thiophene is saturated with H₂ to yield tetrahydrothiophene; with hydrogenation and hydrolysis of the C-S bond, 1-butene is obtained, and with further hydrogenation to butane. In the direct desulfurization (DDS) pathway, hydrolysis of the C-S bond yielded butadiene, with further hydrogenation, 2-butene was obtained and then butane. DDS pathway is the main pathway for thiophene HDS at atmospheric pressure [50, 51]. Thiophene HDS is an exothermic reaction and can be considered irreversible under reaction conditions applied in the industry (~ 300 °C, 50 bar) [52]; due to the significant excess of H₂, this reaction is considered the pseudo-first-order rate reaction.



Scheme 2.1. Reaction network for thiophene HDS over the hydrotreating catalyst.

In this work, catalyst activation and activity test were performed sequentially in a stainless-steel reactor with an inner diameter (I.D.) of 4 mm at ambient pressure. In detail, ~ 76 mg oxidic precursor (75 – 125 μ m) mixed with 200 mg SiC were loaded in the middle of the reactor and sulfided in a flow of 50 mL/min H₂/H₂S (90/10 vol%) at 1 bar at 350 °C for 2 h.

Chapter 2

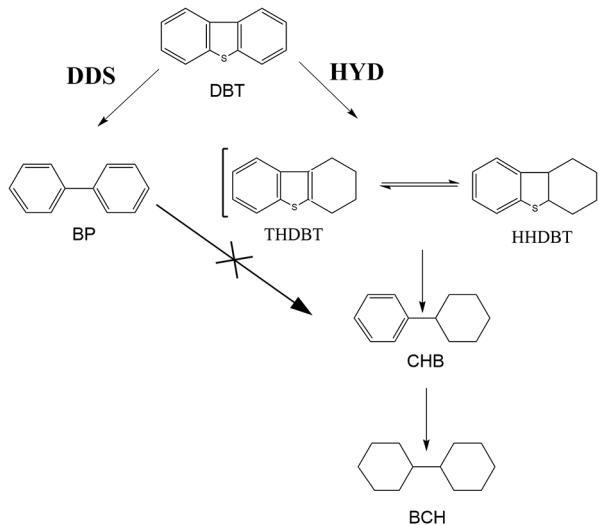
After activation, the temperature was increased to 400 °C, and the reaction feed composed of 4 vol% thiophene in H₂ (100 mL/min) was switched. After steady at 400 °C for 13 h, the steady-state catalyst activity was measured by gas chromatography (GC, Thermo Fisher Scientific) equipped with a flame ionization detector (FID) and an RTX-1 column (length = 30 m, I.D. = 0.32 mm). The reaction rate (r_{Thio}), normalized per mole of Mo, was calculated

$$r_{Thio} = \left(\frac{F_{Thio}}{m_{cat} \omega_{Mo}} \right) X \quad (11)$$

where F_{Thio} is the molar flow of thiophene [$\text{mol}_{Thio} \text{ h}^{-1}$], m_{cat} is the catalyst mass [g], ω_{Mo} is the fraction of Mo [$\text{mol}_{Mo} \text{ g}_{cat}^{-1}$], and X is the conversion.

2.3.2. Dibenzothiophene (DBT) HDS

The HDS of DBT follows two distinct pathways; the DDS route which yields biphenyl (BP) as a product, and the HYD with cyclohexylbenzene (CHB) as the main product. As shown in Scheme 2.2, the C-S bonds cleavage directly without hydrogenating C=C bonds in the DDS route, while in the HYD route, the initial step consists of a gradual saturation of one aromatic ring adjacent to the ring containing sulfur to yield tetrahydro-dibenzothiophene (THDBT) and hexahydro-dibenzothiophene (HHDBT). Following hydrolysis of the C-S bond, CHB is formed. In some cases, CHB can be further hydrogenated to bicyclohexyl (BCH). As less H₂ is consumed to convert DBT into more desirable compounds, DDS is the preferred pathway for DBT HDS [53-55].



Scheme 2.2. Reaction network for DBT HDS over hydrotreating catalyst.

DBT HDS activity was measured in a fixed-bed high-pressure reactor (I.D. = 4 mm, length = 40 cm) under gas and liquid feed trickle flow conditions. Specifically, 200 mg oxidic

precursors (75 – 125 μm) diluted with 1 g SiC were loaded in the reactor and activated at 350 $^{\circ}\text{C}$ for 2 h in a 50 mL/min $\text{H}_2/\text{H}_2\text{S}$ (90/10 vol%) flow. After pretreatment, the temperature was decreased to 250 $^{\circ}\text{C}$, and the pressure was increased to 20 bar. The feed was then switched to the reaction feed, 4 wt% DBT and 2 wt% adamantane in n-hexadecane, with an LHSV of 9.2 hr^{-1} and an H_2/feed ratio of 200 L kg^{-1} . Adamantane was used as the internal reference compound for GC analysis. After remaining at these conditions for 12 h, the steady-state activity was determined. The temperature was then increased to 270 $^{\circ}\text{C}$ and subsequently to 300 $^{\circ}\text{C}$ to measure the corresponding steady-state activity. Products were analyzed by online GC-FID equipped with RTX-1 column with 0.32 mm I.D. and 30 m in length. The HDS reaction kinetic constant, k_{DBT} ($\text{mol mol}_{\text{Mo}}^{-1} \text{h}^{-1}$), was calculated assuming pseudo-first-order kinetics according to equation 12.

$$k_{\text{DBT}} = \left(-\frac{WHSV \omega_{\text{DBT}}}{\omega_{\text{Mo}}} \right) \ln(1 - X) \quad (12)$$

where $WHSV$ is the weight hourly space velocity, ω_{DBT} is the fraction of DBT, ω_{Mo} is the fraction of Mo, and X is the DBT conversion, calculated as follows.

$$X = \left(\frac{c_{\text{DBT}}(\text{inlet}) - c_{\text{DBT}}(\text{outlet})}{c_{\text{DBT}}(\text{inlet})} \right) \cdot 100\% \quad (13)$$

where c_{DBT} is the DBT concentration. The selectivity for DDS and HYD was calculated via

$$S_{\text{DDS}} = \frac{c_{\text{BP}}}{c_{\text{BP}} + c_{\text{CHB}} + c_{\text{BCH}}} \cdot 100\% \quad (14)$$

$$S_{\text{HYD}} = \frac{c_{\text{CHB}} + c_{\text{BCH}}}{c_{\text{BP}} + c_{\text{CHB}} + c_{\text{BCH}}} \cdot 100\% \quad (15)$$

TOF_{edge} , TOF normalized on total Mo edge sites of NiMoS species for catalysts, was calculated to estimate the DBT molecules reacted per second and Mo atom located on the edges of MoS_2 [56] via

$$\text{TOF}_{\text{edge}} = \frac{F_{\text{DBT}} \cdot X_{\text{DBT}} \cdot M_{\text{Mo}}}{W \cdot C_{\text{MoS}_2} \cdot D \cdot 3600} \quad (16)$$

where F_{DBT} is the reactant flow [mol h^{-1}], W is the weight of the catalyst [g], C_{MoS_2} is the effective Mo content in MoS_2 species (wt%), M_{Mo} is the molar mass of Mo and D is the dispersion of NiMoS.

2.3.3. Gas-oil HDS

Gas-oil is a real feed processed in refineries, and due to its composition, the sulfur removal kinetics in gas-oil is complex than the model feed test. Depending on the distribution of sulfur compounds and conversion degree [57], the apparent overall reaction order of gas-oil is between 1.5 and 2 [58]. As this is out of the scope of the present work, we will not

Chapter 2

discuss it further. The gas-oil feed used in this work contains 1.28 wt% S, 234 ppm N, and 1.20 mol kg⁻¹ aromatics.

Gas-oil HDS activity test was conducted in a fix-bed high-pressure reactor with a trickle flow of gas and liquid feed (60 bar, H₂/feed = 350 NL kg⁻¹, LHSV = 1.2 h⁻¹). The reactor (length : 240 mm, 4 mm I.D.) was packed with 0.75 mL catalyst extrudates and sandwiched between two layers of Zirblast (10 cm). Before reaction, catalysts were pretreated with gas-oil feed spiked with 2.69 wt% Sulfrzol at 200 °C for 5 h, the temperature was then increased to 280 °C for 5 h and finally to 315 °C for 5 h. After pretreatment, the temperature was cooled down to 200 °C, and the reaction feed was switched back to the test gas-oil feed. The temperature was then increased to reach a S content of ≤ 10 ppm; data point analysis was done after 470 h reaction time. The sulfur content in products was analyzed by atomic emission spectroscopy-inductively coupled plasma-mass spectroscopy (AES-ICP-MS). Samples out of the reaction were recovered and stored in the glovebox for further characterization.

2.4. References

- [1] J.W. Olesik, Elemental analysis using icp-oes and icp/ms, *Anal. Chem.*, 63 (1991) 12A-21A.
- [2] G. Tyler, S. Jobin Yvon, ICP-OES, ICP-MS and AAS Techniques Compared, ICP Optical Emission Spectroscopy Technical Note, 5 (1995).
- [3] N.W. Hurst, S.J. Gentry, A. Jones, B.D. McNicol, Temperature programmed reduction, *Catal. Rev.-Sci. Eng.*, 24 (1982) 233-309.
- [4] H.F.J. Van't Blik, J.W. Niemantsverdriet, Characterization of bimetallic FeRh/SiO₂ catalysts by temperature programmed reduction, oxidation and Mössbauer spectroscopy, *Appl. Catal.*, 10 (1984) 155-162.
- [5] J.L. Brito, J. Laine, Reducibility of Ni-Mo/Al₂O₃ catalysts: a TPR study, *J. Catal.*, 139 (1993) 540-550.
- [6] N.W. Hurst, S.J. Gentry, A. Jones and BD McNicol, *Catal. Rev.-Sci. Eng.*, 24 (1982) 233.
- [7] J. Torrent, V. Barrón, Diffuse reflectance spectroscopy, *Methods of soil analysis Part 5 – Mineralogical methods*, 5 (2008) 367-387.
- [8] V.M. Sellitto, V. Barrón, G. Palumbo, R. Salzano, C. Colombo, Uso della spettrometria di riflettanza diffusa (DRS) e bi-direzionale (BRF) per lo studio dei suoli vulcanici europei, *Rivista italiana di Telerilevamento*, 40 (2008) 21-34.
- [9] S.N. Thennadil, Relationship between the Kubelka-Munk scattering and radiative transfer coefficients, *JOSA A*, 25 (2008) 1480-1485.
- [10] L.F. Gate, Comparison of the photon diffusion model and Kubelka-Munk equation with the exact solution of the radiative transport equation, *Appl. Opt.*, 13 (1974) 236-238.
- [11] J. Tauc, R. Grigorovici, A. Vancu, Optical properties and electronic structure of amorphous germanium, *physica status solidi (b)*, 15 (1966) 627-637.
- [12] L.A. Lyon, C.D. Keating, A.P. Fox, B.E. Baker, L. He, S.R. Nicewarner, S.P. Mulvaney, M.J. Natan, Raman spectroscopy, *Anal. Chem.*, 70 (1998) 341-362.
- [13] P. Beccat, P. Da Silva, Y. Huiban, S. Kasztelan, Quantitative surface analysis by XPS: application to hydro-treating catalysts; Analyse quantitative de surface par XPS (X-ray photoelectron

- spectroscopy): application aux catalyseurs d'hydrotraitement, *Oil & Gas Science and Technology*, 54 (1999).
- [14] S. Kasztelan, H. Toulhoat, J. Grimblot, J.P. Bonnelle, A geometrical model of the active phase of hydrotreating catalysts, *Appl. Catal.*, 13 (1984) 127-159.
- [15] G. Berhault, M.P. De la Rosa, A. Mehta, M.J. Yácaman, R.R. Chianelli, The single-layered morphology of supported MoS₂-based catalysts–The role of the cobalt promoter and its effects in the hydrodesulfurization of dibenzothiophene, *Appl. Catal. A.*, 345 (2008) 80-88.
- [16] P.A. Nikulshin, A.V. Mozhaev, K.I. Maslakov, A.A. Pimerzin, V.M. Kogan, Genesis of HDT catalysts prepared with the use of Co₂Mo₁₀ HPA and cobalt citrate: Study of their gas and liquid phase sulfidation, *Appl. Catal. B.*, 158 (2014) 161-174.
- [17] P.A. Nikulshin, D.I. Ishutenko, A.A. Mozhaev, K.I. Maslakov, A.A. Pimerzin, Effects of composition and morphology of active phase of CoMo/Al₂O₃ catalysts prepared using Co₂Mo₁₀-heteropolyacid and chelating agents on their catalytic properties in HDS and HYD reactions, *J. Catal.*, 312 (2014) 152-169.
- [18] E.L. Kugler, M. Boudart, Ligand and ensemble effects in the adsorption of carbon monoxide on supported palladium-gold alloys, *J. Catal.*, 59 (1979) 201-210.
- [19] Y.J. Chabal, Surface infrared spectroscopy, *Surf. Sci. Rep.*, 8 (1988) 211-357.
- [20] M. Dierolf, A. Menzel, P. Thibault, P. Schneider, C.M. Kewish, R. Wepf, O. Bunk, F. Pfeiffer, Ptychographic X-ray computed tomography at the nanoscale, *Nature*, 467 (2010) 436-439.
- [21] J. Ihli, L. Bloch, F. Krumeich, K. Wakonig, M. Holler, M. Guizar-Sicairos, Th. Weber, J.C. da Silva, J.A. van Bokhoven, Hierarchical structure of NiMo hydrodesulfurization catalysts determined by ptychographic X-ray computed tomography, *Angew. Chem. Int. Ed.*, 59 (2020) 17266-17271.
- [22] F. Pfeiffer, X-ray ptychography, *Nat. Photonics*, 12 (2018) 9-17.
- [23] M. Holler, M. Guizar-Sicairos, E.H.R. Tsai, R. Dinapoli, E. Müller, O. Bunk, J. Raabe, G. Aeppli, High-resolution non-destructive three-dimensional imaging of integrated circuits, *Nature*, 543 (2017) 402-406.
- [24] K.A. Nugent, Coherent methods in the X-ray sciences, *Adv. Phys.*, 59 (2010) 1-99.
- [25] J.R. Fienup, Phase retrieval algorithms: a comparison, *Appl. Opt.*, 21 (1982) 2758-2769.
- [26] J. Miao, P. Charalambous, J. Kirz, D. Sayre, Extending the methodology of X-ray crystallography to allow imaging of micrometre-sized non-crystalline specimens, *Nature*, 400 (1999) 342-344.
- [27] H.N. Chapman, A. Barty, S. Marchesini, A. Noy, S.P. Hau-Riege, C. Cui, M.R. Howells, R. Rosen, H. He, J.C.H. Spence, High-resolution ab initio three-dimensional X-ray diffraction microscopy, *JOSA A*, 23 (2006) 1179-1200.
- [28] G.J. Williams, H.M. Quiney, B.B. Dhal, C.Q. Tran, K.A. Nugent, A.G. Peele, D. Paterson, M.D. de Jonge, Fresnel coherent diffractive imaging, *Phys. Rev. Lett.*, 97 (2006) 025506.
- [29] H.M.L. Faulkner, J.M. Rodenburg, Movable aperture lensless transmission microscopy: a novel phase retrieval algorithm, *Phys. Rev. Lett.*, 93 (2004) 023903.
- [30] J.M. Rodenburg, A.C. Hurst, A.G. Cullis, B.R. Dobson, F. Pfeiffer, O. Bunk, C. David, K. Jefimovs, I. Johnson, Hard-X-ray lensless imaging of extended objects, *Phys. Rev. Lett.*, 98 (2007) 034801.
- [31] A. Diaz, P. Trtik, M. Guizar-Sicairos, A. Menzel, P. Thibault, O. Bunk, Quantitative X-ray phase nanotomography, *Phys. Rev. B.*, 85 (2012) 020104.
- [32] M. Holler, A. Diaz, M. Guizar-Sicairos, P. Karvinen, E. Färm, E. Härkönen, M. Ritala, A. Menzel, J. Raabe, O. Bunk, X-ray ptychographic computed tomography at 16 nm isotropic 3D resolution, *Sci. Rep.*, 4 (2014) 3857.

Chapter 2

- [33] M. Holler, J. Raabe, A. Diaz, M. Guizar-Sicairos, C. Quitmann, A. Menzel, O. Bunk, An instrument for 3D X-ray nano-imaging, *Rev. Sci. Instrum.*, 83 (2012) 073703.
- [34] M. Holler, M. Odstrčil, M. Guizar-Sicairos, M. Lebugle, E. Müller, S. Finizio, G. Tinti, C. David, J. Zusman, W. Unglaub, et al., Three-dimensional imaging of integrated circuits with macro-to nanoscale zoom, *Nat. Electronics*, 2 (2019) 464-470.
- [35] M. Holler, J. Raabe, Error motion compensating tracking interferometer for the position measurement of objects with rotational degree of freedom, *Opt. Eng.*, 54 (2015) 054101.
- [36] M. Holler, J. Raabe, R. Wepf, S.H. Shahmoradian, A. Diaz, B. Sarafimov, T. Lachat, H. Walther, M. Vitins, OMNY PIN – A versatile sample holder for tomographic measurements at room and cryogenic temperatures, *Rev. Sci. Instrum.*, 88 (2017) 113701.
- [37] S. Gorelick, J. Vila-Comamala, V.A. Guzenko, R. Barrett, M. Salomé, C. David, High-efficiency Fresnel zone plates for hard X-rays by 100 keV e-beam lithography and electroplating, *J. Synchrotron Radiat.*, 18 (2011) 442-446.
- [38] M. Holler, J. Ihli, E.H.R. Tsai, F. Nudelmann, M. Verezhak, W.D.J. van der Bergd, S.H. Shahmoradian, A lathe system for micrometer-sized cylindrical sample preparation at room and cryogenic temperatures, *J. Synchrotron Radiat.*, 27(2) (2020) 472-476.
- [39] P.R. Shearing, J. Gelb, N.P. Brandon, X-ray nano computerized tomography of SOFC electrodes using a focused ion beam sample-preparation technique, *J. Eur. Ceram. Soc.*, 30 (2010) 1809-1814.
- [40] S.H. Shahmoradian, E.H.R. Tsai, A. Diaz, M. Guizar-Sicairos, J. Raabe, L. Spycher, M. Britschgi, A. Ruf, H. Stahlberg, M. Holler, Three-dimensional imaging of biological tissue by cryo X-ray ptychography, *Sci. Rep.*, 7 (2017) 6291.
- [41] M. Odstrčil, M. Lebugle, M. Guizar-Sicairos, C. David, M. Holler, Towards optimized illumination for high-resolution ptychography, *Opt. Express*, 27 (2019) 14981-14997.
- [42] M. Guizar-Sicairos, I. Johnson, A. Diaz, M. Holler, P. Karvinen, H.-C. Stadler, R. Dinapoli, O. Bunk, A. Menzel, High-throughput ptychography using Eiger: scanning X-ray nano-imaging of extended regions, *Opt. Express*, 22 (2014) 14859-14870.
- [43] I. Johnson, A. Bergamaschi, H. Billich, S. Cartier, R. Dinapoli, D. Greiffenberg, M. Guizar-Sicairos, B. Henrich, J. Jungmann, D. Mezza, A. Mozzanica, B. Schmitt, X. Shi, G. Tinti, Eiger: a single-photon counting X-ray detector, *J. Instrum.*, 9 (2014) C05032.
- [44] X. Huang, H. Yan, R. Harder, Y. Hwu, I.K. Robinson, Y.S. Chu, Optimization of overlap uniformness for ptychography, *Opt. Express*, 22 (2014) 12634-12644.
- [45] K. Wakonig, H.-C. Stadler, M. Odstrčil, E.H.R. Tsai, A. Diaz, M. Holler, I. Usov, J. Raabe, A. Menzel, M. Guizar-Sicairos, PtychoShelves, a versatile high-level framework for high-performance analysis of ptychographic data, *J. Appl. Crystallogr.*, 53 (2020) 574-586.
- [46] M. Odstrčil, M. Holler, J. Raabe, M. Guizar-Sicairos, Alignment methods for nanotomography with deep subpixel accuracy, *Opt. Express*, 27 (2019) 36637-36652.
- [47] M. van Heel, M. Schatz, Fourier shell correlation threshold criteria, *J. Struct. Biol.*, 151 (2005) 250-262.
- [48] M.R. Howells, T. Beetz, H.N. Chapman, C. Cui, J.M. Holton, C.J. Jacobsen, J. Kirz, E. Lima, S. Marchesini, H. Miao, D. Sayre, D.A. Shapiro, J.C.H. Spence, D. Starodub, An assessment of the resolution limitation due to radiation-damage in X-ray diffraction microscopy, *J. Electron Spectrosc. Relat. Phenom.*, 170 (2009) 4-12.
- [49] M. Daage, R.R. Chianelli, Structure-function relations in molybdenum sulfide catalysts: the "rim-edge" model, *J. Catal.*, 149 (1994) 414-427.
- [50] A.E. Hargreaves, J.R.H. Ross, An investigation of the mechanism of the hydrodesulfurization of thiophene over sulfided Co-Mo/Al₂O₃ catalysts: II. The effect of promotion by cobalt on the C-S

bond cleavage and double-bond hydrogenation/dehydrogenation activities of tetrahydrothiophene and related compounds, *J. Catal.*, 56 (1979) 363-376.

[51] K.F. McCarty, G.L. Schrader, Deuterodesulfurization of thiophene: an investigation of the reaction mechanism, *J. Catal.*, 103 (1987) 261-269.

[52] M.J. Girgis, B.C. Gates, Reactivities, reaction networks, and kinetics in high-pressure catalytic hydroprocessing, *Ind. Eng. Chem. Res.*, 30 (1991) 2021-2058.

[53] S.A. Ali, S. Ahmed, K.W. Ahmed, M.A. Al-Saleh, Simultaneous hydrodesulfurization of dibenzothiophene and substituted dibenzothiophenes over phosphorus modified CoMo/Al₂O₃ catalysts, *Fuel Process. Technol.*, 98 (2012) 39-44.

[54] P. Zheng, T. Li, K. Chi, C. Xiao, X. Wang, J. Fan, A. Duan, C. Xu, DFT insights into the direct desulfurization pathways of DBT and 4, 6-DMDBT catalyzed by Co-promoted and Ni-promoted MoS₂ corner sites, *Chem. Eng. Science*, 206 (2019) 249-260.

[55] K. Liu, F.T.T. Ng, Effect of the nitrogen heterocyclic compounds on hydrodesulfurization using in situ hydrogen and a dispersed Mo catalyst, *Catal. Today*, 149 (2010) 28-34.

[56] E.J.M. Hensen, P.J. Kooyman, Y. van der Meer, A.M. van der Kraan, V.H.J. de Beer, J.A.R. van Veen, R.A. van Santen, The relation between morphology and hydrotreating activity for supported MoS₂ particles, *J. Catal.*, 199 (2001) 224-235.

[57] G.B. Rabinovich, V.G. Dyrin, A.N. Loginova, M.A. Sharikhina, N.N. Tomina, Development of a mathematical description of the process of hydrodesulfurization of high-sulfur diesel fuel on a spherical wide-pore aluminocobaltmolybdenum catalyst, *Kinet. Catal.(Engl. Transl.);(United States)*, 29 (1988).

[58] H. Topsøe, B.S. Clausen, F.E. Massoth, *Hydrotreating Catalysis: Science and Technology*, in, Berlin, 1996 .

Chapter 2

Chapter 3

Catalyst Composition vs. Catalytic Activity

ABSTRACT

Two series of NiMo/Al₂O₃ catalysts with different Ni/Mo ratios were prepared from two sets of chemical sources ((NH₄)₆Mo₇O₂₄·4H₂O (AHM)/Ni(NO₃)₂·6H₂O and MoO₃/NiCO₃) by incipient wetness impregnation. It was validated that 0.40 is the optimal Ni/Mo ratio in NiMo/Al₂O₃ catalysts for hydrodesulfurization (HDS) process. Furthermore, the influence of calcination, organic additives, and chemical sources on the structure and catalytic activity of two series of 0.40NiMo/Al₂O₃ catalysts were systematically investigated. In each series of catalysts, different organic additives (citric acid (CA), ethylene glycol (EG), nitrilotriacetic acid (NTA), and malic acid (MA)) were added. Compared to the reference catalysts (^{dr}/AHM and ^{dr}/MoO₃), different degrees of improvement in the catalytic activity in both thiophene and dibenzothiophene (DBT) HDS were observed on the calcined catalysts and the catalysts with organic additives, except for NTA. Catalysts with NTA behaved differently in gas-phase thiophene and liquid-phase DBT HDS tests, where significant improvement was observed in the thiophene HDS test, while it showed no impact or even slightly inhibited the DBT HDS. The less active NiMoS particles formed in catalysts with NTA are responsible for the poor activity. More significant influence of chemical sources on catalyst structure and performance was observed for catalysts with additives, since the additives varies the pH level of the impregnation solutions and influences the aggregation of Mo precursors. Generally, the catalysts prepared from MoO₃/NiCO₃ are more active than their counterparts prepared from AHM/Ni(NO₃)₂. MA(1.2)/MoO₃ presents the optimal DBT HDS activity in all catalysts due to its high reducibility, metal dispersion, and high content of the active NiMoS phase. Contrarily, NTA(1.2)/AHM exhibits the least activity.

Chapter 3

3.1. Introduction

Hydrodesulfurization (HDS) is the most widely used process to remove sulfur from crude oils. Because of the varying feedstock quality and the strengthened environmental regulations, more efficient HDS catalysts are needed. HDS is generally carried out over alumina-supported NiMo sulfide catalyst [1], where the promoter atom, Ni, is deposited on the edge of MoS₂ and forms the so-called Ni-Mo-S active phase [2]. This type of catalyst is typically prepared in the form of the oxidic precursor by impregnation γ -Al₂O₃ with impregnation solution containing Ni and Mo followed by drying, calcination, and sulfidation in an H₂S/H₂ gas flow before use.

Preparation of the oxidic precursor is crucial to obtain a catalyst with excellent activity, and the key is the composition of the impregnation solution. In general, metal salts with good solubility in water are the optimal selection in the preparation of impregnation solutions. For instance, the aqueous solution of ammonium heptamolybdate ((NH₄)₆Mo₇O₂₄·4H₂O) and nickel nitrate (Ni(NO₃)₂·6H₂O) [3, 4], or molybdenum trioxide (MoO₃) and nickel carbonate (NiCO₃) [5], or sodium molybdate (Na₂MoO₄·2H₂O) and Ni(NO₃)₂·6H₂O [6] are commonly used for NiMo/Al₂O₃ catalysts preparation. Solutions containing highly condensed and symmetric starting materials, such as Keggin [7, 8] and Anderson complexes [9, 10], were also used. Phosphoric acid (H₃PO₄) is commonly added to the impregnation solution to facilitate metal dissolution. The metal cations and corresponding anions of different chemical sources coexist on the carrier surface during impregnation. Due to the distinct thermal decomposition behaviors and coordination capabilities of these coordination anions, the metal dispersion and metal-support interaction in the oxidic precursors could be different. This structural difference will be further reflected in their catalytic activity. Hence, choosing proper chemical compounds is the precondition for preparing the impregnation solution yielding good catalysts. Unfortunately, no general conclusion has been made regarding the optimal composition of the impregnation solution.

Besides chemical sources, adding organic additive (glycol-type additives or chelating agents) is another approach to enhance catalyst activity. For example, nitrilotriacetic acid (NTA) [5, 11] and ethylenediaminetetraacetic acid (EDTA) [12, 13] were reported to have dramatic influence on the sulfidation behavior of precursors. Generally, NTA and EDTA in the impregnation solution tend to form complex with Ni and Mo [11]. These complexes remain intact on the carrier surface after impregnation and drying procedure, which prevents the direct interaction of Ni and Mo with alumina [14, 15]. As a result, Ni and Mo are more likely to be converted into the active NiMoS phase during sulfidation. However, some controversial results about the promotion of NTA in catalyst performance were reported. L  lias et al. [16]

Catalyst Composition vs. Catalytic Activity

did not observe an apparent positive effect on catalyst activity in dibenzothiophene (DBT) HDS with NTA addition. Van Veen et al. [17] even found a slight decrease in the DBT HDS activity of the catalyst with NTA. Citric acid (CA) [18, 19], tartaric acid (TA) [20], and gluconic acid (GA) are another type of additives used in HDS catalyst preparation. This type of additive can also form complexes with Mo and Ni, which is beneficial to limit the interaction between metals and alumina carrier. The weakened metal-support interaction in favors the metal dispersion on alumina and enhance the reducibility of Mo [18]. Compared to the complexes formed with NTA or EDTA, van Haandel et al. [21] claimed that this type of complex is less stable. Also, due to the interaction between the OH group and the alumina surface, the non-chelating agents, glycols, decrease the metal-support interaction and enhance catalyst activity [22]. On the other hand, the content of the promoters has also been discussed, as it is considered to have significant influence on the structure of the active phase and catalytic activity [23, 24]. Although numerous studies have been performed on related topic, a systematic study on the influence of varying additives on the structure of oxidic precursors and catalytic activity is still rare.

In current work, we investigated the effect of the calcination process, organic additives, and chemical sources on catalyst structure and activity. Two series of catalysts were synthesized from two sets of chemical sources, AHM/Ni(NO₃)₂ and MoO₃/NiCO₃, and CA, EG, NTA, and MA were added in each series of catalysts. X-ray diffraction (XRD), temperature-programmed reduction (TPR), Raman, transmission electron microscopy (TEM), and X-ray photoelectron spectroscopy (XPS) were used to characterize catalyst structure, and their activity was evaluated through the HDS of thiophene and DBT.

3.2. Experimental section

3.2.1. Materials

The chemicals used in this chapter have been listed in Section 2.1, Chapter 2. The same industrial γ -Al₂O₃ carrier (surface area: 300 m² g⁻¹, pore volume: 0.82 cm³ g⁻¹, pore diameter: 8.5 nm) as previous studies [25, 26] was used.

3.2.2. Catalyst preparation

3.2.2.1. *x*NiMo/AHM & *x*NiMo/MoO₃

Two series of NiMo/Al₂O₃ catalysts containing 15 wt% Mo, 2 wt% P (referring to MoO₃ and P₂O₅), and different amounts of Ni (1.67, 2.67, 3.67, 4.67, and 5.67 wt% Ni) were prepared by incipient wetness impregnation of γ -Al₂O₃ extrudates (diameter: 1 mm, length: 3 – 13

Chapter 3

mm) with an aqueous solution of AHM/Ni(NO₃)₂/H₃PO₄ or MoO₃/NiCO₃/H₃PO₄. The impregnation solutions are prepared as follows:

Impregnation solutions using AHM/Ni(NO₃)₂ as metal sources: 2.5 g AHM was dissolved into the H₃PO₄ solution (0.6 mL, 85 wt% in H₂O). Ammonia solution (28 wt%) was used to yield a clear solution. 0.7 – 2.6 g Ni(NO₃)₂ was added into above solution under continuous stirring. After the transparent green solution was obtained, the volume of the solution was adjusted to the total pore volume of alumina with deionized water.

Impregnation solutions using MoO₃/NiCO₃ as metal sources: 0.6 mL H₃PO₄ solution (85 wt% in H₂O), 2.0 g MoO₃, and 0.3 – 1.1 g NiCO₃ were dissolved into deionized water. The mixture was heated till the solution was boiling to speed up the dissolution process. After the transparent green solution was obtained, the volume of the solution was adjusted to the total pore volume of alumina with water.

The impregnated extrudates were kept under slow movement on a roller bank for 2 h and dried at 120 °C overnight. The obtained catalysts are referred to as *x*NiMoP/AHM and *x*NiMoP/MoO₃, where *x* is the molar ratio of Ni/Mo (0.18 – 0.62), AHM and MoO₃ represent the used chemical sources. For example, 0.18NiMoP/MoO₃ means the molar ratio of Ni/Mo is 0.18, and the impregnation solution was prepared using MoO₃/NiCO₃ as chemical sources.

3.2.2.2. *Y*(1.2)/AHM & *Y*(1.2)/MoO₃

Two series of 0.40NiMoP/Al₂O₃ catalysts were prepared from the above-mentioned two sets of chemical sources by incipient wetness impregnation, and CA, EG, NTA, and MA were added in both series. The target composition is 15 wt% Mo, 3.67 wt% Ni, 2 wt% P, and the molar ratio of additives/Mo is set as 1.2. The ratio was chosen to obtain the catalyst with optimal performance [27]. The impregnation solution was prepared as described above, and the respective organic additives were added after the metal salts were dissolved. After impregnation, the extrudates were kept under slow movement on a roller bank for 2 h, and then dried overnight at 120 °C and further calcined at 400 °C for 2 h. To avoid the decomposition of the organic additives before sulfidation, catalysts with organic additives were dried without further calcination. These catalysts are designated as *Y*(1.2)/AHM (^{cal/dr}/AHM) or *Y*(1.2)/MoO₃ (^{cal/dr}/MoO₃), where *Y* represents the organic additive, AHM and MoO₃ are the used chemical sources.

The final metal loadings were determined by inductively coupled plasma optical emission spectroscopy (ICP-OES), and the results are displayed in Tables 3.1, 3.3, and A1.

Catalyst Composition vs. Catalytic Activity

Table 3.1. Metal composition and textural properties of x NiMoP/MoO₃ catalysts as determined by ICP-OES¹ and N₂ physisorption².

Catalyst	Metal loading (wt%) ¹			Ni/Mo molar ratio ¹	Surface area ^{2a} (m ² /g)	Pore volume ^{2b} (cm ³ /g)	Pore diameter ^{2b} (nm)
	Mo	Ni	P				
0.18NiMoP/MoO ₃	13.3	1.4	1.9	0.18	187.1	0.45	9.84
0.29NiMoP/MoO ₃	12.8	2.2	1.8	0.28	199.7	0.47	9.36
0.40NiMoP/MoO ₃	12.4	2.9	1.7	0.38	204.1	0.43	9.22
0.51NiMoP/MoO ₃	12.2	3.6	1.7	0.48	195.6	0.43	9.98
0.62NiMoP/MoO ₃	13.0	4.6	1.8	0.58	193.8	0.41	9.99
γ -Al ₂ O ₃	--	--	--	--	300.0	0.80	9.00

^a: The specific surface area was calculated using the Brunauer-Emmett-Teller (BET) equation.

^b: Total pore volume and pore diameter were determined by an adsorption branch of isotherm using the Barrett-Joyner-Halenda (BJH) model.

3.2.3. Catalytic activity measurement

Thiophene, DBT, and gas-oil HDS tests were performed to evaluate catalyst performance, and the details can be found in Sections 2.3, Chapter 2.

3.2.4. Catalyst activation

The sulfided catalyst samples were prepared by loading ~50 mg oxidic precursor (75 – 125 μ m) in the middle of a valve-sealed stainless-steel reactor (inner diameter: 4 mm), which was then heated up to 350 °C with a ramp rate of 2 °C/min (6 °C/min, without additives) under 1 bar H₂S/H₂ (10/90 vol%) at a flow rate of 50 mL/min. After 2 h, the reactor was cooled down to room temperature under He flow. Sulfided samples were obtained and stored in an N₂-filled glovebox (H₂O < 1 ppm, O₂ < 1 ppm) for further characterization.

3.2.5. Catalyst characterization

The textural properties of x NiMoP/AHM and x NiMoP/MoO₃ were determined by N₂ adsorption at 79 K on a Micromeritics Tristar 3020 instrument. Before measurement, all samples were pretreated at 120 °C under N₂ atmosphere for at least 6 h. TPR, Raman spectroscopy, XRD, XPS, and TEM measurements were performed as described in Section 2.2, Chapter 2.

3.3. Results

3.3.1. x NiMoP/MoO₃ and x NiMoP/AHM

The elemental composition and Ni/Mo molar ratio of x NiMoP/MoO₃ catalysts listed in Table 3.1 are close to the theoretical values, indicating that the catalysts are successfully prepared. N₂ physisorption data show that these samples have a comparable surface area, pore size, and

Chapter 3

pore volume. After metal deposition, the corresponding surface area and pore volume were considerably decreased as expected [28]. A comparable degree of the crystallinity of these catalysts was also observed in their XRD patterns (Figure A1), where five peaks at 19.4°, 37.7°, 39.5°, 45.9°, and 66.9° associated with γ -Al₂O₃ (JCPDS 01-077-0396) were detected [29]. The absence of the typical features of Mo and Ni oxide suggests that the metal oxides are well dispersed on the alumina surface.

The catalyst catalytic activity of these catalysts was evaluated in the HDS of thiophene and DBT. Results in Table 3.2 show that reaction rates in thiophene HDS exhibit a typical volcano shape, which first increase with the increasing amounts of Ni and reach the maximum (73.5 ± 1.3 mol mol_{Mo}⁻¹ h⁻¹) at a molar ratio of Ni/Mo = 0.51, and then decrease by further increase the Ni content. The activity trends in DBT HDS are similar, but the maximum reaction rates appeared at a Ni/Mo ratio of 0.40 (5.0 mol mol_{Mo}⁻¹ h⁻¹ at 250 °C, 19.5 mol mol_{Mo}⁻¹ h⁻¹ at 270 °C, and 242.1 mol mol_{Mo}⁻¹ h⁻¹ at 300 °C). Given the substantial difference between these two test reactions [30], i.e., the size of the thiophene and DBT molecules and different C-S bond strengths, the observed activity differences are reasonable. As DBT is more realistically reflecting the properties of sulfur-containing molecules in a real feed [31], the DBT HDS activity has more reference value [32]. Thus, a Ni/Mo molar ratio of 0.40 is regarded as the optimal composition of catalysts, as found in DBT HDS.

Table 3.2. Thiophene HDS and DBT HDS activity of x NiMoP/MoO₃ catalysts.

Catalyst	Thiophene	DBT		
	Reaction rates (mol mol _{Mo} ⁻¹ h ⁻¹)	Reaction temperature	Reaction rates (mol mol _{Mo} ⁻¹ h ⁻¹)	Conversion (%)
			k _{HDS}	
0.18NiMoP/MoO ₃	44.3 ± 2.1	250 °C	1.9	5.1
		270 °C	9.5	23.1
		300 °C	69.6	85.5
0.29NiMoP/MoO ₃	50.5 ± 0.4	250 °C	3.9	9.8
		270 °C	16.0	34.7
		300 °C	233.2	99.8
0.40NiMoP/MoO ₃	66.1 ± 1.7	250 °C	5.0	12.0
		270 °C	19.5	39.3
		300 °C	242.1	99.8
0.51NiMoP/MoO ₃	73.5 ± 1.3	250 °C	3.5	8.45
		270 °C	17.2	35.3
		300 °C	230.1	99.7
0.62NiMoP/MoO ₃	53.3 ± 1.2	250 °C	2.9	7.4
		270 °C	14.3	32.0
		300 °C	230.0	99.8

To ensure the optimal Ni/Mo molar ratio we obtained in x NiMoP/MoO₃ catalysts is also valid for catalysts prepared from AHM/Ni(NO₃)₂, the corresponding x NiMoP/AHM were

Catalyst Composition vs. Catalytic Activity

synthesized and characterized. The metal composition and textural properties shown in Table A1 present a consistent conclusion as $x\text{NiMoP}/\text{MoO}_3$ catalysts. The catalytic activity in thiophene, DBT, and gas-oil HDS (Table A2) shows that the catalyst with a molar ratio of $\text{Ni}/\text{Mo} = 0.40$ ($0.40\text{NiMoP}/\text{AHM}$) is the most active, which is identical to the activity trend observed in $x\text{NiMoP}/\text{MoO}_3$ DBT HDS.

3.3.2. $Y(1.2)/\text{AHM}$ and $Y(1.2)/\text{MoO}_3$

3.3.2.1. Catalytic activity

Table 3.3 shows the elemental composition of $Y(1.2)/\text{AHM}$ ($^{\text{cal/dr}}/\text{AHM}$) and $Y(1.2)/\text{MoO}_3$ ($^{\text{cal/dr}}/\text{MoO}_3$) catalysts. Ni/Mo molar ratios are in line with the theoretical value of 0.40, Mo, Ni, and P loadings are slightly lower due to the presence of organic additives, which would be decomposed during the sulfidation.

Table 3.3. Elemental composition of oxide NiMo catalysts.

Catalyst	Metal loading (wt%)			Ni/Mo molar ratio
	Mo	Ni	P	
$^{\text{dr}}/\text{AHM}$	12.7	3.4	1.6	0.44
$^{\text{cal}}/\text{AHM}$	14.1	3.	1.8	0.39
CA(1.2)/AHM	9.3	2.3	1.3	0.40
EG(1.2)/AHM	12.8	2.9	1.8	0.38
NTA(1.2)/AHM	8.9	2.0	1.3	0.36
MA(1.2)/AHM	11.3	2.7	1.5	0.40
$^{\text{dr}}/\text{MoO}_3$	12.4	2.9	1.7	0.38
$^{\text{cal}}/\text{MoO}_3$	12.7	3.0	1.7	0.38
CA(1.2)/MoO ₃	9.8	2.2	1.4	0.36
EG(1.2)/MoO ₃	11.9	2.8	1.6	0.38
NTA(1.2)/MoO ₃	10.0	2.3	1.4	0.36
MA(1.2)/MoO ₃	11.4	2.7	1.6	0.39

The catalytic activity of catalysts was evaluated in the HDS of thiophene and DBT. As displayed in Table 3.4, among the catalysts prepared from $\text{AHM}/\text{Ni}(\text{NO}_3)_2$, $^{\text{dr}}/\text{AHM}$ presents the lowest reaction rate of $62.9 \text{ mol mol}_{\text{Mo}}^{-1} \text{ h}^{-1}$ in thiophene HDS. $^{\text{cal}}/\text{AHM}$ has a comparable thiophene HDS activity ($63.1 \text{ mol mol}_{\text{Mo}}^{-1} \text{ h}^{-1}$) with $^{\text{dr}}/\text{AHM}$. CA(1.2)/AHM ($78.1 \text{ mol mol}_{\text{Mo}}^{-1} \text{ h}^{-1}$), EG(1.2)/AHM ($74.0 \text{ mol mol}_{\text{Mo}}^{-1} \text{ h}^{-1}$), and MA(1.2)/AHM ($74.1 \text{ mol mol}_{\text{Mo}}^{-1} \text{ h}^{-1}$) are ca. 1.2 times more active than $^{\text{dr}}/\text{AHM}$, and NTA(1.2)/AHM is the most active with a reaction rate of $101.1 \text{ mol mol}_{\text{Mo}}^{-1} \text{ h}^{-1}$. Similarly, the enhancement of catalytic activity by the calcination and organic additives was also observed in the catalysts prepared from $\text{MoO}_3/\text{NiCO}_3$. According to the reaction rates in thiophene HDS, $^{\text{cal}}/\text{MoO}_3$, CA(1.2)/MoO₃, EG(1.2)/MoO₃, NTA(1.2)/MoO₃ and MA(1.2)/MoO₃ exhibit higher performance than $^{\text{dr}}/\text{MoO}_3$ ($66.1 \text{ mol mol}_{\text{Mo}}^{-1} \text{ h}^{-1}$). In both series of catalysts, the catalyst with NTA shows the highest activity. Besides, it is worth noting that compared to catalysts prepared from $\text{AHM}/\text{Ni}(\text{NO}_3)_2$, the counterparts prepared from $\text{MoO}_3/\text{NiCO}_3$ show higher activity.

Table 3.4. Thiophene and DBT HDS results.

Catalyst	Thiophene		DBT										
	Reaction rates (mol mol _{Mo} ⁻¹ h ⁻¹)	Reaction temperature	Reaction rates (mol mol _{Mo} ⁻¹ h ⁻¹)		Selectivity					Conversion		TOF _{edge} (s ⁻¹)	
			k _{HDS}	k _{DBT}	BP	CHB	BCH	DDS : HYD	X (%)				
dr/AHM	62.9 ± 2.3	250 °C	3.2	58.1	41.9	0	1.4	8.1	0.06				
		270 °C	11.8	54.3	45.7	0	1.2	26.7	--				
		300 °C	93.0	54.5	45.5	0	1.3	91.3	--				
eml/AHM	63.1 ± 1.6	250 °C	4.4	63.3	36.7	0	1.8	12.0	0.07				
		270 °C	16.4	61.5	38.5	0	1.7	38.2	--				
		300 °C	162.1	59.9	40.1	0	1.8	99.1	--				
CA(1.2)/AHM	78.1 ± 0.8	250 °C	4.6	71.4	28.6	0	2.5	8.4	0.03				
		270 °C	17.9	64.5	35.5	0	1.9	29.2	--				
		300 °C	151.3	57.8	42.2	0	1.6	94.6	--				
EG(1.2)/AHM	74.0 ± 6.1	250 °C	5.7	59.8	40.2	0	1.5	14.1	0.09				
		270 °C	18.4	59.2	40.8	0	1.5	38.8	--				
		300 °C	78.1	49.9	50.1	0	1.0	87.5	--				
NTA(1.2)/AHM	101.1 ± 0.6	250 °C	1.6	69.6	30.4	0	2.2	2.9	0.02				
		270 °C	7.9	47.7	52.3	0	0.9	13.6	--				
		300 °C	71.3	40.7	59.3	0	0.6	73.4	--				
MA(1.2)/AHM	74.1 ± 1.7	250 °C	7.8	83.8	16.2	0	5.2	16.7	0.06				
		270 °C	17.7	75.6	24.4	0	3.1	34.1	--				
		300 °C	46.3	62.4	37.6	0	1.7	66.4	--				
dr/MoO ₃	66.1 ± 1.7	250 °C	5.0	62.3	37.7	0	1.7	12.0	0.05				
		270 °C	19.4	60.1	39.9	0	1.6	39.3	--				
		300 °C	237.3	58.0	42.0	0	1.0	99.8	--				
eml/MoO ₃	74.9 ± 1.4	250 °C	5.1	61.7	38.3	0	1.6	12.5	0.05				
		270 °C	19.2	59.9	40.1	0	1.6	39.8	--				
		300 °C	213.9	58.5	41.5	0	1.6	99.6	--				

Catalyst Composition vs. Catalytic Activity

CA(1.2)/MoO ₃	250 °C	13.8	62.3	37.7	0	1.7	30.0	0.11
	270 °C	50.3	60.2	39.8	0	1.5	62.0	--
	300 °C	486.5	49.9	50.1	0	1.0	99.7	--
EG(1.2)/MoO ₃	250 °C	9.1	52.7	47.3	0	1.1	20.2	0.07
	270 °C	31.8	51.2	48.8	0	1.1	54.6	--
	300 °C	398.9	40.6	59.4	0	0.6	100	--
NTA(1.2)/MoO ₃	250 °C	8.3	86.5	13.5	0	6.5	14.3	0.05
	270 °C	18.9	73.6	26.4	0	3.0	29.4	--
	300 °C	82.4	63.6	36.4	0	2.1	78.2	--
MA(1.2)/MoO ₃	250 °C	30.6	54.3	45.7	0	1.2	51.3	0.13
	270 °C	81.2	50.7	49.3	0	1.0	85.2	--
	300 °C	276.6	49.2	47.7	3.1	1.0	100	--

Chapter 3

The promotional effect of calcination and additives was also observed in DBT HDS. For example, MA(1.2)/AHM is 1.4 times more active than dr /AHM at 250 °C; MA(1.2)/MoO₃, the most active among the catalysts prepared from MoO₃/NiCO₃, shows a 5.1 times higher activity than dr /MoO₃ at 250 °C. However, the performance of catalysts with NTA is inconsistent with the observation in thiophene HDS. NTA(1.2)/AHM is less active than dr /AHM, and NTA(1.2)/MoO₃ only shows a comparable activity with dr /MoO₃. The reaction rates at 250 °C and 270 °C decrease as the following order: MA(1.2)/AHM > EG(1.2)/AHM > CA(1.2)/AHM > cal (1.2)/AHM > dr (1.2)/AHM > NTA(1.2)/AHM and MA(1.2)/MoO₃ > CA(1.2)/MoO₃ > EG(1.2)/MoO₃ > NTA(1.2)/MoO₃ > cal (1.2)/AHM > dr (1.2)/AHM. Furthermore, the differences in catalytic activity between the catalysts prepared from different chemical sources were also observed. Generally, catalysts prepared from MoO₃/NiCO₃ are relatively more active than those prepared from AHM/Ni(NO₃)₂, but the gap of catalytic activity between the two series of catalysts gradually decreases with the increasing temperature.

Besides reaction rates, DBT conversion, product distribution, and turnover frequency (TOF_{edge}) are also listed in Table 3.4. As described in Section 2.3, Chapter 2, DBT conversion follows two distinct pathways: the direct desulfurization (DDS) pathway and the hydrogenation (HYD) pathway. The DDS route yields biphenyl (BP) as the main product, and cyclohexylbenzene (CHB) is the main product of the HYD route. Bicyclohexyl (BCH) can also be observed under certain circumstances. The primary reaction pathway in this work is DDS, as the selectivity to BP in our catalysts system ranges from 53 % to 84 % at 250 °C. The proportion of the DDS pathway decreases with increasing temperature, as shown in Table 3.4. To explain the activity changes of catalysts depending on the composition and characteristics of the active NiMoS species, the turnover frequencies (TOF, s⁻¹) normalized by the total Mo edge sites (Mo^{IV}_{edge}) of NiMoS species were calculated according to equation 16 in Chapter 2. Among these catalysts, MA(1.2)/MoO₃ shows the maximum TOF_{edge} value, and the catalyst with NTA addition is the least active in both series of catalysts.

3.3.2.2. Characterization of the oxidic precursors

To investigate the reasons for the activity difference of catalysts, a more detailed structural characterization of these catalysts was carried out. The physiochemical structure of oxidic precursors was measured using XRD, TPR, and Raman spectroscopy.

Figure 3.1 shows the XRD patterns of oxide NiMo catalysts, where four broad diffraction peaks located at $2\theta = 37.7^\circ$, 39.5° , 45.9° , and 66.9° , attributed to γ -Al₂O₃ (JCPDS 01-077-0396), were detected in all samples. Except for MA(1.2)/AHM, no other apparent signals of

Catalyst Composition vs. Catalytic Activity

crystalline phases were observed, suggesting the good dispersion of metal oxides on the alumina carrier. For MA(1.2)/AHM, another set of sharp peaks at $2\theta = 21.2^\circ, 24.0^\circ, 26.3^\circ, 30.6^\circ, 32.5^\circ, 36.0^\circ, 43.9^\circ, 48.1^\circ, 50.6^\circ, 51.9^\circ, 55.6^\circ, 62.7^\circ,$ and 64.7° were detected, suggesting the existence of crystalline $(\text{NH}_4)_3\text{PO}_4(\text{MoO}_3)_{12}\cdot 4\text{H}_2\text{O}$, which may form in the impregnation solution or on the alumina surface during the drying process.

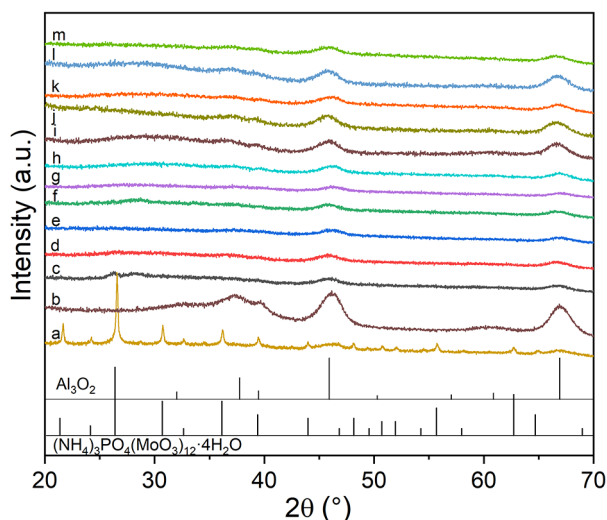


Figure 3.1. XRD patterns of oxidic precursors of a) MA(1.2)/AHM b) $\gamma\text{-Al}_2\text{O}_3$ c) dr/AHM d) cal/AHM e) CA(1.2)/AHM f) EG(1.2)/AHM g) NTA(1.2)/AHM h) MoO_3 i) cal/MoO_3 j) CA(1.2)/ MoO_3 k) EG(1.2)/ MoO_3 l) NTA(1.2)/ MoO_3 m) MA(1.2)/ MoO_3 .

Figure 3.2 shows the TPR profiles of the oxidic catalysts. In general, the reduction profiles of these catalysts are comparable, which all exhibit a sharp peak with intense H_2 consumption at a low reduction temperature, ca. 400°C . Additionally, continuous H_2 consumption is presented in a broad temperature region with a maximum centered at ca. 700°C [33]. According to the literature, peaks at low temperatures can be assigned to the reduction of Ni oxide species and different polymolybdates in weak connection with the support surface [34], and the broad features at high temperatures are attributed to the deep reduction of all other Mo species, including tetrahedral Mo^{4+} species strongly binding to the support. In $\text{NiMo}/\text{Al}_2\text{O}_3$ catalyst system, Ni^{2+} species are usually reduced simultaneously with Mo^{6+} in the low-temperature area, resulting in overlapping reduction peaks [35, 36]. This overlap increases the difficulty of extracting the reduction information of Ni. Also, as Mo is the main phase, only the behavior of Mo reduction is discussed here.

The reduction peak area is positively quantitatively related to H_2 consumption. By comparing the area of reduction peaks, partial reduction of Mo^{6+} into Mo^{4+} is considered to be the main reduction reaction, as most of the H_2 is consumed in this process. The temperature of the

Chapter 3

main reduction peak (T_m) was monitored, where T_m of $^{dr}/\text{AHM}$, $^{cal}/\text{AHM}$, $\text{CA}(1.2)/\text{AHM}$, $\text{EG}(1.2)/\text{AHM}$, $\text{NTA}(1.2)/\text{AHM}$, and $\text{MA}(1.2)/\text{AHM}$ is detected to be 409 °C, 398 °C, 404 °C, 399 °C, 421 °C, and 403 °C, respectively. $^{dr}/\text{MoO}_3$, $^{cal}/\text{MoO}_3$, $\text{CA}(1.2)/\text{MoO}_3$, $\text{EG}(1.2)/\text{MoO}_3$, $\text{NTA}(1.2)/\text{MoO}_3$ and $\text{MA}(1.2)/\text{MoO}_3$ show the T_m of 410 °C, 401 °C, 399 °C, 397 °C, 412 °C, and 390 °C. In both series of catalysts, catalysts after calcination or with other organic additives show lower T_m than the reference catalyst ($^{dr}/\text{AHM}$ or $^{dr}/\text{MoO}_3$) except for NTA. The reduced T_m indicated the weaker metal-support interaction in these catalysts. It is noticed that $^{dr}/\text{AHM}$ and $^{dr}/\text{MoO}_3$ have comparable reducibility, so as $^{cal}/\text{AHM}$ and $^{cal}/\text{MoO}_3$. Whereas the catalysts prepared from $\text{MoO}_3/\text{NiCO}_3$ combined with additives show higher reducibility than their counterparts prepared from $\text{AHM}/\text{Ni}(\text{NO}_3)_2$.

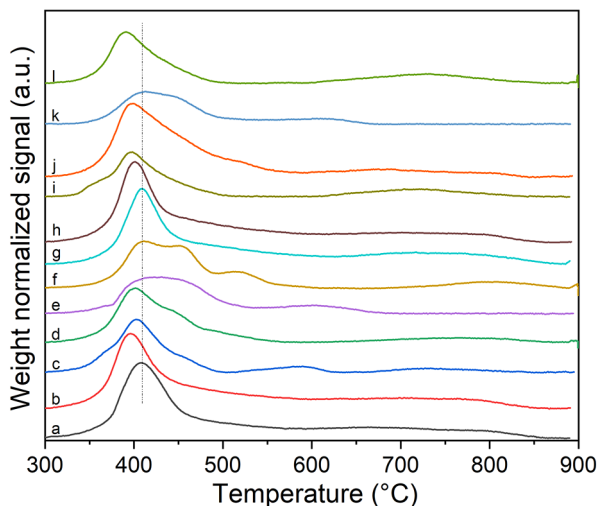


Figure 3.2. TPR profiles of the oxidic precursors of a) $^{dr}/\text{AHM}$ b) $^{cal}/\text{AHM}$ c) $\text{CA}(1.2)/\text{AHM}$ d) $\text{EG}(1.2)/\text{AHM}$ e) $\text{NTA}(1.2)/\text{AHM}$ f) $\text{MA}(1.2)/\text{AHM}$ g) $^{dr}/\text{MoO}_3$ h) $^{cal}/\text{MoO}_3$ i) $\text{CA}(1.2)/\text{MoO}_3$ j) $\text{EG}(1.2)/\text{MoO}_3$ k) $\text{NTA}(1.2)/\text{MoO}_3$ l) $\text{MA}(1.2)/\text{MoO}_3$.

Besides the difference in T_m , the shape of the TPR profiles of the catalysts was also different, especially in the low-temperature reduction region. For example, in the TPR profile of $^{dr}/\text{AHM}$, only one symmetric sharp peak was observed, which indicates that the metal-support interaction in $^{dr}/\text{AHM}$ was relatively uniform. However, in the TPR profile of $\text{EG}(1.2)/\text{AHM}$, one peak and two low-intensity shoulders were detected. The different Mo-support interactions derived from the different polymolybdate species on the alumina surface should be responsible for these three peaks. The distinct polymolybdate species were also observed in other catalysts with additives, suggesting that additives did change the Mo coordination during the preparation.

The Raman spectroscopy was performed to explore the nature of Mo and Ni oxide species presenting on the alumina surface [14]. As shown in Figure 3.3, four samples without organic

Catalyst Composition vs. Catalytic Activity

additives ($^{dr}/AHM$, $^{cal}/AHM$, $^{dr}/MoO_3$, and $^{cal}/MoO_3$) have comparable characteristics with five bands located at 950 cm^{-1} , 910 cm^{-1} , 570 cm^{-1} , 360 cm^{-1} , and 220 cm^{-1} . According to the literature, the strong band at 950 cm^{-1} with a broad low-frequency shoulder at 910 cm^{-1} and two less intense bands at 360 cm^{-1} and 220 cm^{-1} are the characteristics of the vibrational signature of octahedrally coordinated polymolybdate species [37, 38]. In detail, the band at 950 cm^{-1} is assigned to the $\nu_s(\text{Mo}=\text{O})$ stretching modes of $\text{Mo}=\text{O}_t$ structure in $\text{Mo}_7\text{O}_{24}^{6-}$ species [39, 40]. The band at 360 cm^{-1} is assigned to the $\delta(\text{Mo}=\text{O})$ deformation modes of $\text{Mo}=\text{O}_t$ groups, and the band at 220 cm^{-1} is due to the $\delta(\text{Mo}-\text{O}-\text{Mo})$ deformation vibration of $\text{Mo}-\text{O}-\text{Mo}$ bonds in polymolybdate species [41, 42]. The band at 570 cm^{-1} is assigned to $\text{Al}-\text{O}$ stretching mode [43]. Besides, the band at 1045 cm^{-1} observed in $^{dr}/AHM$ is due to the $\nu_s(\text{NO}_3)$ stretching vibration of the NO_3^- group originating from $\text{Ni}(\text{NO}_3)_2$ [44], which was also detected in the other four dried-only catalysts prepared from $\text{AHM}/\text{Ni}(\text{NO}_3)_2$ ($\text{CA}(1.2)/\text{AHM}$, $\text{EG}(1.2)/\text{AHM}$, $\text{NTA}(1.2)/\text{AHM}$, $\text{MA}(1.2)/\text{AHM}$). As nitrate would decompose under higher temperature, it was not observed in the spectrum of $^{cal}/\text{AHM}$.

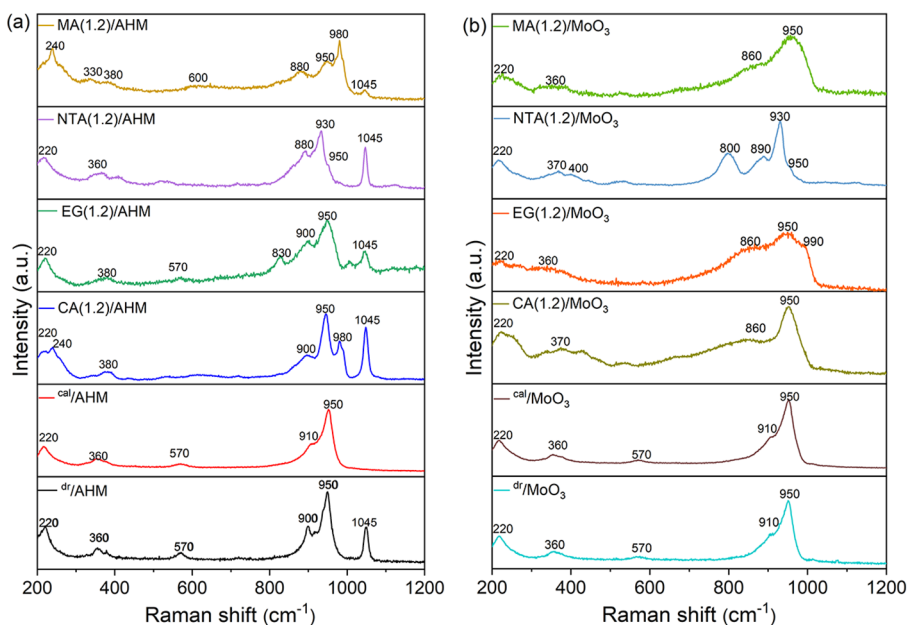


Figure 3.3. Raman spectra of oxide catalysts.

Changes in the Mo coordination were observed in the catalysts with organic additives. Besides the bands described above, bands at 980 cm^{-1} , 880 cm^{-1} , 600 cm^{-1} , 380 cm^{-1} , and 240 cm^{-1} were also observed in $\text{MA}(1.2)/\text{AHM}$. Bands at 980 cm^{-1} and 880 cm^{-1} are assigned to the $\nu_s(\text{Mo}=\text{O})$ and $\nu_{as}(\text{Mo}=\text{O})$ stretching vibration of $\text{Mo}=\text{O}_t$ structures in $[\text{PMo}_{12}\text{O}_{40}]^{3-}$ species [45], which has been identified in its XRD pattern. The band at 380 cm^{-1} is due to the $\delta(\text{Mo}=\text{O})$ deformation mode of $\text{Mo}=\text{O}_t$ groups, and the one at 240 cm^{-1} can be assigned to

Chapter 3

the $\delta(\text{Mo-O-Mo})$ deformation mode of Mo-O-Mo groups in $[\text{PMo}_{12}\text{O}_{40}]^{3-}$ species [46]. In the spectrum of CA(1.2)/AHM, bands at 980 cm^{-1} , 380 cm^{-1} , and 240 cm^{-1} were observed, which can be respectively attributed to the $\nu_s(\text{Mo=O})$ stretching vibration, the $\delta(\text{Mo=O})$ deformation mode of Mo=O_t structures and the $\delta(\text{Mo-O-Mo})$ deformation mode of Mo-O-Mo in the aggregated molybdenum species, e.g., $\text{Mo}_8\text{O}_{26}^{4-}$ [47, 48]. The band observed at 830 cm^{-1} in EG(1.2)/AHM is due to the $\nu_{\text{as}}(\text{Mo=O})$ stretching vibration of Mo=O_t structures in tetrahedrally coordinated molybdate species [49]. Besides the characteristics of octahedrally coordinated polymolybdenum species, a band at 930 cm^{-1} in NTA(1.2)/AHM was also observed, which relates to the $\nu_{\text{as}}(\text{Mo=O})$ stretching vibration of Mo=O_t structures in $\text{Mo}_8\text{O}_{26}^{4-}$ species [50]. In CA(1.2)/ MoO_3 , a band at 860 cm^{-1} was detected and assigned to the $\nu_s(\text{Mo-O-Mo})$ stretching vibration of Mo-O-Mo structures of surface molybdate in octahedral coordination [48]. Beyond the difference in coordination state, it is worth discussing the shape of the bands. Normally, the bandwidth in Raman spectra can reflect the degrees of crystallinity to some extent, e.g., the broader bands in MA(1.2)/ MoO_3 and EG(1.2)/ MoO_3 indicate higher metal dispersion and structural disorder degree. The difference of the Mo coordination in oxidic precursors has already presented in the respective impregnation solutions (Figure A2), which is attributed to the pH-dependent feature of Mo aggregation and the formation of the different species, e.g., MoO_4^{2-} or $\text{Mo}_7\text{O}_{24}^{6-}$.

3.3.2.3. Catalyst sulfidation

The sulfidation behavior of catalysts is essential in the formation the final structure in sulfided catalysts. Therefore, XPS measurements were performed to monitor the sulfidation degrees of Mo and Ni in the catalysts sulfided at different temperatures. The XPS results including the binding energies of the main features and the atomic percentages of different Mo and Ni species, are presented in Table A3, and the corresponding XPS spectra of Mo 3d, S 2s, and Ni 2p are shown in Figures A3 and A4. The XPS spectra of Mo 3d and S 2s region can be deconvoluted into three doublets related to different Mo oxidation states and one characteristic peak of S^{2-} (B.E. = $226.3 \pm 0.2\text{ eV}$). Three Mo 3d doublets are assigned to Mo^{6+} in MoO_3 (B.E. $3d_{5/2} = 232.7 \pm 0.4\text{ eV}$), Mo^{5+} in oxysulfide species (B.E. $3d_{5/2} = 230.9 \pm 0.3\text{ eV}$) and Mo^{4+} in MoS_2 (B.E. $3d_{5/2} = 229.0 \pm 0.2\text{ eV}$). The Ni $2p_{3/2}$ spectra were deconvoluted in three components at $856.8 \pm 0.2\text{ eV}$, $854.6 \pm 0.5\text{ eV}$, and $853.7 \pm 0.5\text{ eV}$, ascribing to NiO_x , NiMoS , and NiS_x , respectively [51, 52]. The spectra of the oxidic precursors were fitted in the same way.

Figure 3.4 shows the sulfidation profile of catalysts. It can be noticed that the Mo mainly presented as Mo^{4+} species in all catalysts after sulfided at $350\text{ }^\circ\text{C}$ for 2 h. The catalysts in both series show a comparable Mo sulfidation degree (expressed as $\text{Mo}^{4+}/\text{Mo}_T$, where Mo_T

Catalyst Composition vs. Catalytic Activity

= Mo⁴⁺ + Mo⁵⁺ + Mo⁶⁺) and Ni sulfidation degree, (NiS_x + NiMoS)/(NiS_x + NiMoS + NiO_x) [25, 27]. However, the sulfidation behavior varies in the catalysts with different organic additives. The sulfidation behavior of Mo in ^{cal}/AHM and EG(1.2)/AHM is comparable to that of ^{dr}/AHM. The sulfidation of Mo started at 50 °C and was nearly completed at 250 °C. With the addition of CA, NTA, and MA, the Mo sulfidation started at a lower temperature and took place in a wider temperature range. MA(1.2)/AHM showed an even lower Mo sulfidation rate, which was not completed until the temperature increased to 350 °C. Similarly, the sulfidation of Ni started from 150 °C and completed at 350 °C in NTA(1.2)/AHM, while the sulfidation for other catalysts started at room temperature and was almost completed at 150 °C. For catalysts prepared from MoO₃/NiCO₃, the sulfidation of Mo in ^{dr}/MoO₃ started at room temperature and was complete at 150 °C. With the addition of CA, EG, NTA, and MA, the Mo sulfidation started at a higher temperature and took place in a broader temperature range. The effect of organic additives on the sulfidation behavior of Ni is more significant than that on the sulfidation of Mo. The sulfidation of Ni in ^{dr}/MoO₃ was almost completed at 50 °C. While for the catalysts with CA, EG, and MA addition, the sulfidation rate slowed down, and the sulfidation was completed at ca. 150 °C. Furthermore, the temperature of complete sulfidation of Ni in catalyst with NTA addition was up to 250 °C. Calcination, however, did not have notable influence on the sulfidation behavior of the catalysts notably. In most catalysts, the sulfidation rate of Ni was slightly faster than that of Mo, except for the catalysts with NTA (NTA(1.2)/AHM and NTA(1.2)/MoO₃) and MA(1.2)/MoO₃. It needs to be further noted that the organic additives used here mainly decompose in the temperature range between 200 °C and 500 °C (Figure A4), which is above the sulfidation temperature of all catalysts except NTA(1.2)/AHM and NTA(1.2)/MoO₃, as reported in Ref. [21].

3.3.2.4. Characterization of sulfided catalysts

As described above, the surface composition and oxidation states of Mo and Ni in sulfided catalysts were monitored by XPS. The relevant information obtained from XPS measurement, including the Mo dispersion over the alumina surface (Mo/Al), the promoter ratio in the active NiMoS phase slabs ((Ni/Mo)_{slab}), and the edge sites ratio in NiMoS phase ((Ni/Mo)_{edge}), as well as the effective Ni in the active NiMoS phase, are listed in Table 3.5. The data shows that all catalysts have a similar Mo dispersion over the alumina surface. It can also be noticed that the catalysts after calcination and with additives have a higher effective amount of Ni in NiMoS species than the reference catalysts (^{dr}/AHM and ^{dr}/MoO₃), suggesting that calcination and additives could promote the formation of the active NiMoS phase, and the increased active phase is the reason for the improvement of catalytic activity.

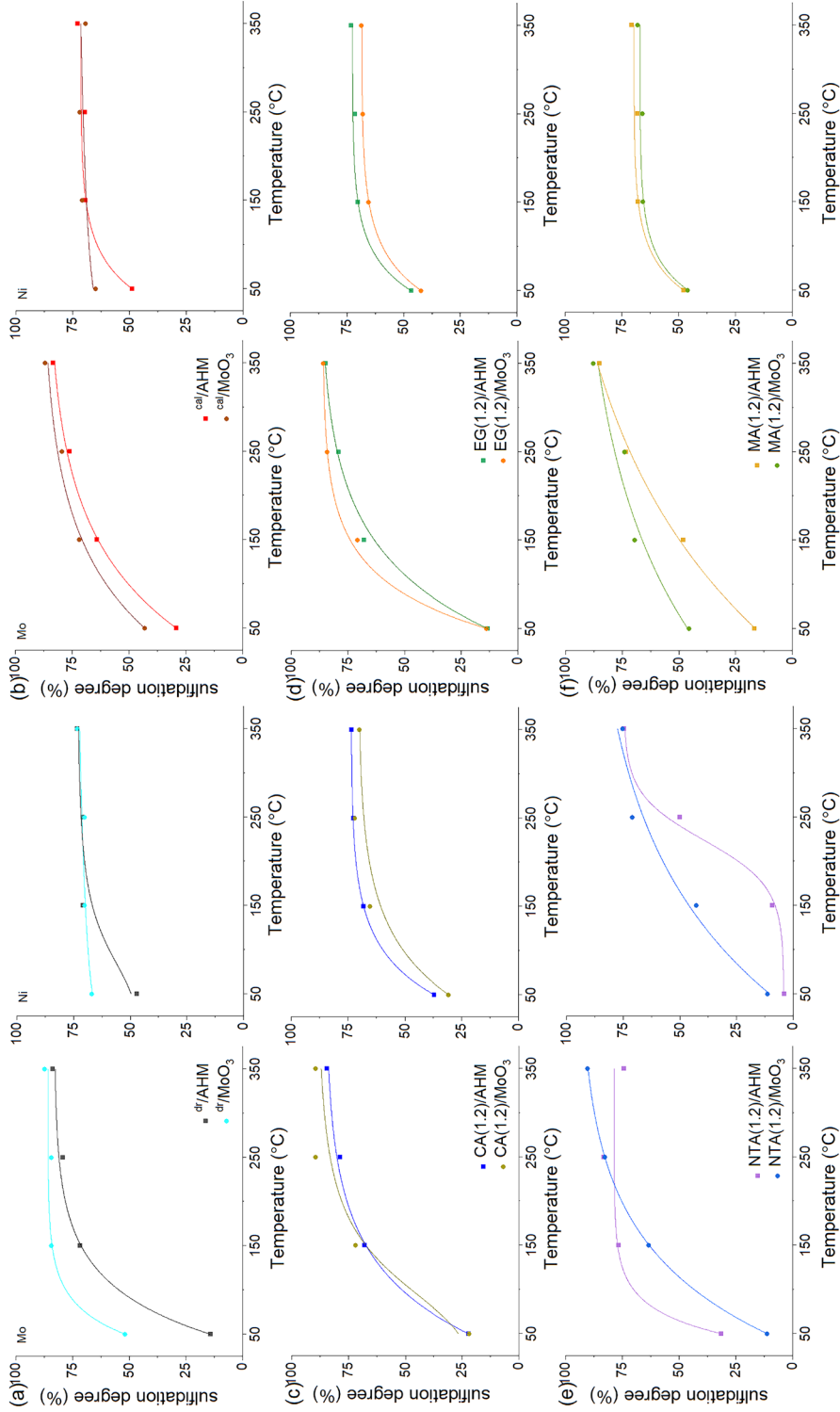


Figure 3.4. Degree of sulfidation of Mo and Ni in catalysts sulfided from 50 °C to 350 °C determined by XPS.

Catalyst Composition vs. Catalytic Activity

Table 3.5. XPS fit results of sulfided samples.

Sample	S/(Ni+Mo) molar ratio	Mo/Al molar ratio	(Ni/Mo) _{slab} ^a	(Ni/Mo) _{edge} ^b	Effective amount (wt%) of Ni in NiMoS ^c
^{dr} /AHM	1.87	0.08	0.06	0.22	0.11
^{cal} /AHM	1.73	0.08	0.07	0.27	0.15
CA(1.2)/AHM	1.75	0.11	0.16	0.57	0.24
EG(1.2)/AHM	1.73	0.08	0.09	0.35	0.13
NTA(1.2)/AHM	1.91	0.09	0.07	0.27	0.16
MA(1.2)/AHM	1.60	0.05	0.17	0.55	0.22
^{dr} /MoO ₃	1.75	0.10	0.09	0.36	0.20
^{cal} /MoO ₃	1.87	0.09	0.09	0.32	0.19
CA(1.2)/MoO ₃	1.88	0.09	0.10	0.37	0.22
EG(1.2)/MoO ₃	1.82	0.10	0.11	0.42	0.23
NTA(1.2)/MoO ₃	1.72	0.08	0.12	0.46	0.26
MA(1.2)/MoO ₃	2.00	0.09	0.14	0.47	0.32

^a Ni/Mo ratio in the NiMoS slabs calculated from XPS results (equation 6 in Chapter 2)

^b Ni/Mo ratio in the NiMoS edges calculated from XPS and TEM results (equation 7 in Chapter 2)

^c Effective Ni content in total NiMoS species from XPS results (equation 5 in Chapter 2)

TEM images of the sulfided catalysts, respective particle size distribution, and stacking degrees are displayed in Figure 3.5. The average particle size (L), average stacking layer number (N), dispersion of NiMoS particles (D), and the specific distribution of particle size and stacking number are listed in Table 3.6. The results show that catalysts prepared from AHM/Ni(NO₃)₂ have a comparable average particle size (ca. 3.7 nm). The average stacking number for ^{dr}/AHM, ^{cal}/AHM, CA(1.2)/AHM, EG(1.2)/AHM, NTA(1.2)/AHM, and MA(1.2)/AHM is 2.3, 2.0, 1.6, 1.8, 1.4, and 1.7, respectively. In these catalysts, NTA(1.2)/AHM has the lowest average stacking number (1.4), and MA(1.2)/AHM has the highest active NiMoS phase dispersion. For catalysts prepared from MoO₃/NiCO₃, varying degrees of decrease in average particle size were observed in catalysts after calcination and with additives, compared to ^{dr}/MoO₃ (L = 3.9 nm). The average stacking degree for ^{cal}/MoO₃ is 1.8, slightly lower than ^{dr}/MoO₃ (1.9). The stacking number for CA(1.2)/MoO₃ and NTA(1.2)/MoO₃ further decreased to 1.5, while the average stacking number for EG(1.2)/MoO₃ and MA(1.2)/MoO₃ is 2.0. Note that all catalysts prepared from MoO₃/NiCO₃ show a similar particle stacking behavior with mainly single layers and stacks of 2 layers of MoS₂. In these catalysts, NTA(1.2)/MoO₃ shows the lowest average stacking number (1.5), MA(1.2)/MoO₃ shows the smallest average particle size of 3.2 nm, the highest average stacking degree (2.0) and the highest dispersion of NiMoS (0.30). The high stacking degree and appropriate length of MoS₂ particles in MA(1.2)/MoO₃ is considered to be the precondition of forming the active NiMoS II phase.

Chapter 3

Figure 3.5.1. HR-TEM micrographs of a) dr/AHM b) cat/AHM c) CA(1.2)/AHM d) EG(1.2)/AHM e) NTA(1.2)/AHM f) MA(1.2)/AHM . The respective particle size distribution and stacking degrees are plotted on the right of each image.

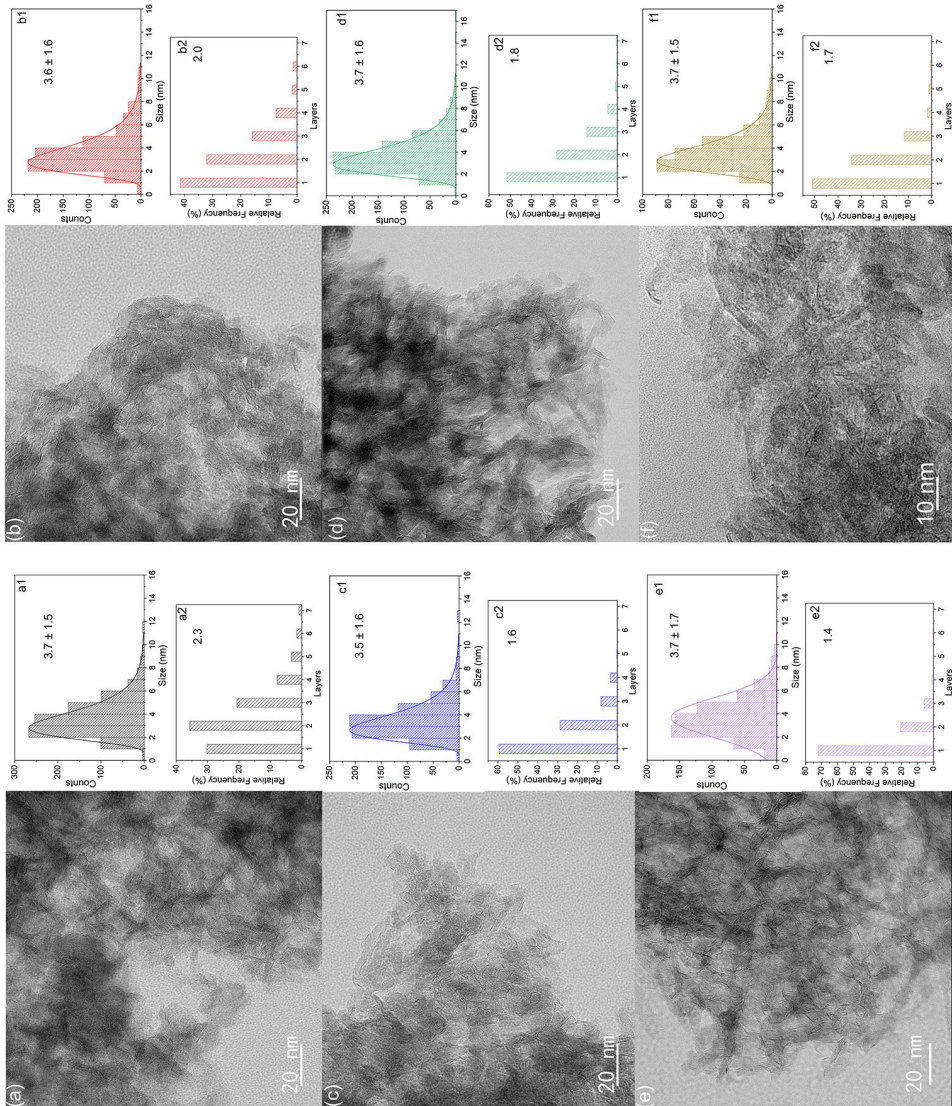


Figure 3.5.2. HR-TEM micrographs of g) dr/MoO_3 ; h) cal/MoO_3 ; i) CA(1.2)/MoO_3 ; j) EG(1.2)/MoO_3 ; k) NTA(1.2)/MoO_3 and l) MA(1.2)/MoO_3 . The respective particle size distribution and stacking degrees are plotted on the right of each image.

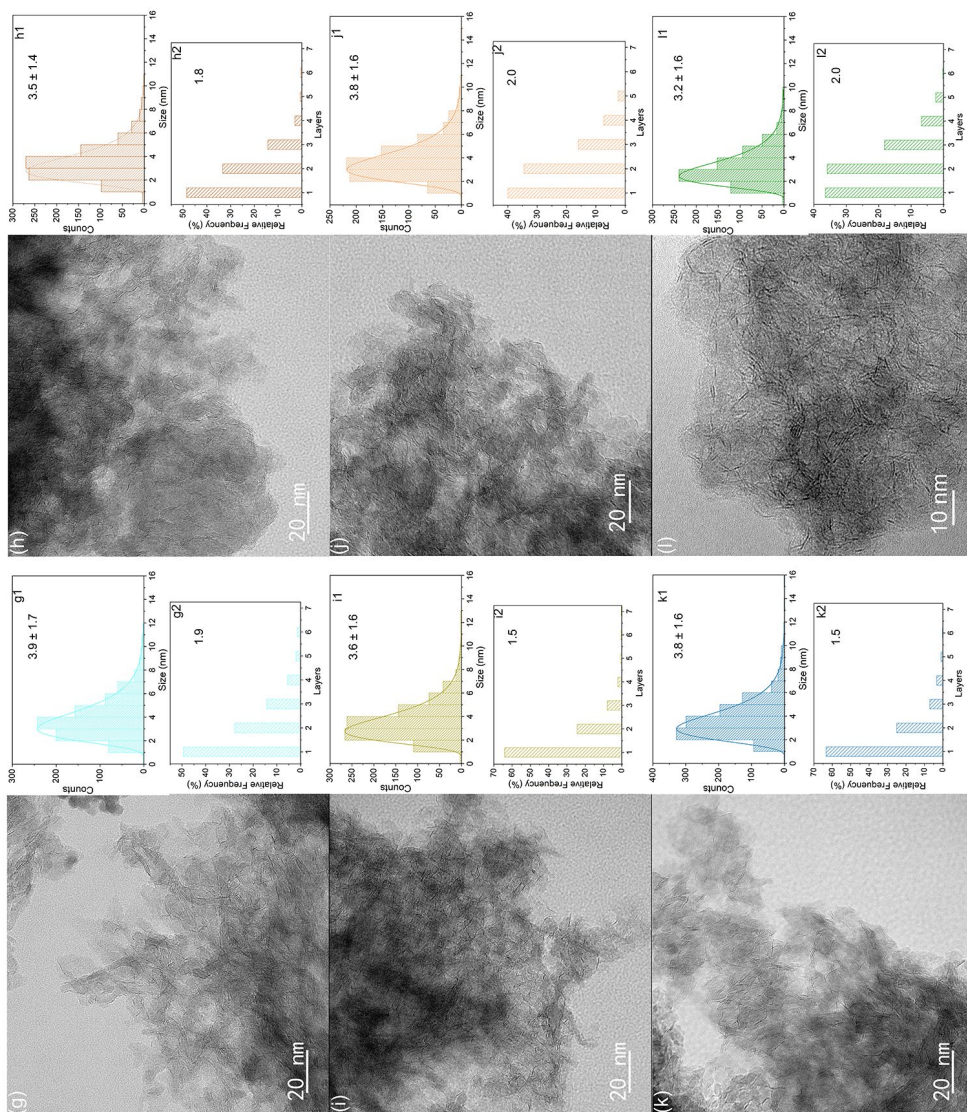


Table 3.6. Morphological characteristics of sulfided catalysts as determined by and calculated from TEM micrographs.

Sample	Average length L (nm)	Average stacking number N	Dispersion of NiMoS D ^a	Distribution of particle size (rel%)					Distribution of stacking number (rel%)			
				<2	2-4	4-6	6-8	>8	1	2	3	>4
^{dt} /AHM	3.7 ± 1.5	2.3	0.27	10.8	53.8	28.3	5.5	1.6	30.2	35.7	20.6	13.5
^{cat} /AHM	3.6 ± 1.6	2.0	0.26	10.5	57.6	21.9	7.9	2.1	41.4	32.1	15.9	10.6
CA(1.2)/AHM	3.5 ± 1.6	1.6	0.28	13.5	56.7	23.3	5.0	1.5	59.4	28.7	8.2	3.7
EG(1.2)/AHM	3.7 ± 1.6	1.8	0.26	8.7	56.1	27.0	6.0	2.2	51.5	28.3	14.3	5.9
NTA(1.2)/AHM	3.7 ± 1.7	1.4	0.26	13.1	49.3	28.4	7.2	2.0	72.0	20.5	6.0	1.5
MA(1.2)/AHM	3.7 ± 1.5	1.7	0.31	8.7	57.1	26.5	5.2	2.5	50.9	34.1	11.6	3.4
^{dt} /MoO ₃	3.9 ± 1.7	1.9	0.25	9.3	50.9	28.1	9.2	2.5	49.4	27.8	14.2	8.6
^{cat} /MoO ₃	3.5 ± 1.4	1.8	0.28	11.4	59.8	23.0	4.5	1.3	48.5	33.3	14.3	3.9
CA(1.2)/MoO ₃	3.6 ± 1.6	1.5	0.27	12.1	56.9	23.5	5.9	1.6	64.1	24.4	7.9	3.6
EG(1.2)/MoO ₃	3.8 ± 1.6	2.0	0.26	8.1	53.8	29.4	7.3	1.4	40.0	34.5	15.9	9.6
NTA(1.2)/MoO ₃	3.8 ± 1.6	1.5	0.26	8.3	55.6	28.6	5.1	2.4	63.4	25.0	7.1	4.5
MA(1.2)/MoO ₃	3.2 ± 1.6	2.0	0.30	18.1	57.0	20.8	3.2	0.9	36.4	35.8	18.2	9.6

^a NiMoS dispersion (D) calculated from TEM results (Equation 10, Chapter 2).

3.4. Discussion

To understand the influence of calcination process, organic additives, and chemical sources on the structure and catalytic activity of NiMo/Al₂O₃ catalysts, two series of catalysts using AHM/Ni(NO₃)₂ and MoO₃/NiCO₃ as starting materials were synthesized, where four additives (CA, EG, NTA, MA) were added, and one additive-free catalyst after calcination was also included. The physiochemical structure of the oxidic precursors were characterized with XRD, TPR, and Raman spectroscopy, and the sulfidation behavior of catalysts was monitored by XPS. The structure of the sulfided particle was measured with TEM. The catalytic activity of sulfided catalysts was evaluated in the HDS of thiophene, DBT and gas-oil.

3.4.1. Effect of calcination

^{cal}/AHM exhibits higher reaction rate in DBT HDS than ^{dr}/AHM due to the higher fraction of the effective amount of Ni in NiMoS (0.15 wt%). As reported in the literature, the active NiMoS phase plays the key role in the Ni-promoted HDS catalysts [53, 54]. The difference in metal-support interaction should be the origin of the structural difference. ^{cal}/AHM shows a lower T_m (398 °C) than ^{dr}/AHM (409 °C) in TPR, which suggests a weaker metal-support interaction in ^{cal}/AHM resulting in higher reducibility. The weaker metal-support interaction, to some extent, increases the metal dispersion on ^{cal}/AHM, leading to the formation of the active NiMoS phase with higher activity. However, the activity difference is not reflected in the metal sulfidation behavior, and the two catalysts show a comparable sulfidation degree of Mo and Ni. Additional, only slight difference was observed in thiophene HDS activity between ^{dr}/AHM and ^{cal}/AHM.

The activity improvement effect of calcination in DBT HDS is less evident for catalysts prepared from MoO₃/NiCO₃. ^{dr}/MoO₃ and ^{cal}/MoO₃ show comparable DBT HDS activity. However, ^{cal}/MoO₃ does show a higher thiophene HDS activity than ^{dr}/MoO₃, which is attributed to a higher active NiMoS phase dispersion caused by the lower metal-support interaction. The type of active sites or the intrinsic activity difference of active sites should be responsible for the different degrees of enhancement in activity in thiophene and DBT HDS tests.

3.4.2. Effect of additives

The catalytic activity of catalysts with CA (CA(1.2)/AHM and CA(1.2)/MoO₃) was improved compared to the two reference catalysts (^{dr}/AHM and ^{dr}/MoO₃). The activity enhancement effect was also reported in other publications, where the activity was attributed

Chapter 3

enhancement to the formation of more active sites [55, 56], higher dispersion of the active phase [57, 58], or a higher sulfidation degree of Mo [56, 59]. In CA(1.2)/MoO₃, XPS results evidence that more active NiMoS phase is formed (Table 3.5) due to the slower Ni sulfidation rate compared to ^{dr}/MoO₃. Besides, higher dispersion of the active NiMoS phase is also detected (Table 3.6). This sulfidation behavior and active phase dispersion suggest weaker metal-support interaction in CA(1.2)/MoO₃, which could be further confirmed by the decreased T_m value. The above observations also apply to CA(1.2)/AHM. Furthermore, CA(1.2)/MoO₃ is more active than CA(1.2)/AHM. The DBT HDS reaction rate in CA(1.2)/MoO₃ is two times higher than that of CA(1.2)/AHM due to the higher intrinsic activity of the active sites in CA(1.2)/MoO₃ as the TOF_{edge} value shown. CA(1.2)/MoO₃, however, is only 20 % more active than CA(1.2)/AHM in thiophene HDS, from which we infer that the active sites in DBT HDS are different from those in thiophene HDS or function in differently mechanism as Castillo-Villalón et al. proposed [60].

With EG addition, catalytic activity in thiophene HDS increased by 20 % – 30 %. For DBT HDS, TOF_{edge} values of EG(1.2)/AHM and EG(1.2)/MoO₃ improved by 50 % and 40 % compared to ^{dr}/AHM and ^{dr}/MoO₃, respectively. The improved performance derives from the higher content of the active NiMoS phase, caused by the increased Mo sulfidation rate in EG(1.2)/MoO₃. The weaker metal-support interaction observed in TPR is responsible for this different sulfidation behavior. However, the structural difference in the oxidic precursor was not reflected in its morphology, where ^{dr}/MoO₃ and EG(1.2)/MoO₃ showed a comparable average particle size and stacking degree. Although the origin of the beneficial influence of this non-chelating additive was proposed to be the connection between glycol and alumina [61], no direct evidence was observed in this work. Likewise, the structural differences observed between EG(1.2)/AHM and ^{dr}/AHM are the reason for the activity difference.

The role of NTA is relatively complicated because it performs differently in gas-phase thiophene and liquid-phase DBT HDS tests. The addition of NTA substantially improves catalyst activity in thiophene HDS. The reaction rates of NTA(1.2)/AHM and NTA(1.2)/MoO₃ are $101.1 \pm 0.6 \text{ mol mol}_{\text{Mo}}^{-1} \text{ h}^{-1}$ and $111.3 \pm 2.9 \text{ mol mol}_{\text{Mo}}^{-1} \text{ h}^{-1}$, respectively, which are 1.6 and 1.7 times higher than that of ^{dr}/AHM and ^{dr}/MoO₃. Interestingly, NTA(1.2)/MoO₃ does not show any pronounced enhancement in liquid-phase DBT HDS, and an obvious inhibiting effect was even observed in NTA(1.2)/AHM. The different behavior of NTA additive in these two tests was also reported by Hiroshima et al. [62] and van Veen et al. [17, 63]. They stated that the ‘gas–liquid-phase controversy’ is a generic phenomenon in hydrotreating reactions over metal sulfide catalysts, as there are several parameters that can influence the effect of NTA, e.g., the absence of a calcination step before sulfidation, the activation stage, and the activity test conditions et al. A noticeable decrease

Catalyst Composition vs. Catalytic Activity

in the stacking degree of MoS₂ slabs observed in NTA(1.2)/AHM and NTA(1.2)/MoO₃ suggests higher metal dispersion than the two reference catalysts. Higher sulfidation degrees of Mo and Ni in the sulfided catalysts and relative Ni content in the NiMoS active phase were also detected. We attribute the increase of the active phase to the slowed sulfidation rate of Ni, which increases the possibility for Ni to participate in the formation of the active NiMoS phase, even though there is a stronger metal-support interaction in their oxidic precursors, as TPR data indicated. We noticed that the majority of MoS₂ particles in NTA(1.2)/AHM and NTA(1.2)/MoO₃ present as single-layer structures (> 60 %). As reported in the literature [64], the single-layer structure is usually strongly connected to the alumina carrier by forming the Mo-O-Al structure (consistent with TPR), which prefers to transform into the intrinsic less active NiMoS phase after sulfidation. The less active sites could also be another reason for the low DBT HDS activity in NTA(1.2)/AHM and NTA(1.2)/MoO₃.

MA is another α -hydroxycarboxylic acid used in catalyst synthesis. The catalytic activity of catalysts with MA was improved as CA, especially in DBT HDS. MA(1.2)/AHM and MA(1.2)/MoO₃ show the highest activity in each series of catalysts. As reported in the literature, there are two types of active NiMoS particles in NiMo/Al₂O₃ catalysts, type I and type II [17]. These two types of particles are formed based on different metal-support interactions in catalysts. Typically, type II has a higher intrinsic activity than type I. The high catalytic performance of MA(1.2)/MoO₃ is because of the existence of more active type II NiMoS particles. Since the typical characteristics of type II active NiMoS phase, e.g., high metal dispersion, small particle size, and higher stacking degree of MoS₂ particles caused by the weak metal-support interaction, were observed in MA(1.2)/MoO₃. Besides, higher content of the active NiMoS phase is also responsible for the increased activity. Structural differences between MA(1.2)/AHM and MA(1.2)/MoO₃ are observed. XRD data shows that except for the feature of γ -Al₂O₃, a crystalline structure of polymolybdate species is observed in MA(1.2)/AHM, which is also reflected in its Raman spectrum. The sharp bands observed in Raman suggest a high crystallinity and distinct Mo coordination states in MA(1.2)/AHM, while the metals are well dispersed on the alumina surface with uniform coordination states in MA(1.2)/MoO₃. Consequently, a different metal-support interaction between these two catalysts was observed, leading to the morphology and metal dispersion difference in their sulfided phase. However, deep structure characterization is still needed to further explore the different performance of MA in these two catalysts.

3.4.3. Effect of chemical sources

As introduced above, the Mo aggregation in the impregnation solution is a pH-dependent process, and with different pH levels, Mo aggregation varies. The effect of chemical sources

Chapter 3

on catalysts without additives (dried-only and calcined) was not apparent with comparable metal coordination state and metal-support interaction (Figures 3.2, 3.3). After sulfidation, a comparable metal dispersion and sulfidation state were observed, as well as similar catalytic activity was obtained. In these cases, the pH of the impregnation solution is quite similar, which leads to a comparable Mo aggregation, as shown in the Raman spectra of the respective impregnation solution (Figure A3.3). While more significant influence of starting materials on catalytic activity was observed for catalysts with additives. As listed in Table 3.6, the TOF_{edge} value of catalysts with additives prepared from $\text{MoO}_3/\text{NiCO}_3$ is at least 2 times higher than their counterpart catalysts prepared from $\text{AHM}/\text{Ni}(\text{NO}_3)_2$, except for NTA. The reason leading to the difference is complicated. Firstly, it is believed that the pH of the impregnation solutions varies with additives, which could change the aggregation of Mo. The coordination behavior of the additives in the impregnation also varies with the pH environment of the solution, which leads to different aggregation species. During the impregnation and the following drying process, the distinct properties of these complexes, such as the varying decomposition, and different adsorption ability, are reflected in their structure. As a result, the more complex the system is, the more susceptible the coordination states of Mo and Ni are to the solution environment (preparation conditions) [65].

In a word, the catalysts with $\text{MoO}_3/\text{NiCO}_3$ as starting materials show higher performance than the counterpart catalysts prepared from $\text{AHM}/\text{Ni}(\text{NO}_3)_2$. To understand the improved mechanism of catalytic activity, a more in-depth structure characterization should be performed.

3.5. Conclusions

Herein, two series of $\text{NiMo}/\text{Al}_2\text{O}_3$ catalysts with different Ni/Mo ratios (0.18 – 0.62) were synthesized from two sets of chemical sources ($(\text{NH}_4)_6\text{Mo}_7\text{O}_{24}$ (AHM)/ $\text{Ni}(\text{NO}_3)_2$ and $\text{MoO}_3/\text{NiCO}_3$) by the incipient wetness impregnation. By comparing their activity in thiophene, dibenzothiophene (DBT), and gas-oil HDS, catalysts with a Ni/Mo ratio of 0.4 was validated to be the optimal composition. Furthermore, a systematical study was carried out to investigate the effects of calcination, organic additives, and chemical sources on the structure and performance of $\text{NiMo}/\text{Al}_2\text{O}_3$ catalysts. The metal-support interaction decrease in calcined catalysts, and more active NiMoS phases were formed after sulfidation, leading to a relatively higher activity. The organic additives (citric acid (CA), ethylene glycol (EG), nitrilotriacetic acid (NTA), and malic acid (MA)) show a varying enhancement in catalytic activity. Generally, the catalysts with additives show weaker metal-support interaction, leading to higher reducibility. The weak metal-support interaction promotes metal sulfidation and dispersion, further increasing the formation of more active NiMoS phase. The effect of

Catalyst Composition vs. Catalytic Activity

NTA is much more complex than the other three additives, as it shows significant reinforcement in catalytic activity in thiophene HDS, while no promotion or little inhibition effect was observed in the DBT HDS. The formation of a less active NiMoS phase should be part of the reason for the low DBT HDS activity. The chemical sources have more significant effect on catalysts with additives than those without additives, suggesting that the complex system is easily affected by chemical sources. Additionally, the catalysts prepared from MoO₃/NiCO₃ show higher activity than those prepared from AHM/Ni(NO₃)₂. The DBT HDS results show that MA(1.2)/MoO₃ exhibits the best catalytic efficiency in all catalysts, while NTA(1.2)/AHM is the least active.

3.6. References

- [1] J.A.R. van Veen, What's new? On the development of sulphidic HT catalysts before the molecular aspects, *Catal. Today*, 292 (2017) 2-25.
- [2] H. Topsøe, B.S. Clausen, R. Candia, C. Wivel, S. Mørup, In situ Mössbauer emission spectroscopy studies of unsupported and supported sulfided Co-Mo hydrodesulfurization catalysts: Evidence for and nature of a Co-Mo-S phase, *J. Catal.*, 68 (1981) 433-452.
- [3] M. Sun, D. Nicosia, R. Prins, The effects of fluorine, phosphate and chelating agents on hydrotreating catalysts and catalysis, *Catal. Today*, 86 (2003) 173-189.
- [4] Y.V. Vatutina, O.V. Klimov, E.A. Stolyarova, K.A. Nadeina, I.G. Danilova, Y.A. Chesalov, E.Y. Gerasimov, I.P. Prosvirin, A.S. Noskov, Influence of the phosphorus addition ways on properties of CoMo-catalysts of hydrotreating, *Catal. Today*, 329 (2019) 13-23.
- [5] L. Medici, R. Prins, Structure of oxidic NiMo/SiO₂ hydrotreating catalyst precursors, *J. Catal.*, 163 (1996) 28-37.
- [6] Y. Gao, W. Han, X. Long, H. Nie, D. Li, Preparation of hydrodesulfurization catalysts using MoS₃ nanoparticles as a precursor, *Appl. Catal. B: Environ.*, 224 (2018) 330-340.
- [7] L. Lizama, T. Klimova, Highly active deep HDS catalysts prepared using Mo and W heteropolyacids supported on SBA-15, *Appl. Catal. B: Environ.*, 82 (2008) 139-150.
- [8] A. Alsalmeh, N. Alzaqri, A. Alsaleh, M.R.H. Siddiqui, A. Alotaibi, E.F. Kozhevnikova, I.V. Kozhevnikov, Efficient Ni-Mo hydrodesulfurization catalyst prepared through Keggin polyoxometalate, *Appl. Catal. B: Environ.*, 182 (2016) 102-108.
- [9] S. Damyanova, A.A. Spojakina, D.M. Shopov, Study of low-percentage alumina-supported nickel-molybdenum catalysts by ESR spectroscopy and magnetic measurements, *Appl. Catal.*, 48 (1989) 177-186.
- [10] G. Plazenet, E. Payen, J. Lynch, Cobalt-molybdenum interaction in oxidic precursors of zeolite-supported HDS catalysts, *Phys. Chem. Chem. Phys.*, 4 (2002) 3924-3929.
- [11] A.J. van Dillen, R.J.A.M. Terörde, D.J. Lensveld, J.W. Geus, K.P. de Jong, Synthesis of supported catalysts by impregnation and drying using aqueous chelated metal complexes, *J. Catal.*, 216 (2003) 257-264.
- [12] M.S. Rana, J. Ramírez, A. Gutiérrez-Alejandre, J. Ancheyta, L. Cedeño, S.K. Maity, Support effects in CoMo hydrodesulfurization catalysts prepared with EDTA as a chelating agent, *J. Catal.*, 246 (2007) 100-108.
- [13] L. Coulier, V.H.J. de Beer, J.A.R. van Veen, J.W. Niemantsverdriet, Correlation between hydrodesulfurization activity and order of Ni and Mo sulfidation in planar silica-supported NiMo catalysts: the influence of chelating agents, *J. Catal.*, 197 (2001) 26-33.

Chapter 3

- [14] S. Badoga, K.C. Mouli, K.K. Soni, A.K. Dalai, J. Adjaye, Beneficial influence of EDTA on the structure and catalytic properties of sulfided NiMo/SBA-15 catalysts for hydrotreating of light gas oil, *Appl. Catal. B: Environ.*, 125 (2012) 67-84.
- [15] R. Cattaneo, F. Rota, R. Prins, An XAFS study of the different influence of chelating ligands on the HDN and HDS of γ -Al₂O₃-supported NiMo catalysts, *J. Catal.*, 199 (2001) 318-327.
- [16] M.A. L lias, P.J. Kooyman, L. Mariey, L. Oliviero, A. Travert, J. van Gestel, J.A.R. van Veen, F. Mauge, Effect of NTA addition on the structure and activity of the active phase of cobalt-molybdenum sulfide hydrotreating catalysts, *J. Catal.*, 267 (2009) 14-23.
- [17] J.A.R. van Veen, H.A. Colijn, P.A.J.M. Hendriks, A.J. van Welsenens, On the formation of type I and type II NiMoS phases in NiMo/Al₂O₃ hydrotreating catalysts and its catalytic implications, *Fuel Process. Technol.*, 35 (1993) 137-157
- [18] P. Castillo-Villal n, J. Ramirez, J.A. Vargas-Luciano, Analysis of the role of citric acid in the preparation of highly active HDS catalysts, *J. Catal.*, 320 (2014) 127-136.
- [19] D. Valencia, T. Klimova, Citric acid loading for MoS₂-based catalysts supported on SBA-15. New catalytic materials with high hydrogenolysis ability in hydrodesulfurization, *Appl. Catal. B: Environ.*, 129 (2013) 137-145.
- [20] P.A. Nikulshin, D.I. Ishutenko, A.A. Mozhaev, K.I. Maslakov, A.A. Pimerzin, Effects of composition and morphology of active phase of CoMo/Al₂O₃ catalysts prepared using Co₂Mo₁₀-heteropolyacid and chelating agents on their catalytic properties in HDS and HYD reactions, *J. Catal.*, 312 (2014) 152-169.
- [21] L. van Haandel, G.M. Bremmer, E.J.M. Hensen, Th. Weber, The effect of organic additives and phosphoric acid on sulfidation and activity of (Co)Mo/Al₂O₃ hydrodesulfurization catalysts, *J. Catal.*, 351 (2017) 95-106.
- [22] D. Nicosia, R. Prins, The effect of glycol on phosphate-doped CoMo/Al₂O₃ hydrotreating catalysts, *J. Catal.*, 229 (2005) 424-438.
- [23] P.A. Nikulshin, A.V. Mozhaev, A.A. Pimerzin, V.V. Konovalov, A.A. Pimerzin, CoMo/Al₂O₃ catalysts prepared on the basis of Co₂Mo₁₀-heteropolyacid and cobalt citrate: effect of Co/Mo ratio, *Fuel*, 100 (2012) 24-33.
- [24] Q. Gao, T.N.K. Ofosu, S. Ma, V.G. Komvokis, C.T. Williams, K. Segawa, Catalyst development for ultra-deep hydrodesulfurization (HDS) of dibenzothiophenes. I: Effects of Ni promotion in molybdenum-based catalysts, *Catal. Today*, 164 (2011) 538-543.
- [25] L. van Haandel, G.M. Bremmer, E.J.M. Hensen, Th. Weber, Influence of sulfiding agent and pressure on structure and performance of CoMo/Al₂O₃ hydrodesulfurization catalysts, *J. Catal.*, 342 (2016) 27-39.
- [26] M. Li, J. Ihli, M.A. Verheijen, M. Holler, M. Guizar-Sicairos, J.A. van Bokhoven, E.J.M. Hensen, Th. Weber, Alumina-Supported NiMo Hydrotreating Catalysts – Aspects of 3D Structure, Synthesis, and Activity, *J. Phys. Chem. C*, 126 (2022) 18536-18549.
- [27] D. Nicosia, R. Prins, The effect of phosphate and glycol on the sulfidation mechanism of CoMo/Al₂O₃ hydrotreating catalysts: an in situ QEXAFS study, *J. Catal.*, 231 (2005) 259-268.
- [28] Y. Muhammad, C. Li, Dibenzothiophene hydrodesulfurization using in situ generated hydrogen over Pd promoted alumina-based catalysts, *Fuel Process. Technol.*, 92 (2011) 624-630.
- [29] S. Damyanova, A. Spojakina, K. Jiratova, Effect of mixed titania-alumina supports on the phase composition of NiMo/TiO₂-Al₂O₃ catalysts, *Appl. Catal. A: Gen.*, 125 (1995) 257-269.
- [30] P. Castillo-Villal n, J. Ramirez, R. Cuevas, P. V zquez, R. Casta eda, Influence of the support on the catalytic performance of Mo, CoMo, and NiMo catalysts supported on Al₂O₃ and TiO₂ during the HDS of thiophene, dibenzothiophene, or 4, 6-dimethyldibenzothiophene, *Catal. Today*, 259 (2016) 140-149.

Catalyst Composition vs. Catalytic Activity

- [31] J. Escobar, M.C. Barrera, J.A. De Los Reyes, M.A. Cortés, V. Santes, E. Gómez, J.G. Pacheco, Effect of Mo and Co loading in HDS catalysts supported on solvo-thermally treated ZrO_2 - TiO_2 mixed oxides, *Catal. Today*, 133 (2008) 282-291.
- [32] H. Tanaka, M. Boulinguez, M. Vrinat, Hydrodesulfurization of thiophene, dibenzothiophene and gas oil on various Co-Mo/ TiO_2 - Al_2O_3 catalysts, *Catal. Today*, 29 (1996) 209-213.
- [33] H. Kim, J.J. Lee, S.H. Moon, Hydrodesulfurization of dibenzothiophene compounds using fluorinated NiMo/ Al_2O_3 catalysts, *Appl. Catal. B: Environ.*, 44 (2003) 287-299.
- [34] V. Zuzaniuk, R. Prins, Synthesis and characterization of silica-supported transition-metal phosphides as HDN catalysts, *J. Catal.*, 219 (2003) 85-96.
- [35] J.L. Brito, J. Laine, Reducibility of Ni-Mo/ Al_2O_3 catalysts: a TPR study, *J. Catal.*, 139 (1993) 540-550.
- [36] B. Scheffer, P. Molhoek, J.A. Moulijn, Temperature-programmed reduction of NiO- WO_3 / Al_2O_3 hydrodesulphurization catalysts, *Appl. Catal.*, 46 (1989) 11-30.
- [37] D.S. Zingg, L.E. Makovsky, R.E. Tischer, F.R. Brown, D.M. Hercules, A surface spectroscopic study of molybdenum-alumina catalysts using X-ray photoelectron, ion-scattering, and Raman spectroscopies, *J. Phys. Chem.*, 84 (1980) 2898-2906.
- [38] C.C. Williams, J.G. Ekerdt, J.M. Jehng, F.D. Hardcastle, I.E. Wachs, A Raman and ultraviolet diffuse reflectance spectroscopic investigation of alumina-supported molybdenum oxide, *J. Phys. Chem.*, 95 (1991) 8791-8797.
- [39] H. Tian, C.A. Roberts, I.E. Wachs, Molecular structural determination of molybdena in different environments: Aqueous solutions, bulk mixed oxides, and supported MoO_3 catalysts, *J. Phys. Chem. C*, 114 (2010) 14110-14120.
- [40] A.G. Kalampounias, G. Tsilomelekis, R.W. Berg, S. Boghosian, Molybdenum (VI) oxosulfato complexes in MoO_3 - $K_2S_2O_7$ - K_2SO_4 molten mixtures: stoichiometry, vibrational properties, and molecular structures, *J. Phys. Chem. A*, 116 (2012) 8861-8872.
- [41] G. Deo, I.E. Wachs, Predicting molecular structures of surface metal oxide species on oxide supports under ambient conditions, *J. Phys. Chem.*, 95 (1991) 5889-5895.
- [42] J. Moreau, O. Delpoux, E. Devers, M. Digne, S. Loridant, Impregnation of decamolybdocobaltate heteropolyanions over γ -alumina: detailed description of the physico-chemical phenomena, *Langmuir*, 29 (2013) 207-215.
- [43] Z. Liu, W. Han, D. Hu, S. Sun, A. Hu, Z. Wang, Y. Jia, X. Zhao, Q. Yang, Effects of Ni- Al_2O_3 interaction on NiMo/ Al_2O_3 hydrodesulfurization catalysts, *J. Catal.*, 387 (2020) 62-72.
- [44] A. Rochet, B. Baubet, V. Moizan, E. Devers, A. Hugon, C. Pichon, E. Payen, V. Briois, Influence of the preparation conditions of oxidic NiMo/ Al_2O_3 catalysts on the sulfidation ability: a quick-XAS and raman spectroscopic study, *J. Phys. Chem. C*, 119 (2015) 23928-23942.
- [45] J. Jiang, I. May, M.J. Sarsfield, M. Ogden, D.O. Fox, C.J. Jones, P. Mayhew, A spectroscopic study of the dissolution of cesium phosphomolybdate and zirconium molybdate by ammonium carbamate, *J. Solution Chem.*, 34 (2005) 443-468.
- [46] A.K. Cuentas-Gallegos, C. Frausto, L.A. Ortiz-Frade, G. Orozco, Raman spectra of hybrid materials based on carbon nanotubes and $Cs_3PMo_{12}O_{40}$, *Vib. Spectrosc.*, 57 (2011) 49-54.
- [47] V. La Parola, G. Deganello, C.R. Tewell, AM. Venezia, Structural characterisation of silica supported CoMo catalysts by UV Raman spectroscopy, XPS and X-ray diffraction techniques, *Appl. Catal. A: Gen.*, 235 (2002) 171-180.
- [48] G. Mestl, T.K.K. Srinivasan, Raman spectroscopy of monolayer-type catalysts: supported molybdenum oxides, *Catal. Rev.*, 40 (1998) 451-570.
- [49] M.A. Vuurman, I.E. Wachs, In situ Raman spectroscopy of alumina-supported metal oxide catalysts, *J. Phys. Chem.*, 96 (1992) 5008-5016.

Chapter 3

- [50] K. Segawa, T. Soeya, I.E. Wachs, Surface structures of supported molybdenum oxide catalysts under ambient conditions, *J. Catal.*, 136 (1992) 539-553.
- [51] B.W. Hoffer, A.D. van Langeveld, J.-P. Janssens, R.L.C. Bonn , C.M. Lok, J.A. Moulijn, Stability of highly dispersed Ni/Al₂O₃ catalysts: effects of pretreatment, *J. Catal.*, 192 (2000) 432-440.
- [52] J. Escobar, M.C. Barrera, J.A. Toledo, M.A. Cort s-J come, C. Angeles-Ch vez, S. N n ez, V. Santes, E. G mez, L. D az, E. Romero et al. Effect of ethyleneglycol addition on the properties of P-doped NiMo/Al₂O₃ HDS catalysts: Part I. Materials preparation and characterization, *Appl. Catal. B: Environ.*, 88 (2009) 564-575.
- [53] C. Liu, J. Mei, G. Wang, J. Chang, Q. Meng, D. Hu, C. Xiao, Y. Shi, A. Duan, Y. Gong, Tailoring NiMoS active phases with high hydrodesulfurization activity through facilely synthesized supports with tunable mesostructure and morphology, *J. Catal.*, 387 (2020) 170-185.
- [54] S. Jiang, S. Ding, Q. Jiang, Y. Zhou, S. Yuan, X. Geng, G. Yang, C. Zhang, Effects of Al introduction methods for Al-SBA-15 on NiMoS active phase morphology and hydrodesulfurization reaction selectivities, *Fuel*, 330 (2022) 125493.
- [55] T. Fujikawa, Highly active HDS catalyst for producing ultra-low sulfur diesel fuels, *Top. Catal.*, 52 (2009) 872-879.
- [56] M.O. Kazakov, M.A. Kazakova, Y.V. Vatutina, T.V. Larina, Y.A. Chesalov, E.Y. Gerasimov, I.P. Prosvirin, O.V. Klimov, A.S. Noskov, Comparative study of MWCNT and alumina supported CoMo hydrotreating catalysts prepared with citric acid as chelating agent, *Catal. Today*, 357 (2020) 221-230.
- [57] E.J.M. Hensen, V.H.J. de Beer, J.A.R. van Veen, R.A. van Santen, A refinement on the notion of type I and II (Co)MoS phases in hydrotreating catalysts, *Catal. Lett.*, 84 (2002) 59-67.
- [58] A. Pimerzin, A. Mozhaev, A. Varakin, K. Maslakov, P. Nikulshin, Comparison of citric acid and glycol effects on the state of active phase species and catalytic properties of CoPMo/Al₂O₃ hydrotreating catalysts, *Appl. Catal. B: Environ.*, 205 (2017) 93-103.
- [59] Y. Yoshimura, N. Matsubayashi, T. Sato, H. Shimada, A. Nishijima, Molybdate catalysts prepared by a novel impregnation method: Effect of citric acid as a ligand on the catalytic activities, *Appl. Catal. A: Gen.*, 79 (1991) 145-159.
- [60] P. Castillo-Villal n, J. Ramirez, R. Casta eda, Relationship between the hydrodesulfurization of thiophene, dibenzothiophene, and 4, 6-dimethyl dibenzothiophene and the local structure of Co in Co-Mo-S sites: Infrared study of adsorbed CO, *J. Catal.*, 294 (2012) 54-62.
- [61] A. Stanislaus, A. Marafi, M.S. Rana, Recent advances in the science and technology of ultra low sulfur diesel (ULSD) production, *Catal. Today*, 153 (2010) 1-68.
- [62] K. Hiroshima, T. Mochizuki, T. Honma, T. Shimizu, M. Yamada, High HDS activity of Co-Mo/Al₂O₃ modified by some chelates and their surface fine structures, *Appl. Surf. Sci.*, 121 (1997) 433-436.
- [63] H.R. Reinhoudt, C.H.M. Boons, A.D. van Langeveld, J.A.R. van Veen, S.T. Sic, J.A. Moulijn, On the difference between gas-and liquid-phase hydrotreating test reactions, *Appl. Catal. A: Gen.*, 207 (2001) 25-36.
- [64] R. Candia, O. S rensen, J. Villadsen, N.Y. Tops e, B.S. Clausen, H. Tops e, Effect of sulfiding temperature on activity and structures of Co-Mo/Al₂O₃ catalysts. ii, *Bulletin des Soci t s Chimiques Belges*, 93 (1984) 763-774.
- [65] L. Oliviero, F. Maug , P. Afanasiev, C. Pedraza-Parra, C. Geantet, Organic additives for hydrotreating catalysts: a review of main families and action mechanisms, *Catal. Today*, 377 (2021) 3-16.

3.7. Appendix A

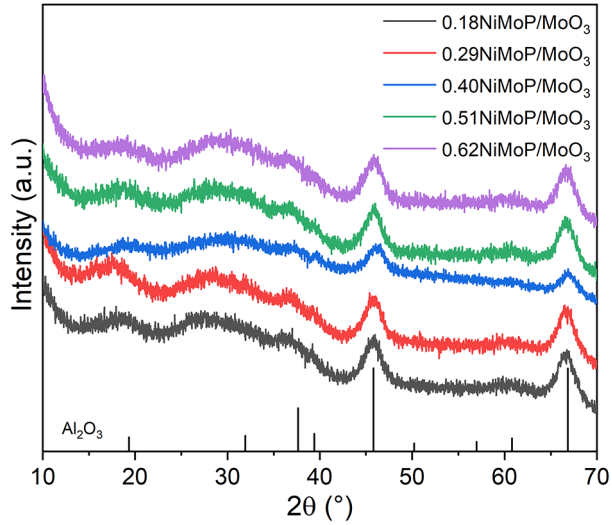


Figure A1. XRD patterns of oxidic precursors of x NiMoP/MoO₃ catalysts.

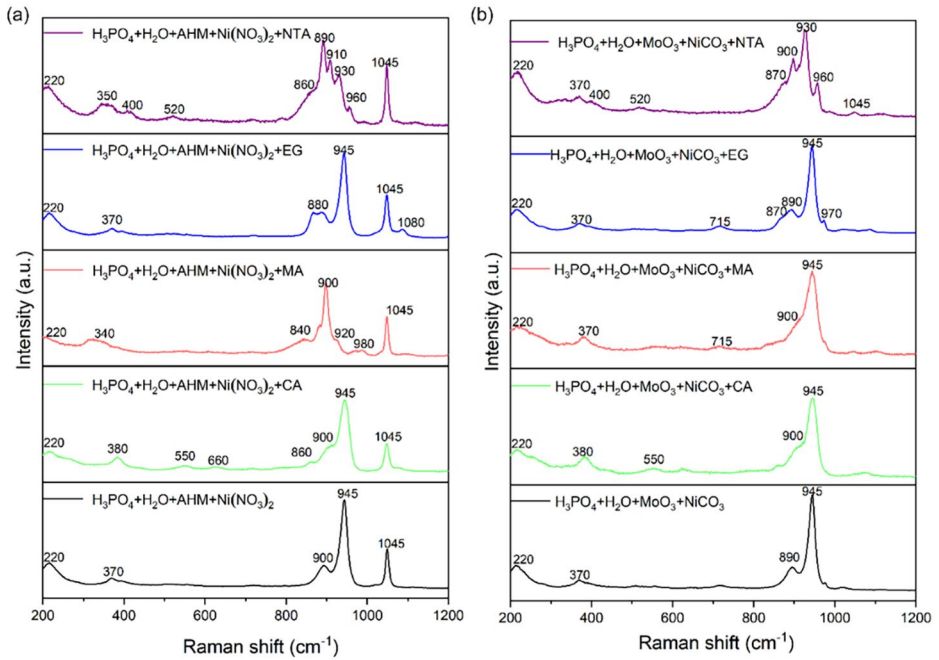
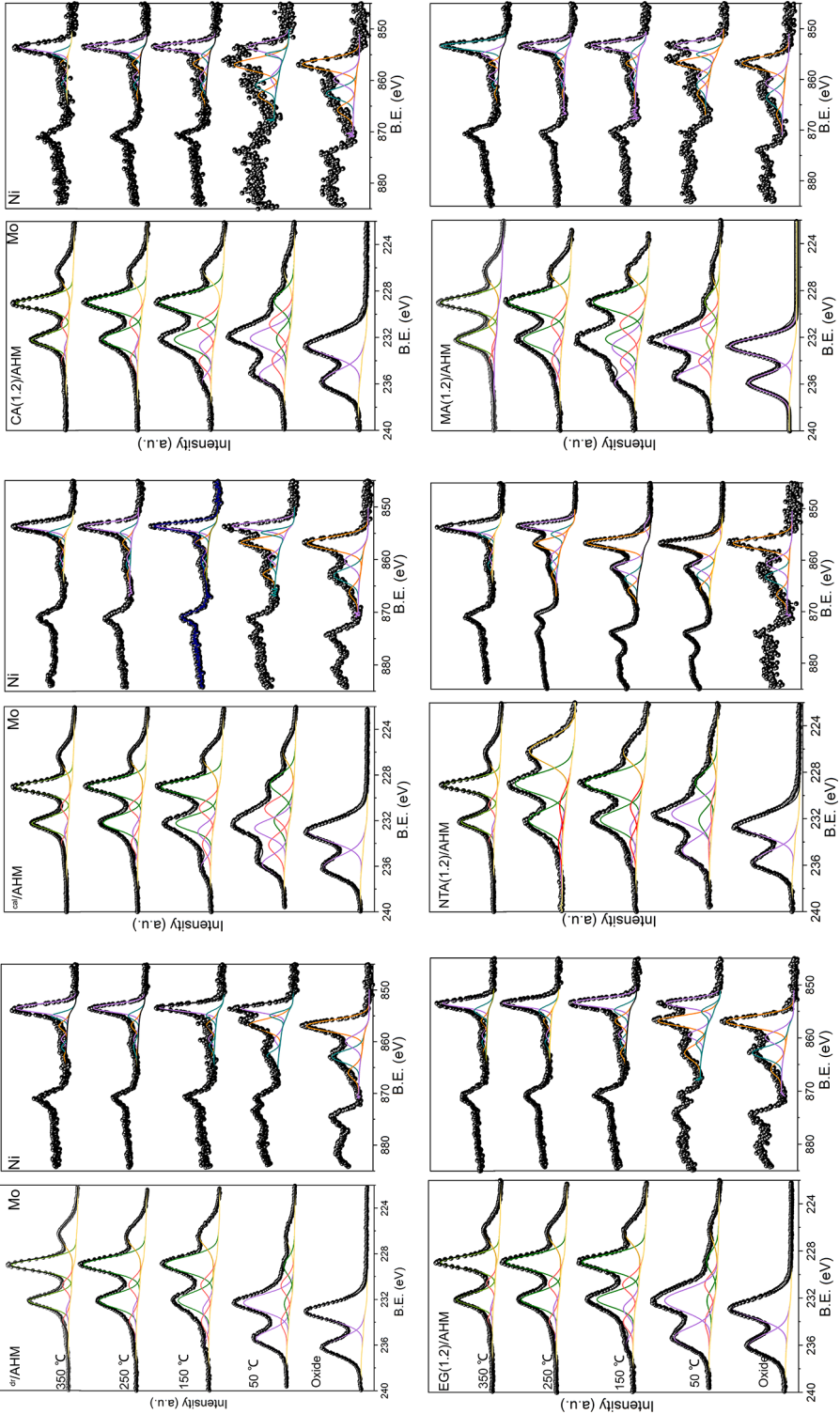


Figure A2. Raman spectra of respective impregnation solution.

Chapter 3



Catalyst Composition vs. Catalytic Activity

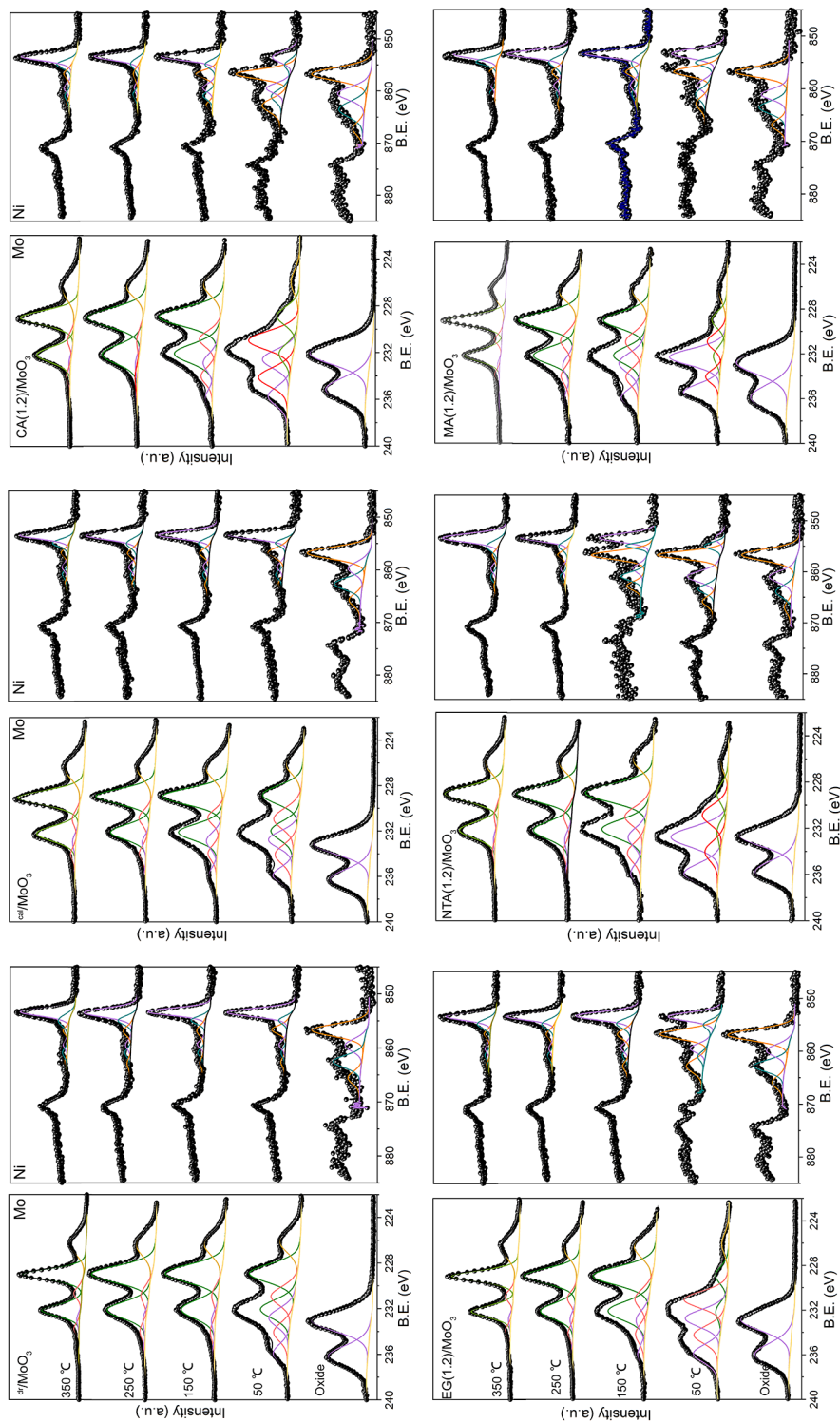


Figure A3. Mo 3d and Ni 2p XP spectra of corresponding oxides and catalysts sulfided at 50 °C, 150 °C, 250 °C, and 350 °C in 1 bar H₂S/H₂.

Chapter 3

TP-MS. The temperature-programmed reduction and mass spectroscopy analysis was performed to characterize the decomposition situation of catalysts. Typically, ~50 mg samples were loaded in a quartz tubular flow reactor. The sample was first pretreated at 120 °C for 1 h in 50 mL/min He flows and then heated in a gas mixture (95 mL/min He and 5 mL/min H₂) at a rate of 5 °C/min to 800 °C. The main products, H₂O, CO, O₂, and CO₂, were followed by online MS (MS, Balzer TPG-300) during the reduction.

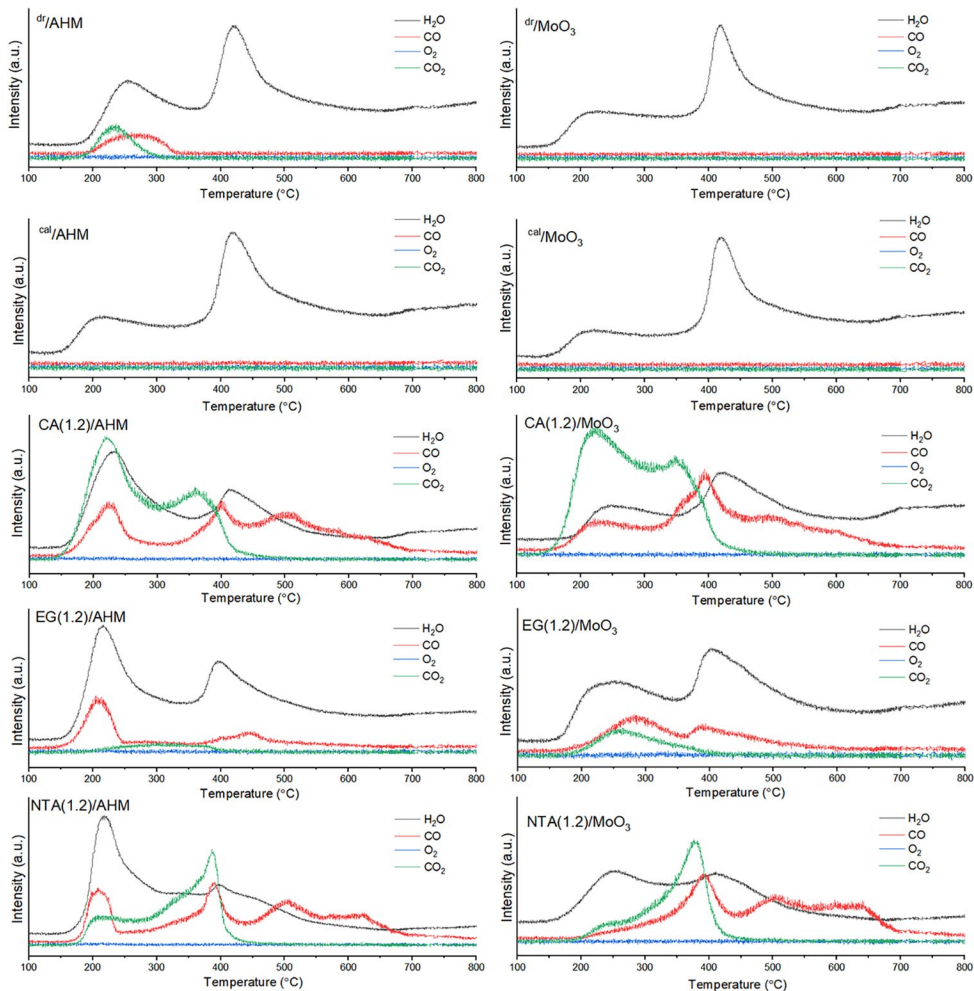


Figure A4. Temperature-programmed decomposition profiles of oxitic precursors.

Table A1. Metal composition and textural properties of xNiMoP/AHM catalysts as determined by ICP-OES ¹ and N₂ physisorption ².

Catalyst	Metal loading (wt%) ¹			Ni/Mo molar ratio ¹	Surface area ^{2a} (m ² /g)	Pore volume ^{2b} (cm ³ /g)	Pore diameter ^{2b} (nm)
	Mo	Ni	P				
0.18NiMoP/AHM	12.0	1.3	1.7	0.17	131.6	0.40	10.19
0.29NiMoP/AHM	12.1	2.1	1.7	0.28	113.4	0.31	9.20
0.40NiMoP/AHM	12.7	3.4	1.6	0.44	106.1	0.30	9.30
0.51NiMoP/AHM	11.0	3.2	1.5	0.48	107.5	0.32	7.58
0.62NiMoP/AHM	11.2	3.4	1.6	0.49	117.7	0.28	8.05

^a: The specific surface area was calculated using the Brunauer-Emmett-Teller (BET) equation.

^b: Total pore volume and pore diameter were determined by an adsorption branch of isotherm using the Barrett-Joyner-Halenda (BJH) model.

Table A2. Thiophene, DBT and gas-oil HDS activity of xNiMoP/AHM catalysts.

Catalyst	Thiophene		DBT		Gas-oil	
	Reaction rates (mol mol _{Mo} ⁻¹ h ⁻¹)	Reaction temperature	Reaction rates (mol mol _{Mo} ⁻¹ h ⁻¹) k _{HDS}	Conversion (%)	Reaction rates	Reaction rates
0.18NiMoP/AHM	37.5 ± 1.2	250 °C	2.6	6.3	6.0	
		270 °C	9.5	21.3		
		300 °C	55.7	79.5		
0.29NiMoP/AHM	38.5 ± 1.4	250 °C	2.4	5.9	9.2	
		270 °C	9.6	21.6		
		300 °C	61.9	82.1		
0.40NiMoP/AHM	62.9 ± 2.3	250 °C	3.2	8.1	15.0	
		270 °C	11.8	26.7		
		300 °C	93.0	91.3		
0.51NiMoP/AHM	40.8 ± 3.5	250 °C	3.1	6.8	13.3	
		270 °C	12.1	23.9		
		300 °C	93.6	87.2		
0.62NiMoP/AHM	53.4 ± 1.2	250 °C	2.5	5.8	13.4	
		270 °C	10.3	21.5		
		300 °C	76.7	84.7		

Table A3. Binding energy and atomic percentage of samples sulfided under 1 bar H₂S/H₂ at different temperatures and their respective oxidic precursors (oxide).

Catalyst	Temperature (°C)	Binding energy (eV)												Fractions (%)					
		Mo 3d5/2						Ni 2p3/2						Mo 3d			Ni 2p		
		Mo ⁴⁺	Mo ⁵⁺	Mo ⁶⁺	NiS _x	NiMoS	NiO _x	Mo ⁴⁺	Mo ⁵⁺	Mo ⁶⁺	NiS _x	NiMoS	NiO _x	Mo ⁴⁺	Mo ⁵⁺	Mo ⁶⁺	NiS _x	NiMoS	NiO _x
dr/AHM	oxide	--	--	233.0	--	--	856.9	--	--	100	--	--	100	--	--	100	--	--	100
	50	229.1	230.8	232.3	853.5	854.9	856.7	14.3	17.1	68.6	47.1	11.6	41.3	14.8	16.1	73.5	16.3	10.2	
	150	228.9	230.7	232.9	853.4	854.8	856.9	71.7	17.5	10.8	71.0	14.2	14.8	12.9	15.0	5.5	71.0	16.1	12.9
	250	228.9	230.7	233.0	853.5	854.9	856.8	79.5	15.0	5.5	71.0	16.1	12.9	10.2	12.2	4.0	73.5	16.3	10.2
	350	229.0	230.8	233.0	853.5	854.8	856.9	83.8	12.2	4.0	73.5	16.3	10.2	100	--	--	--	--	100
cat/AHM	oxide	--	--	232.9	--	--	856.9	--	--	100	--	--	100	--	--	100	--	--	100
	50	228.8	230.9	232.6	853.6	854.9	856.7	29.2	28.7	42.1	48.9	13.6	37.5	16.9	16.8	69.5	13.7	16.9	
	150	229.0	230.9	232.9	853.6	854.9	856.8	64.3	18.9	16.8	69.5	13.7	16.9	13.2	14.4	9.4	69.7	17.1	13.2
	250	229.0	230.8	233.0	853.7	854.9	856.8	76.2	14.4	9.4	69.7	17.1	13.2	9.3	12.6	4.0	72.8	18.0	9.3
	350	229.0	230.8	233.0	853.5	854.9	856.8	83.4	12.6	4.0	72.8	18.0	9.3	100	--	--	--	--	100
CA(1.2)/AHM	oxide	--	--	232.8	--	--	856.8	--	--	100	--	--	100	--	--	100	--	--	100
	50	228.8	230.8	232.1	853.4	854.9	856.9	22.2	31.1	30.7	37.2	8.5	54.3	22.5	13.5	68.2	9.3	22.5	
	150	229.0	230.9	232.7	853.4	855.0	856.7	68.0	18.5	13.5	68.2	9.3	22.5	10.9	4.8	72.8	16.3	10.9	
	250	229.0	230.7	233.1	853.4	854.9	856.7	78.8	16.4	4.8	72.8	16.3	10.9	9.3	11.8	3.6	73.6	17.0	9.3
	350	229.0	230.9	233.0	853.4	854.8	856.8	84.6	11.8	3.6	73.6	17.0	9.3	100	--	--	--	--	100
EG(1.2)/AHM	oxide	--	--	232.8	--	--	856.8	--	--	100	--	--	100	--	--	100	--	--	100
	50	228.9	230.8	232.2	853.4	854.9	856.8	13.4	13.1	55.5	46.9	16.3	36.8	13.1	13.6	70.3	16.6	13.1	
	150	228.9	230.8	232.9	853.3	854.9	856.7	68.0	18.5	13.6	70.3	16.6	13.1	11.5	6.5	71.6	16.9	11.5	
	250	229.0	230.8	232.9	853.4	854.9	856.7	79.2	14.4	6.5	71.6	16.9	11.5	8.1	4.0	73.3	18.6	8.1	
	350	229.0	230.7	233.0	853.4	854.9	856.8	85.0	11.0	4.0	73.3	18.6	8.1	100	--	--	--	--	100
NTA(1.2)/AHM	oxide	--	--	232.9	--	--	856.7	--	--	100	--	--	100	--	--	100	--	--	100
	50	228.9	230.9	231.6	853.4	--	856.8	31.5	5.2	63.3	4.1	0	95.9	9.6	10.0	9.4	0	90.6	
	150	228.9	230.9	232.9	853.4	--	856.7	76.8	13.2	10.0	9.4	0	90.6	34.5	5.2	50.1	15.3	34.5	
	250	229.0	230.8	232.8	853.3	854.9	856.8	83.2	11.6	5.2	50.1	15.3	34.5	9.7	3.9	74.8	15.5	9.7	
	350	229.1	230.8	232.9	853.4	854.9	856.9	84.3	11.9	3.9	74.8	15.5	9.7	100	--	--	--	--	100
MA(1.2)/AHM	oxide	--	--	232.7	--	--	856.8	--	--	100	--	--	100	--	--	100	--	--	100
	50	229.0	230.9	232.3	853.3	855.0	856.7	16.7	20.6	62.7	47.9	15.8	36.3	15.8	20.6	62.7	47.9	15.8	36.3

Catalyst Composition vs. Catalytic Activity

	150	229.0	230.9	232.8	853.3	855.0	856.8	48.3	23.1	28.6	68.0	17.2	14.8
	250	229.0	230.8	233.0	853.4	854.9	856.8	73.5	16.6	9.9	68.3	19.7	12.0
	350	229.0	230.9	233.0	853.4	855.0	856.8	85.1	10.7	4.2	70.8	21.2	8.1
	oxide	--	--	232.9	--	--	856.7	--	--	100	--	--	100
d_r/MoO_3	50	228.9	230.9	232.8	853.4	854.9	856.8	51.9	21.2	26.9	66.8	10.8	22.4
	150	229.0	230.8	233.0	853.3	854.9	856.8	84.2	10.0	5.8	70.0	17.0	13.0
	250	229.0	230.8	232.9	853.5	854.9	856.9	84.2	11.5	4.4	70.1	18.2	11.7
	350	229.0	230.7	232.9	853.3	854.9	856.8	87.3	8.9	3.8	73.2	20.3	6.5
	oxide	--	--	233.0	--	--	856.8	--	--	100	--	--	--
e_{al}/MoO_3	50	228.8	230.9	232.7	853.4	854.9	856.8	43.0	30.3	26.7	64.9	14.1	21.0
	150	228.9	230.8	232.8	853.4	854.9	856.8	71.8	14.3	13.9	70.7	15.7	13.7
	250	228.	230.8	233.0	853.4	854.9	856.8	79.4	14.9	5.7	71.9	15.8	12.2
	350	229.1	230.9	232.9	853.4	854.9	856.8	86.8	8.6	4.6	69.3	21.1	9.6
	oxide	--	--	232.7	--	--	856.7	--	--	100	--	--	--
CA(1.2)/ MoO_3	50	228.9	230.9	232.6	853.5	854.9	856.7	21.8	47.9	30.3	30.6	10.5	58.9
	150	228.9	230.8	232.8	853.4	854.9	856.8	71.9	17.7	10.4	65.3	12.8	21.9
	250	229.0	230.9	232.9	853.3	854.7	856.8	89.5	6.1	4.4	72.0	16.7	11.3
	350	229.0	230.9	232.8	853.3	854.9	856.7	89.4	7.7	2.9	69.9	22.0	8.1
	oxide	--	--	232.8	--	--	856.9	--	--	100	--	--	--
EG(1.2)/ MoO_3	50	228.9	231.0	232.7	853.4	854.9	856.7	13.7	44.5	41.8	42.4	10.1	47.5
	150	228.9	231.0	232.9	853.3	854.8	856.8	70.8	17.1	12.1	65.4	18.8	15.8
	250	228.9	230.9	232.8	853.4	854.9	856.8	84.2	10.8	4.9	68.1	20.1	11.8
	350	229.0	230.7	232.8	853.4	854.8	856.8	85.8	10.9	3.3	68.6	22.3	9.1
	oxide	--	--	232.9	--	--	856.7	--	--	100	--	--	--
NTA(1.2)/ MoO_3	50	229.0	230.8	232.7	853.4	854.9	856.7	11.3	25.2	63.5	11.2	19.4	69.5
	150	228.9	231.0	232.7	853.3	854.9	856.7	63.3	21.5	15.2	42.7	12.9	44.4
	250	229.0	230.9	232.9	853.3	854.9	856.7	82.6	11.2	6.2	71.0	15.2	13.8
	350	229.0	230.9	232.9	853.3	854.9	856.8	90.2	6.2	3.5	75.2	18.3	6.6
	oxide	--	--	232.7	--	--	856.8	--	--	100	--	--	--
MA(1.2)/ MoO_3	50	229.0	231.0	232.7	853.4	855.0	856.8	45.4	29.9	24.7	45.9	23.4	30.7
	150	229.0	230.9	233.1	853.3	854.9	856.8	69.4	19.1	11.5	65.6	24.1	10.3
	250	229.0	230.9	233.0	853.4	854.9	856.8	73.8	16.2	10.0	65.8	24.2	10.0
	350	229.0	230.7	233.0	853.4	854.9	856.8	87.7	9.3	3.0	68.0	24.7	7.3
	oxide	--	--	233.0	--	--	856.8	--	--	100	--	--	--

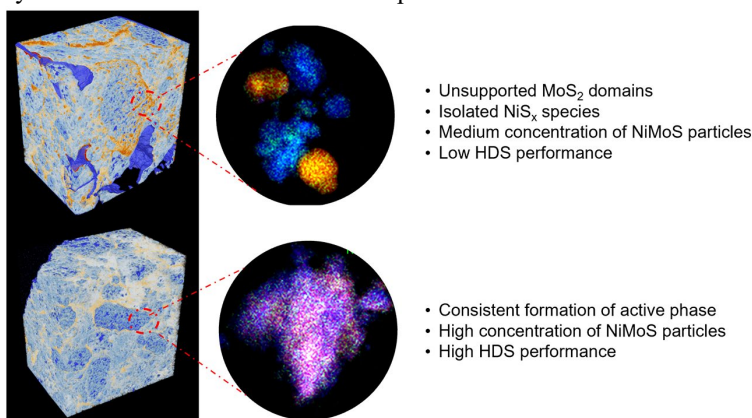
Chapter 3

Chapter 4

Alumina Supported NiMo Hydrotreating Catalysts - Aspects of 3D Structure, Synthesis and Activity

ABSTRACT

Preparation conditions have a vital effect on the structure of alumina-supported hydrodesulfurization catalysts. To explore this effect, we prepared two NiMo/Al₂O₃ samples with the same target composition by using different chemical sources, and characterizing the oxidic NiMo precursors, sulfided and spent catalysts to understand the influence of catalyst structure on performance. The sample prepared from (NH₄)₆Mo₇O₂₄·4H₂O/Ni(NO₃)₂ (MA(1.2)/AHM) contains Mo in the oxidic precursor predominantly in tetrahedral coordination in the form of crystalline domains, which show low reducibility and strong metal-support interactions. This property influences the sulfidation process such that the sulfidation of Ni and Mo occur tendentially separately with a decreased efficiency to form active Ni-Mo-S particles. Moreover, inactive unsupported MoS₂ particles or isolated NiS_x species are formed, which are either washed off during catalytic reaction, or aggregated to larger particles as seen in scanning transmission electron microscopy/energy dispersive X-ray spectroscopy (STEM/EDX). Oxidic precursor of the sample synthesized using NiCO₃/MoO₃ as metal sources (MA(1.2)/MoO₃), however, contains Mo in octahedral coordination, shows higher reducibility of the metal species as well as weaker metal-support interactions than that of MA(1.2)/AHM; these properties allow an efficient sulfidation of Mo and Ni, such that formation of active Ni-Mo-S particles is the main product. Ptychographic X-ray computed tomography, STEM, and EDX measurements show that the structure formed during sulfidation is stable under operation conditions. The structural differences explain the HDS activity difference between these two samples.



Chapter 4

4.1. Introduction

Catalytic hydrodesulfurization (HDS) is a mature technology used to remove sulfur from crude oil to produce ultra clean fuels. Typically, HDS catalysts consist of sulfides of Mo and Ni or Mo and Co, supported on a high surface area alumina ($\gamma\text{-Al}_2\text{O}_3$) [1] carrier. These catalysts are usually prepared in the form of oxidic precursors by impregnating the carrier with the metals followed by drying and calcination. Catalyst activation is done by sulfidation in an $\text{H}_2\text{S}/\text{H}_2$ gas flow at elevated temperature (around 400 °C), yielding NiMo or CoMo sulfide phases. The structure of these sulfide phases is described in the so-called Co-Mo-S model [2]; Co or Ni promotor atoms are located at the edges of nanosized MoS_2 particles. With sharpening global environmental regulations, a strong demand for fuels containing only traces of sulfur (10 ppm or less) was created. To satisfy market needs, highly active catalysts of increased lifetime and stability are needed, prompting the exploration of several synthesis processes [3, 4].

The traditional workflow of producing HDS catalysts consists of impregnation, drying, calcination, activation (sulfidation). In the early 2000 a modified workflow gained traction since it yielded catalysts of higher activity. In this workflow organic additives, such as glycols, ethylenediaminetetraacetic acid (EDTA) or nitrilotriacetic acid (NTA), were added to the catalyst formulation [5-8]. Since these additives would decompose or oxidize under typical calcination conditions (400 °C in air), the calcination step was omitted. The effect organic additives have on catalytic performance has been explored in numerous studies, linking changes in structure, density and stability of the active phase to performance [6, 9-21]. These uncalcined catalyst types show a low tendency to form Mo-O-Al bonds, which advances the formation of type II catalysts. Compared to the organic additive free and calcined type I catalysts, which are characterized by a strong interaction with the support, type II catalysts are generally more active [22]. Besides organic additives, phosphorus is another important component in the formation of highly active hydrotreating catalysts [23, 24]; experimental observations have shown that the presence of phosphorus promotes the stacking of MoS_2 -type particles by lowering metal-support interactions and enhancing the formation of type II phases [25-27].

A critical variable in catalyst preparation is the metal formulation. Since the series of oxomolybdates with the monomeric MoO_4^{2-} anion and the neutral solid MoO_3 as end members is accessible via pH-dependent aggregation processes [28, 29], there are several ways to design the impregnation solution. The most commonly used recipe to prepare Ni, Mo and P containing hydrotreating catalysts utilizes aqueous solutions of ammonium heptamolybdate ($(\text{NH}_4)_6\text{Mo}_7\text{O}_{24}\cdot 4\text{H}_2\text{O}$, AHM), nickel nitrate ($(\text{Ni}(\text{NO}_3)_2\cdot 6\text{H}_2\text{O})$) and

NiMo/Al₂O₃ Hydrotreating Catalysts - Aspects of 3D Structure, Synthesis and Activity

phosphoric acid [25, 30]. Moving towards the end members of the oxymolybdate series, molybdenum trioxide (MoO₃), nickel carbonate (NiCO₃) and phosphoric acid [31], or sodium molybdate (Na₂MoO₄·2H₂O) and nickel nitrate (Ni(NO₃)₂) [32] are other feasible sources of Mo and Ni. Some studies utilized highly condensed and symmetric starting materials such as Keggin [33, 34] and Anderson complexes [35, 36]. Overall, there is no clear answer as to which type of impregnation solution yields the best catalysts.

Characterization studies conducted over the years have a focus on describing the active NiMoS phase at atomic or nanometer scale, e.g., utilizing EXAFS to explore the coordination number of Mo [37-40] to determine particle size and stacking degree of NiMoS particles, or the degree of edge decoration through promotor atoms; Active site(s) and molecular reaction routes of Co-Mo-S structures synthesized on Au(111) were monitored by means of Scanning Tunneling Microscopy (STM) [41]; and first-principles calculations were used to describe particle structure [42, 43] as well as mechanisms of reactions taking place at the active sites located on the edges of Co-Mo-S and Ni-Mo-S nanocrystals [42, 44, 45]. To a much lesser extent information regarding metal dispersion on alumina or the influence and change of the alumina pore structure on and during metal deposition can be found.

Here, we investigate two hydrotreating catalysts, where malic acid (MA) and phosphorus were added to the NiMo catalyst formulation by co-impregnation [6, 7]. These two catalysts were prepared on the same alumina carrier with identical metal and phosphorus loadings and contain the same organic additive. The only difference is that they were prepared by using two different impregnation solutions. MA(1.2)/AHM was prepared with AHM and Ni(NO₃)₂ as Mo and Ni sources (route A), while catalyst MA(1.2)/MoO₃ prepared from MoO₃ and NiCO₃ (route B). Thus, the difference lies in the impregnation chemistry brought about by these impregnation solutions, which will be shown to lead to substantial structural differences of the active phases. For a more comprehensive understanding of the structure difference, we present a detailed structural characterization of these two samples and discuss their performance levels on structural grounds. Catalyst characterization is based on physical methods, spectroscopy, diffraction, tomography and catalytic activity measurements. In particular, we used N₂ physisorption and temperature-programmed reduction (TPR) as physical methods, and X-ray photoelectron spectroscopy (XPS), Raman and X-Ray diffraction (XRD) as standard spectroscopy and diffraction methods. 2D and 3D imaging methods including scanning transmission electron microscopy (STEM), energy dispersive X-ray spectroscopy (EDX) and ptychographic X-ray computed tomography (PXCT) were used for advanced structural characterization. The catalytic activity of samples was evaluated in thiophene, dibenzothiophene (DBT) and gas oil HDS tests.

Chapter 4

4.2. Experimental section

4.2.1. Catalyst preparation

Two types of NiMo/Al₂O₃ catalysts prepared from two sets of different metal salts with malic acid (MA) as additive were prepared by incipient wetness impregnation of γ -Al₂O₃ [46] extrudates with an aqueous solution of respective metal salts and additive. The target composition of both types is 15 wt% Mo, 3.67 wt% Ni, 2 wt% P (referenced to MoO₃, NiO and P₂O₅), and MA in a molar ratio of 1.2 per atom Mo. Phosphorus was added in the form of H₃PO₄, which does also facilitate metal dissolution [24, 47]. The two types of NiMo/Al₂O₃ catalysts and associated preparation routes are subsequently referred to as MA(1.2)/AHM, MA(1.2)/MoO₃/Route A and B.

Route A: 8.1 g AHM were slowly added to an aqueous solution of H₃PO₄ (2.2 g, 85 wt% in H₂O). Ammonia (28 %) was added following yielding an initially clear solution, which under continuous stirring results in a light-yellow solution. Next 5.3 g Ni(NO₃)₂·6H₂O were added under stirring, which results in a transparent green solution. To obtain the final impregnation solution, 7.4 g MA was added. By adding deionized water, the volume of the impregnation solution was finally adjusted to the pore volume of alumina. The pH of the final impregnation solution is 5.

Route B: 6.6 g MoO₃, 2.2 g NiCO₃ and 2.2 g H₃PO₄ solution (85 wt% in H₂O) were dissolved in deionized water under constant stirring and heated till boiling yielding a clear green solution to which 7.4 g MA were added. The pH of the final solution is < 1.

16.4 mL impregnation solution were then added to each 20 g alumina extrudes (diameter: 1 mm, length: 3 – 13 mm). The extrudates were kept for a period of two hours under slow movement on a roller bank and subsequently dried over night at 120 °C yielding the catalyst precursors (oxide). To preserve the malic acid for the subsequent sulfidation process, the prepared samples were not calcined [48]. Freshly sulfided catalysts and spent samples recovered from the gas oil HDS test are referred to as (sulfide) and (spent), respectively. The final metal loading of these catalysts was determined by inductively coupled plasma optical emission spectroscopy (ICP-OES) and the results are compiled in Table 4.1.

4.2.2. Catalyst activation.

To prepare the sulfided catalyst samples, ~50 mg oxidic precursor (75 – 125 μ m) were loaded in the middle of a valve-sealed stainless-steel reactor with an inner diameter of 4 mm and heated up to 350 °C with a 2 °C/min ramp rate in 1 bar H₂/H₂S (90/10 vol%) at a flow rate of 50 mL/min. The sample was kept under these conditions for 2 h and subsequently cooled to room temperature in He atmosphere. The sulfided catalyst were then transferred to and

stored in an N₂-filled glovebox for further characterization. During sulfidation, malic acid is decomposed and the decomposition products are released. The final active catalyst does not contain any organic compounds.

4.2.3. Catalytic activity measurements

The catalytic performance of MA(1.2)/AHM and MA(1.2)/MoO₃ was evaluated via the gas-phase thiophene, liquid-phase DBT HDS and gas-oil HDS reaction. Detailed information regarding these reactions can be found in Section 2.3, Chapter 2.

4.2.4. Catalyst characterization.

N₂ physisorption: Textural properties, i.e., specific surface area, pore volume and average pore size, were determined by means of N₂ physisorption in a Micromeritics AutoChem apparatus (Figure B1). Prior to physisorption measurements, samples were pretreated over night with N₂ at 120 °C.

XRD, TPR, and Raman spectroscopy of the oxidic precursors were conducted according to the specific procedures described in Section 2.2, Chapter 2.

XPS spectra of oxidic precursors, fresh sulfided samples and respective spent samples were recorded at room temperature using a Thermo Scientific K-Alpha spectrometer. Detailed measurement and data analysis can be found in Section 2.2, Chapter 2.

PXCT: 3D structural measurements were carried out by means of PXCT [49-51]. PXCT is a lens less quantitative imaging technique in which each tomographic projection is calculated by means of ptychographic phase-retrieval algorithms [52, 53]. Tomographic reconstruction retrieves the complex-valued refractive index of the examined sample, providing tomograms of both phase and amplitude contrast [53]. Away from sample-relevant absorption edges, the retrieved refractive index decrement values can be converted to electron density as described in Diaz et al. [54]. Measurements were carried out at the cSAXS beamline of the Swiss Light Source at 6.2 keV photon energy at room temperature in an inert atmosphere. A series of sample cylinders, ≈ 25 μm in diameter, extracted central, from a catalyst pellet of MA(1.2)/AHM (sulfide), MA(1.2)/MoO₃ (sulfide), MA(1.2)/AHM (spent), and MA(1.2)/MoO₃ (spent) were examined. The sample cylinders or pillars were prepared using a micro-lath and focus-ion-beam (FIB) milling, Figure 2.12 [55]. The obtained quantitative electron density tomograms possess, on average, a half-period spatial resolution of 40 nm, which was evaluated through Fourier shell correlation (FSC, Figure B2) [56]. Tomogram acquisition and analysis can be found in Appendix B.

Table 4.1. Catalyst composition, surface area, pore volume and diameter determined by ICP-AES^a and N₂ physisorption^b.

Catalyst	Loading (wt.%) ^a			Ni/Mo molar ratio ^a	Surface area ^b (m ² /g)	Pore volume ^{*b} (cm ³ /g)	Pore diameter ^{*b} (nm)
	Mo	Ni	P				
MA(1.2)/AHM (oxide)	11.32	2.65	1.53	0.4	112	0.2	10.4
MA(1.2)/AHM (sulfide)	10.42	2.81	1.44	0.4	--	--	--
MA(1.2)/AHM (spent)	9.16	2.57	1.33	0.5	--	--	--
MA(1.2)/MoO ₃ (oxide)	11.36	2.70	1.57	0.4	201	0.2	7.2
MA(1.2)/MoO ₃ (sulfide)	10.70	2.56	1.43	0.4	--	--	--
MA(1.2)/MoO ₃ (spent)	10.69	2.57	1.31	0.4	--	--	--
γ -Al ₂ O ₃	--	--	--	--	300	0.8	9.0

*Values determined from the BJH method applied to the adsorption branch of the isotherm. (Figure B1)

Table 4.2. Gas-phase thiophene HDS reaction rates and liquid-phase dibenzothiophene HDS reaction rate constants of MA(1.2)/AHM and MA(1.2)/MoO₃.

Catalyst (sulfide)	Thiophene Reaction rates (mol mol _{Mo} ⁻¹ h ⁻¹)	DBT				Gas-oil Reaction rate constants (mol mol _{Mo} ⁻¹ h ⁻¹)	
		Reaction temperature	Conversion (%)	Selectivity			Reaction rate constants (mol mol _{Mo} ⁻¹ h ⁻¹)
				BP	CHB		
MA(1.2)/AHM	74.1 ± 1.7	230 °C	7.6	90.0	10.0	3.4	
		250 °C	16.7	83.8	16.2	7.8	
		270 °C	34.1	75.6	24.4	17.7	
MA(1.2)/MoO ₃	101.9 ± 0.8	230 °C	25.4	57.8	42.2	12.5	
		250 °C	51.3	54.3	45.7	30.6	
		270 °C	85.2	50.7	49.3	81.2	

STEM and EDX: the local morphology and elemental composition of the sulfide and spent catalysts was determined by STEM and EDX using a probe corrected JEOL ARM 200F transmission electron microscope. Sample preparation and data analysis procedure are described in Chapter 2. The correlation between Mo and Ni was calculated via MATLAB, as shown in Figure B3, details can be found in Appendix B.

4.3. Results

4.3.1. Catalytic activity

Table 4.2 shows the catalytic activity of MA(1.2)/AHM and MA(1.2)/MoO₃ in gas-phase thiophene HDS tests at atmospheric pressure, liquid-phase DBT HDS at 20 bar and liquid-phase gas oil HDS at 60 bar. The catalytic activity of MA(1.2)/MoO₃ in atmospheric thiophene HDS is higher than that of MA(1.2)/AHM, i.e., 101.9 mol mol_{Mo}⁻¹ hr⁻¹ compared to 74.1 mol mol_{Mo}⁻¹ hr⁻¹. In DBT HDS at 270 °C, the activity difference is significantly larger as can be derived from respective reaction rate constants of 17.7 mol mol_{Mo}⁻¹ hr⁻¹ and 81.2 mol mol_{Mo}⁻¹ hr⁻¹ for MA(1.2)/AHM (sulfide) and MA(1.2)/MoO₃ (sulfide), respectively. The gas oil HDS test does also clearly differentiate the two samples i.e., 4.96 mol mol_{Mo}⁻¹ hr⁻¹ for MA(1.2)/AHM and 22.31 mol mol_{Mo}⁻¹ hr⁻¹ for MA(1.2)/MoO₃. The products of the DBT HDS reaction are also listed in Table 4.2, where it can be noticed that the main products are biphenyl (BP) and cyclohexylbenzene (CHB), no bicyclohexyl (BCH) was observed under our reaction conditions.

4.3.2. Physio-chemical bulk characterization of the oxidic catalyst precursor

To investigate the origin of these activity differences we first acquired powder XRD (Figure 4.1a), TPR (Figure 4.1b), BET data (Table 4.1, Figure B1), and Raman spectra (Figure 4.2) of the supported catalysts in their oxidic precursor form.

XRD; sample MA(1.2)/MoO₃ (oxide) exhibits characteristic diffraction peaks at $2\theta = 46^\circ$ and 67° attributed to γ -Al₂O₃ (JCPDS 01-077-0396). The absence of other diffraction features points to highly dispersed, nanoscopic or amorphous species. The XRD pattern of MA(1.2)/AHM (oxide) is different. Next to above-mentioned reflections caused by γ -Al₂O₃, a set of sharp diffraction peaks at $2\theta = 10.7^\circ, 15.3^\circ, 18.4^\circ, 21.2^\circ, 24.0^\circ, 26.3^\circ, 30.6^\circ, 32.5^\circ, 36.0^\circ, 43.9^\circ, 48.1^\circ, 50.6^\circ, 51.9^\circ, 55.6^\circ, 62.7^\circ,$ and 64.7° indicate the presence of crystalline (NH₄)₃PO₄(MoO₃)₁₂·4H₂O (JCPDS 00-009-0412). The crystallite size as estimated from the Scherrer equation [57] is 60 nm. (NH₄)₃PO₄(MoO₃)₁₂·4H₂O crystallites may form in the impregnation solution or on the alumina surface upon drying. The differences in the metal speciation on the alumina surface in the two samples leads to a higher surface area for sample MA(1.2)/MoO₃ (oxide) and accounts for the different N₂ physisorption results (Table 4.1).

Chapter 4

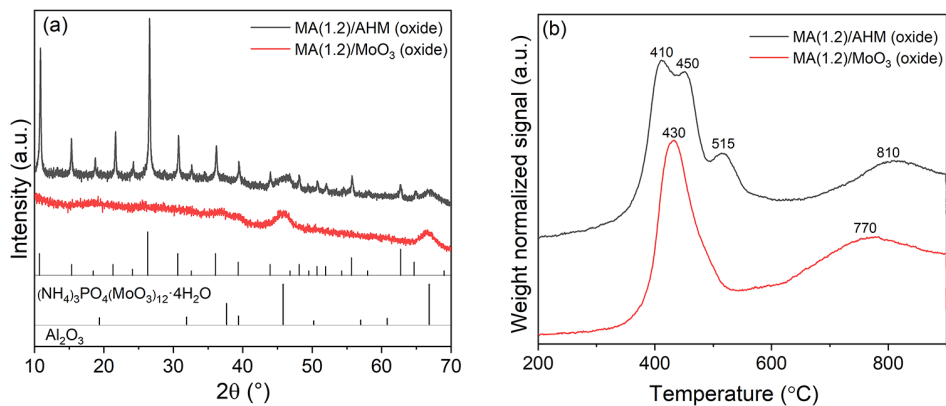


Figure 4.1. (a) XRD pattern and (b) TPR curves of MA(1.2)/AHM and MA(1.2)/MoO₃.

The reducibility of MA(1.2)/AHM (oxide) and MA(1.2)/MoO₃ (oxide) was explored by means of TPR. Overall, their reduction profiles are rather similar. In Figure 4.1b, both catalysts exhibit dominant reduction peaks around 400 °C and 800 °C. The low temperature reduction peaks can be attributed to a reduction of Ni oxide species, as well as a partial reduction of polymolybdates that have a weak interaction with the support (Mo⁶⁺ to Mo⁴⁺) [58, 59]. The broad peak at the higher temperature is attributed to the deep reduction of all Mo species, including tetrahedrally coordinated Mo⁴⁺ species. The differences in TPR profiles between samples are as follows. In the low temperature reduction region, sample MA(1.2)/AHM (oxide) shows three reduction peaks at 410 °C, 452 °C, and 516 °C, while only one peak occurs at 390 °C in sample MA(1.2)/MoO₃ (oxide). Differences in Mo-support interactions due to distinctly different oxomolybdate species likely account for the existence of three reduction peaks in the low temperature reduction area in MA(1.2)/AHM (oxide). In MA(1.2)/MoO₃ (oxide), differences in the precursor structures are small, so that Mo-support interactions are more uniform and result in one (broad) reduction peak. Consistently, the high temperature reduction peak in sample MA(1.2)/MoO₃ (oxide) is centered around 770 °C and is ~40 °C lower than the corresponding peak in MA(1.2)/AHM (oxide), again indicating a weaker metal-support interaction in MA(1.2)/MoO₃ (oxide). This type of interaction for MA(1.2)/MoO₃ also leads to a higher MoS₂ crystallites stacking upon sulfidation and is commonly agreed as a requirement for the formation of type II Ni-Mo-S phases [25, 60, 61].

Following, we used Raman spectroscopy to determine the nature of Mo and Ni oxide species present on the alumina surface (Figure 4.2) [11]. The Raman spectra of sample MA(1.2)/MoO₃ (oxide) shows a broad band at 950 cm⁻¹ together with a shoulder at 860 cm⁻¹ and two less intense bands at 360 cm⁻¹ and 225 cm⁻¹, which are considered to be the vibrational signature of octahedrally coordinated polymolybdate species [62-64]. The spectrum of sample MA(1.2)/AHM (oxide), exhibits in addition a band at 1047 cm⁻¹, which

is assigned to the $\nu_s(\text{NO}_3)$ stretching vibration of nitrate anions (originating from the nickel nitrate source) [65]. The main bands at 980 cm^{-1} , 880 cm^{-1} , 600 cm^{-1} , 380 cm^{-1} and 240 cm^{-1} are due to $[\text{PMo}_{12}\text{O}_{40}]^{3-}$ species, as confirmed in the XRD. Detailed band assignments can be found in [66, 67]. In addition, to the band position implied differences in coordination state, the shape of the bands themselves is worth noting. The widths of Raman bands are frequently positively correlated with the degree of crystallinity of the probed material, as such the sharp bands in the spectrum of sample MA(1.2)/AHM (oxide) point to mainly crystalline species, while the broad bands in the spectrum of sample MA(1.2)/MoO₃ (oxide) indicate a higher degree of structural disorder. The Mo coordination difference observed above already exists in the respective impregnation solutions (Figure B4), and the reason for this difference is that Mo aggregation is a pH-dependent process yielding different oxomolybdates, e.g., MoO₄²⁻ and MoO₃ as explained in the Introduction.

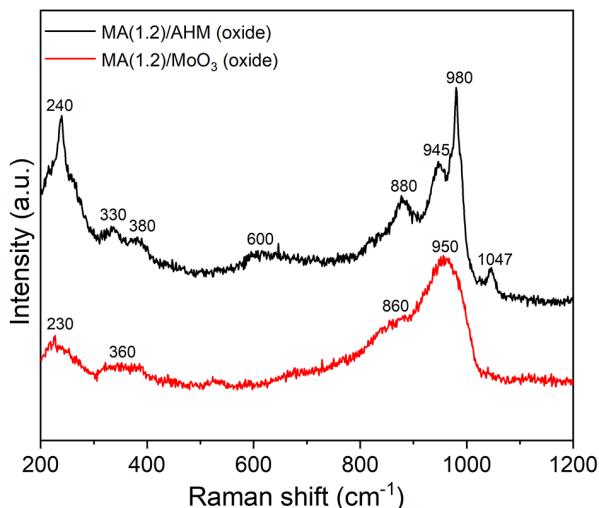


Figure 4.2. Raman spectra of MA(1.2)/AHM and MA(1.2)/MoO₃.

4.3.3. Changes in catalyst composition during activation/sulfidation

Temperature-dependent changes during sulfidation of MA(1.2)/AHM and MA(1.2)/MoO₃ were followed by means of XPS (Figure 4.3). Binding energies (B.E.) of main features and atomic percentages of Mo and Ni species according to their contribution to the overall signal envelope are compiled in Table B2. For MA(1.2)/AHM (sulfide) and MA(1.2)/MoO₃ (sulfide), three doublets related to different Mo oxidation states, together with the S 2s signal characteristic of S²⁻ (falling in the same spectral range at a B.E. > of 226.3 eV) can be identified. The three Mo 3d doublets are assigned to Mo⁶⁺ in MoO₃ (B.E. 3d_{5/2} = 232.9 ± 0.4 eV), Mo⁵⁺ in oxysulfide species (B.E. 3d_{5/2} = 230.8 ± 0.4 eV) and Mo⁴⁺ in MoS₂ (B.E. 3d_{5/2} = 229.1 ± 0.5 eV). The Ni 2p spectra can be deconvoluted into three components [68]: oxidic Ni (856.4 ± 0.6), NiMoS species (854.6 ± 0.4 eV) and sulfided Ni (853.3 ± 0.2 eV), along

Chapter 4

with their respective satellites [69, 70]. The spectra of MA(1.2)/AHM (oxide) and MA(1.2)/MoO₃ (oxide) were fitted in the same way with oxidic contributions only.

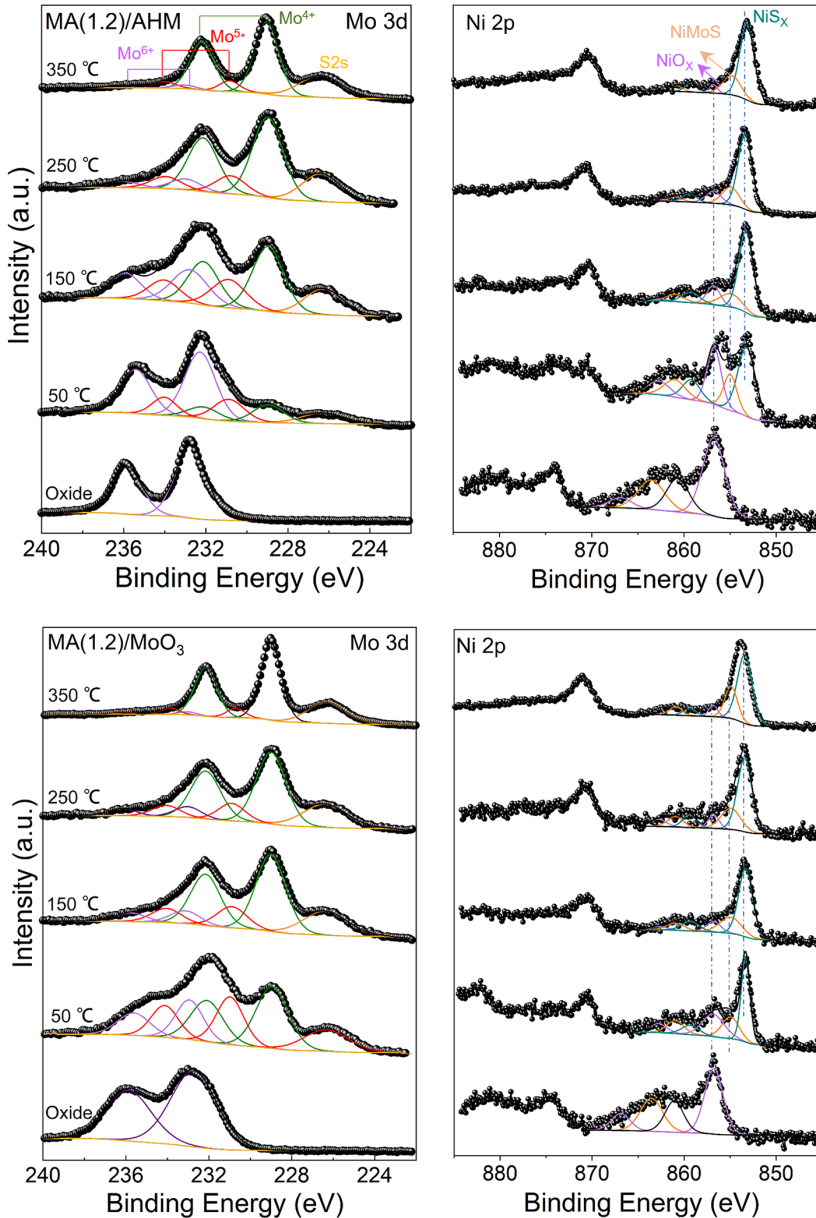


Figure 4.3. Mo 3d and Ni 2p XPS spectra of MA(1.2)/AHM (top) and MA(1.2)/MoO₃ (bottom) obtained after sulfidation (room temperature to 350 °C, 1 bar H₂S/H₂). Experimental data are presented by open circles and the fit by a black curve. The fits for Mo 3d are composed of Mo⁴⁺ (green), Mo⁵⁺ (pink), Mo⁶⁺ (purple) as well as S²⁻ 2s signal (yellow). Ni 2p_{3/2} fits are composed of Ni as in NiO_x (purple), NiMoS (orange) and NiS_x (blue).

Figure 4.4 shows the sulfidation profile of MA(1.2)/AHM (sulfide) and MA(1.2)/MoO₃ (sulfide). While the final sulfidation degree of Mo and Ni is comparable in both samples, the evolution towards this end value differs. For MA(1.2)/AHM (sulfide), the sulfidation rate of Ni is faster than that of Mo, from which we conclude that a substantial portion of Ni is sulfided before the formation of MoS₂ has started. This could mean that this part of Ni remains as isolated NiS_x particles and will thus not participate in the formation of the catalytically active Ni-Mo-S phase [12, 71, 72]. In MA(1.2)/MoO₃ (sulfide), the situation is reversed, i.e., Mo sulfidation precedes that of Ni, meaning MoS₂ particles already exist when Ni sulfidation starts, providing the right environment for Ni-Mo-S formation [73]. The concentration of NiMoS species in MA(1.2)/AHM (sulfide) and MA(1.2)/MoO₃ (sulfide) as extracted from XPS (Table 4.3) verified this assumption.

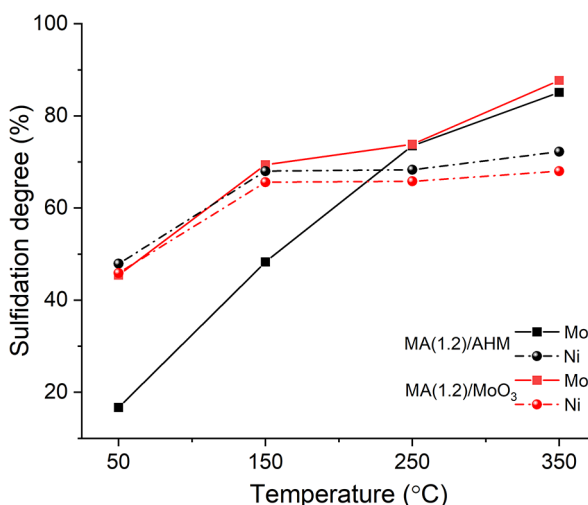


Figure 4.4. Temperature dependent sulfidation profile of Mo and Ni in MA(1.2)/AHM and MA(1.2)/MoO₃ at four different temperatures and 1 bar H₂S/H₂ as determined by XPS.

4.3.4 Spatial resolved analysis of sulfided and spent catalysts

To investigate how the different preparation routes affect the catalyst structure and composition locally, sulfided and spent catalysts of MA(1.2)/AHM and MA(1.2)/MoO₃ were characterized by means of PXCT and STEM/EDX. This combination of techniques provides information from the micron scale (PXCT) to the nano scale (STEM/EDX).

Figure 4.5 shows volume renderings and sagittal cuts through the PXCT acquired electron density tomograms of MA(1.2)/AHM (sulfide and spent) and MA(1.2)/MoO₃ (sulfide and spent). As the half-period spatial resolution of these tomograms is on average 40 nm, Figure B2, local or direct compositional analysis is restricted to larger mesopores (and above) and or reliant on partial volume analysis utilizing a priori compositional knowledge. Partial

Chapter 4

volume effects refer to the occupancy of a single voxel by multiple, spatially unresolved, components, leading to a fractional occupancy-related electron density [50]. The theoretical electron densities of the main sample or catalyst components are $0.785 \text{ n}_e \text{ \AA}^{-3}$ for amorphous Al_2O_3 and $1.1 \text{ n}_e \text{ \AA}^{-3}$ for NiMoO_2 . Further information can be found in Table B1. Based on these values, we consider that an electron density below that of amorphous Al_2O_3 can be directly related to the degree of internal porosity. Similarly, an electron density above that of amorphous Al_2O_3 provides information about the amount of MoS_2 clusters present within a selected voxel (see supporting information for detailed tomogram analysis information). Adhering to this interpretation we can identify four compositionally distinct domains in the acquired electron density tomograms, which are spatially resolved pores, low-density (high-internal porosity) alumina, high-density (low-internal porosity) alumina and areas rich in MoS_2 species, $> 30 \text{ vol\%}$.

A metal deposition difference can be observed between MA(1.2)/AHM (sulfide) and MA(1.2)/ MoO_3 (sulfide) (Figure 5(a, b) and 5(c, d)). Visible in MA(1.2)/AHM (sulfide), are isolated areas or clusters rich in MoS_2 species (dark orange dots) and continuous *circular* domains rich in MoS_2 species, potentially caused by a diffusion limited drying process and reflective of metal aggregation. These domains are absent in MA(1.2)/ MoO_3 (sulfide), displaying a more homogenous distribution of MoS_2 . A further, evidence of this can be found in the fact that the smaller clusters present in MA(1.2)/ MoO_3 have a lower electron density compared to MA(1.2)/ MoO_3 , i.e., the corresponding voxel possess a lower MoS_2 concentration.

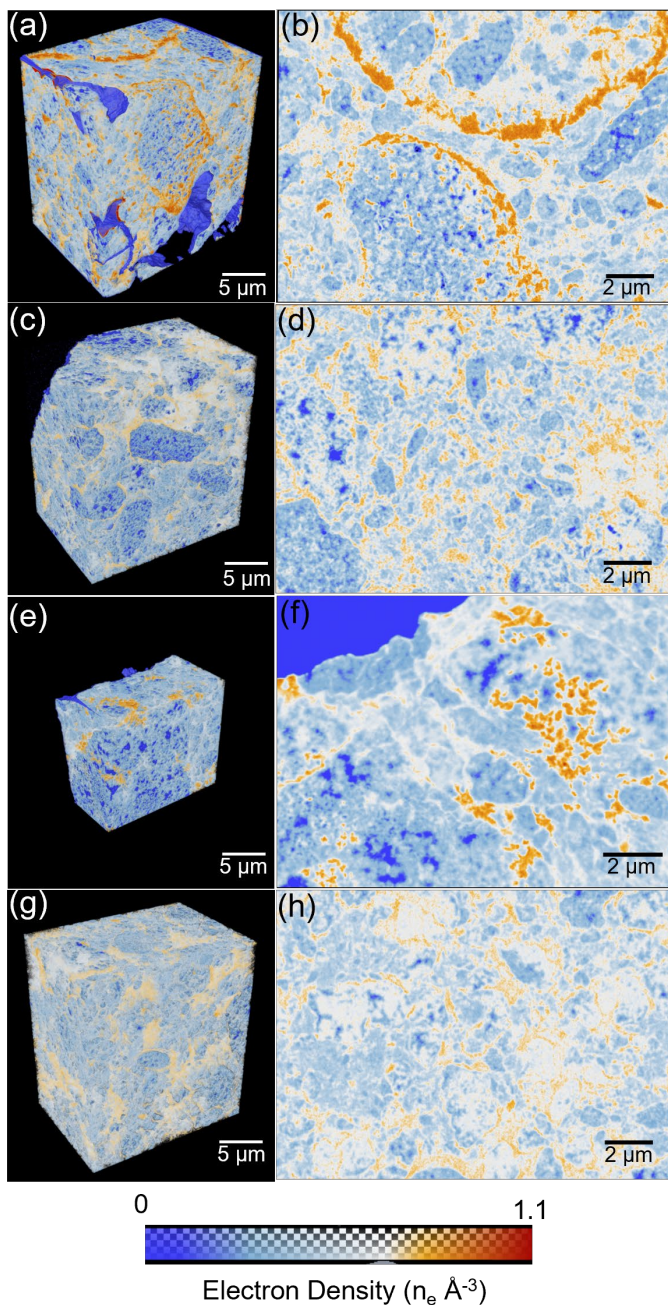


Figure 4.5. Ptychographic X-Ray computed tomography of MA(1.2)/AHM (sulfide & spent) and sample MA(1.2)/MoO₃ (sulfide & spent). Shown are volume renderings of and virtual cuts through the PXCT acquired electron density tomograms of MA(1.2)/AHM (sulfide) (a, b), MA(1.2)/MoO₃ (sulfide) (c, d), MA(1.2)/AHM (spent) (e, f) and MA(1.2)/MoO₃ (spent) (g, h). The color map ranging from blue to red indicates an increase in electron density.

Chapter 4

This metal deposition behavior is also found in the tomogram corresponding electron density histograms (Figure 4.6). Here, we see a shoulder in the high electron density region (bottom right area) for MA(1.2)/AHM (sulfide); while in MA(1.2)/MoO₃ (sulfide), no such high electron density area is observed. From the PXCT data, we can infer that the metal dispersion in MA(1.2)/MoO₃ (sulfide) is much higher than in MA(1.2)/AHM (sulfide). Looking at the sagittal cuts through the tomograms of these two samples, it can also be noticed that the above-mentioned high electron density and MoS₂ rich regions, did not uniformly from throughout the alumina domain. Visible in the sagittal cuts is a diminishing electron density gradient from the larger pore space into high-density alumina domains. This observed electron density gradient can result from particle aggregation at the boundary of high and low density alumina due to metal deposition limitation encountered upon entering these domains, i.e., a result of pore transport limitations [50]. These limitations appear to be much stronger in sample MA(1.2)/AHM (sulfide). No such gradient is observable in the low-density or high porosity alumina domains.

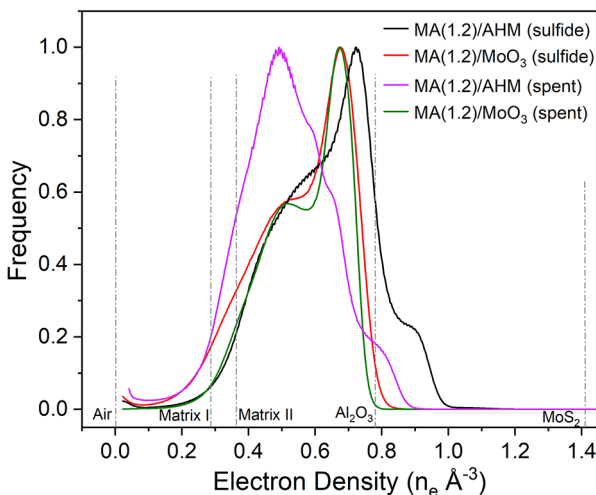


Figure 4.6. Tomogram corresponding electron density histograms of MA(1.2)/AHM (sulfide & spent) and MA(1.2)/MoO₃ (sulfide & spent). The electron density of selected reference components is indicated by the dotted lines.

Focusing on the spatially resolved pore structure we observe further differences between these two samples (Figure B5). While the pores in MA(1.2)/MoO₃ (sulfide) have a diameter between 60 – 420 nm, the pores found within MA(1.2)/AHM (sulfide) are slightly larger with a diameter distributed in the range of 60 – 760 nm. As the composition of catalyst and support material are the same, we infer that this difference was caused by specific interactions of the impregnation solution with the alumina carrier, resulting in alterations of the pore structure. The unchanged pore size distribution between the sulfide and their respective spent samples (Figure B5) provides further evidence that structural differences of the carrier between

NiMo/Al₂O₃ Hydrotreating Catalysts - Aspects of 3D Structure, Synthesis and Activity

MA(1.2)/AHM (sulfide) and MA(1.2)/MoO₃ (sulfide) were introduced during catalyst preparation. Moreover, it demonstrates that liquid phase sulfidation used in the gas oil test does not change the hierarchical structure of the catalysts, which makes a comparison between sulfide samples (gas phase sulfidation) and spent samples (liquid phase sulfidation) used for stability study, reasonable.

As shown in Figure 4.5 and Figure 4.6, the electron densities of MA(1.2)/MoO₃ (sulfide) and MA(1.2)/MoO₃ (spent) are comparable, indicating that activity test conditions did not cause much difference to the structure of MA(1.2)/MoO₃ (sulfide). For MA(1.2)/AHM (sulfide) we do observe a significant change following the activity test. Visible is a decrease of the high electron density components, the histogram peak previously associated with MoS₂ cluster changes in position from 0.9 n_e/Å³ to ~0.8 n_e/Å³ and decreases in relative intensity. To understand why the high electron density region decreases, elemental analysis was conducted (Table 4.1). The results show that the metal contents in MA(1.2)/AHM (spent) (9.16 wt% Mo, 2.57 wt% Ni) is lower than in MA(1.2)/AHM (sulfide) (10.42 wt% Mo, 2.81 wt% Ni), from which we conclude that metal, presumably in the form of MoS₂ species, was washed off under the gas oil activity test conditions.

As the here acquired PXCT data are limited in spatial resolution and chemical element insensitive, we mechanically fractured the catalyst pellets to obtain electron microscopy compatible specimen. Subsequent examination using STEM and EDX mapping allowed us to probe the effect preparation, activation and use had on the structure of the active MoS₂ platelets as well as the catalysts local elemental composition.

Figure 4.7a shows STEM images of MA(1.2)/AHM and MA(1.2)/MoO₃ and provides information on the length distribution of MoS₂ platelets as well as their layers distribution. The mean length of MoS₂ platelets in MA(1.2)/AHM (sulfide) is 3.7 nm with an average 1.7 layers per particle; particles in MA(1.2)/MoO₃ (sulfide) are smaller (3.2 nm) with a higher number of layers (2.0). The feature of a small particle size and high degree of stacking per particle is often considered a prerequisite to the formation of type II NiMoS phases [71].

While the activity test had no effect on the mean length of MoS₂ platelets in MA(1.2)/AHM (spent), a slight increase in mean length can be observed in MA(1.2)/MoO₃ (spent). Additionally, a noticeable de-stacking was observed: the average number of layers per particle decreased from 1.7 (MA(1.2)/AHM (sulfide)) to 1.3 (MA(1.2)/AHM (spent)) and from 2.0 (MA(1.2)/MoO₃ (sulfide)) to 1.6 (MA(1.2)/MoO₃ (spent)), Figure 4.7b. De la Rossa et al. [74] assign this de-stacking behavior during catalyst operation to the pressure applied in the HDS activity test, since at high pressure, the formation of multilayered stacks through

Chapter 4

van der Waals forces seems counterbalanced by the strong interaction of adsorbed substances favoring stabilization of single MoS₂ layers.

To probe the elemental distribution in the prepared catalysts on the nanoscale we referred to a combination of HAADF STEM and EDX mapping. Figure 4.8a, HAADF STEM reveals the presence of two morphologically distinctly different phases in MA(1.2)/AHM (sulfide). EDX derived compositional maps of Mo, Ni, and Al, Figures 4.8b and 4.8c, suggest these phases to correspond to unsupported NiMoS particles and isolated NiS_x species. As suggested by XPS, this could be the result of the faster sulfidation rate of Ni under the chosen preparation conditions. In MA(1.2)/MoO₃ (sulfide), the metals are dominantly homogeneously dispersed as expected for Ni-Mo-S particles. The spatial correlation of Ni and Mo, i.e., their dispersion behavior, can be quantified using a normalized Ni-Mo correlation degree extracted from EDX mapping data, as shown in Figure B3. Here it is shown that the average correlation degree in MA(1.2)/AHM (sulfide) is 0.7, while it is 0.9 in MA(1.2)/MoO₃ (sulfide). After the gas oil test, the average Ni-Mo correlation degree, for MA(1.2)/AHM (spent) and MA(1.2)/MoO₃ (spent), decreased to 0.7 and 0.5, respectively. The origin of this decrease could be owed to an aggregation of MoS₂ and NiS_x, during the gas oil activity test (see EDX data of MA(1.2)/AHM (spent) and MA(1.2)/MoO₃ (spent) in Figures B6 and B7). Under the testing conditions, NiS_x will have a sufficiently high mobility to enable aggregation [75].

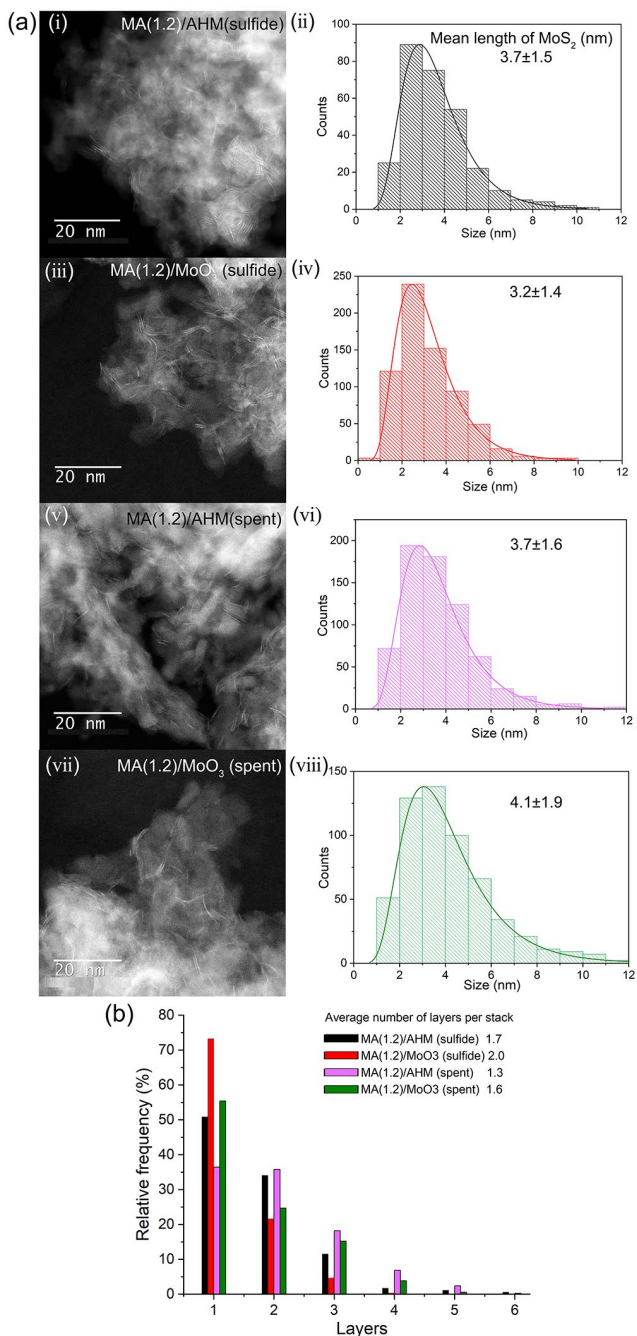


Figure 4.7. (a) High-angle annular dark-field (HAADF) STEM images and length distribution of MoS₂ platelets of (i, ii) MA(1.2)/AHM (sulfide), (iii, iv) MA(1.2)/MoO₃ (sulfide), (v, vi) MA(1.2)/AHM (spent) and (vii, viii) MA(1.2)/MoO₃ (spent); (b) stacking distribution and the average number of layers per stack of four prepared samples (MA(1.2)/AHM (sulfide), MA(1.2)/MoO₃ (sulfide), MA(1.2)/AHM (spent), and MA(1.2)/MoO₃ (spent)).

Chapter 4

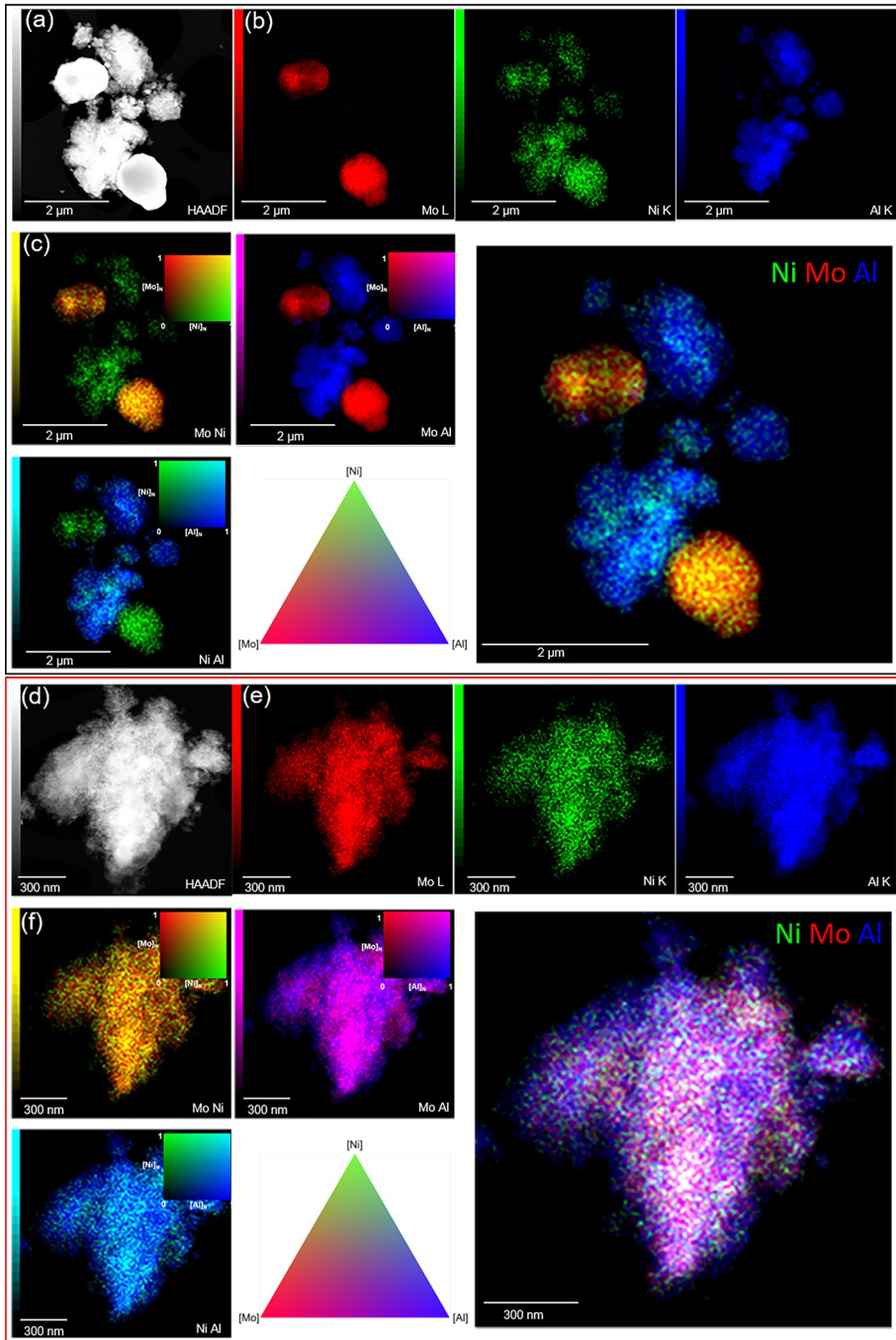


Figure 4.8. Electron microscopy of MA(1.2)/AHM (sulfide) (top) and MA(1.2)/MoO₃ (sulfide) (bottom). a, d) High-angle annular dark-field (HAADF) STEM image. b, e) Energy dispersive X-ray spectroscopy (EDX) maps of Mo, Ni and Al corresponding to the STEM image of (a) and (d). c, f) Normalized (N) and merged EDX maps of Mo, Ni and Al.

4.4. Discussion

The comparative analysis of two “compositionally” identical alumina supported NiMo hydrotreating catalysts, originating from different preparation methodologies, revealed pronounced differences in both catalytic activity and stability. Examination of the supported catalysts in the oxidic precursor state, the active sulfide and post-use or spent state revealed these difference to be a result of compositional and structural modifications of both the support and the catalyst.

The oxidic precursors were characterized by means of TPR, XRD and Raman spectroscopy. The results indicate that in MA(1.2)/AHM and MA(1.2)/MoO₃, Mo and Ni species exist on the alumina carrier surface in different coordination states. As consequences, MA(1.2)/AHM and MA(1.2)/MoO₃ exhibit varying degrees of metal-support interactions (Figure 4.1, 4.2) and ultimately a distinct response to hydrogen reduction, as well as sulfidation, i.e., to the transformation of Ni-Mo-O into Ni-Mo-S phases. XPS results (Figure 4.3, 4.4) show that both samples arrive at the same degree of Mo and Ni sulfidation at the end of the sulfidation process, however the evolution towards the state is different. In sample MA(1.2)/AHM (sulfide), most part of Ni is sulfided before the pronounced formation of MoS₂ has started, so it is likely this part of Ni remains as isolated NiS_x particles and will not participate in forming the catalytically active Ni-Mo-S phase. This interpretation is also supported by STEM/EDX data, which show unsupported MoS₂ particles and isolated NiS_x species (Figures 4.8b, c). MA(1.2)/MoO₃ (sulfide) behaves differently; MoS₂ particles already exist when Ni sulfidation starts, incorporation of Ni into the edges of existing MoS₂ particles is the predominant utilization of Ni, yielding an enhanced formation of NiMoS particles (higher content), which is in line with the distribution pattern of Ni and Mo shown in STEM/EDX (Figure 4.8e and 4.8f). This structure can be further verified via the normalized Ni-Mo correlation degree (Figure B7), extracted from the EDX mapping data, since a higher average degree of Ni-Mo correlation detected in MA(1.2)/MoO₃ (sulfide) is the expected appearance for a sample consisting predominantly of NiMoS particles. This difference in sulfidation chemistry indicates that MA(1.2)/AHM (oxide) has a higher metal-support interaction than MA(1.2)/MoO₃ (oxide), and this is reflected as a lower degree of stacking and larger MoS₂ particles in MA(1.2)/AHM (sulfide) as observed by STEM (Figure 4.7). Different metal coordination and metal-support interactions in the oxidic precursors are not the only changes caused by preparation conditions; changes in the (pore)structure of the alumina carrier are also observed. Pore diameter distribution values extracted from PXCT data (Figure B5) show that MA(1.2)/AHM (sulfide) has larger pores compared to MA(1.2)/MoO₃ (sulfide), most likely formed as the result of partial alumina dissolution during the preparation (impregnation) process. The pore diameter data derived from BET measurements underpin this assumption

Chapter 4

(Table 4.1); MA(1.2)/AHM (oxide) has a larger pore diameter than MA(1.2)/MoO₃ (oxide). The alumina dissolution process can be considered to be a consequence of the formation of heteropolymolybdate, as initially proposed by Carrier et al [76]. They conclude that alumina dissolution occurs in the presence of molybdates, and especially in the pH range between 4 and 6. As mentioned in section 4.2.2, the pH value of impregnation solution A is around 5 and does thus fall into this pH range, whereas the pH of solution B is < 1. However, the pore size distribution of the sulfide samples with their respective spent samples is comparable.

Industrial hydrotreating catalysts are prepared and delivered as oxidic precursors, which makes it necessary to understand their structure. However, true understanding of catalytic performance lies in characterizing the structure of the active sulfides and relate their structures to performance data. To understand the 3D structure of our two sulfided samples, we used PXCT measurements to reveal metal dispersion and pore structure at the micrometer scale. PXCT is a technology that provides information on electron density differences in the measured samples. By comparing volume rendering and sagittal cuts of MA(1.2)/AHM (sulfide) and MA(1.2)/MoO₃ (sulfide) (Figure 4.5), major differences can be seen; the uniform distributed electron density indicates that metals are well dispersed in MA(1.2)/MoO₃ (sulfide), while for MA(1.2)/AHM (sulfide), besides the part of the well-distributed metals, two remarkable circular areas with high electron density, likely regions of increased metal (MoS₂) concentration can also be observed. However, based on the PXCT data, it cannot be decided if metal aggregation processes cause this high electron density. To get a better understanding of that, we performed STEM/EDX, where large unsupported MoS₂ and isolated NiS_x patches were detected in MA(1.2)/AHM (sulfide) (Figure 4.8a). Hence, it is reasonable to consider that this part of metals, which according to our XPS data did not participate in the formation of Ni-Mo-S particles exist as isolated MoS₂ and NiS_x species. Likely, these species aggregate under operation conditions; similar types of larger, isolated MoS₂ and NiS_x patches are observed in MA(1.2)/AHM (spent) and MA(1.2)/MoO₃ (spent) (Figures B6 and B7). Furthermore, an obvious difference in electron density between MA(1.2)/AHM (sulfide) and MA(1.2)/MoO₃ (spent) observed in the extracted PXCT data (Figure 4.5a, b, e, f, and Figure 4.6) indicates that metal domains in MA(1.2)/AHM (sulfide) are not stable under operation conditions. To verify if this change is due to a change of metal concentration during the catalytic activity test, we determined metal concentrations in the fresh sulfided and spent samples by means of ICP measurements (Table 4.1). MA(1.2)/AHM (spent) contains 12.1 % less Mo and 9 % less Ni than MA(1.2)/AHM (sulfide), which means that this portion was washed off during the activity test. This was different for MA(1.2)/MoO₃; ICP data show similar metal contents in MA(1.2)/MoO₃ (sulfide) (10.70 wt% Mo, 2.56 wt% Ni) and MA(1.2)/MoO₃ (spent) (10.69 wt% Mo, 2.57 wt% Ni). Here PXCT and STEM/EDX results both consistently show a Ni and Mo distribution pattern in line with

the existence of NiMoS particles and confirm our interpretation of the XPS data that the metals are largely leveraged into forming active and sufficiently stable NiMoS particles. A summary of samples properties and differences are given in Scheme 4.1.

	oxidic precursor	sulfided catalyst	spent catalyst
MA(1.2)/AHM	<ul style="list-style-type: none"> • crystalline metal domains • tetrahedral Mo coordination • low reducibility • strong metal-support interactions 	<ul style="list-style-type: none"> • unsupported MoS₂ domains • isolated NiS_x species • medium concentration of NiMoS particles 	<ul style="list-style-type: none"> • alumina pore structure changed • decreased metal content
MA(1.2)/MoO₃	<ul style="list-style-type: none"> • well dispersed metals • octahedral metal coordination • high reducibility • medium metal-support interactions 	<ul style="list-style-type: none"> • consistent formation of active phase • high concentration of NiMoS particles 	<ul style="list-style-type: none"> • alumina pore structure unchanged • no metal loss

Scheme 4.1. Summary of samples properties.

4.5. Conclusions

We have investigated two HDS catalysts (MA(1.2)/AHM and MA(1.2)/MoO₃) that are *compositionally identical*, same alumina carrier, organic additive, metal and phosphorus loading, but that are prepared under different conditions, i.e., different sources of Mo and Ni were used for the impregnation solutions. While the impregnation solution of MA(1.2)/AHM was made from (NH₄)₆Mo₇O₂₄ (AHM)/Ni(NO₃)₂ as metal sources, MoO₃/NiCO₃ were used in the case of MA(1.2)/MoO₃. The structural differences between these two catalyst samples, caused by changes in preparation conditions, were studied in detail by characterizing the oxidic precursors, the sulfided and the spent state of these catalyst by means of TPR, XRD, Raman spectroscopy, PXCT, STEM and EDX. Our results indicate that the alumina pore structure is quite different between these two samples after impregnation and larger pores are formed in MA(1.2)/AHM (oxide) during preparation. Further, MA(1.2)/MoO₃ (oxide) has a higher reducibility of the metal species and a weaker metal-support interaction. After sulfidation, the metals are well dispersed on the alumina carrier surface and primarily occur as active NiMoS particles, which are stable and do not visibly change during operation. MA(1.2)/AHM (sulfide) however is very different. Only part of the metal converts into active NiMoS particles, while the remaining metal occurs as unsupported MoS₂ and isolated NiS_x clusters, which are either washed off during operation, or aggregate into larger, unsupported NiMo domains. This structural description explains the enormous activity differences between these two samples and explains why MA(1.2)/MoO₃ (sulfide) is much more active than MA(1.2)/AHM (sulfide).

Chapter 4

In this work, we revisited a problem of catalyst preparation and identified a critical performance driver that was largely overlooked in many studies, i.e., the chemicals used to design an impregnation solution. Not only could we show that impregnation solutions based on AHM – a source of molybdenum used in many studies – yield catalysts of low performance, but we were also able to explain this finding by structural properties and visualize those in the 3D space. Pushing catalyst innovation in a mature technology like hydrodesulfurization is challenging and requires in-depth understanding of catalyst activity relations across different length scales of catalyst structure.

4.6. References

- [1] C. Song, An overview of new approaches to deep desulfurization for ultra-clean gasoline, diesel fuel and jet fuel. *Catal. Today*, 2003, 86 (1-4), 211-263.
- [2] H. Topsøe, B.S. Clausen, R. Candia, C. Wivel, S. Mørup, In situ Mössbauer emission spectroscopy studies of unsupported and supported sulfided Co-Mo hydrodesulfurization catalysts: Evidence for and nature of a Co-Mo-S phase, *J. Catal.*, 68 (1981) 433-452.
- [3] H. Topsøe, B.S. Clausen, F.E. Massoth, Hydrotreating catalysis, in: *Catalysis*, Springer, 1996, pp. 1-269.
- [4] S. Bag, A.F. Gaudette, M.E. Bussell, M.G. Kanatzidis, Spongy chalcogels of non-platinum metals act as effective hydrodesulfurization catalysts, *Nat. Chem.*, 1 (2009) 217-224.
- [5] F.A. Braggio, M. Dorneles de Mello, B.C. Magalhães, J.L. Zotin, M.A.P. Silva, Effects of citric acid addition method on the activity of NiMo/ γ -Al₂O₃ catalysts in simultaneous hydrodesulfurization and hydrodenitrogenation reactions, *Energy & Fuels*, 33 (2019) 1450-1457.
- [6] M.A. Lélías, P.J. Kooyman, L. Mariey, L. Oliviero, A. Travert, J. van Gestel, J.A.R. van Veen, F. Maugé, Effect of NTA addition on the structure and activity of the active phase of cobalt-molybdenum sulfide hydrotreating catalysts, *J. Catal.*, 267 (2009) 14-23.
- [7] A. Griboval, P. Blanchard, E. Payen, M. Fournier, J.L. Dubois, Alumina supported HDS catalysts prepared by impregnation with new heteropolycompounds. Comparison with catalysts prepared by conventional Co-Mo-P coimpregnation, *Catal. Today*, 45 (1998) 277-283.
- [8] L. van Haandel, G. Bremmer, E.J.M. Hensen, Th. Weber, The effect of organic additives and phosphoric acid on sulfidation and activity of (Co)Mo/Al₂O₃ hydrodesulfurization catalysts, *J. Catal.*, 351 (2017) 95-106.
- [9] J. Escobar, M.C. Barrera, J.A. de Los Reyes, J.A. Toledo, V. Santes, J.A. Colín, Effect of chelating ligands on Ni-Mo impregnation over wide-pore ZrO₂-TiO₂, *J. Mol. Catal. A*, 287 (2008) 33-40.
- [10] L. Peña, D. Valencia, T. Klimova, CoMo/SBA-15 catalysts prepared with EDTA and citric acid and their performance in hydrodesulfurization of dibenzothiophene, *Appl. Catal. B: Environ.*, 147 (2014) 879-887.
- [11] S. Badoga, K.C. Mouli, K.K. Soni, A. Dalai, J. Adjaye, Beneficial influence of EDTA on the structure and catalytic properties of sulfided NiMo/SBA-15 catalysts for hydrotreating of light gas oil, *Appl. Catal. B: Environ.*, 125 (2012) 67-84.
- [12] D. Nicosia, R. Prins, The effect of phosphate and glycol on the sulfidation mechanism of CoMo/Al₂O₃ hydrotreating catalysts: an in situ QEXAFS study, *J. Catal.*, 231 (2005) 259-268.
- [13] T. Kubota, N. Rinaldi, K. Okumura, T. Honma, S. Hirayama, Y. Okamoto, In situ XAFS study of the sulfidation of Co-Mo/B₂O₃/Al₂O₃ hydrodesulfurization catalysts prepared by using citric acid as a chelating agent, *Appl. Catal. A: Gen.*, 373 (2010) 214-221.

NiMo/Al₂O₃ Hydrotreating Catalysts - Aspects of 3D Structure, Synthesis and Activity

- [14] H. Wu, A. Duan, Z. Zhao, D. Qi, J. Li, B. Liu, G. Jiang, J. Liu, Y. Wei, X. Zhang, Preparation of NiMo/KIT-6 hydrodesulfurization catalysts with tunable sulfidation and dispersion degrees of active phase by addition of citric acid as chelating agent, *Fuel*, 130 (2014) 203-210.
- [15] F.A. Braggio, M.D. Mello, B.C. Magalhães, J.L. Zotin, M.A. Silva, Effect of pH on activity of NiMo/Al₂O₃ catalysts prepared with citric acid in simultaneous hydrodesulfurization and hydrodenitrogenation reactions, *Catal. Lett.*, 147 (2017) 1104-1113.
- [16] M.L. Ramos, M.M. Caldeira, V.M.S. Gil, NMR spectroscopy study of the complexation of D-gluconic acid with tungsten (VI) and molybdenum (VI), *Carbohydr. Res.*, 304 (1997) 97-109.
- [17] Y. Zhang, W. Han, X. Long, H. Nie, Redispersion effects of citric acid on CoMo/ γ -Al₂O₃ hydrodesulfurization catalysts, *Catal. Commun.*, 82 (2016) 20-23.
- [18] R. Cattaneo, F. Rota, R. Prins, An XAFS study of the different influence of chelating ligands on the HDN and HDS of γ -Al₂O₃-supported NiMo catalysts, *J. Catal.*, 199 (2001) 318-327.
- [19] T. Shimizu, K. Hiroshima, T. Honma, T. Mochizuki, M. Yamada, Highly active hydrotreatment catalysts prepared with chelating agents, *Catal. Today*, 45 (1998) 271-276.
- [20] L. Coulier, V.H.J. de Beer, J.A.R. van Veen, J.W. Niemantsverdriet, On the formation of cobalt-molybdenum sulfides in silica-supported hydrotreating model catalysts, *Top. Catal.*, 13 (2000) 99-108.
- [21] L. Medici, R. Prins, The influence of chelating ligands on the sulfidation of Ni and Mo in NiMo/SiO₂ hydrotreating catalysts. *J. Catal.*, 196, 163 (1), 38-49.
- [22] T.K.T. Ninh, L. Massin, D. Laurenti, M. Vrinat, A new approach in the evaluation of the support effect for NiMo hydrodesulfurization catalysts, *Appl. Catal. A: Gen.*, 407 (2011) 29-39.
- [23] T. Yamamoto, T. Kubota, Y. Okamoto, Effect of phosphorus addition on the active sites of a Co-Mo/Al₂O₃ catalyst for the hydrodesulfurization of thiophene, *Appl. Catal. A: Gen.*, 328 (2007) 219-225.
- [24] M. Villarroel, P. Baeza, F. Gracia, N. Escalona, P. Avila, F.J. Gil-Llambias, Phosphorus effect on Co//Mo and Ni//Mo synergism in hydrodesulphurization catalysts, *Appl. Catal. A: Gen.*, 364 (2009) 75-79.
- [25] M. Sun, D. Nicosia, R. Prins, The effects of fluorine, phosphate and chelating agents on hydrotreating catalysts and catalysis, *Catal. Today*, 86 (2003) 173-189.
- [26] D. Ferdous, A.K. Dalai, J. Adjaye, A series of NiMo/Al₂O₃ catalysts containing boron and phosphorus: Part I. Synthesis and characterization, *Appl. Catal. A: Gen.*, 260 (2004) 137-151.
- [27] P. Atanasova, T. Tabakova, C. Vladov, T. Halachev, A.L. Agudo, Effect of phosphorus concentration and method of preparation on the structure of the oxide form of phosphorus-nickel-tungsten/alumina hydrotreating catalysts, *Appl. Catal. A: Gen.*, 161 (1997) 105-119.
- [28] M.L.H. Green, An introduction to the chemistry of molybdenum, *Studies in Inorganic Chemistry*, 19 (1994) 94-94.
- [29] A.F. Wells, *Structural inorganic chemistry*, Oxford university press, 2012.
- [30] Y.V. Vatutina, O.V. Klimov, E.A. Stolyarova, K.A. Nadeina, I.G. Danilova, Y.A. Chesalov, E.Y. Gerasimov, I.P. Prosvirin, A.S. Noskov, Influence of the phosphorus addition ways on properties of CoMo-catalysts of hydrotreating, *Catal.Today*, 329 (2019) 13-23.
- [31] L. Medici, R. Prins, Structure of oxidic NiMo/SiO₂ hydrotreating catalyst precursors, *J. Catal.*, 163 (1996) 28-37.
- [32] Y. Gao, W. Han, X. Long, H. Nie, D. Li, Preparation of hydrodesulfurization catalysts using MoS₃ nanoparticles as a precursor, *Appl. Catal. B: Environ.*, 224 (2018) 330-340.
- [33] L. Lizama, T. Klimova, Highly active deep HDS catalysts prepared using Mo and W heteropolyacids supported on SBA-15, *Appl. Catal. B: Environ.*, 82 (2008) 139-150.

Chapter 4

- [34] A. Alsalmeh, N. Alzaqri, A. Alsaleh, M.R.H. Siddiqui, A. Alotaibi, E.F. Kozhevnikova, I.V. Kozhevnikov, Efficient Ni–Mo hydrodesulfurization catalyst prepared through Keggin polyoxometalate, *Appl. Catal. B: Environ.*, 182 (2016) 102-108.
- [35] S. Damyanova, A.A. Spojakina, D.M. Shopov, Study of low-percentage alumina-supported nickel-molybdenum catalysts by ESR spectroscopy and magnetic measurements, *Appl. Catal.*, 48 (1989) 177-186.
- [36] G. Plazenet, E. Payen, J. Lynch, Cobalt–molybdenum interaction in oxidic precursors of zeolite-supported HDS catalysts, *Phys. Chem. Chem. Phys.*, 4 (2002) 3924-3929.
- [37] T. Shido, R. Prins, Why EXAFS underestimated the size of small supported MoS₂ particles, *J. Phys. Chem. B*, 102 (1998) 8426-8435.
- [38] R. Cattaneo, Th. Weber, T. Shido, R. Prins, A quick EXAFS study of the sulfidation of NiMo/SiO₂ hydrotreating catalysts prepared with chelating ligands, *J. Catal.*, 191 (2000) 225-236.
- [39] R. Radhakrishnan, S.T. Oyama, Y. Ohminami, K. Asakura, Structure of MnO_x/Al₂O₃ Catalyst: A Study Using EXAFS, In Situ Laser Raman Spectroscopy and ab Initio Calculations, *J. Phys. Chem. B*, 105 (2001) 9067-9070.
- [40] C.F. Weise, H. Falsig, P.G. Moses, S. Helveg, M. Brorson, L.P. Hansen, Single-atom Pt promotion of industrial Co-Mo-S catalysts for ultra-deep hydrodesulfurization, *J. Catal.*, 403 (2021) 74-86.
- [41] J.V. Lauritsen, S. Helveg, E. Lægsgaard, I. Stensgaard, B.S. Clausen, H. Topsøe, F. Besenbacher, Atomic-scale structure of Co–Mo–S nanoclusters in hydrotreating catalysts, *J. Catal.*, 197 (2001) 1-5.
- [42] H. Schweiger, P. Raybaud, G. Kresse, H. Toulhoat, Shape and edge sites modifications of MoS₂ catalytic nanoparticles induced by working conditions: a theoretical study, *J. Catal.*, 207 (2002) 76-87.
- [43] H. Schweiger, P. Raybaud, H. Toulhoat, Promoter sensitive shapes of Co(Ni)MoS nanocatalysts in sulfo-reductive conditions, *J. Catal.*, 212 (2002) 33-38.
- [44] P. Raybaud, J. Hafner, G. Kresse, S. Kasztelan, H. Toulhoat, Structure, energetics, and electronic properties of the surface of a promoted MoS₂ catalyst: an ab initio local density functional study, *J. Catal.*, 190 (2000) 128-143.
- [45] Th. Weber, J.A.R. van Veen, A density functional theory study of the hydrodesulfurization reaction of dibenzothiophene to biphenyl on a single-layer NiMoS cluster, *Catal. Today*, 130 (2008) 170-177.
- [46] L. van Haandel, A. Longo, W. Bras, E.J.M. Hensen, Th. Weber, Activation of Co-Mo-S hydrodesulfurization catalysts under refinery conditions – A combined SAXS/XAS study, *ChemCatChem*, 11 (2019) 5013-5017.
- [47] V. Sundaramurthy, A.K. Dalai, J. Adjaye, Effect of phosphorus addition on the hydrotreating activity of NiMo/Al₂O₃ carbide catalyst, *Catal. Today*, 125 (2007) 239-247.
- [48] O.U. Valdés-Martínez, C.E. Santolalla-Vargas, V. Santes, J.A. de los Reyes, B. Pawelec, J.L.G. Fierro, Influence of calcination on metallic dispersion and support interactions for NiRu/TiO₂ catalyst in the hydrodeoxygenation of phenol, *Catal. Today*, 329 (2019) 149-155.
- [49] M. Dierolf, A. Menzel, P. Thibault, P. Schneider, C.M. Kewish, R. Wepf, O. Bunk, F. Pfeiffer, Ptychographic X-ray computed tomography at the nanoscale, *Nature*, 467 (2010) 436-439.
- [50] J. Ihli, L. Bloch, F. Krumeich, K. Wakonig, M. Holler, M. Guizar-Sicairos, Th. Weber, J.C. da Silva, J.A. van Bokhoven, Hierarchical structure of NiMo hydrodesulfurization catalysts determined by ptychographic X-Ray computed tomography, *Angew. Chem. Int. Ed.*, 59 (2020) 17266-17271.
- [51] F. Pfeiffer, X-ray ptychography, *Nat. Photonics.*, 12 (2018) 9-17.
- [52] K. Wakonig, H.-C. Stadler, M. Odstrčil, E.H.R. Tsai, A. Diaz, M. Holler, I. Usov, J. Raabe, A. Menzel, M. Guizar-Sicairos, PtychoShelves, a versatile high-level framework for high-performance analysis of ptychographic data, *J. Appl. Crystallogr.*, 53 (2020) 574-586.

NiMo/Al₂O₃ Hydrotreating Catalysts - Aspects of 3D Structure, Synthesis and Activity

- [53] P. Thibault, M. Dierolf, A. Menzel, O. Bunk, C. David, F. Pfeiffer, High-resolution scanning x-ray diffraction microscopy, *Science*, 321 (2008) 379-382.
- [54] A. Diaz, P. Trtik, M. Guizar-Sicairos, A. Menzel, P. Thibault, O. Bunk, Quantitative x-ray phase nanotomography, *Phys. Rev. B*, 85 (2012) 020104.
- [55] M. Holler, J. Ihli, E.H.R.Tsai, F. Nudelmann, M. Verezhak, W.D.J. van de Berg, S.H. Shahmoradian, A lathe system for micrometer-sized cylindrical sample preparation at room and cryogenic temperatures. *J. Synchrotron Radiat.*, 2020, 27 (2), 472-476.
- [56] M. van Heel, M. Schatz, Fourier shell correlation threshold criteria, *J. Struct. Biol.*, 151 (2005) 250-262.
- [57] C.E. Scott, M.J. Perez-Zurita, L.A. Carbognani, H. Molero, G. Vitale, H.J. Guzmán, P. Pereira-Almao, Preparation of NiMoS nanoparticles for hydrotreating, *Catal. Today*, 250 (2015) 21-27.
- [58] V. Zuzaniuk, R. Prins, Synthesis and characterization of silica-supported transition-metal phosphides as HDN catalysts, *J. Catal.*, 219 (2003) 85-96.
- [59] R. Thomas, E.M. van Oers, V.H.J. de Beer, J. Medema, J.A. Moulijn, Characterization of γ -alumina-supported Molybdenum oxide and tungsten oxide; reducibility of the oxidic state versus hydrodesulfurization activity of the sulfided state, *J. Catal.*, 76 (1982) 241-253.
- [60] K.A. Nadeina, M.O. Kazakov, I.G. Danilova, A.A. Kovalskaya, E.A. Stolyarova, P.P. Dik, E.Y. Gerasimov, I.P. Prosvirin, Y.A. Chesalov, O.V. Klimov, A.S. Noskov, The influence of B and P in the impregnating solution on the properties of NiMo/ γ - δ -Al₂O₃ catalysts for VGO hydrotreating, *Catal. Today*, 329 (2019) 2-12.
- [61] J.A.R. van Veen, H.A. Colijn, P.A.J.M. Hendriks, A.J. van Welsenens, On the formation of type I and type II NiMoS phases in NiMo/Al₂O₃ hydrotreating catalysts and its catalytic implications, *Fuel Process. Technol.*, 35 (1993) 137-157.
- [62] D.S. Zingg, L.E. Makovsky, R.E. Tischer, F.R. Brown, D.M. Hercules, A surface spectroscopic study of molybdenum-alumina catalysts using x-ray photoelectron, ion-scattering, and Raman spectroscopies, *J. Phys. Chem.*, 84 (1980) 2898-2906.
- [63] P. Dufresne, E. Payen, J. Grimblot, J.P. Bonnelle, Study of Ni-Mo- γ -catalysts catalysts by X-ray photoelectron and Raman spectroscopy. Comparison with Co-Mo- γ -catalysts, *J. Phys. Chem.*, 85 (1981) 2344-2351.
- [64] C.C. Williams, J.G. Ekerdt, J.M. Jehng, F.D. Hardcastle, I.E. Wachs, A Raman and ultraviolet diffuse reflectance spectroscopic investigation of alumina-supported molybdenum oxide, *J. Phys. Chem.*, 95 (1991) 8791-8797.
- [65] J.M. Alia, Raman spectroscopic studies of ion-ion interactions in aqueous and nonaqueous electrolyte solutions, *Practical Spectroscopy series*, 28 (2001) 617-682.
- [66] J. Jiang, I. May, M.J. Sarsfield, M. Ogden, D.O. Fox, C.J. Jones, P. Mayhew, A spectroscopic study of the dissolution of cesium phosphomolybdate and zirconium molybdate by ammonium carbamate, *J. Solution Chem.*, 34 (2005) 443-468.
- [67] A.K. Cuentas-Gallegos, C. Frausto, L.A. Ortiz-Frade, G. Orozco, Raman spectra of hybrid materials based on carbon nanotubes and Cs₃PMo₁₂O₄₀, *Vib. Spectrosc.*, 57 (2011) 49-54.
- [68] B. Guichard, M. Roy-Auberger, E. Devers, C. Legens, P. Raybaud, Aging of Co (Ni) MoP/Al₂O₃ catalysts in working state, *Catal. Today*, 130 (2008) 97-108.
- [69] B.W. Hoffer, A.D. van Langeveld, J.-P. Janssens, R.L.C. Bonn , C.M. Lok, J.A. Moulijn, Stability of highly dispersed Ni/Al₂O₃ catalysts: effects of pretreatment, *J. Catal.*, 192 (2000) 432-440.
- [70] J. Escobar, M.C. Barrera, J.A. Toledo, M.A. Cort s-J come, C. Angeles-Ch vez, S. N n ez, V. Santes, E. G mez, L. D az, E. Romero, J.G. Pacheco Effect of ethyleneglycol addition on the properties of P-doped NiMo/Al₂O₃ HDS catalysts: Part I. Materials preparation and characterization, *Appl. Catal. B: Environ.*, 88 (2009) 564-575.

Chapter 4

[71] L. van Haandel, G.M. Bremmer, E.J.M. Hensen, Th. Weber, Influence of sulfiding agent and pressure on structure and performance of CoMo/Al₂O₃ hydrodesulfurization catalysts, *J. Catal.*, 342 (2016) 27-39.

[72] R. Cattaneo, T. Shido, R. Prins, The relationship between the structure of NiMo/SiO₂ catalyst precursors prepared in the presence of chelating ligands and the hydrodesulfurization activity of the final sulfided catalysts, *J. Catal.*, 185 (1999) 199-212.

[73] L. van Haandel, G. Smolentsev, J.A. van Bokhoven, E.J.M. Hensen, Th. Weber, Evidence of Octahedral Co–Mo–S Sites in Hydrodesulfurization Catalysts as Determined by Resonant Inelastic X-ray Scattering and X-ray Absorption Spectroscopy, *ACS Catal.*, 10 (2020) 10978-10988.

[74] M.P. De la Rosa, S. Texier, G. Berhault, A. Camacho, M.J. Yácaman, A. Mehta, S. Fuentes, J.A. Montoya, F. Murrieta, R.R. Chianelli, Structural studies of catalytically stabilized model and industrial-supported hydrodesulfurization catalysts, *J. Catal.*, 225 (2004) 288-299.

[75] S. Eijssbouts, L.C.A. van den Oetelaar, J.N. Louwen, R.R. van Puijenbroek, G.C. van Leerdam, Changes of MoS₂ morphology and the degree of Co segregation during the sulfidation and deactivation of commercial Co–Mo/Al₂O₃ hydroprocessing catalysts, *Ind. Eng. Chem. Res.*, 46 (2007) 3945-3954.

[76] X. Carrier, J.F. Lambert, M. Che, Ligand-promoted alumina dissolution in the preparation of MoO_x/γ-Al₂O₃ catalysts: evidence for the formation and deposition of an Anderson-type alumino heteropolymolybdate, *J. Am. Chem. Soc.*, 119 (1997) 10137-10146.

4.7. Appendix B

4.7.1. Method

Detailed methods and parameters used for PXCT data preparation and mounting, data acquisition and reconstruction, resolution evaluation and dose evaluation are described in Section 2.2.8, Chapter 2.

Tomogram analysis. Analysis, segmentation, and 3D rendering was carried out using Avizo and Fiji [1]. Due to the good spatial-resolution and signal-to-noise ratio, the analysis was limited to the phase or the electron density tomograms [2]. The real part of the scattering factor associated with the retrieved phase of Al₂O₃, i.e., the main sample component, is ~50x larger compared to the imaginary part of the scattering factor associated with the absorption. Further, to exclude any potential sample preparation artefacts near the edges we virtually extracted, roughly equal sized, sub-volumes from the centre of each of the imaged sample volumes.

Component identification and subsequent segmentation was achieved by comparing calculated electron densities of known catalyst components, e.g., air, Al₂O₃, MoS₂, with measured electron densities. Provided in Table B1 are electron densities of known catalysts and reference compounds. Tomograms were component segmented by interactive thresholding and followed by morphological operations to refine the segmentation further. To isolate the present macropores we selected an electron density threshold of 0.156 n_e Å⁻³. Assuming a binary composition of air and amorphous Al₂O₃ the selected cut-off value considers voxels with a composition of > 80 % pores and < 20 % Al₂O₃ to be pores. To isolate the two Al₂O₃ phases (high and low micro- and meso-porosity) we applied a threshold of 0.32 n_e Å⁻³. The contribution of monolayer MoS₂ per voxel to electron density was also considered, it shows that the electron density will increase by 3 % with the addition of one monolayer MoS₂, which is negligible compared to the contribution of Al₂O₃ domain, given over 90 % electron density was contributed by matrix. Hence, with the overall consideration and to simplify the segmentation process for isolating two Al₂O₃ phases, the component of MoS₂ was not included. Lastly, to visualize cluster of MoS₂, we applied an electron density threshold of 0.96 n_e Å⁻³. Assuming a binary composition of amorphous Al₂O₃ the selected cut-off value highlights cluster that are at minimum composed to 30 vol% MoS₂. The isolated pore-networks were further subjected to 3D thickness map calculations to extract pore size distributions (PSD), see Figure B5. Pores with a diameter smaller than 60 nm were excluded from the shown size distributions, in view of resolution limits. Although the spatial resolution of the tomograms is insufficient to resolve individual MoS₂ monolayers, using the known densities of both MoS₂ and Al₂O₃, we can convert voxel-level electron density values to an

Chapter 4

approximate volumetric or mass fraction MoS₂ cluster concentration [3]. To note, we neglect the added Ni in this approximation, in view of the minor presence in the catalyst, and the possible contribution of pores in this partial volume-based analysis. As such the reported MoS₂ cluster concentrations are representative of their maximum concentration.

Energy dispersive X-ray (EDX) image analysis. Around 5 EDX images were used for image analysis for each catalyst. In order to use numerical values to express the correlation between Mo and Ni more directly, instead of just using the visual impressions, a programmed algorithm was coded in MATLAB. The number of pixels in all images is 218 × 226. For the calculation, an area of interest is chosen showing the catalyst. Then the numerical value for two elements on each pixel are compared to each other and a statistical correlation between the values of two elements for the entire image is calculated. This correlation ranges from -1 to 1, meaning totally uncorrelated to fully correlated respectively. This calculation is carried out for each element combination, including the correlation between Mo and Ni (Figure B3).

Table B1. Electron density of the selected reference compounds.

Compound	Formula	ED $n_e/\text{\AA}^3$
Air		0.000
water	H ₂ O	0.334
Phosphoric acid	H ₃ PO ₄	0.578
Amorphous Alumina	Al ₂ O ₃	0.785
Metallic Molybdenum	Mo	2.689
Metallic Nickel	Ni	2.561
Molybdenum sulfide	MoS ₂	1.409
Molybdenum trioxide	MoO ₃	1.295
Nickel Oxide	NiO	1.936
Nickel Sulfide	NiS	1.795
NiMO ₂	15 wt%Mo, 3.67 wt%Ni	1.168

The electron densities of considered reference compounds were calculated using tabulated molecular weight and mass density values[4].

Table B2. Binding energy and atomic percentage of MA(1.2)/AHM (sulfide) and MA(1.2)/MoO₃ (sulfide) sulfided under 1 bar H₂S/H₂ at various temperatures and their respective oxide precursors (oxide).

Sample	Temperature (°C)	Binding energy (eV)												Fractions (%)					
		Mo 3d5/2						Ni 2p3/2						Mo 3d			Ni 2p		
		Mo ⁴⁺	Mo ⁵⁺	Mo ⁶⁺	NiS _x	NiMoS	NiO _x	Mo ⁴⁺	Mo ⁵⁺	Mo ⁶⁺	NiS _x	NiMoS	NiO _x	Mo ⁴⁺	Mo ⁵⁺	Mo ⁶⁺	NiS _x	NiMoS	NiO _x
MA(1.2)/AHM	350	229.0	230.9	233.0	853.4	855.0	856.8	85.1	10.7	4.2	70.8	21.2	8.1						
	250	229.0	230.8	233.0	853.4	854.9	856.8	73.5	16.6	9.9	68.3	19.7	12.0						
	150	229.0	230.9	232.8	853.3	855.0	856.8	48.3	23.1	28.6	68.0	17.2	14.8						
	50	229.0	230.9	232.3	853.3	855.0	856.7	16.7	20.6	62.7	47.9	15.8	36.3						
	oxide	--	--	232.7	--	--	856.8	0	0	100	0	--	--	100					
MA(1.2)/MoO ₃	350	229.0	230.7	233.0	853.4	854.9	856.8	87.7	9.3	3.0	68.0	24.7	7.3						
	250	229.0	230.9	233.0	853.4	854.9	856.8	73.8	16.2	10.0	65.8	24.2	10.0						
	150	229.0	230.9	233.1	853.3	854.9	856.8	69.4	19.1	11.5	65.6	24.1	10.3						
	50	229.0	231.0	232.7	853.3	855.0	856.8	45.4	29.9	24.7	45.9	23.4	30.7						
	oxide	--	--	232.7	--	--	856.8	0	0	100	0	--	--	100					

Chapter 4

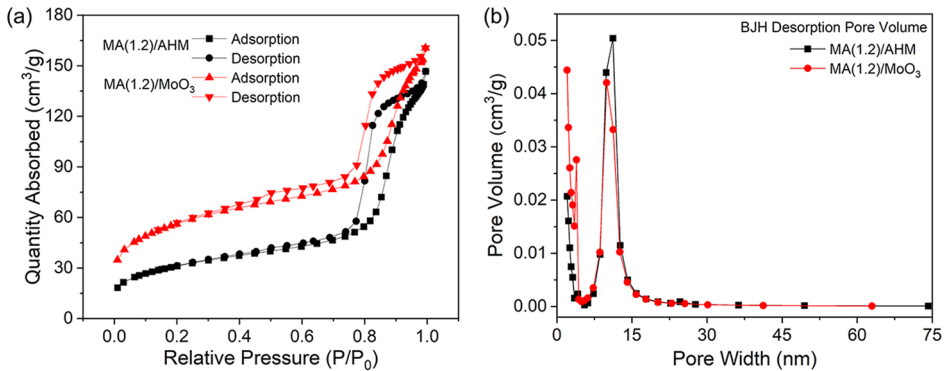


Figure B1. (a) N_2 adsorption-desorption isotherm of MA(1.2)/AHM (oxide) and MA(1.2)/ MoO_3 (oxide); (b) Pore size analysis results from isotherms shown in (a).

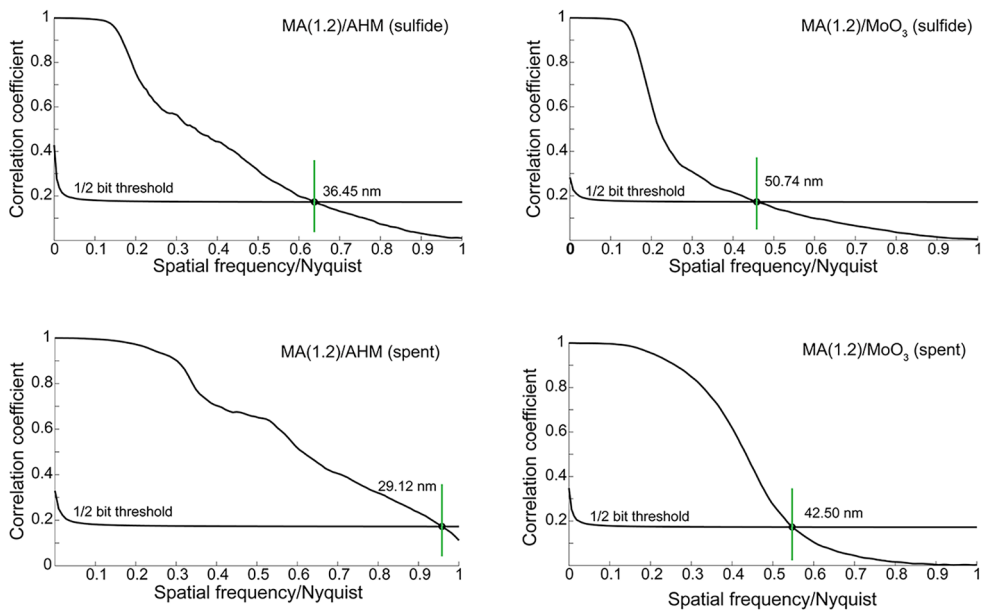


Figure B2. Fourier shell correlation (FSC) line plots of the electron density tomograms of examined catalyst pillars acquired at 6.2 keV. The selected threshold for determining the half-period spatial resolution was the $\frac{1}{2}$ bit criterion. The Voxel size for all tomograms is $(23.26 \text{ nm})^3$. The intersection of correlation profile and the selected threshold (green line) provides an estimate of the achieved spatial resolution. The full-period resolution is twice the half-period resolution estimates.

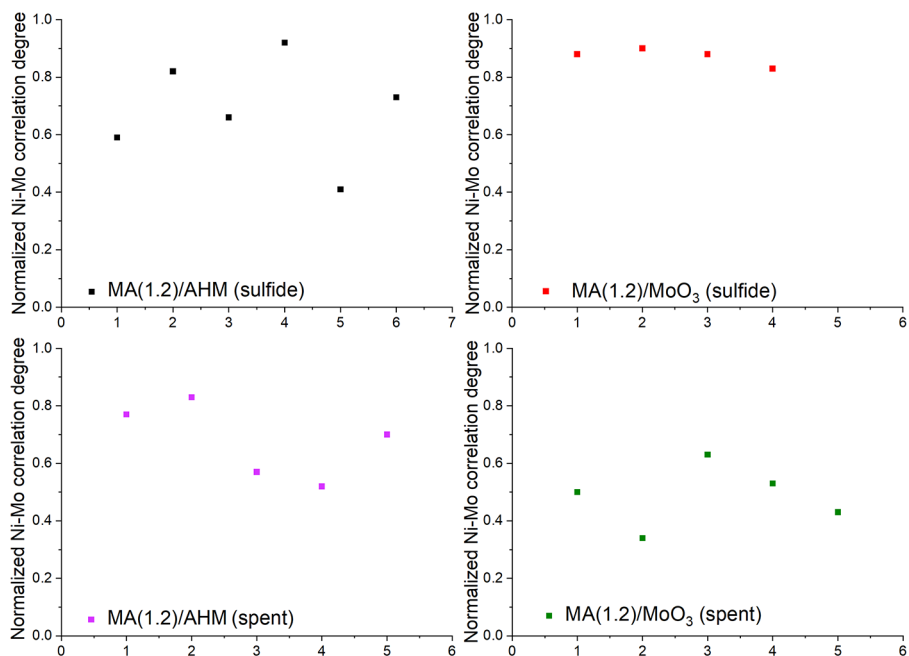


Figure B3. Normalized Ni-Mo correlation degree of samples MA(1.2)/AHM (sulfide), MA(1.2)/MoO₃ (sulfide), MA(1.2)/AHM (spent) and MA(1.2)/MoO₃ (spent) extracted from EDX mapping data. X-axis is just number of labels for each data point, representing the selected area used for calculation.

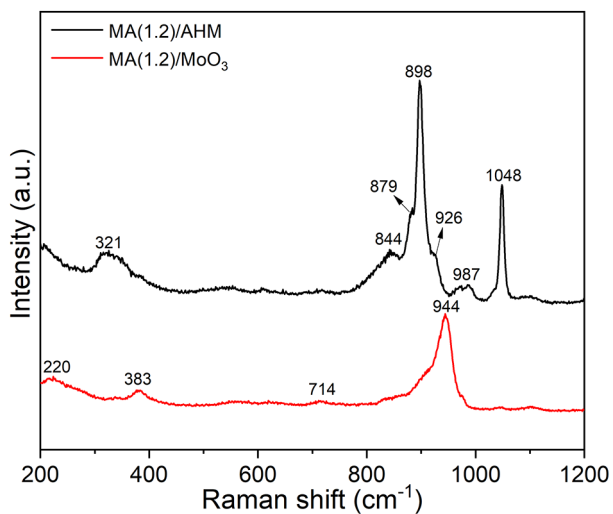


Figure B4. Raman spectra of two respective impregnation solutions.

Chapter 4

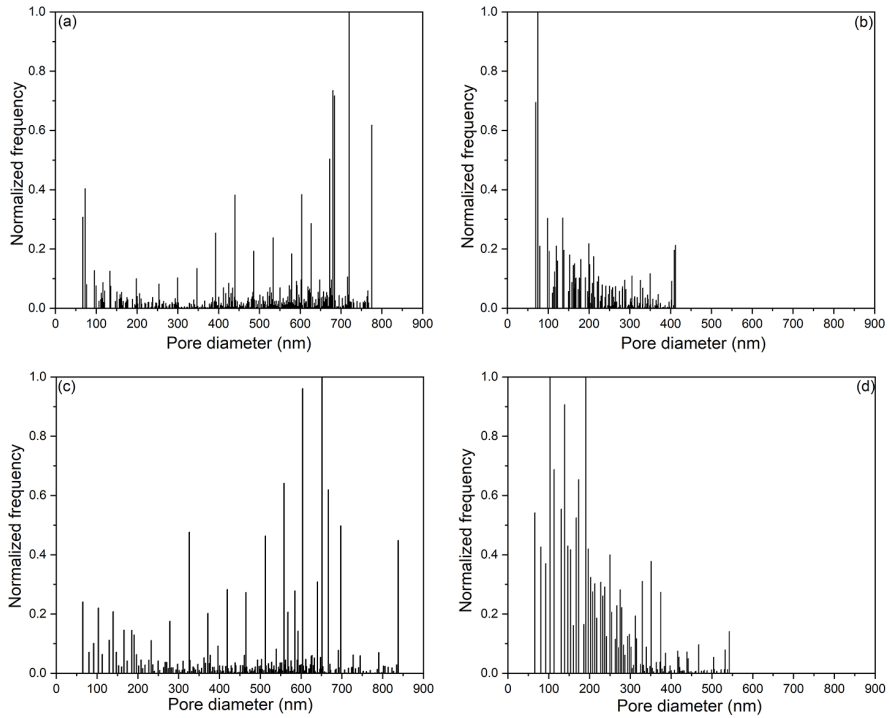


Figure B5. Pore size distribution of PXCT extracted, spatially resolved, pores. Shown are normalized frequency pore size distributions for samples (a) MA(1.2)/AHM (sulfide), (b) MA(1.2)/MoO₃ (sulfide), (c) MA(1.2)/AHM (spent), and (d) MA(1.2)/MoO₃ (spent). Only pores with a diameter greater 60 nm were considered for analysis. The respective relative volume of spatially resolved pores in these four samples is 1.44 %, 2.3 %, 0.63 %, and 0.14 %.

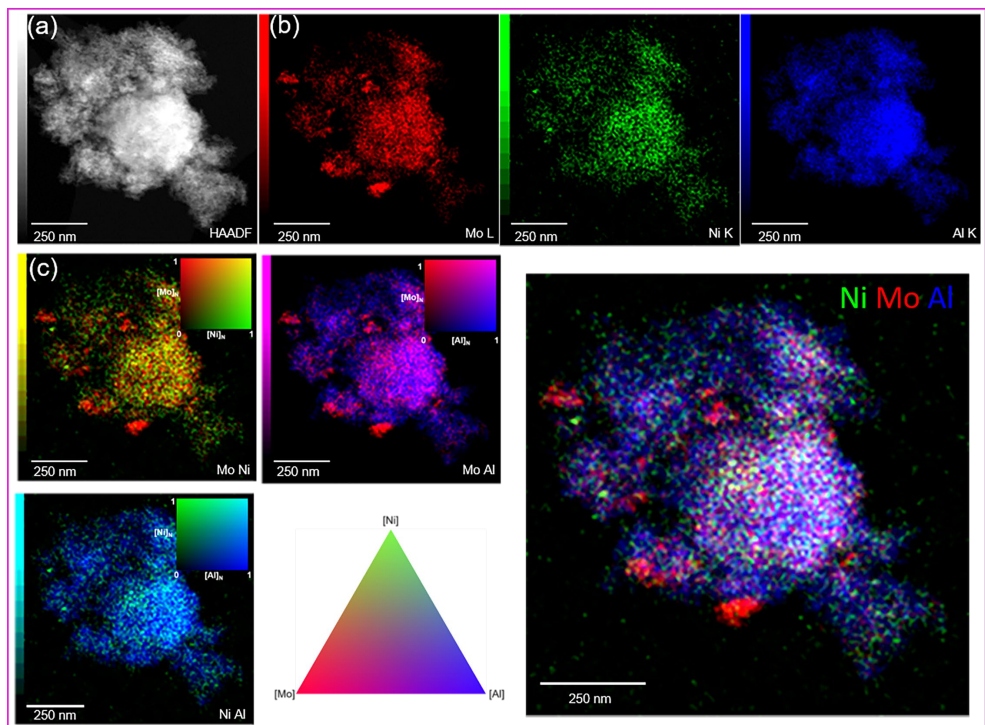


Figure B6. Electron microscopy of MA(1.2)/AHM (spent). a) HAADF STEM image. b) EDX maps of Mo, Ni and Al corresponding to the STEM image of (a). c) Normalized (N) and merged EDX maps of Mo, Ni and Al.

Chapter 4

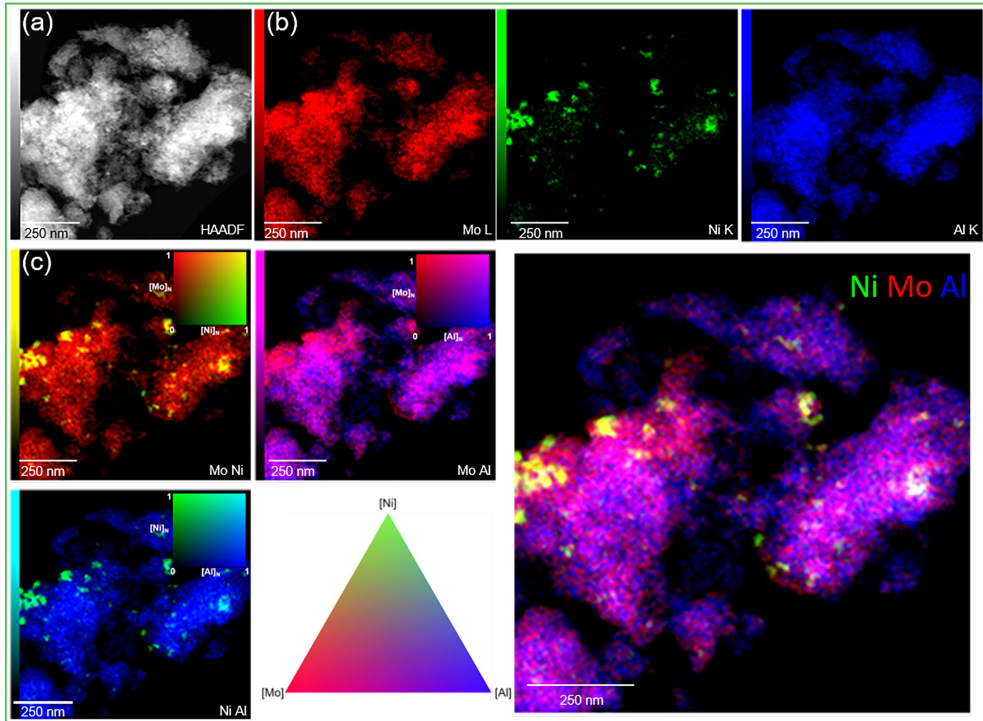


Figure B7. Electron microscopy of MA(1.2)/MoO₃ (spent). a) HAADF STEM image. b) EDX maps of Mo, Ni and Al corresponding to the STEM image of (a). c) Normalized (N) and merged EDX maps of Mo, Ni and Al.

4.7.2. References

- [1] J. Schindelin, I. Arganda-Carreras, E. Frise, V. Kaynig, M. Longair, T. Pietzsch, S. Preibisch, C. Rueden, S. Saalfeld, B. Schmid, J.-Y. Tinevez, D.J. White, V. Hartenstein, K. Eliceiri, P. Tomancak, A. Cardona, Fiji: an open-source platform for biological-image analysis, *Nat. Methods*, 9 (2012) 676-682.
- [2] A. Groso, R. Abela, M. Stampanoni, Implementation of a fast method for high resolution phase contrast tomography, *Opt. Express*, 14 (2006) 8103-8110.
- [3] J. Ihli, M.A. Levenstein, Y.-Y. Kim, K. Wakonig, Y. Ning, A. Tatani, A.N. Kulak, D.C. Green, M. Holler, S.P. Armes, F.C. Meldrum, Ptychographic X-ray tomography reveals additive zoning in nanocomposite single crystals, *Chem. Sci.*, 11 (2020) 355-363.
- [4] A. Diaz, P. Trtik, M. Guizar-Sicairos, A. Menzel, P. Thibault, O. Bunk, Quantitative x-ray phase nanotomography, *Phy. Rev. B*, 85 (2012) 020104.

Chapter 5

Predicting Catalytic Activity from Oxidic Precursor Properties

ABSTRACT

The surface structure of alumina-supported NiMo hydrodesulfurization (HDS) catalysts was characterized by means of temperature-programmed reduction (TPR), X-ray photoelectron spectroscopy (XPS), Raman, X-ray diffraction (XRD) and UV-visible diffuse reflectance spectroscopy (UV-vis DRS). By plotting the absorption edge energy (E_g) extracted from UV-vis DRS and dibenzothiophene (DBT) HDS activity, an empirical linear relationship was found, indicating the DBT HDS activity of measured catalyst increases with decreasing E_g value. An analogous linear relation between the reducibility of oxidic precursors of NiMo/Al₂O₃ catalysts and their DBT conversion was also observed; the result indicates that the catalyst with higher reducibility shows higher tendency to form active NiMoS particles, and such structure consequently leads to high DBT HDS activity.

Chapter 5

5.1. Introduction

Hydrodesulfurization (HDS) catalysts play an essential role in the HDS process; they are used to remove sulfur atoms from crude oil to produce ultra-low sulfur oil to meet environmental regulations [1, 2]. Typical HDS catalysts consist of MoS₂ clusters promoted by Ni and supported on γ -Al₂O₃ [3]. These catalysts are usually prepared as oxidic precursors by impregnating γ -Al₂O₃ with solutions containing metal sources, followed by drying and calcination. Catalyst activation is done by sulfidation of the oxidic precursors in an H₂S/H₂ gas flow at an elevated temperature (around 400 °C), yielding NiMo sulfide phases.

For decades, studies have been conducted to characterize the structure of the sulfided active phase in HDS catalysts theoretically and experimentally to explore the structure-performance relationship [4-8]. However, due to the air sensitivity of the sulfided catalyst, structure characterization is always challenging. Compared to the sulfided active phase, the corresponding oxidic precursor is much easier to assess and characterize, which is why industrial hydrotreating catalysts are always prepared and stored in the form of oxide phases. Besides, the metal-support interactions on the oxidic precursor strongly influence the metal dispersion on the alumina carrier, the formation of active NiMoS species during the sulfidation and catalyst HDS activity [9]. This makes the insight into the structure of oxide precursors an essential part of catalyst development [10]. Therefore, it would be a significant advantage if correlations between the structure of oxidic precursors and the performance of sulfided catalysts could be linked. It would provide us a chance to gain a deep understanding of the catalytic performance on a structural basis. As mentioned above, the active phases of HDS catalysts are generated by means of sulfidation, a reductive treatment, which makes the reduction characteristics of the oxidic catalysts essential. Temperature-programmed reduction (TPR) [11] is a reasonable technique used to study the reduction properties of oxide catalysts. By conducting TPR measurement, Rajagopal et al. [12] noticed that the reducibility of Mo increases with increasing Mo loading. Using TPR, Thomas et al. [13] found a correlation between reducibility and activity in several MoO₃/ γ -Al₂O₃ catalysts.

UV-visible diffuse reflectance spectroscopy (UV-vis DRS) is a technique used to explore the local structure of the supported oxide catalysts. The structure of supported W [14, 15], Mo [16, 17], and supported V catalysts [18] has been studied, and the authors claim that the edge energy (E_g) of ligand-to-metal charge transfer processes contains information about the local structure of the supported metal oxides. A correlation between E_g and the number of next nearest metal neighbors (N_{Mo}) of the Mo oxide compounds was first proposed by Weber [16]. This methodology was then extended by several researchers [19], and the domain size of the surface oxide species was also accounted for in Ref. [20]. However, the compounds used in

Predicting Catalytic Activity from Oxidic Precursor Properties

the studies are pure bulk chemicals with defined crystalline structures, which do not represent the interference of the metal-support interactions as present in supported catalysts. These limitations make it difficult to directly apply the proposed correlation to a supported HDS catalysts system.

NiMo/Al₂O₃ catalysts used in this work were prepared by the incipient wetness impregnation method with identical metal loadings (close to the industrial-type catalyst) and with different organic additives (citric acid (CA), ethylene glycol (EG), nitrilotriacetic acid (NTA), malic acid (MA), tri-ethylene glycol (TEG), gluconic acid (GA)). Organic additives were added to promote catalyst performance; with different additives, the structure of the oxidic precursors varies, as observed in Chapter 3. The structure difference among these catalysts lies in the impregnation and coordination chemistry brought by the impregnation solutions. As additives have a coordination preference for Ni and Mo in the impregnation solution, the Mo coordination states and metal-support interactions in our catalysts system differ from that in Mo/Al₂O₃ catalysts. Therefore, exploring a general correlation that can be used in a NiMo/Al₂O₃ catalyst system is reasonable. Around twenty alumina-supported NiMo oxide catalysts were characterized by means of TPR, UV-vis DRS, Raman, X-ray diffraction (XRD), and X-ray photoelectron spectroscopy (XPS), and the catalyst HDS performances were evaluated using DBT as probe molecules. The reducibility information, absorption edge energy (E_g) extracted from TPR and UV-vis and the obtained DBT conversion were used for correlation exploration. By plotting these data, the correlations between the structural properties of oxidic precursors and the catalytic performance are expected.

5.2. Experimental section

5.2.1. Materials

The chemicals used in this chapter are described in Section 2.1, Chapter 2. The same industrial γ -Al₂O₃ carrier (surface area: 300 m² g⁻¹, pore volume: 0.82 cm³ g⁻¹, pore diameter: 8.5 nm) as in the previous studies [6, 9, 21] was used.

5.2.2. Catalyst preparation

Two series catalysts prepared from two sets of chemical sources ((NH₄)₆Mo₇O₂₄·4H₂O (AHM)/Ni(NO₃)₂ and MoO₃/NiCO₃) were synthesized by incipient wetness impregnation of γ -Al₂O₃ extrudates [6, 21, 22] with an aqueous solution containing respective metal salts. In each series catalysts, various additives (citric acid (CA), ethylene glycol (EG), nitrilotriacetic acid (NTA), malic acid (MA), triethylene glycol (TEG)) were added. The catalysts were denoted as $Y(1.2)/AHM$ and $Y(1.2)/MoO_3$, Y is the used additive, AHM/MoO₃ represents the

Chapter 5

used chemical sources, 1.2 is the molar ratio of additives and Mo. The detailed preparation procedures can be found in Chapter 3. The target compositions are 15 wt% Mo, 3.67 wt% Ni, 2 wt% P (referenced to MoO₃, NiO, and P₂O₅). Samples without organic additives were denoted as ^{dr}/AHM, ^{cal}/AHM, ^{dr}/MoO₃, and ^{cal}/MoO₃.

Catalysts with the same metal loadings (15 wt% Mo, 3.67 wt% Ni, 2 wt% P) but a lower organic additive content (a molar ratio of 0.6 per atom Mo) were prepared via the same method as described above. These catalysts are denoted as *Y*(0.6)/MoO₃. Likewise, *Y* represents the organic additives used (CA, EG, NTA, MA, TEG, and gluconic acid (GA)); MoO₃ indicates the catalysts were prepared from MoO₃/NiCO₃.

The final composition was determined by inductively coupled plasma optical emission spectroscopy (ICP-OES), and the results are listed in Table 5.1.

Table 5.1. Elemental composition of prepared catalysts.

Catalyst	Loading (wt%)			Ni/Mo (molar ratio)
	Mo	Ni	P	
^{dr} /AHM	12.7	3.4	1.6	0.44
^{cal} /AHM	14.2	3.4	1.8	0.39
CA(1.2)/AHM	9.3	2.3	1.3	0.40
EG(1.2)/AHM	12.8	2.9	1.8	0.38
NTA(1.2)/AHM	8.9	2.0	1.3	0.36
MA(1.2)/AHM	11.3	2.7	1.5	0.40
^{dr} /MoO ₃	12.4	2.9	1.7	0.38
^{cal} /MoO ₃	12.7	3.0	1.7	0.38
CA(1.2)/MoO ₃	9.8	2.2	1.4	0.36
EG(1.2)/MoO ₃	11.9	2.8	1.6	0.38
NTA(1.2)/MoO ₃	10.0	2.3	1.4	0.36
TEG(1.2)/MoO ₃	10.4	2.4	1.5	0.38
MA(1.2)/MoO ₃	11.4	2.7	1.6	0.39
CA(0.6)/MoO ₃	11.4	2.7	1.6	0.39
EG(0.6)/MoO ₃	12.7	2.9	1.7	0.38
NTA(0.6)/MoO ₃	10.6	2.5	1.4	0.38
MA(0.6)/MoO ₃	11.5	2.7	1.6	0.39
GA(0.6)/MoO ₃	11.1	2.6	1.5	0.38
TEG(0.6)/MoO ₃	11.9	2.8	1.6	0.38

5.2.3. Catalyst characterization

TPR, UV-vis DRS, Raman spectroscopy, XRD, and X-ray photoelectron spectroscopy (XPS) were conducted as described in Chapter 2.

5.2.4. Catalytic activity measurement

Predicting Catalytic Activity from Oxidic Precursor Properties

DBT HDS was conducted using the procedure described in section 2.3, Chapter 2.

5.3. Results

All catalysts have a comparable Ni/Mo ratio as in Table 5.1. The Mo and Ni loadings in catalysts prepared with additives were lower than those without organic additives ($^{dr}/\text{AHM}$, $^{cal}/\text{AHM}$, $^{dr}/\text{MoO}_3$, and $^{cal}/\text{MoO}_3$) due to the presence of organic additives, which decomposes during catalysts activation. Figure 5.1 shows XRD patterns of the oxide catalysts. It can be noticed that besides four broad diffraction peaks at $2\theta = 37.7^\circ$, 39.5° , 45.9° , and 66.9° attributed to amorphous $\gamma\text{-Al}_2\text{O}_3$ (JCPDS 01-077-0396) [23], no other apparent signal of crystalline phases were observed, suggesting that Mo and Ni are well-dispersed on the alumina carrier. The crystalline structure information of the other twelve catalysts can be found in Chapter 3.

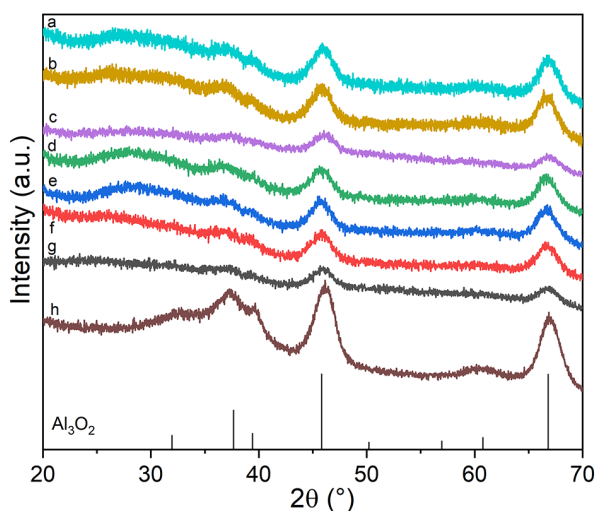


Figure 5.1. XRD pattern of oxidic precursors of a) TEG(1.2)/MoO₃ b) CA(0.6)/MoO₃ c) EG(0.6)/MoO₃ d) NTA(0.6)/MoO₃ e) GA(0.6)/MoO₃ f) TEG(0.6)/MoO₃ g) MA(0.6)/MoO₃ h) $\gamma\text{-Al}_2\text{O}_3$.

UV-vis DRS spectra of the oxidic precursors are displayed in Figure 5.2a. The absorption bands corresponding to ligand-to-metal charge transfer $\text{O}^{2-} \rightarrow \text{Mo}^{6+}$ [24, 25] were observed between 200 and 400 nm. In detail, the peak at ca. 260 nm is assigned to isolated molybdate species in tetrahedral coordination [26, 27]. Signal at 330 nm was observed in EG(1.2)/MoO₃, TEG(1.2)/MoO₃, MA(1.2)/MoO₃, TEG(0.6)/MoO₃, and GA(0.6)/MoO₃; signal at 410 nm was detected in CA(1.2)/AHM, NTA(1.2)/AHM, NTA(1.2)/MoO₃ and NTA(0.6)/MoO₃. In the spectrum of EG(1.2)/AHM, a signal at 430 nm was observed. According to the literature, these three signals can be assigned to the polymeric molybdenum species with octahedral coordination [28]. Bands at 630 nm, 670 nm, 700 nm, and 740 nm observed in the range of 500 – 750 nm indicate the presence of octahedral Ni oxide species [29, 30]. The dispersion

Chapter 5

of Mo species in these catalysts was evaluated using the absorption edge energy (E_g) [16, 31] extracted from the UV-vis DRS spectroscopy. Determination of the E_g values was done by finding the intercept on the X-axis of the tangent line in the low-energy rise of the plot of $[F(R_\infty) hv]^2$ vs. hv , where $F(R_\infty)$ is the Kubelka–Munk function and hv is the incident photon energy [32]. The adsorption edges of catalysts are shown in Figure 5.2b, and the specific E_g values are listed in Table 5.2. In both series of catalysts, the catalysts after calcination and with additives show a lower E_g value than $^{dr}/\text{AHM}$ and $^{dr}/\text{MoO}_3$, except for NTA. This means that catalysts after calcination and with additives have a smaller Mo particle size [16] [31] than $^{dr}/\text{AHM}$ and $^{dr}/\text{MoO}_3$. Catalysts with NTA (NTA(1.2)/AHM, NTA(1.2)/MoO₃, and NTA(0.6)/MoO₃), however, have a larger particle size, as they show higher E_g than $^{dr}/\text{AHM}$ and $^{dr}/\text{MoO}_3$.

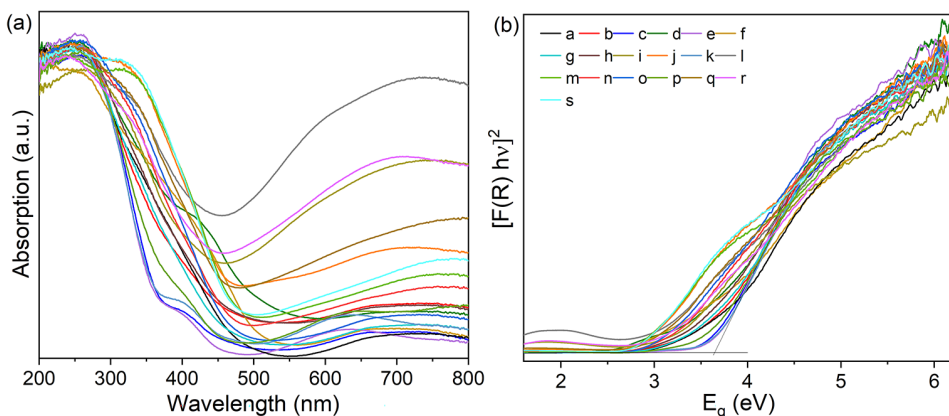


Figure 5.2. (a) UV-vis DRS spectra and (b) UV absorption edges of a) $^{dr}/\text{AHM}$ b) $^{cal}/\text{AHM}$ c) CA(1.2)/AHM d) EG(1.2)/AHM e) NTA(1.2)/AHM f) MA(1.2)/AHM g) $^{dr}/\text{MoO}_3$ h) $^{cal}/\text{MoO}_3$ i) CA(1.2)/MoO₃ j) EG(1.2)/MoO₃ k) NTA(1.2)/MoO₃ l) MA(1.2)/MoO₃ m) TEG(1.2)/MoO₃ n) CA(0.6)/MoO₃ o) EG(0.6)/MoO₃ p) NTA(0.6)/MoO₃ q) MA(0.6)/MoO₃ r) GA(0.6)/MoO₃ s) TEG(0.6)/MoO₃.

Table 5.2. Absorption edge energy (E_g) and temperature at maximum H₂ consumption (T_m) of the oxidic precursors of catalysts.

Catalyst	E_g (eV)	T_m (°C)	Catalyst	E_g (eV)	T_m (°C)
$^{dr}/\text{AHM}$	3.63	409	$^{dr}/\text{MoO}_3$	3.48	410
$^{cal}/\text{AHM}$	3.53	398	$^{cal}/\text{MoO}_3$	3.42	401
CA(1.2)/AHM	3.57	404	CA(1.2)/MoO ₃	3.16	399
EG(1.2)/AHM	3.42	399	EG(1.2)/MoO ₃	2.94	397
NTA(1.2)/AHM	3.66	421	NTA(1.2)/MoO ₃	3.65	412
MA(1.2)/AHM	3.44	403	TEG(1.2)/MoO ₃	3.04	400
CA(0.6)/MoO ₃	3.11	396	MA(1.2)/MoO ₃	2.92	390
EG(0.6)/MoO ₃	3.06	403	MA(0.6)/MoO ₃	3.02	410
NTA(0.6)/MoO ₃	3.56	402	GA(0.6)/MoO ₃	2.99	398
TEG(0.6)/MoO ₃	2.88	396			

Predicting Catalytic Activity from Oxidic Precursor Properties

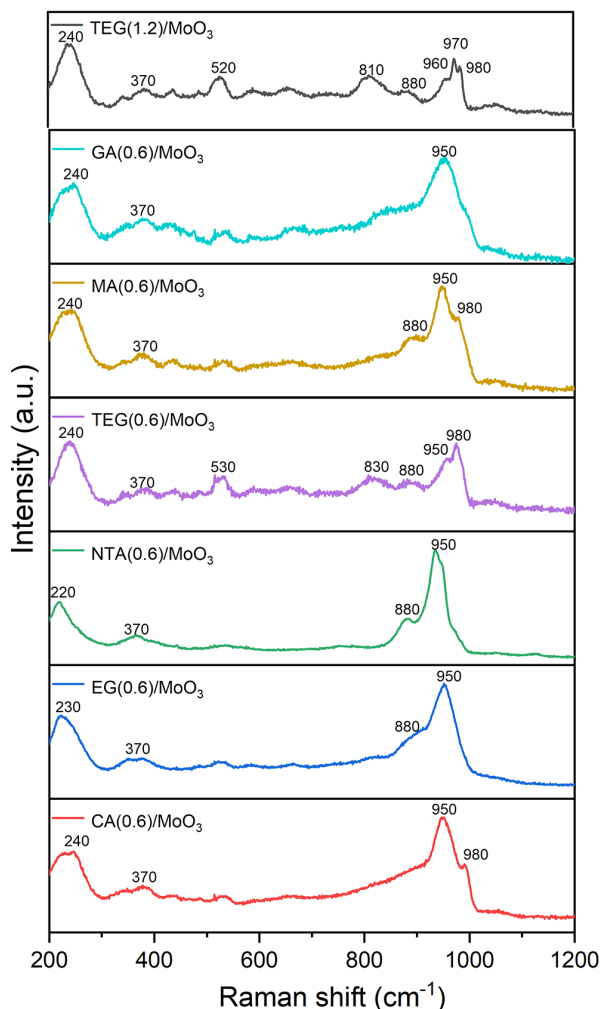


Figure 5.3. Raman spectra of oxide catalysts.

The nature of the Mo oxide species present on the alumina surface was further examined by Raman spectroscopy [33]. Y(0.6)/MoO₃ shares the similar characteristics with Y(1.2)/MoO₃, where the bands located at 950 cm⁻¹, 370 cm⁻¹, and ~230 cm⁻¹ were observed. The band at 950 cm⁻¹ is assigned to the $\nu_s(\text{Mo}=\text{O})$ stretching mode of Mo=O_t structure in Mo₇O₂₄⁶⁻ species [34, 35]; the one at 370 cm⁻¹ is associated with the $\delta(\text{Mo}=\text{O})$ deformation modes of Mo=O_t groups and the band at 230 cm⁻¹ is assigned to the $\delta(\text{Mo}-\text{O}-\text{Mo})$ deformation vibration of the bridging Mo-O-Mo bonds in polymolybdate species [36, 37]. The presence of these bands indicates the presence of octahedrally coordinated polymolybdate species. Two bands at 980 cm⁻¹ and 880 cm⁻¹ were observed in multiple samples, which according to the literature, are associated with the $\nu_s(\text{Mo}=\text{O})$ and $\nu_{as}(\text{Mo}=\text{O})$ stretching vibration modes of the Mo=O_t bonds in the aggregated molybdenum species [38-40]. The band at 840 cm⁻¹ in the spectrum of

Chapter 5

TEG(0.6)/MoO₃ and GA(0.6)/MoO₃ was arising from the $\nu_s(\text{Mo}=\text{O})$ stretching vibration of the Mo=O_t bond in tetrahedrally coordinated molybdate [41]. Besides above-mentioned bands, bands at 970 cm⁻¹, 960 cm⁻¹, 810 cm⁻¹, and 520 cm⁻¹ were also detected in TEG(1.2)/MoO₃. Bands at 970 cm⁻¹ and 960 cm⁻¹ are attributed to the $\nu_s(\text{Mo}=\text{O})$ stretching mode of Mo=O_t structure in more polymerized Mo oxide entities, e.g., Mo₈O₂₆⁴⁻ species [36], and the one at 810 cm⁻¹ probably due to the $\nu_{as}(\text{Mo}-\text{O}-\text{Mo})$ vibrational modes of Mo-O-Mo bond in isolated MoO₄²⁻ species [42, 43].

The reducibility of oxide catalysts was explored using TPR. It can be seen from Figure 5.4 that all samples exhibit a similar profile, where there is a sharp peak at a low reduction temperature, ca. 400 °C, followed by a continuous H₂ consumption over a broad temperature region with a maximum at ca. 700 °C as previously reported for NiMo catalysts [44, 45]. The reduction peak at low temperatures can be attributed to the reduction of Ni oxide species and the partial reduction of polymolybdates that are weakly connected with the support (Mo⁶⁺ to Mo⁴⁺) [13, 46]. The broad feature at high temperatures is attributed to the deep reduction of all Mo species, including tetrahedrally coordinated Mo⁴⁺ species. Based on the H₂ consumption, reducing Mo⁶⁺ to Mo⁴⁺ is considered the main reduction step in all catalysts. The maximum temperature of the main reduction peak (T_m) was extracted from TPR profiles and listed in Table 5.2. In both catalyst series, the reducibility of catalysts after calcination and with additives was improved compared to ^{dr}/AHM and ^{dr}/MoO₃, indicating a lower metal-support interaction in these catalysts. The exceptions are NTA(1.2)/AHM and NTA(1.2)/MoO₃, as they have a higher T_m than ^{dr}/AHM and ^{dr}/MoO₃.

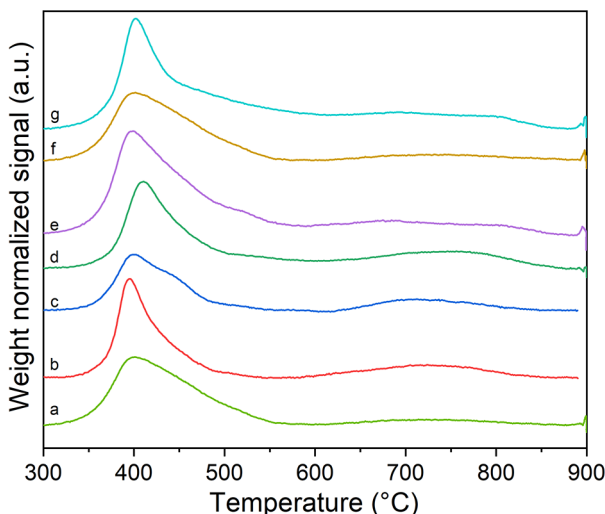


Figure 5.4. TPR profile of a) TEG(1.2)/MoO₃, b) CA(0.6)/MoO₃, c) NTA(0.6)/MoO₃, d) MA(0.6)/MoO₃, e) GA(0.6)/MoO₃, f) TEG(0.6)/MoO₃, g) EG(0.6)/MoO₃.

Predicting Catalytic Activity from Oxidic Precursor Properties

With a further look at the TPR spectra, it can be noticed that the reduction area in the low-temperature region is not always symmetric, indicating that not only one reduction step occurred. To get a clear insight into the reduction profile of calculated samples, the deconvolution analysis using the Gaussian function and a multi-peak fit procedure was conducted (Figure C1). Detailed deconvolution information, including T_m , H_2 consumption (as calculated from the area under the curve, 300 °C – 900 °C), and width at half-height ($\Delta T_{1/2}/^\circ\text{C}$), are listed in Table 5.3. The metal loadings with mmol Mo(Ni)/g as a unit, the equivalent of the data measured by ICP (Table 5.1), are also listed. The different reduction stages are numbered in the table according to the temperature of the component bands.

The total H_2 consumption of these catalysts is lower than the values expected for a complete reduction of MoO_3 to Mo^0 and NiO to Ni^0 , indicating that Mo and Ni are partially reduced under the applied conditions, represented as the reduction degree < 1 . The above-mentioned reduction of Ni oxide species and partial reduction of polymolybdates (Mo^{6+} to Mo^{4+}) in the low-temperature area was also reflected in the deconvolution profile of these catalysts, where two components contributing to the total reduction reaction were identified (300 – 500 °C). For example, two peaks at 395 °C and 445 °C were observed in EG(1.2)/ MoO_3 , as listed in Table 5.3. Considering the H_2 consumption of each component and the Mo and Ni content, the peak located at 395 °C (with maximum H_2 consumption) is assigned to the reduction of polymolybdates that are weakly connected with the alumina carrier, while the one located at 445 °C is due to the reduction of Ni. This assignment applies to most catalysts except for NTA(1.2)/AHM. The peak at 400 °C in NTA(1.2)/AHM is attributed to the reduction of Ni, and the peak at 440 °C is assigned to the reduction of Mo species. As mentioned above, the components in the high-temperature area (500 – 900 °C) are assigned to the further reduction of tetrahedrally coordinated Mo species and Ni species that are strongly bonded to the alumina carrier [11].

XPS analysis was carried out to determine the surface composition and the oxidation state of Mo and Ni in sulfided catalysts. The XPS spectra were decomposed into three doublets related to different Mo oxidation states and one S 2s peak characteristic of S^{2-} (B.E. = 226.3 ± 0.2 eV). The three Mo 3d doublets are assigned to Mo^{6+} in MoO_3 (B.E. $3d_{5/2} = 232.7 \pm 0.4$ eV), Mo^{5+} in oxysulfide species (B.E. $3d_{5/2} = 230.9 \pm 0.3$ eV) and Mo^{4+} in MoS_2 (B.E. $3d_{5/2} = 229.0 \pm 0.2$ eV). The deconvolution of the Ni 2p_{3/2} profiles was also conducted; each Ni 2p spectrum was resolved in three components [47] at 856.8 ± 0.2 eV, 854.6 ± 0.5 eV, and 853.7 ± 0.5 eV, ascribing to NiS_x , NiMoS, and NiO_x species, respectively along with their respective satellites [48, 49]. The corresponding fitting results of the respective sulfided catalysts are displayed in Figure C2 and listed in Table 5.4.

Table 5.3. Results of TPR study of the prepared samples

Sample	dr/AHM			cat/AHM			CA(1.2)/AHM			EG(1.2)/AHM		
	T _m /°C	ΔT _{1/2} /°C	mmol H ₂ /g	T _m /°C	ΔT _{1/2} /°C	mmol H ₂ /g	T _m /°C	ΔT _{1/2} /°C	mmol H ₂ /g	T _m /°C	ΔT _{1/2} /°C	mmol H ₂ /g
Mo content (mmol/g)		1.32		1.47			0.97					1.34
Ni content (mmol/g)		0.6		0.57			0.39					0.50
H ₂ consumption (mmol/g)		2.05		2.02			1.00					1.19
Reduction degree ^a		0.45		0.41			0.30					0.26
	T _m /°C	ΔT _{1/2} /°C	mmol H ₂ /g	T _m /°C	ΔT _{1/2} /°C	mmol H ₂ /g	T _m /°C	ΔT _{1/2} /°C	mmol H ₂ /g	T _m /°C	ΔT _{1/2} /°C	mmol H ₂ /g
1	409	56	0.95	397	42	0.59	403	63	0.75	402	54	0.68
2	477	110	0.44	442	140	0.81	462	33	0.07	448	33	0.13
3	654	192	0.53	645	205	0.53	578	61	0.09	480	81	0.23
4	788	79	0.09	772	82	0.12	740	100	0.09	758	139	0.14
Sample	NTA(1.2)/AHM						MA(1.2)/AHM					
Mo content (mmol/g)		0.93		1.18			1.29					1.32
Ni content (mmol/g)		0.33		0.45			0.49					0.50
H ₂ consumption (mmol/g)		1.11		1.35			1.94					1.95
Reduction degree ^a		0.36		0.34			0.44					0.44
	T _m /°C	ΔT _{1/2} /°C	mmol H ₂ /g	T _m /°C	ΔT _{1/2} /°C	mmol H ₂ /g	T _m /°C	ΔT _{1/2} /°C	mmol H ₂ /g	T _m /°C	ΔT _{1/2} /°C	mmol H ₂ /g
1	400	30	0.07	414	59	0.67	409	56	0.85	402	52	0.89
2	440	95	0.83	458	34	0.23	494	121	0.51	471	86	0.39
3	594	103	0.20	512	69	0.27	716	211	0.59	567	128	0.27
4				800	106	0.16				728	157	0.39
Sample	CA(1.2)/MoO ₃						EG(1.2)/MoO ₃					
Mo content (mmol/g)		1.02		1.24			0.93					1.18
Ni content (mmol/g)		0.37		0.48			0.33					0.46
H ₂ consumption (mmol/g)		0.95		1.95			0.84					1.08
Reduction degree ^a		0.28		0.46			0.27					0.27
	NTA(1.2)/MoO ₃						MA(1.2)/MoO ₃					

Predicting Catalytic Activity from Oxidic Precursor Properties

	$T_m/^\circ\text{C}$	$\Delta T_{1/2}/^\circ\text{C}$	mmol H_2/g	$T_m/^\circ\text{C}$	$\Delta T_{1/2}/^\circ\text{C}$	mmol H_2/g	$T_m/^\circ\text{C}$	$\Delta T_{1/2}/^\circ\text{C}$	mmol H_2/g	$T_m/^\circ\text{C}$	$\Delta T_{1/2}/^\circ\text{C}$	mmol H_2/g
1	399	63	0.62	395	53	0.63	410	61	0.45	394	53	0.63
2	460	47	0.09	445	47	0.16	455	47	0.18	445	47	0.16
3	718	128	0.23	724	138	0.29	510	115	0.14	724	138	0.29
4				779	74	0.07	610	67	0.08			
Sample	TEG(1.2)/MoO ₃			CA(0.6)/MoO ₃			TEG(0.6)/MoO ₃			EG(0.6)/MoO ₃		
Mo content (mmol/g)	1.08			1.18			1.24			1.32		
Ni content (mmol/g)	0.41			0.46			0.47			0.50		
H ₂ consumption (mmol/g)	1.23			1.19			1.26			2.06		
Reduction degree ^a	0.34			0.30			0.30			0.46		
	$T_m/^\circ\text{C}$	$\Delta T_{1/2}/^\circ\text{C}$	mmol H_2/g	$T_m/^\circ\text{C}$	$\Delta T_{1/2}/^\circ\text{C}$	mmol H_2/g	$T_m/^\circ\text{C}$	$\Delta T_{1/2}/^\circ\text{C}$	mmol H_2/g	$T_m/^\circ\text{C}$	$\Delta T_{1/2}/^\circ\text{C}$	mmol H_2/g
1	410	81	0.86	399	48	0.69	404	72	0.72	406	60	0.80
2	484	74	0.27	452	50	0.19	470	86	0.40	490	157	0.78
3	727	136	0.11	721	145	0.30	739	157	0.14	690	145	0.38
4										796	76	0.11
Sample	NTA(0.6)/MoO ₃			GA(0.6)/MoO ₃			MA(0.6)/MoO ₃					
Mo content (mmol/g)	1.11			1.15			1.20					
Ni content (mmol/g)	0.43			0.44			0.46					
H ₂ consumption (mmol/g)	0.90			2.07			1.62					
Reduction degree ^a	0.24			0.53			0.40					
	$T_m/^\circ\text{C}$	$\Delta T_{1/2}/^\circ\text{C}$	mmol H_2/g	$T_m/^\circ\text{C}$	$\Delta T_{1/2}/^\circ\text{C}$	mmol H_2/g	$T_m/^\circ\text{C}$	$\Delta T_{1/2}/^\circ\text{C}$	mmol H_2/g	$T_m/^\circ\text{C}$	$\Delta T_{1/2}/^\circ\text{C}$	mmol H_2/g
1	401	51	0.45	404	70	1.01	416	69	0.84			
2	445	42	0.18	476	106	0.59	506	123	0.31			
3	486	70	0.08	675	175	0.39	731	175	0.39			
4	724	113	0.20	799	78	0.08						

^a $\alpha = 1$ corresponds to the reduction of MoO₃ to Mo⁰ and NiO to Ni⁰ according to the composition of the samples in each case.

Table 5.4. Binding energy and atomic percentage of different Mo and Ni species in measured catalysts sulfided under 1 bar H₂S/H₂ at 350 °C.

Temperature (°C)	Binding energy (eV)												Fractions (%)					
	Mo 3d5/2				Ni 2p3/2				Mo 3d				Ni 2p					
	Mo ⁴⁺	Mo ⁵⁺	Mo ⁶⁺	NiS _x	NiMoS	NiO _x	Mo ⁴⁺	Mo ⁵⁺	Mo ⁶⁺	NiS _x	NiMoS	NiO _x						
d ^r /AHM	229.0	230.8	233.0	853.5	854.8	856.9	83.8	12.2	4.0	73.5	16.3	10.2						
e ⁿ /AHM	229.0	230.8	232.9	853.5	854.9	856.8	83.4	12.6	4.0	72.8	18.0	9.3						
CA(1.2)/AHM	229.0	230.9	233.0	853.4	854.8	856.8	84.6	11.8	3.6	73.6	17.0	9.3						
EG(1.2)/AHM	229.0	230.7	233.0	853.4	854.9	856.8	85.0	11.0	4.0	73.3	18.6	8.1						
NTA(1.2)/AHM	229.1	230.8	232.9	853.4	854.9	856.9	84.3	11.9	3.9	74.8	15.5	9.7						
MA(1.2)/AHM	229.0	230.9	233.0	853.4	855.0	856.8	85.1	10.7	4.2	70.8	21.2	8.1						
d ^r /MoO ₃	229.0	230.7	232.9	853.3	854.9	856.8	87.3	8.9	3.8	73.2	20.3	6.5						
e ⁿ /MoO ₃	229.1	230.9	232.9	853.4	854.9	856.8	86.8	8.6	4.6	69.3	21.1	9.6						
CA(1.2)/MoO ₃	229.0	230.9	232.8	853.3	854.9	856.7	89.4	7.7	2.9	69.9	22.0	8.1						
EG(1.2)/MoO ₃	229.0	230.7	232.8	853.4	854.8	856.8	85.8	10.9	3.3	68.6	22.3	9.1						
NTA(1.2)/MoO ₃	229.0	230.9	232.9	853.3	854.9	856.8	90.2	6.2	3.5	75.2	18.3	6.6						
MA(1.2)/MoO ₃	229.0	230.7	233.0	853.4	854.9	856.8	87.7	9.3	3.0	68.0	24.7	7.3						
TEG(1.2)/MoO ₃	229.0	230.8	233.0	853.4	854.9	856.9	86.3	10.6	3.1	72.6	20.0	7.5						
CA(0.6)/MoO ₃	229.0	231.0	233.0	853.4	854.9	856.9	88.3	9.1	2.6	72.4	18.0	9.6						
EG(0.6)/MoO ₃	228.9	230.8	232.7	853.4	854.9	856.9	85.8	10.4	3.8	71.1	20.5	8.4						
NTA(0.6)/MoO ₃	229.0	231.0	233.0	853.4	854.8	856.8	87.8	9.6	2.6	72.1	19.2	8.7						
MA(0.6)/MoO ₃	229.0	230.7	232.8	853.3	854.8	856.9	85.0	11.9	3.1	73.5	20.9	5.6						
GA(0.6)/MoO ₃	229.0	230.7	232.8	853.3	854.7	856.9	85.0	11.8	3.2	66.7	23.1	10.2						
TEG(0.6)/MoO ₃	229.1	230.8	232.9	853.3	854.8	856.9	84.7	11.3	4.0	71.2	20.5	8.3						

Predicting Catalytic Activity from Oxidic Precursor Properties

The catalytic activity of catalysts was evaluated in HDS of DBT at 20 bar at 250 °C, 270 °C, and 300 °C. To avoid repetition, only the results of TEG(1.2)/MoO₃ and Y(0.6)/MoO₃ are listed here. As described in Chapter 2, the DBT converted via the direct desulfurization (DDS) pathway and the hydrogenation (HYD) pathway with biphenyl (BP) and cyclohexylbenzene (CHB) as the main product, respectively [50]. Since the DDS pathway consumes substantially less H₂, it is considered the preferred route for DBT HDS. The main products in our system are BP and CHB, partially hydrogenated intermediates (hexahydro-dibenzothiophene (HHDBT) and tetrahydro-dibenzothiophene (THCBT)) were never observed, and the fully saturated product, bicyclohexyl (BCH), was only detected in a low concentration as the product of GA(0.6)/MoO₃ at 300 °C.

Table 5.5. DBT HDS results

Catalyst	DBT						
	Reaction temperature	Reaction rates (mol mol _{Mo} ⁻¹ h ⁻¹)	Selectivity				Conversion X (%)
		k _{HDS}	BP	CHB	BCH	DDS : HYD	
TEG(1.2)/MoO ₃	250 °C	8.5	53.9	46.1	0	1.2	16.8
	270 °C	28.4	52.2	47.8	0	1.1	45.8
	300 °C	464.4	45.3	54.7	0	0.8	100
CA(0.6)/MoO ₃	250 °C	5.1	51.9	48.1	0	1.1	9.7
	270 °C	20.5	50.4	49.6	0	1.0	39.3
	300 °C	290.9	49.0	51.0	0	0.9	99.9
EG(0.6)/MoO ₃	250 °C	5.9	58.2	41.8	0	1.4	14.4
	270 °C	22.8	57.1	42.9	0	1.4	45.2
	300 °C	272.2	54.1	45.9	0	1.3	99.9
NTA(0.6)/MoO ₃	250 °C	5.3	58.0	42.0	0	1.4	11.1
	270 °C	21.6	53.9	46.1	0	1.2	37.9
	300 °C	274.9	49.6	50.4	0	1.0	99.8
GA(0.6)/MoO ₃	250 °C	12.1	49.0	51.0	0	1.0	24.3
	270 °C	41.5	49.3	50.7	0	1.0	61.6
	300 °C	424.1	40.3	57.4	0.3	0.7	100
MA(0.6)/MoO ₃	250 °C	11.3	51.4	48.6	0	1.1	23.7
	270 °C	39.1	50.9	49.1	0	1.0	60.8
	300 °C	405.5	41.5	58.5	0	0.7	100
TEG(0.6)/MoO ₃	250 °C	10.4	52.8	47.2	0	1.1	22.8
	270 °C	33.5	52.7	47.3	0	1.1	56.4
	300 °C	66.6	56.8	43.2	0	1.3	100

Specific reaction rates, product distribution and DBT conversion in DBT HDS are listed in Table 5.5. The catalysts show a significant variation in performance under testing conditions. Generally, catalysts with additives show a varied improved HDS performance compared to ^{dr}/MoO₃, except for CA(0.6)/MoO₃ and NTA(0.6)/MoO₃. GA(0.6)/MoO₃ has the highest DBT HDS activity in these catalysts, with a 24.6 % DBT conversion at 250 °C, 61.6 % conversion at 270 °C, and 100 % conversion at 300 °C. The results are consistent with the literature that DBT conversion improves with the increase of temperature [51, 52], the selectivity also varies with the increase of temperature. As in the low reaction temperature,

Chapter 5

the DDS route is the main reaction pathway with BP as the main product, while with the increasing temperature, the HYD route is enhanced.

5.4. Discussion

As mentioned above, the dispersion and the content of the active NiMoS phase played a significant role in catalyst catalytic performance [53]. To define the role of the active NiMoS phase in our catalyst system, the contribution of NiMoS species to Ni 2p spectra was revealed by deconvolution of XPS spectra, as listed in Table 5.4. By plotting the content of active NiMoS phase with DBT conversion, positive correlations at three reaction temperatures were observed as shown in Figure 5.5; the correlation suggests that the catalyst with the higher content of the active NiMoS phase shows a better performance, which is consistent with the published work [53].

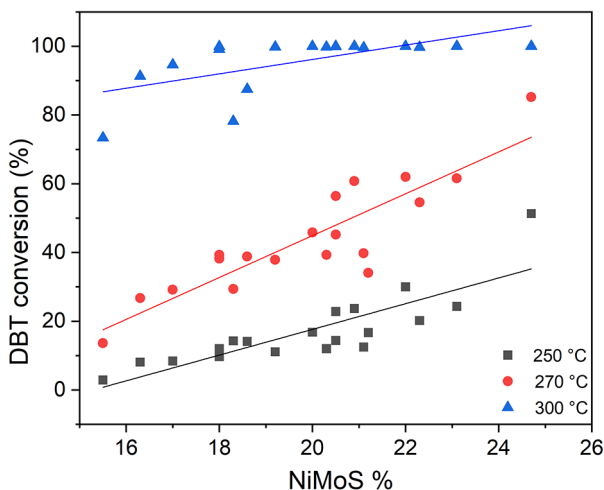


Figure 5.5. Correlation between the content of active NiMoS phase extracted from XPS spectra and the corresponding DBT conversion of measured catalysts.

Correlation of absorption edge energy (E_g) with DBT HDS performance. UV-vis DRS is considered a promising technique to explore the local structure of transition metal oxides, e.g., M-O-M bond length, the coordination number, and domain particle size. Weber [16] proposed a linear correlation between E_g and the local degree of Mo clusters aggregation, $N_{Mo}=16-3.8 E_g$, based on five inconsistent E_g values collected from different publications. Later, Wachs et al. [34] tried to refine this methodology by using around ten Mo-containing oxide chemicals to explore the correlation between E_g and an average number of covalent bridging M-O-M bonds of the central Mo species. They observed a similar inverse linear correlation, $N_{Mo-O-Mo}=11.8 - 2.6 E_g$. Analogous correlations for V(V) and W(VI) species were also reported [17, 18]. Noted is that all compounds used in this research are bulk, well-

Predicting Catalytic Activity from Oxidic Precursor Properties

structured, crystalline materials, which is different from the support catalysts used in our study. As discussed in the former chapters, the metal-support interactions influence the metal dispersion and reducibility in catalyst. The additives and promotor atoms, Ni, in catalysts also change the coordination states of Mo to a certain degree, which makes the catalyst structure different from the Mo-only catalyst system. Further, the metal oxide in the oxidic NiMo/Al₂O₃ catalyst is amorphous as XRD data shown, which increases the difficulty of deducing the specific structure of the catalysts than the bulk, crystalline materials. Therefore, the obtained E_g can only be considered an average value that contributed from different Mo coordination. The detailed coordination condition or the number of Mo species in our catalyst cannot be derived from E_g directly. To elucidate the structure of NiMo/Al₂O₃ HDS catalyst, complementary techniques, like Raman, are needed.

Even so, the general structure information regarding the Mo species distribution and particle sizes deduced from E_g is still valuable [31]. With this information considered, a correlation between E_g and HDS performance, presented by the DBT conversion of catalysts at three different temperatures, was explored. As shown in Figure 5.6, an inverse linear correlation between E_g and DBT conversion was observed, suggesting the catalyst with lower E_g has a higher DBT HDS activity. This empirical correlation can be used as a primary guide to distinguish the catalyst from a bunch of designed and synthesized catalysts; additional characterization would be needed for detailed structure information.

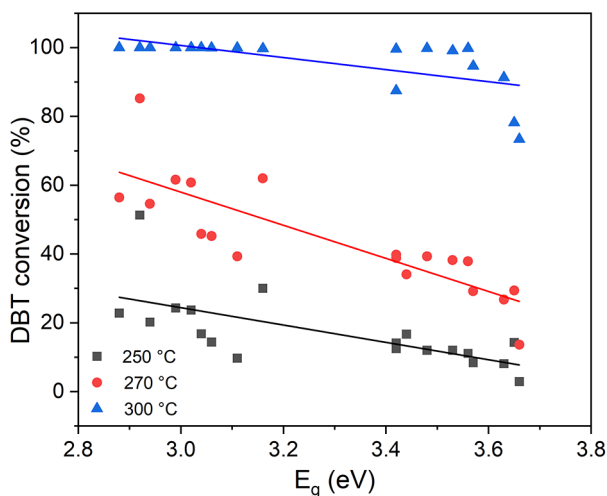


Figure 5.6. Correlation between absorption energy (E_g) and DBT conversion.

Correlation of reducibility with DBT HDS performance. The reducibility of Mo oxides in NiMo/Al₂O₃ catalyst altered by metal-support interactions affects Mo dispersion and the characteristics of the formed surface species. The sulfidation degree of catalysts is also

Chapter 5

influenced by the reducibility of the oxidic precursors, as described in the former work [9]. To determine the correlation between the reducibility of oxidic precursors and the performance of the sulfided catalysts, we collected T_m and DBT conversion from TPR and DBT HDS to represent the reducibility and HDS activity of the catalysts. By plotting, an empirical inverse linear correlation between T_m and DBT conversion was observed (Figure 5.7). This correlation is analogous and complementary to the correlation observed between E_g and DBT conversion. It suggests that in NiMo/Al₂O₃ HDS catalyst, the oxidic precursor with a lower T_m (higher reducibility) shows a higher HDS activity. The underlying reason is that the higher reducibility commonly caused by the weaker metal-support interaction [54, 55], and this type of metal-support interaction is evident in favor of forming the sulfided active NiMoS species [56, 57], the key to HDS catalysts. It also suggests that the reduction of the transition metal compounds is a crucial step in transforming the oxidic precursor catalyst into the sulfided catalyst [22], which makes TPR a promising technique for preliminary screening of the oxidic HDS catalysts.

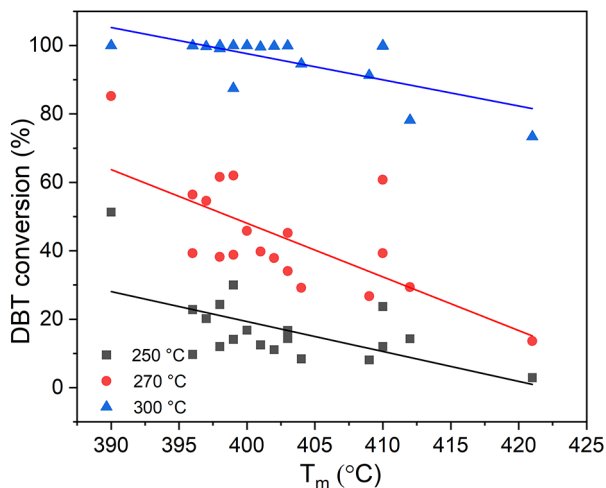


Figure 5.7. Correlation between the maximum temperature of reduction peak (T_m) and DBT conversion.

5.5. Conclusions

In this work, the correlation between the physical and structural properties of oxidic precursors of NiMo/Al₂O₃ catalysts and the hydrodesulfurization (HDS) activity of the sulfided catalysts was explored. Series of NiMo/Al₂O₃ catalysts were prepared by the incipient wetness impregnation and characterized by means of temperature-programmed reduction (TPR), X-ray photoelectron spectroscopy (XPS), Raman, X-ray diffraction (XRD) and UV-visible diffuse reflectance spectroscopy (UV-vis DRS). The HDS activity of catalysts was evaluated in dizenzothiophene (DBT) HDS. The structure-activity relationship

Predicting Catalytic Activity from Oxidic Precursor Properties

was revealed by establishing an inverse linear correlation between the absorption edge energy (E_g) and the DBT conversion. This correlation indicates that catalysts with lower E_g (smaller particle size) show higher activity. Due to the complicated formulation of catalysts, the amorphous metal state, and the influence of the metal-support interaction, specific structure information of Mo, i.e., the average number of nearest Mo neighbors in the clusters, the number of next nearest neighbors of Mo, cannot be extracted from E_g .

An analogously empirical correlation between the reducibility of oxide catalysts (T_m , extracted from UV-vis DRS) and the HDS catalytic activity (DBT conversion) of sulfided catalysts was also established as supplementary. The results suggest that the catalyst with high reducibility (low T_m) shows a high HDS performance. As the high reducibility is the consequences of the low metal-support interaction, this interaction is in favor of the formation of the active NiMoS phase during the sulfidation, which is the key to the high activity (Figure 5.5). These two correlations confirm that metal dispersion and metal-support interaction in the oxide NiMo/Al₂O₃ catalyst play an essential role in catalyst performance.

5.6. References

- [1] C. Song, An overview of new approaches to deep desulfurization for ultra-clean gasoline, diesel fuel and jet fuel, *Catal. Today*, 86 (2003) 211-263.
- [2] H. Topsøe, B.S. Clausen, F.E. Massoth, *Hydrotreating catalysis*, in: *Catalysis*, Springer, 1996, pp. 1-269.
- [3] H. Topsøe, R. Candia, N.Y. Topsøe, B.S. Clausen, H. Topsøe, On The State of the Co-Mo-S Model, *Bulletin des Sociétés Chimiques Belges*, 93 (1984) 783-806.
- [4] X. Bai, Q. Li, L. Shi, C. Ling, J. Wang, Edge promotion and basal plane activation of MoS₂ catalyst by isolated Co atoms for hydrodesulfurization and hydrodenitrogenation, *Catal. Today*, 350 (2020) 56-63.
- [5] F.L. Deepak, R. Esparza, B. Borges, X. Lopez-Lozano, M. Jose-Yacamán, Direct imaging and identification of individual dopant atoms in MoS₂ and WS₂ catalysts by aberration corrected scanning transmission electron microscopy, *ACS Catal.*, 1 (2011) 537-543.
- [6] L. van Haandel, G.M. Bremmer, E.J.M. Hensen, Th. Weber, Influence of sulfiding agent and pressure on structure and performance of CoMo/Al₂O₃ hydrodesulfurization catalysts, *J. Catal.*, 342 (2016) 27-39.
- [7] M. Daage, R.R. Chianelli, Structure-function relations in molybdenum sulfide catalysts: the "rim-edge" model, *J. Catal.*, 149 (1994) 414-427.
- [8] J.V. Lauritsen, F. Besenbacher, Atom-resolved scanning tunneling microscopy investigations of molecular adsorption on MoS₂ and CoMoS hydrodesulfurization catalysts, *J. Catal.*, 328 (2015) 49-58.
- [9] M. Li, J. Ihli, M.A. Verheijen, M. Holler, M. Guizar-Sicairos, J.A. van Bokhoven, E.J.M. Hensen, Th. Weber, Alumina-Supported NiMo Hydrotreating Catalysts – Aspects of 3D Structure, Synthesis, and Activity, *J. Phys. Chem. C*, 126 (2022) 18536-18549.
- [10] E. Payen, S. Kasztelan, J. Grimblot, In situ Laser Raman Spectroscopy of the sulphiding of WO₃(MoO₃)/ γ -Al₂O₃ catalysts, *J. Mol. Struct.*, 174 (1988) 71-76.
- [11] J.L. Brito, J. Laine, Reducibility of Ni-Mo/Al₂O₃ catalysts: a TPR study, *J. Catal.*, 139 (1993) 540-550.

Chapter 5

- [12] S. Rajagopal, H.J. Marini, J.A. Marzari, R. Miranda, Silica-alumina-supported acidic molybdenum catalysts-TPR and XRD characterization, *J. Catal.*, 147 (1994) 417-428.
- [13] R. Thomas, E.M. van Oers, V.H.J. de Beer, J. Medema, J.A. Moulijn, Characterization of γ -alumina-supported Molybdenum oxide and tungsten oxide; reducibility of the oxidic state versus hydrodesulfurization activity of the sulfided state, *J. Catal.*, 76 (1982) 241-253.
- [14] L.G. Teoh, J. Shieh, W.H. Lai, I.M. Hung, M.H. Hon, Structure and optical properties of mesoporous tungsten oxide, *J. Alloys Compd.*, 396 (2005) 251-254.
- [15] I.E. Wachs, T. Kim, E.I. Ross, Catalysis science of the solid acidity of model supported tungsten oxide catalysts, *Catal. Today*, 116 (2006) 162-168.
- [16] R.S. Weber, Effect of local structure on the UV-visible absorption edges of molybdenum oxide clusters and supported molybdenum oxides, *J. Catal.*, 151 (1995) 470-474.
- [17] X. Gao, I.E. Wachs, Investigation of surface structures of supported vanadium oxide catalysts by UV-vis-NIR diffuse reflectance spectroscopy, *J. Phys. Chem. B*, 104 (2000) 1261-1268.
- [18] E.I. Ross-Medgaarden, I.E. Wachs, Structural determination of bulk and surface tungsten oxides with UV-Vis diffuse reflectance spectroscopy and Raman spectroscopy, *J. Phys. Chem. C*, 111 (2007) 15089-15099.
- [19] M. Scheithauer, R.K. Grasselli, H. Knözinger, Genesis and structure of WO_x/ZrO_2 solid acid catalysts, *Langmuir*, 14 (1998) 3019-3029.
- [20] D. Gazzoli, M. Valigi, R. Dragone, A. Marucci, G. Mattei, Characterization of the zirconia-supported tungsten oxide system by laser Raman and diffuse reflectance spectroscopies, *J. Phys. Chem. B*, 101 (1997) 11129-11135.
- [21] J. Ihli, L. Bloch, F. Krumeich, K. Wakonig, M. Holler, M. Guizar-Sicairos, Th. Weber, J.C. da Silva, J.A. van Bokhoven, Hierarchical Structure of NiMo Hydrodesulfurization Catalysts Determined by Ptychographic X-Ray Computed Tomography, *Angew. Chem. Int. Ed.*, 59 (2020) 17266-17271.
- [22] L. van Haandel, A. Longo, W. Bras, E.J.M. Hensen, Th. Weber, Activation of Co-Mo-S hydrodesulfurization catalysts under refinery conditions – A combined SAXS/XAS study, *ChemCatChem*, 11 (2019) 5013-5017.
- [23] A. Bhat, G.B. Megeri, C. Thomas, H. Bhargava, C. Jeevitha, S. Chandrashekar, G.M. Madhu, Adsorption and optimization studies of lead from aqueous solution using γ -Alumina, *J. Environ. Chem. Eng.*, 3 (2015) 30-39.
- [24] L. Peña, D. Valencia, T. Klimova, CoMo/SBA-15 catalysts prepared with EDTA and citric acid and their performance in hydrodesulfurization of dibenzothiophene, *Appl. Catal. B: Environ.*, 147 (2014) 879-887.
- [25] J. Xu, T. Huang, Y. Fan, Highly efficient NiMo/SiO₂-Al₂O₃ hydrodesulfurization catalyst prepared from gemini surfactant-dispersed Mo precursor, *Appl. Catal. B: Environ.*, 203 (2017) 839-850.
- [26] O.Y. Gutiérrez, G.A. Fuentes, C. Salcedo, T. Klimova, SBA-15 supports modified by Ti and Zr grafting for NiMo hydrodesulfurization catalysts, *Catal. Today*, 116 (2006) 485-497.
- [27] D. Gao, A. Duan, X. Zhang, Z. Zhao, E. Hong, J. Li, H. Wang, Synthesis of NiMo catalysts supported on mesoporous Al-SBA-15 with different morphologies and their catalytic performance of DBT HDS, *Appl. Catal. B: Environ.*, 165 (2015) 269-284.
- [28] S. Higashimoto, Y. Hu, R. Tsumura, K. Iino, M. Matsuoka, H. Yamashita, Y.G. Shul, M. Che, M. Anpo, Synthesis, characterization and photocatalytic reactivities of Mo-MCM-41 mesoporous molecular sieves: Effect of the Mo content on the local structures of Mo-oxides, *J. Catal.*, 235 (2005) 272-278.
- [29] C. Lepetit, M. Che, Discussion on the coordination of Ni²⁺ ions to lattice oxygens in calcined faujasite-type zeolites followed by diffuse reflectance spectroscopy, *J. Phys. Chem.*, 100 (1996) 3137-3143.

Predicting Catalytic Activity from Oxidic Precursor Properties

- [30] G.R. Rossman, R.D. Shannon, R.K. Waring, Origin of the yellow color of complex nickel oxides, *J. Solid State Chem.*, 39 (1981) 277-287.
- [31] L. van Haandel, G.M. Bremmer, E.J.M. Hensen, Th. Weber, The effect of organic additives and phosphoric acid on sulfidation and activity of (Co)Mo/Al₂O₃ hydrodesulfurization catalysts, *J. Catal.*, 351 (2017) 95-106.
- [32] D.G. Barton, M. Shtein, R.D. Wilson, S.L. Soled, E. Iglesia, Structure and electronic properties of solid acids based on tungsten oxide nanostructures, *J. Phys. Chem. B*, 103 (1999) 630-640.
- [33] S. Badoga, K.C. Mouli, K.K. Soni, A.K. Dalai, J. Adjaye, Beneficial influence of EDTA on the structure and catalytic properties of sulfided NiMo/SBA-15 catalysts for hydrotreating of light gas oil, *Appl. Catal. B: Environ.*, 125 (2012) 67-84.
- [34] H. Tian, C.A. Roberts, I.E. Wachs, Molecular structural determination of molybdena in different environments: Aqueous solutions, bulk mixed oxides, and supported MoO₃ catalysts, *J. Phys. Chem.*, 114 (2010) 14110-14120.
- [35] A.G. Kalampounias, G. Tsilomelekis, R.W. Berg, S. Boghosian, Molybdenum (VI) oxosulfato complexes in MoO₃-K₂S₂O₇-K₂SO₄ molten mixtures: Stoichiometry, vibrational properties, and molecular structures, *J. Phys. Chem.*, 116 (2012) 8861-8872.
- [36] G. Deo, I.E. Wachs, Predicting molecular structures of surface metal oxide species on oxide supports under ambient conditions, *J. Phys. Chem.*, 95 (1991) 5889-5895.
- [37] J. Moreau, O. Delpoux, E. Devers, M. Digne, S. Loricant, Impregnation of decamolybdocobaltate heteropolyanions over γ -alumina: detailed description of the physico-chemical phenomena, *Langmuir*, 29 (2013) 207-215.
- [38] V. La Parola, G. Deganello, C.R. Tewell, A.M. Venezia, Structural characterisation of silica supported CoMo catalysts by UV Raman spectroscopy, XPS and X-ray diffraction techniques, *Appl. Catal. A: Gen.*, 235 (2002) 171-180.
- [39] G. Mestl, T.K.K. Srinivasan, Raman spectroscopy of monolayer-type catalysts: supported molybdenum oxides, *Catal. Rev.*, 40 (1998) 451-570.
- [40] Z. Wei, C. Wei, Q. Xin, Study of the Reducing and Sulfiding Process of Mo-Supported Catalyst by in situ LRS [J], *Acta Physico-Chimica Sinica*, 10 (1994) 402-408.
- [41] M.A. Vuurman, I.E. Wachs, In situ Raman spectroscopy of alumina-supported metal oxide catalysts, *J. Phys. Chem.*, 96 (1992) 5008-5016.
- [42] S.C. Chang, M.A. Leugers, S.R. Bare, Surface chemistry of magnesium oxide-supported molybdenum oxide: an in situ Raman spectroscopic study, *J. Phys. Chem.*, 96 (1992) 10358-10365.
- [43] A. Guevara-Lara, A. López-Benítez, G. Berhault, J.A. Melo-Banda, R. Silva-Rodrigo, Addition of cerium to alumina-supported NiMo catalysts for dibenzothiophene hydrodesulfurization application, *Top. Catal.*, 65 (2022) 1286-1300.
- [44] P. Arnoldy, M.C. Franken, B. Scheffer, J.A. Moulijn, Temperature-programmed reduction of CoO-MoO₃/Al₂O₃ catalysts, *J. Catal.*, 96 (1985) 381-395.
- [45] H. Kim, J.J. Lee, S.H. Moon, Hydrodesulfurization of dibenzothiophene compounds using fluorinated NiMo/Al₂O₃ catalysts, *Appl. Catal. B: Environ.*, 44 (2003) 287-299.
- [46] V. Zuzaniuk, R. Prins, Synthesis and characterization of silica-supported transition-metal phosphides as HDN catalysts, *J. Catal.*, 219 (2003) 85-96.
- [47] B. Guichard, M. Roy-Auberger, E. Devers, C. Legens, P. Raybaud, Aging of Co(Ni)MoP/Al₂O₃ catalysts in working state, *Catal. Today*, 130 (2008) 97-108.
- [48] B.W. Hoffer, A.D. van Langeveld, J.-P. Janssens, R.L.C. Bonn , C.M. Lok, J.A. Moulijn, Stability of highly dispersed Ni/Al₂O₃ catalysts: effects of pretreatment, *J. Catal.*, 192 (2000) 432-440.
- [49] J. Escobar, M.C. Barrera, J.A. Toledo, M.A. Cort s-J come, C. Angeles-Ch vez, S. N n ez, V. Santes, E. G mez, L. D az, E. Romero, J.G. Pacheco, Effect of ethyleneglycol addition on the properties

Chapter 5

of P-doped NiMo/Al₂O₃ HDS catalysts: Part I. Materials preparation and characterization, Appl. Catal. B: Environ., 88 (2009) 564-575.

[50] Th. Weber, J.A.R. van Veen, A density functional theory study of the hydrodesulfurization reaction of dibenzothiophene to biphenyl on a single-layer NiMoS cluster, Catal. Today, 130 (2008) 170-177.

[51] H. Farag, D.D. Whitehurst, K. Sakanishi, I. Mochida, Carbon versus alumina as a support for Co-Mo catalysts reactivity towards HDS of dibenzothiophenes and diesel fuel, Catal. Today, 50 (1999) 9-17.

[52] A. Wang, Y. Wang, T. Kabe, Y. Chen, A. Ishihara, W. Qian, Hydrodesulfurization of dibenzothiophene over siliceous MCM-41-supported catalysts: I. Sulfided Co-Mo catalysts, J. Catal., 199 (2001) 19-29.

[53] C. Liu, J. Mei, G. Wang, J. Chang, Q. Meng, D. Hu, C. Xiao, Y. Shi, A. Duan, Y. Gong, Tailoring NiMoS active phases with high hydrodesulfurization activity through facilely synthesized supports with tunable mesostructure and morphology, J. Catal., 387 (2020) 170-185.

[54] L. Qu, W. Zhang, P.J. Kooyman, R. Prins, MAS NMR, TPR, and TEM studies of the interaction of NiMo with alumina and silica-alumina supports, J. Catal., 215 (2003) 7-13.

[55] Y. Ji, Z. Zhao, A. Duan, G. Jiang, J. Liu, Comparative study on the formation and reduction of bulk and Al₂O₃-supported cobalt oxides by H₂-TPR technique, J. Phys. Chem. C, 113 (2009) 7186-7199.

[56] E.J.M. Hensen, P.J. Kooyman, Y. van der Meer, A.M. van der Kraan, V.H.J. de Beer, J.A.R. van Veen, R.A. van Santen, The relation between morphology and hydrotreating activity for supported MoS₂ particles, J. Catal., 199 (2001) 224-235.

[57] Z. Liu, W. Han, D. Hu, S. Sun, A. Hu, Z. Wang, Y. Jia, X. Zhao, Q. Yang, Effects of Ni-Al₂O₃ interaction on NiMo/Al₂O₃ hydrodesulfurization catalysts, J. Catal., 387 (2020) 62-72.

5.7. Appendix C

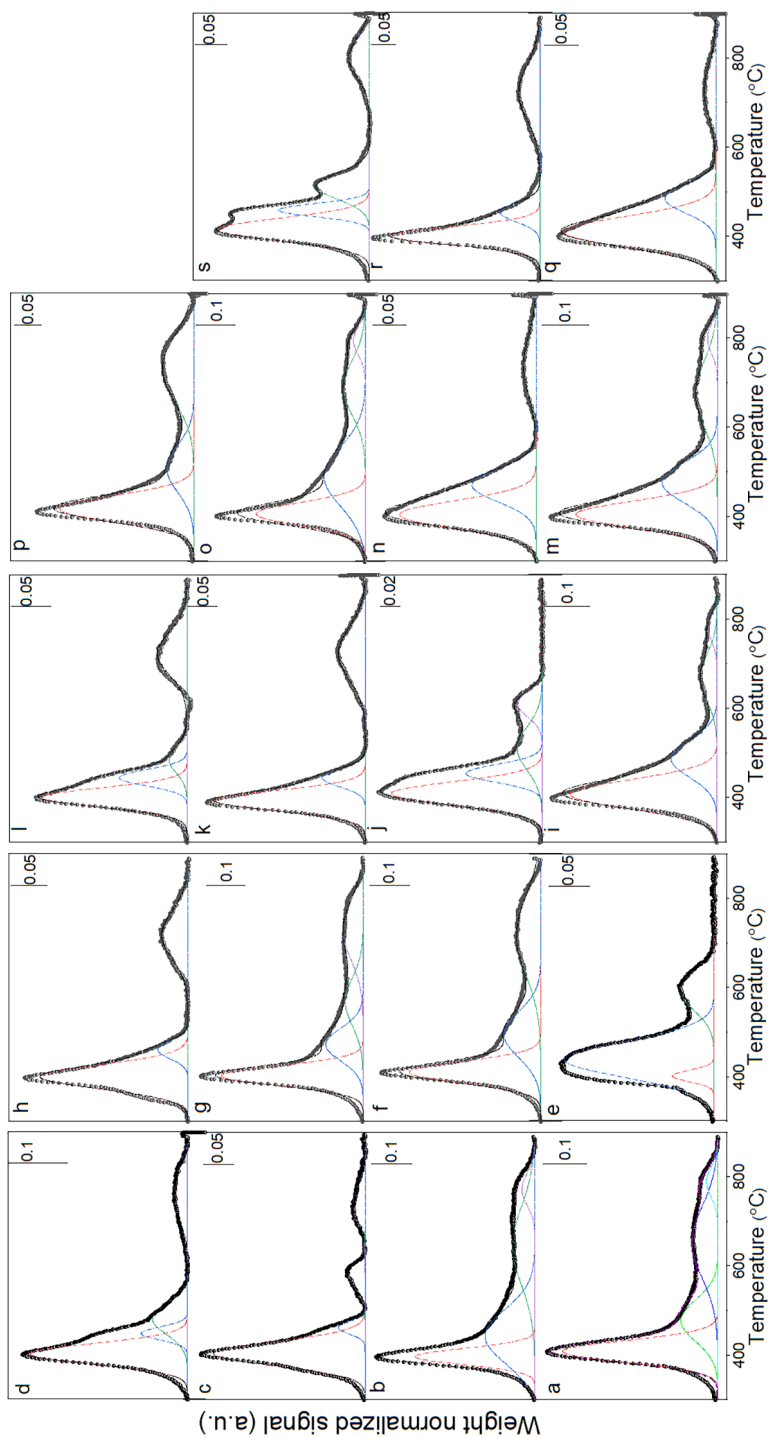


Figure C1. Deconvolution analysis of the TPR profile of a) dr/AHM b) ca/AHM c) $CA(1.2)/AHM$ d) $EG(1.2)/AHM$ e) $NTA(1.2)/AHM$ f) dr/MoO_3 g) ca/MoO_3 h) $CA(1.2)/MoO_3$ i) $EG(1.2)/MoO_3$ j) $NTA(1.2)/MoO_3$ k) $MA(1.2)/MoO_3$ l) $NTA(0.6)/MoO_3$ m) $GA(0.6)/MoO_3$ n) $TEG(0.6)/MoO_3$ o) $EG(0.6)/MoO_3$ p) $MA(0.6)/MoO_3$ q) $TEG(1.2)/MoO_3$ r) $CA(0.6)/MoO_3$ s) $MA(1.2)/AHM$.

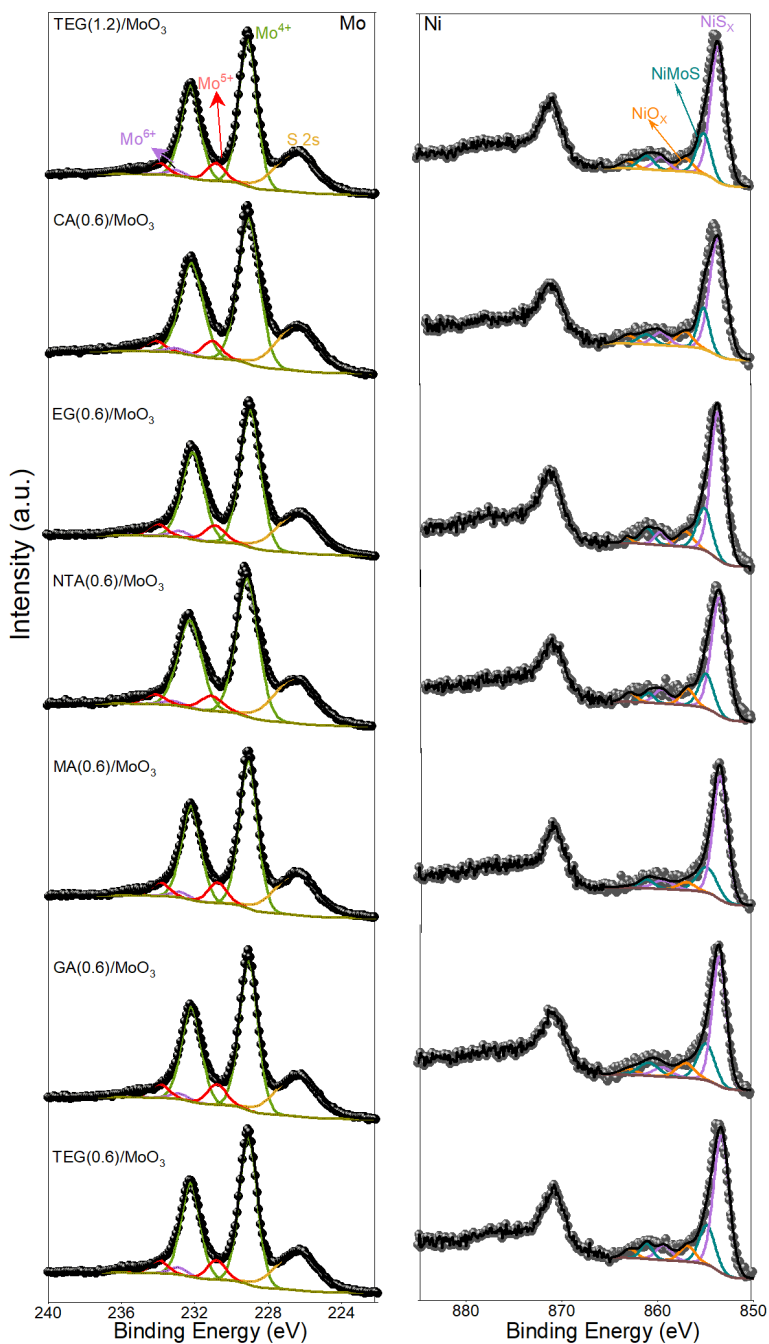


Figure C2. Mo 3d and Ni 2p XPS spectra of catalysts sulfided at 350 °C in 1 bar H₂S/H₂. The Mo 3d fits are composed of Mo⁴⁺ (green), Mo⁵⁺ (red), Mo⁶⁺ (purple), as well as of the S 2s signal (yellow). Ni 2p _{3/2} fits are composed of Ni²⁺ as in NiS (purple), NiMoS (blue), and NiO (orange). The background is represented by a black line.

Chapter 6

A non-boehmite derived γ -alumina and its utilization in HDS catalysis

ABSTRACT

A self-made alumina ($\text{Al}_2\text{O}_3(\text{self-made})$) was successfully prepared by a one-step grinding synthesis route. The NiMo/ Al_2O_3 catalyst prepared with $\text{Al}_2\text{O}_3(\text{self-made})$ as support presents a comparable performance with the one possessing identical formulation but prepared with $\text{Al}_2\text{O}_3(\text{commercial})$ as support. g- $\text{Ni}_{2.9}\text{Mo}_{6.7}$, catalyst with metal loading of 6.7 wt% Mo, 2.9 wt% Ni, was prepared by the grinding method, where the Ni and Mo sources were in situ incorporated during the preparation of alumina. The metal loadings are the highest metal amount can be incorporated into the scheme of alumina with grinding method. For comparison, sample i- $\text{Ni}_{2.9}\text{Mo}_{6.7}$ with the same metal loadings supported on $\text{Al}_2\text{O}_3(\text{self-made})$ was prepared by incipient wetness impregnation. The characterization results indicate that compared to g- $\text{Ni}_{2.9}\text{Mo}_{6.7}$, there is a weaker metal-support interaction in i- $\text{Ni}_{2.9}\text{Mo}_{6.7}$, which promotes the metal dispersion on the alumina carrier and the formation of active NiMoS phase during the sulfidation. The structural difference between these two catalysts explains why i- $\text{Ni}_{2.9}\text{Mo}_{6.7}$ has a higher HDS activity than g- $\text{Ni}_{2.9}\text{Mo}_{6.7}$. To optimize these two catalysts, g- $\text{Ni}_{2.9}\text{Mo}_{6.7}+\text{i-Ni}_{0.77}\text{Mo}_{8.3}$ and i- $\text{Ni}_{2.9}\text{Mo}_{6.7}+\text{i-Ni}_{0.77}\text{Mo}_{8.3}$ with higher metal loadings were prepared by a two-step impregnation. The activity data shows that the DBT conversion increased for catalysts with higher metal loadings; however, no intrinsic activity of Mo increase was observed. g- $\text{Ni}_{2.9}\text{Mo}_{6.7}+\text{i-Ni}_{0.77}\text{Mo}_{8.3}$ and g- $\text{Ni}_{2.9}\text{Mo}_{6.7}$ show the same turnover frequency of 0.025 s^{-1} ; i- $\text{Ni}_{2.9}\text{Mo}_{6.7}+\text{i-Ni}_{0.77}\text{Mo}_{8.3}$ shows a lower turnover frequency (0.051 s^{-1}) than i- $\text{Ni}_{2.9}\text{Mo}_{6.7}$ (0.060 s^{-1}). The more active NiMoS phase in i- $\text{Ni}_{2.9}\text{Mo}_{6.7}+\text{i-Ni}_{0.77}\text{Mo}_{8.3}$ is the reason for its high activity. However, the reason for the varying effect of second-step impregnation still needs to be clarified, as the content and the activity of the active NiMoS phase changed during the second-step impregnation.

Chapter 6

6.1. Introduction

With rigorous emission control for automobiles, the oil industry is producing ultra-low sulfur diesel fuel (ULSD), which is a cleaner fuel only containing a maximum of 10 ppm of sulfur [1]. This level will likely be further decreased by environmental legislation in subsequent years. The increasing demand for low-sulfur fuels puts pressure on the development of highly active catalysts [2].

Ni-promoted $\text{MoS}_2/\text{Al}_2\text{O}_3$ catalysts are the most extensively used hydrodesulfurization (HDS) catalysts in the refining industry [3-5], and $\gamma\text{-Al}_2\text{O}_3$ is one of the commonly used supports due to its low price and outstanding textural and mechanical properties [6]. Typically, $\gamma\text{-Al}_2\text{O}_3$ is prepared through thermal dehydration of well-defined boehmite at a temperature between 400 and 450 °C [7], which results in the low surface area (less than 250 m^2/g) and a small pore volume (less than 0.5 cm^3/g) of the commercial $\gamma\text{-Al}_2\text{O}_3$ [8]. To prepare the high-surface-area alumina ($S_{\text{BET}} > 250 \text{ m}^2/\text{g}$) with adjustable pore structure, different preparation methods, such as the sol-gel routes [9, 10], templating [11-14], have been employed. Ji et al. [15] synthesized a high-surface-area alumina (552 – 560 m^2/g) via a sol-gel route. Ionic surfactants (carboxylic acid, sodium dodecyl sulfate) and neutral surfactants (polypropylene oxide) [13, 16, 17] have been used as chemical templates in the preparation of mesoporous alumina. Thermal decomposition of alumina precursors is also a practical way to synthesize $\gamma\text{-Al}_2\text{O}_3$, Hu et al. [18] successfully prepared a $\gamma\text{-Al}_2\text{O}_3$ with a surface area of 511 m^2/g by the thermal decomposition of ammonium aluminum carbonate hydroxide ($\text{NH}_4\text{AlO}(\text{OH})\text{HCO}_3$).

Supported HDS catalysts are commonly prepared by a conventional wetness impregnation method [19-22], where the active metal species are simultaneously or sequentially loaded on the premade support. Hydrothermal deposition [23] and sol-gel synthesis [24, 25] are the other two widely used methods to prepare HDS catalysts. However, a complicated and time-consuming process is always required for these methods, and the active metal species tend to agglomerate into large crystallites on the support surface. In the past few years, synthesizing supported catalysts by a one-step preparation route has attracted considerable interest [26]. Comparing to impregnation, the one-step preparation route is favorable for even dispersion of metallic species, since metal precursor can be incorporated during the preparation of support. Lai et al. [27] prepared a highly dispersed bimetallic $\text{NiMo-Al}_2\text{O}_3$ catalyst by an efficient one-step synthesis method, where they used urea as precipitant and starch as template, and the catalyst showed an excellent dibenzothiophene (DBT) HDS activity. Liu et al. [28] synthesized an ordered mesoporous $\text{NiMo-Al}_2\text{O}_3$ catalyst by a facile one-step evaporation-induced self-assembly method with the non-ionic tri-block polymer P123 as a structure-directing agent and anhydrous ethanol as solvent. They claimed that this catalyst

A non-boehmite derived γ -alumina and its utilization in HDS catalysis

showed a high HDS activity. Mesoporous NiMo- Al_2O_3 catalysts were synthesized by Tu et al. [29] by a single-step preparation method without using any structure-directing agent, and used in the quinoline hydrodenitrogenation (HDN) test. They believed that the textural properties and metal-support interaction in NiMo catalysts could be controlled by adjusting the hydrolysis process. By using chelate additives, they concluded that the catalytic HDN performance was selective to the agglomeration of Mo species. Li et al. [30] synthesized a NiMo/ Al_2O_3 catalyst via a solvent-free one-step synthesis method. They studied the effect of polyethylene glycol (PEG) on the precursor thermal decomposition. They noticed that with the increase of PEG, the specific surface area and pore volume of the catalyst increased, which benefited the sulfidation and Mo species and the dispersion of MoS_2 , which consequently led to higher activity.

In this work, a self-made alumina ($\text{Al}_2\text{O}_3(\text{self-made})$) was synthesized by a one-step preparation route. g- $\text{Ni}_{2.9}\text{Mo}_{6.7}$ was synthesized by the same one-step grinding route based on in situ incorporating Ni and Mo during Al_2O_3 preparation. For comparison, i- $\text{Ni}_{2.9}\text{Mo}_{6.7}$ with the same composition was synthesized by incipient wetness impregnation with $\text{Al}_2\text{O}_3(\text{self-made})$ as support. To optimize these two catalysts, g- $\text{Ni}_{2.9}\text{Mo}_{6.7}+\text{i-Ni}_{0.77}\text{Mo}_{8.3}$ and i- $\text{Ni}_{2.9}\text{Mo}_{6.7}+\text{i-Ni}_{0.77}\text{Mo}_{8.3}$ were prepared by a two-step impregnation. We studied the effect of preparation workflow and the two-step impregnation on the catalysts' structure and activity. The structure of these catalysts was characterized by means of temperature programmed reduction (TPR), UV-visible diffuse reflectance spectroscopy (UV-vis DRS), Raman spectroscopy, X-ray diffraction (XRD), X-ray photoelectron spectroscopy (XPS), and transmission electron microscopy (TEM). The catalytic activity of catalysts was evaluated in the HDS of thiophene and DBT.

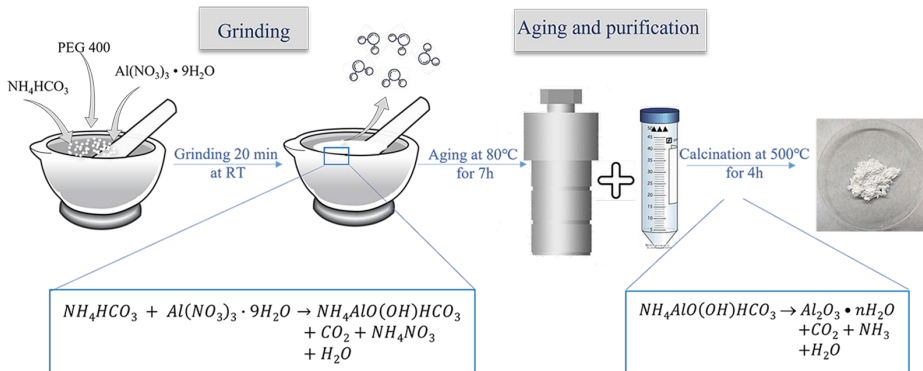
6.2. Experimental section

6.2.1. Catalyst preparation

Self-made alumina ($\text{Al}_2\text{O}_3(\text{self-made})$) was prepared by decomposing ammonium aluminum carbonate hydroxide ($\text{NH}_4\text{AlO}(\text{OH})\text{HCO}_3$, AACH) using a one-step preparation route [18]. The whole procedure is illustrated in Scheme 6.1. In detail, 0.2 mL of PEG-400 were fully mixed with 15.8 g NH_4HCO_3 in an agate mortar. 18.8 g $\text{Al}(\text{NO}_3)_3 \cdot 9\text{H}_2\text{O}$ was added into above mixture and ground for another 30 min. The chemical reaction between $\text{Al}(\text{NO}_3)_3 \cdot 9\text{H}_2\text{O}$ and NH_4HCO_3 occurred during grinding, yielding AACH, CO_2 , and NH_4NO_3 . The obtained white moist paste was transferred into a Teflon-lined stainless-steel autoclave and aged at 80 °C for 7 h. The solid precipitation was washed with deionized water and ethanol for three times and centrifuged to remove the impurities, followed by drying at 80 °C in a vacuum oven for 3 h,

Chapter 6

AACH was formed (Figure D1). After calcining at 500 °C under air for 4 h, Al₂O₃(self-made) was obtained.



g-Ni_{2.9}Mo_{6.7} was synthesized using the same one-step preparation method based on in situ incorporating Mo and Ni precursors during the preparation of Al₂O₃(self-made). In detail, 0.2 mL PEG-400 was fully mixed with 15.8 g NH₄HCO₃ in an agate mortar. 18.8 g Al(NO₃)₃·9H₂O, 0.4 g (NH₄)₆Mo₇O₂₄·4H₂O (AHM), and 0.4 g Ni(NO₃)₂·6H₂O were added into above mixture and ground for another 30 min. Following by the same aging, washing, drying and calcination procedures as described above, g-Ni_{2.9}Mo_{6.7} with metal loadings of 6.7 wt% Mo, 2.9 wt% Ni (highest metals amount can be incorporated into alumina structure) was obtained. i-Ni_{2.9}Mo_{6.7} with the same metal loading was prepared via incipient wetness impregnation with Al₂O₃(self-made) (75 – 125 μm) as support. The impregnation solution was prepared by dissolving 0.8 g AHM and 0.9 g Ni(NO₃)₂ in a 2 mL mixture of deionized water and ammonium hydroxide. The final volume of the impregnation solution was adjusted to 5 mL according to the PV of 5.3 g Al₂O₃(self-made). After impregnation, the precursors were kept for 2 h under slow movement on a roller bank and subsequently dried at 120 °C overnight. After calcination at 400 °C for 2 h, i-Ni_{2.9}Mo_{6.7} was obtained.

Two NiMo/Al₂O₃ catalysts (i-Ni_{2.9}Mo_{6.7}+i-Ni_{0.77}Mo_{8.3} and g-Ni_{2.9}Mo_{6.7}+i-Ni_{0.77}Mo_{8.3}) with higher metal loadings (15 wt% Mo, 3.67 wt% Ni) were synthesized by impregnating g-Ni_{2.9}Mo_{6.7} (PV = 1.06 cm³/g, 75 – 125 μm) and i-Ni_{2.9}Mo_{6.7} (PV = 0.5 cm³/g, 75 – 125 μm) with respective impregnation solutions containing Mo and Ni. To impregnate 4.8 g g-Ni_{2.9}Mo_{6.7}, 5 mL solution containing 0.7 g AHM and 0.2 g Ni(NO₃)₂ was prepared. 5 mL impregnation solution containing 1.5 g AHM and 0.4 g Ni(NO₃)₂ was prepared to impregnate 10 g i-Ni_{2.9}Mo_{6.7}. After drying at 120 °C overnight and calcined at 400 °C for 2 h, the catalysts were obtained. The final metal loadings of catalysts were determined by inductively coupled plasma optical emission spectroscopy (ICP-OES), and the results are displayed in Table 6.1.

A non-boehmite derived γ -alumina and its utilization in HDS catalysis

6.2.2. Catalyst activation

To prepare the sulfided sample, ca. 50 mg oxidic precursors (75 – 125 μm) were loaded in the middle of a valve-sealed stainless-steel reactor (inner diameter: 4 mm, length: 240 mm) and heated up to 350 °C with a 6 °C/min ramp rate under 1 bar $\text{H}_2\text{S}/\text{H}_2$ (10/90 vol%) at a flow rate of 50 mL/min. The sample was kept under these conditions for 2 h and subsequently cooled to room temperature under a He atmosphere. Sulfided samples were then transferred to a N_2 -filled glovebox ($\text{O}_2 < 1$ ppm, $\text{H}_2\text{O} < 1$ ppm) without exposure to air for further characterization.

6.2.3. Catalytic activity measurement

Gas-phase thiophene and liquid-phase DBT HDS tests were conducted to determine catalyst activity. Reaction procedures and data processing details are listed in section 2.3, Chapter 2.

6.2.4. Catalyst characterization

N_2 adsorption isotherms were measured at 79 K on a Micromeritics Tristar 3020 instrument. Before analysis, samples were heated at 120 °C under N_2 atmosphere for at least 6 h. TPR, Raman, UV-vis DRS, XRD, XPS, and TEM were performed according to the procedures described in Chapter 2.

NMR spectroscopy. The ^{27}Al magic-angle spinning nuclear magnetic resonance (MAS NMR) spectra of Al_2O_3 (self-made) and Al_2O_3 (commercial) were measured at room temperature with a 11.7 T Bruker DMX500 NMR spectrometer, operated at 132 MHz. The spectra were recorded with a spinning rate of 25 kHz and a single excitation pulse length of 1 μs with a 1 s repetition time. Before measurement, the sample was fully hydrated in a desiccator containing water vapor.

IR spectroscopy. IR spectra of Al_2O_3 (self-made) and Al_2O_3 (commercial) were recorded in the range of 4000 – 400 cm^{-1} on a Bruker Vertex 70v spectrometer equipped with a Mercury-Cadmium-Telluride (MCT) detector. The spectra were collected at a 2 cm^{-1} resolution and 64 scans. A self-supporting wafer of the sample with a diameter of 13 mm was made by pressing ca. 10 mg powdered samples with a certain pressure. Prior to the recording of the background, the cell was calcined at 400 °C for 4 h and vacuumed for 2 h. Sample wafers were dehydrated at 400 °C in O_2/He (33 vol%) for 1 h, then vacuum the cell at 400 °C for 1 h. After cooling the cell to 30 °C under dynamic vacuum, the spectra were recorded.

6.3. Results and discussion

6.3.1. Alumina

Chapter 6

The textural properties of Al_2O_3 (self-made) and Al_2O_3 (commercial) were measured using N_2 physisorption. As data in Table 6.1 and Figure D2 show, Al_2O_3 (self-made) has a lower surface area, a comparable pore volume and a larger pore size than Al_2O_3 (commercial). Figure 6.1 shows the XRD patterns of Al_2O_3 (self-made) and Al_2O_3 (commercial), where a typical characteristic of $\gamma\text{-Al}_2\text{O}_3$ (JCPDS 01-077-0396) with four broad diffraction peaks located at $2\theta = 37.7^\circ$, 39.5° , 45.9° , and 66.9° is observed in both catalysts. Compared to Al_2O_3 (commercial), Al_2O_3 (self-made) has lower peak intensities, indicating lower crystallinity of Al_2O_3 (self-made).

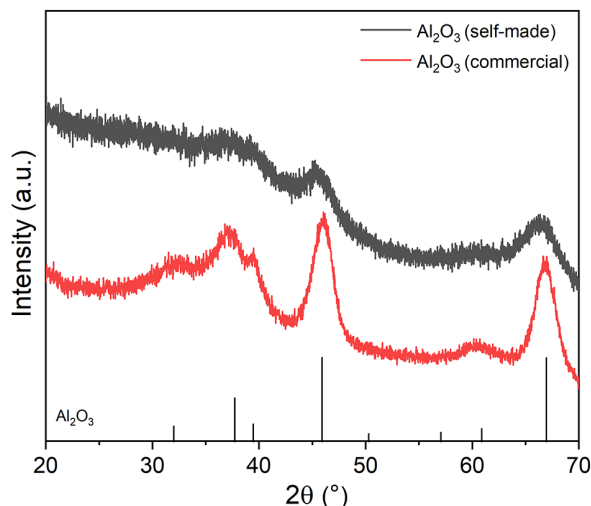


Figure 6.1. XRD patterns of Al_2O_3 (commercial) and Al_2O_3 (self-made).

The nature of hydroxyl groups on Al_2O_3 (self-made) and Al_2O_3 (commercial) was investigated using IR spectroscopy. As shown in Figure 6.2a, three intense bands at 3590 cm^{-1} , 3675 cm^{-1} , 3730 cm^{-1} , and two shoulders at 3755 cm^{-1} and 3770 cm^{-1} , are detected in Al_2O_3 (commercial). Bands at 3770 cm^{-1} and 3755 cm^{-1} can be assigned to the $\nu(\text{OH})$ stretching vibration of OH groups that are terminally connected to Al^{3+} in tetrahedral or octahedral coordination (I_a and I_b configurations) as illustrated in Figure D3. The band at 3730 cm^{-1} is attributed to the $\nu(\text{OH})$ stretching mode of bridging OH groups, in which the OH groups are connected to two Al^{3+} species respectively in tetrahedra or octahedral coordination (II_a type) or connected to two Al^{3+} species in octahedral coordination (II_b type). While the bands at 3590 cm^{-1} and 3675 cm^{-1} are attributed to $\nu(\text{OH})$ stretching mode of the bridging OH groups (III type) [31-34]. Bands at 3675 cm^{-1} , 3730 cm^{-1} , and 3770 cm^{-1} are observed in Al_2O_3 (self-made). We deconvoluted the hydroxyl region of the IR spectra to reveal more details regarding the composition of OH groups. As shown in Figure 6.2b, four OH groups with relatively different contributions are discovered. The proportion of the band at 3770 cm^{-1} in Al_2O_3 (self-made) is 2.6 %, while the number in Al_2O_3 (commercial) is 7.8 %,

A non-boehmite derived γ -alumina and its utilization in HDS catalysis

indicating relatively less tetrahedral coordinated alumina exists in Al_2O_3 (self-made). This conclusion is supported by NMR results (Figure 6.3), where six(IV)- and four(IV)-coordinated Al at 8 and 66 ppm with a relative 64 % and 36 % amount are detected in Al_2O_3 (commercial) [35]. The relative amount of Al(IV) and Al(VI) in Al_2O_3 (self-made), however, is 17.1 % and 70.1 %, and the lower Al(IV) in Al_2O_3 (self-made) is due to the presence of Al(V) (at 35 ppm). Al(V) was further verified with ^{27}Al MQ MAS NMR spectra (Figure D4), and compared to Al_2O_3 (commercial), the presence of Al(V) (12.8 %) in Al_2O_3 (self-made) comes at the expense of Al(IV).

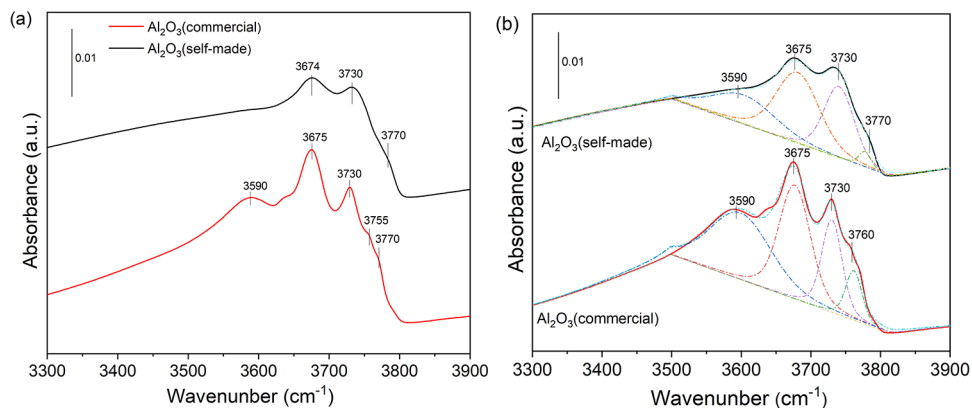


Figure 6.2. Hydroxyl regions of FTIR spectra of Al_2O_3 (commercial) and Al_2O_3 (self-made) (spectra are normalized by the weight of samples).

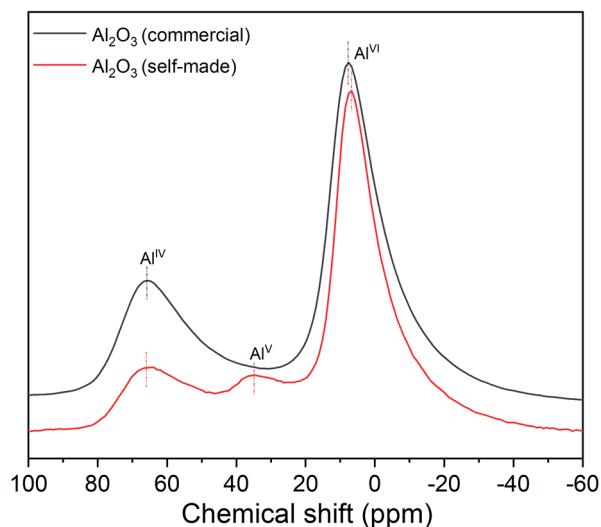


Figure 6.3. ^{27}Al MAS spectra of hydrated Al_2O_3 (commercial) and Al_2O_3 (self-made).

To evaluate the influence of the structure of alumina on catalyst activity, two catalysts, $\text{NiMo-PA}^{\text{dr}}/\text{Al}_2\text{O}_3$ (commercial) and $\text{NiMo-PA}^{\text{dr}}/\text{Al}_2\text{O}_3$ (self-made), with the same overall compositions were prepared using Al_2O_3 (self-made) and Al_2O_3 (commercial) as support.

Chapter 6

These two catalysts have comparable metal loadings (Table 6.1) and metal dispersions (Figure D5). As shown in the XRD patterns (Figure D5), only four diffraction peaks located at $2\theta = 37.7^\circ, 39.5^\circ, 45.9^\circ, 66.9^\circ$ attributed to the characteristic of $\gamma\text{-Al}_2\text{O}_3$ are observed. The absence of XRD signals of Mo and Ni oxides indicates that their particle sizes are below the detection limit of XRD, evidencing that Mo and Ni oxides are well dispersed on the alumina carrier [36]. However, a clear difference in crystallinity between these two catalysts is observed. NiMo-PA^{dr}/Al₂O₃(commercial) shows a higher peak intensity, i.e., higher crystallinity, than NiMo-PA^{dr}/Al₂O₃(self-made). This crystallinity difference is consistent with the previously observed crystallinity difference between two bare alumina, suggesting impregnation had negligible effect on the structure of the alumina carrier.

The HDS activity of NiMo-PA^{dr}/Al₂O₃(commercial) and NiMo-PA^{dr}/Al₂O₃(self-made) was evaluated in the DBT HDS. Table 6.2 shows that NiMo-PA^{dr}/Al₂O₃(commercial) has a comparable reaction rate and selectivity as NiMo-PA^{dr}/Al₂O₃(self-made), where the direct desulfurization (DDS) pathway with biphenyl (BP) as the main product is the main reaction pathway in both catalysts. Based on the activity data, we infer that Al₂O₃(self-made) performs equally well as Al₂O₃(commercial) as the carrier.

Table 6.2. DBT HDS results of NiMo-PA^{dr}/Al₂O₃(self-made) and NiMo-PA^{dr}/Al₂O₃(commercial).

Catalyst	DBT					
	Reaction temperature	Reaction rates (mol mol _{Mo} ⁻¹ h ⁻¹)	Selectivity			Conversion
		k _{HDS}	BP	CHB	DDS : HYD	X (%)
NiMo-PA ^{dr} /Al ₂ O ₃ (self-made)	250 °C	14.7	66.9	33.1	2.0	32.8
	270 °C	29.3	62.3	37.7	1.7	54.8
	300 °C	360.8	58.3	41.7	1.4	100.0
NiMo-PA ^{dr} /Al ₂ O ₃ (commercial)	250 °C	18.4	67.0	33.0	2.0	35.4
	270 °C	48.6	63.6	36.4	1.7	68.4
	300 °C	413.3	52.4	47.6	1.1	100.0

6.3.2. Alumina supported catalysts

g-Ni_{2.9}Mo_{6.7} was synthesized by this one-step synthesis route with metal sources in situ incorporated during the preparation of Al₂O₃(self-made). For comparison, i-Ni_{2.9}Mo_{6.7} with the same metal loadings was prepared by an incipient wetness impregnation. g-Ni_{2.9}Mo_{6.7}+i-Ni_{0.77}Mo_{8.3} and i-Ni_{2.9}Mo_{6.7}+i-Ni_{0.77}Mo_{8.3} were synthesized by a two-step impregnation with extra metals deposition.

ICP-OES (Table 6.1) results show that metal loadings in g-Ni_{2.9}Mo_{6.7}, i-Ni_{2.9}Mo_{6.7}, and i-Ni_{2.9}Mo_{6.7}+i-Ni_{0.77}Mo_{8.3} are close to the theoretical values. While the molar ratio of Ni/Mo in g-Ni_{2.9}Mo_{6.7}+i-Ni_{0.77}Mo_{8.3} is slightly lower, and the reason for this difference needs to be further explored. Physisorption data in Figure D6 show that these four samples have type IV isotherms. g-Ni_{2.9}Mo_{6.7} and i-Ni_{2.9}Mo_{6.7} have comparable surface areas, which both decreased

A non-boehmite derived γ -alumina and its utilization in HDS catalysis

to a varying degree with further metal deposition as expected. Pore size distribution derived from the adsorption branch of isotherms shows that $g\text{-Ni}_{2.9}\text{Mo}_{6.7}$ and $g\text{-Ni}_{2.9}\text{Mo}_{6.7}+i\text{-Ni}_{0.77}\text{Mo}_{8.3}$ have a relatively larger pore size than their counterpart catalysts, $i\text{-Ni}_{2.9}\text{Mo}_{6.7}$ and $i\text{-Ni}_{2.9}\text{Mo}_{6.7}+i\text{-Ni}_{0.77}\text{Mo}_{8.3}$.

Figure 6.4 shows the XRD patterns of these four catalysts, where except for three broad diffraction peaks located at $2\theta = 37.7^\circ$, 45.9° , and 66.9° attributed to the (311), (400), and (440) planes of $\gamma\text{-Al}_2\text{O}_3$ (JCPDS 01-077-0396) [37], no diffraction signals of Mo and Ni species are identified, suggesting the high dispersion of metal oxides on the alumina carrier. Compared to $i\text{-Ni}_{2.9}\text{Mo}_{6.7}$ and $i\text{-Ni}_{2.9}\text{Mo}_{6.7}+i\text{-Ni}_{0.77}\text{Mo}_{8.3}$ (Figure 6.4b), $g\text{-Ni}_{2.9}\text{Mo}_{6.7}$, and $g\text{-Ni}_{2.9}\text{Mo}_{6.7}+i\text{-Ni}_{0.77}\text{Mo}_{8.3}$ (Figure 6.4a) show a relatively lower peak intensity. The low crystallinity in $g\text{-Ni}_{2.9}\text{Mo}_{6.7}$ and $g\text{-Ni}_{2.9}\text{Mo}_{6.7}+i\text{-Ni}_{0.77}\text{Mo}_{8.3}$ is possibly because during the co-grinding (one-step preparation route) process, Mo atoms might dope into the structure of alumina and changed its crystallinity. With the two-step impregnation, metal redispersion occurred and the crystallinity of $g\text{-Ni}_{2.9}\text{Mo}_{6.7}+i\text{-Ni}_{0.77}\text{Mo}_{8.3}$ did slightly increased.

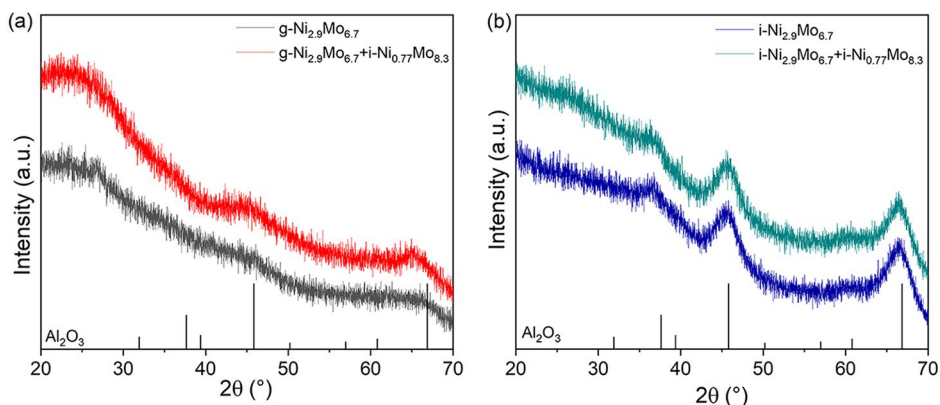


Figure 6.4. XRD patterns of oxidic precursors of a) $g\text{-Ni}_{2.9}\text{Mo}_{6.7}+i\text{-Ni}_{0.77}\text{Mo}_{8.3}$, $g\text{-Ni}_{2.9}\text{Mo}_{6.7}$ and b) $i\text{-Ni}_{2.9}\text{Mo}_{6.7}$, $i\text{-Ni}_{2.9}\text{Mo}_{6.7}+i\text{-Ni}_{0.77}\text{Mo}_{8.3}$.

TPR profiles of these four catalysts are presented in Figure 6.5. Three broad peaks centered at 350°C , 570°C , and 710°C were observed in the spectrum of $i\text{-Ni}_{2.9}\text{Mo}_{6.7}$. According to literature, the peak at 380°C is assigned the reduction of Mo^{6+} to Mo^{4+} [38, 39]. The features in the high-temperature area are attributed to the deep reduction of all other Mo species, including tetrahedrally coordinated Mo^{4+} species, and Ni species strongly connected to the alumina. In $g\text{-Ni}_{2.9}\text{Mo}_{6.7}$, an intense peak at 470°C , a shoulder at 420°C , and two peaks centered at 630°C and 780°C were detected. Compared to $i\text{-Ni}_{2.9}\text{Mo}_{6.7}$, these peaks were located at higher temperatures, suggesting the stronger metal-support interaction (lower reducibility) in $g\text{-Ni}_{2.9}\text{Mo}_{6.7}$. Further, we noticed that the shape of the peaks in the low-temperature area between these two catalysts is different. The unsymmetric broad peak in the

Chapter 6

spectrum of $g\text{-Ni}_{2.9}\text{Mo}_{6.7}$ suggests that there are multiple components (with different metal-support interactions) contribute to this reduction peak, and there is probably only one component exists in $i\text{-Ni}_{2.9}\text{Mo}_{6.7}$. So, we infer that the metal coordination states and metal-support interactions are diversiform in $g\text{-Ni}_{2.9}\text{Mo}_{6.7}$, while more uniform in $i\text{-Ni}_{2.9}\text{Mo}_{6.7}$.

$i\text{-Ni}_{2.9}\text{Mo}_{6.7}+i\text{-Ni}_{0.77}\text{Mo}_{8.3}$ shows lower reduction temperatures compared to $g\text{-Ni}_{2.9}\text{Mo}_{6.7}+i\text{-Ni}_{0.77}\text{Mo}_{8.3}$, suggesting a weaker metal-support interaction and higher reducibility of $i\text{-Ni}_{2.9}\text{Mo}_{6.7}+i\text{-Ni}_{0.77}\text{Mo}_{8.3}$. It can also be noticed that $i\text{-Ni}_{2.9}\text{Mo}_{6.7}+i\text{-Ni}_{0.77}\text{Mo}_{8.3}$ shows a stronger metal-support interaction compared to $i\text{-Ni}_{2.9}\text{Mo}_{6.7}$. While $g\text{-Ni}_{2.9}\text{Mo}_{6.7}+i\text{-Ni}_{0.77}\text{Mo}_{8.3}$ shows a weaker metal-support interaction compared to $g\text{-Ni}_{2.9}\text{Mo}_{6.7}$. This observation suggests that the second-step impregnation changes the metal-support interactions in $i\text{-Ni}_{2.9}\text{Mo}_{6.7}$ and $g\text{-Ni}_{2.9}\text{Mo}_{6.7}$ in varying degrees. It still needs to be determined whether the metal loaded in the first-step performs equally in structure and performance to the metal loaded in second-step impregnation.

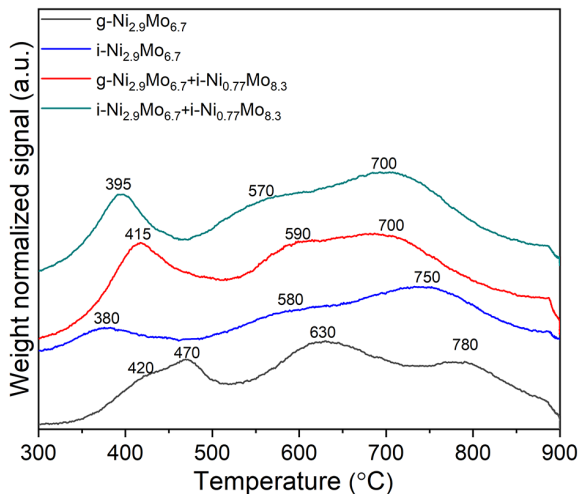


Figure 6.5. TPR profiles of $g\text{-Ni}_{2.9}\text{Mo}_{6.7}$, $i\text{-Ni}_{2.9}\text{Mo}_{6.7}$, $g\text{-Ni}_{2.9}\text{Mo}_{6.7}+i\text{-Ni}_{0.77}\text{Mo}_{8.3}$, and $i\text{-Ni}_{2.9}\text{Mo}_{6.7}+i\text{-Ni}_{0.77}\text{Mo}_{8.3}$.

The nature of Mo and Ni oxides nanostructures was further examined with UV-vis DRS and Raman spectroscopy. The adsorption edge energy (E_g) of catalysts, determined from the position of the low energy rise in catalysts' UV-vis spectrum (Figure 6.6), is used to establish the particle size and the extent of agglomeration of metal oxides [40]. The lower E_g value, the smaller particle size. E_g values for $g\text{-Ni}_{2.9}\text{Mo}_{6.7}$, $i\text{-Ni}_{2.9}\text{Mo}_{6.7}$, $g\text{-Ni}_{2.9}\text{Mo}_{6.7}+i\text{-Ni}_{0.77}\text{Mo}_{8.3}$, and $i\text{-Ni}_{2.9}\text{Mo}_{6.7}+i\text{-Ni}_{0.77}\text{Mo}_{8.3}$ are respectively 4.2 eV, 3.8 eV, 3.6 eV, and 3.5 eV, so the particle sizes of these catalysts decrease in the order of $i\text{-Ni}_{2.9}\text{Mo}_{6.7}+i\text{-Ni}_{0.77}\text{Mo}_{8.3} > g\text{-Ni}_{2.9}\text{Mo}_{6.7}+i\text{-Ni}_{0.77}\text{Mo}_{8.3} > i\text{-Ni}_{2.9}\text{Mo}_{6.7} > g\text{-Ni}_{2.9}\text{Mo}_{6.7}$. As discussed in Chapter 5, in $\text{NiMo}/\text{Al}_2\text{O}_3$ catalysts system (with same metal loadings), a linear correlation between E_g and

A non-boehmite derived γ -alumina and its utilization in HDS catalysis

HDS activity (DBT conversion) exists, which means the catalyst with lower E_g shows a higher DBT conversion. If the correlation still applies, DBT conversion of these four catalysts should follow this order: $i\text{-Ni}_{2.9}\text{Mo}_{6.7}+i\text{-Ni}_{0.77}\text{Mo}_{8.3} > g\text{-Ni}_{2.9}\text{Mo}_{6.7}+i\text{-Ni}_{0.77}\text{Mo}_{8.3}$, $i\text{-Ni}_{2.9}\text{Mo}_{6.7} > g\text{-Ni}_{2.9}\text{Mo}_{6.7}$. The DBT HDS results in Table 6.6 are consistent with this speculation.

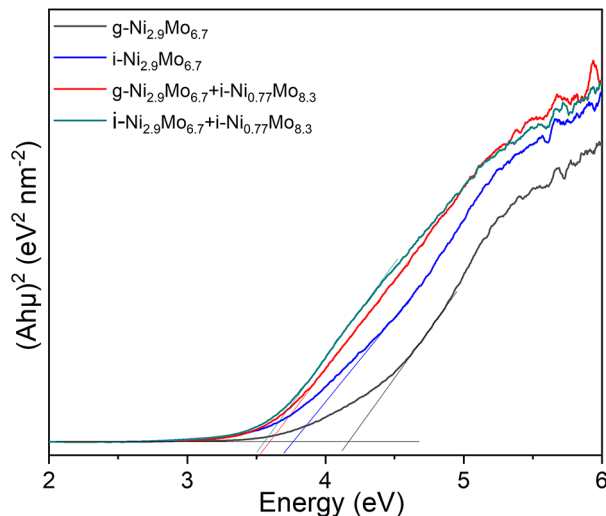


Figure 6.6. Determination of edge energy from UV-vis DRS of $g\text{-Ni}_{2.9}\text{Mo}_{6.7}$, $i\text{-Ni}_{2.9}\text{Mo}_{6.7}$, $g\text{-Ni}_{2.9}\text{Mo}_{6.7}+i\text{-Ni}_{0.77}\text{Mo}_{8.3}$, and $i\text{-Ni}_{2.9}\text{Mo}_{6.7}+i\text{-Ni}_{0.77}\text{Mo}_{8.3}$.

Figure 6.7 shows the Raman spectra of these four samples. $g\text{-Ni}_{2.9}\text{Mo}_{6.7}$ and $g\text{-Ni}_{2.9}\text{Mo}_{6.7}+i\text{-Ni}_{0.77}\text{Mo}_{8.3}$ exhibit similar characteristics, where four bands at 220 cm^{-1} , 320 cm^{-1} , 840 cm^{-1} , and 950 cm^{-1} are detected. According to the literature, the band at 950 cm^{-1} is assigned to $\nu_s(\text{Mo}=\text{O})$ stretching mode of $\text{Mo}=\text{O}_{2t}$ structure in $\text{Mo}_7\text{O}_{24}^{6-}$ species [40, 41]. Bands at 840 cm^{-1} and 320 cm^{-1} are due to the $\nu_{as}(\text{Mo}=\text{O})$ stretching mode and $\delta(\text{Mo}=\text{O})$ deformation mode of $\text{Mo}=\text{O}_{2t}$ structure in MoO_4^{2-} species [42]. The band at 220 cm^{-1} is assigned to the $\delta(\text{Mo}-\text{O}-\text{Mo})$ deformation vibration of the $\text{Mo}-\text{O}-\text{Mo}$ bond in polymolybdate species [43, 44]. Likewise, similar features are observed in $i\text{-Ni}_{2.9}\text{Mo}_{6.7}$ and $i\text{-Ni}_{2.9}\text{Mo}_{6.7}+i\text{-Ni}_{0.77}\text{Mo}_{8.3}$. Besides the bands described above (220 cm^{-1} , 840 cm^{-1} , and 950 cm^{-1}), bands at 280 cm^{-1} , 930 cm^{-1} , and 990 cm^{-1} are also observed in $i\text{-Ni}_{2.9}\text{Mo}_{6.7}$. Band at 930 cm^{-1} and 990 cm^{-1} are assigned to $\nu_{as}(\text{Mo}=\text{O})$ and $\nu_s(\text{Mo}=\text{O})$ stretching vibration of $\text{Mo}=\text{O}_t$ structures in the agglomerated Mo species, e.g., $\text{Mo}_8\text{O}_{26}^{4-}$ [45, 46].

Representative TEM micrographs of $g\text{-Ni}_{2.9}\text{Mo}_{6.7}$, $i\text{-Ni}_{2.9}\text{Mo}_{6.7}$, $g\text{-Ni}_{2.9}\text{Mo}_{6.7}+i\text{-Ni}_{0.77}\text{Mo}_{8.3}$, and $i\text{-Ni}_{2.9}\text{Mo}_{6.7}+i\text{-Ni}_{0.77}\text{Mo}_{8.3}$ after activation in a $\text{H}_2\text{S}/\text{H}_2$ (10/90 vol%) flow at $350\text{ }^\circ\text{C}$ for 2 h are displayed in Figure 6.8, where layered MoS_2 platelets are visualized as black lines. The average MoS_2 particle size in $g\text{-Ni}_{2.9}\text{Mo}_{6.7}$ is 2.8 nm with an average 1.1 layers per stack of MoS_2 particles. A smaller particle size (2.2 nm) and comparable stacking degree (1.2) are

Chapter 6

observed in $i\text{-Ni}_{2.9}\text{Mo}_{6.7}$. As described in the literature [47], the small particle size and a high stacking degree in $i\text{-Ni}_{2.9}\text{Mo}_{6.7}$ are the features of type II active NiMoS phases. Besides, compared to $g\text{-Ni}_{2.9}\text{Mo}_{6.7}$, $i\text{-Ni}_{2.9}\text{Mo}_{6.7}$ has a higher dispersion of NiMoS phase (0.45) (Table 6.3). $g\text{-Ni}_{2.9}\text{Mo}_{6.7}+i\text{-Ni}_{0.77}\text{Mo}_{8.3}$ shows comparable mean particle size (2.8 nm), stacking degree (1.1), and NiMoS dispersion (0.34) to $g\text{-Ni}_{2.9}\text{Mo}_{6.7}$. A notable increase of mean particle size and a slight increase in stacking degree in $i\text{-Ni}_{2.9}\text{Mo}_{6.7}+i\text{-Ni}_{0.77}\text{Mo}_{8.3}$ are observed compared to $i\text{-Ni}_{2.9}\text{Mo}_{6.7}$. The observed mean particle size increase is because of the formation of larger particles in $i\text{-Ni}_{2.9}\text{Mo}_{6.7}+i\text{-Ni}_{0.77}\text{Mo}_{8.3}$. As the particle size distribution report in Table 6.3 shows that compared to $i\text{-Ni}_{2.9}\text{Mo}_{6.7}$, where only 1.8 % of MoS_2 is larger than 4 nm in size, in $i\text{-Ni}_{2.9}\text{Mo}_{6.7}+i\text{-Ni}_{0.77}\text{Mo}_{8.3}$, this number is 25.7 %. As a result of larger particle size and higher stacking degree, a decrease of active NiMoS phase dispersion is observed in $i\text{-Ni}_{2.9}\text{Mo}_{6.7}+i\text{-Ni}_{0.77}\text{Mo}_{8.3}$. Due to the intrinsic structural differences between $g\text{-Ni}_{2.9}\text{Mo}_{6.7}$ and $i\text{-Ni}_{2.9}\text{Mo}_{6.7}$, e.g., metal-support interaction, metal coordination states, the second-step impregnation performs differently on $g\text{-Ni}_{2.9}\text{Mo}_{6.7}$ and $i\text{-Ni}_{2.9}\text{Mo}_{6.7}$. The minor changes observed in $g\text{-Ni}_{2.9}\text{Mo}_{6.7}$ suggest that the structure of $g\text{-Ni}_{2.9}\text{Mo}_{6.7}$ is more stable under the impregnation solution owing to the stronger metal-support interaction in its oxidic precursor.

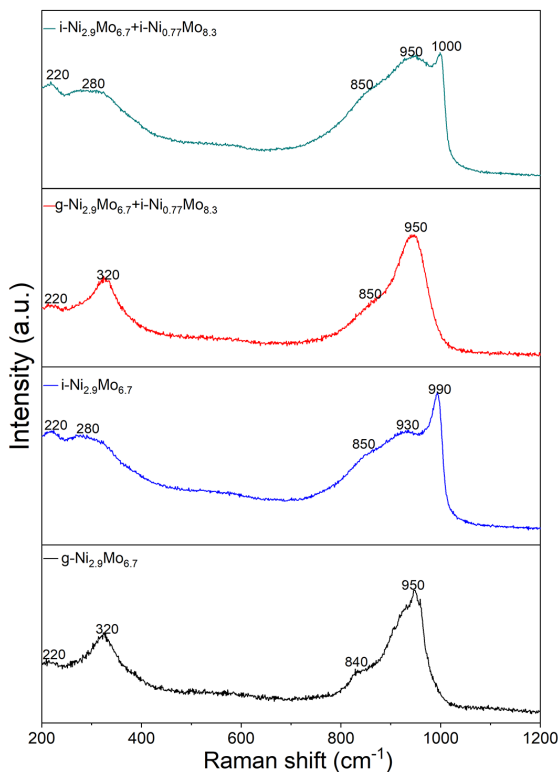


Figure 6.7. Raman spectra of $g\text{-Ni}_{2.9}\text{Mo}_{6.7}$, $i\text{-Ni}_{2.9}\text{Mo}_{6.7}$, $g\text{-Ni}_{2.9}\text{Mo}_{6.7}+i\text{-Ni}_{0.77}\text{Mo}_{8.3}$, and $i\text{-Ni}_{2.9}\text{Mo}_{6.7}+i\text{-Ni}_{0.77}\text{Mo}_{8.3}$.

A non-boehmite derived γ -alumina and its utilization in HDS catalysis

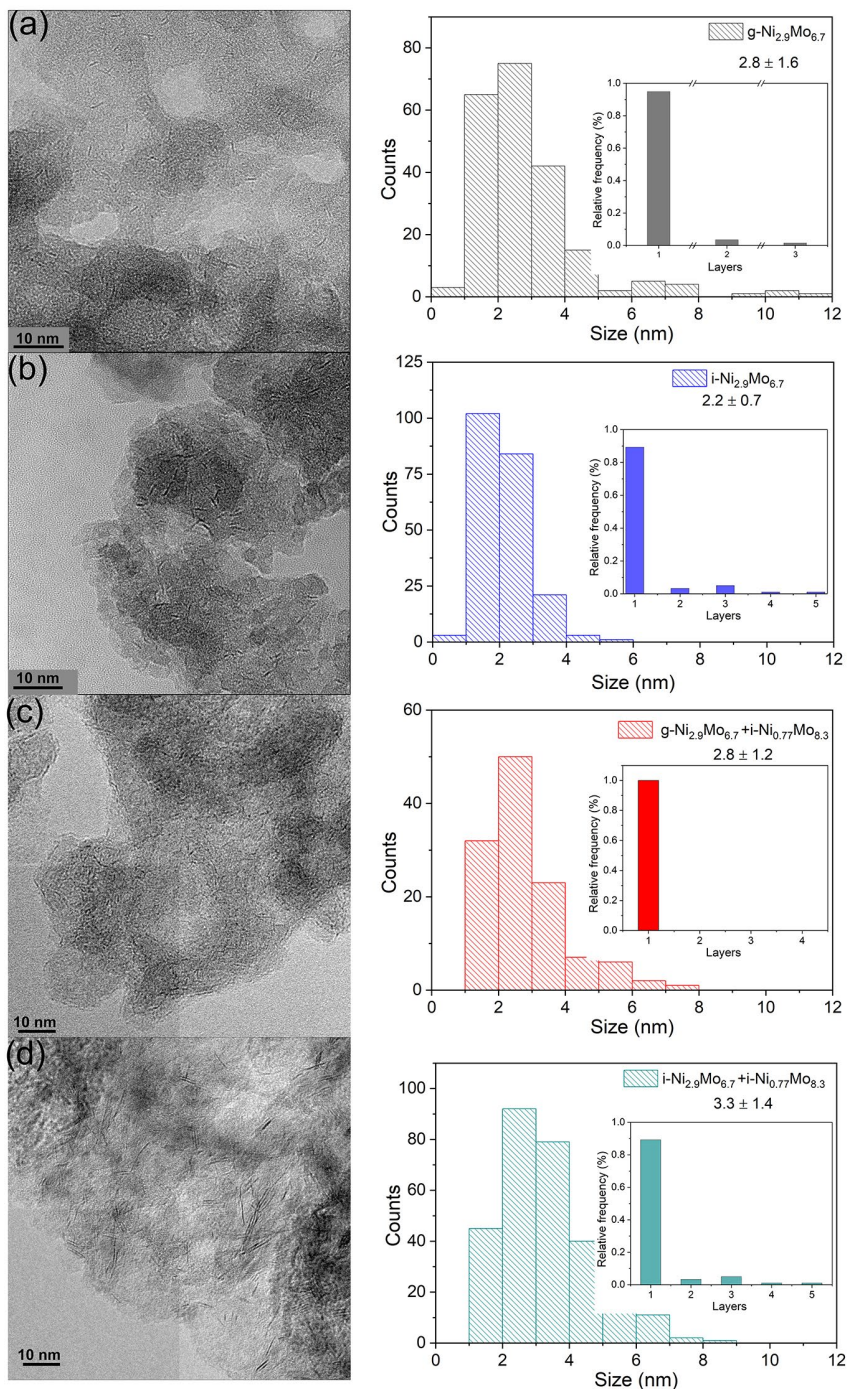


Figure 6.8. TEM micrographs of a) $g\text{-Ni}_{2.9}\text{Mo}_{6.7}$ b) $i\text{-Ni}_{2.9}\text{Mo}_{6.7}$ c) $g\text{-Ni}_{2.9}\text{Mo}_{6.7} + i\text{-Ni}_{0.77}\text{Mo}_{8.3}$ d) $i\text{-Ni}_{2.9}\text{Mo}_{6.7} + i\text{-Ni}_{0.77}\text{Mo}_{8.3}$. The respective particle size distribution and stacking degrees are plotted on the right of each image.

Table 6.3. Morphological characteristics of prepared catalysts as determined by and calculated from TEM micrographs.

Sample	Average length L (nm)	Average stacking number N	Dispersion of NiMoS (D) ^a	Distribution of particle size (rel %)				Distribution of stacking number (rel %)			
				<2	2-4	4-6	>6	1	2	3	>4
g-Ni_{2.9}Mo_{6.7}	2.8 ± 1.6	1.1	0.31	31.6	54.4	7.9	6.1	30.2	35.7	20.6	13.5
i-Ni_{2.9}Mo_{6.7}	2.2 ± 0.7	1.2	0.45	49.1	49.1	1.8	0	89.3	3.4	5.1	2.2
g-Ni_{2.9}Mo_{6.7}+i-Ni_{10.77}Mo_{8.3}	2.8 ± 1.6	1.0	0.34	26.4	60.3	10.7	2.6	100	0	0	0
i-Ni_{2.9}Mo_{6.7}+i-Ni_{10.77}Mo_{8.3}	3.3 ± 1.4	1.4	0.31	15.5	58.8	21.0	4.7	67.0	28.4	3.4	1.2

^a NiMoS dispersion calculated from TEM results (Equation 11 in Chapter 2).

Table 6.4. XPS fitting results of four catalysts.

Sample	Binding energy (eV)						Fractions (%)					
	Mo 3d5/2		Ni 2p3/2		Mo 3d		Ni 2p		NiO _x		NiMoS	
	Mo ⁴⁺	Mo ⁵⁺	Mo ⁶⁺	NiS _x	NiMoS	NiO _x	Mo ⁴⁺	Mo ⁵⁺	Mo ⁶⁺	NiS _x	NiMoS	NiO _x
g-Ni_{2.9}Mo_{6.7}	229.0	231.0	233.1	853.1	855.2	856.7	79.3	14.7	6.0	65.9	14.0	20.1
i-Ni_{2.9}Mo_{6.7}	228.8	230.8	232.7	853.2	855.4	856.6	80.2	12.3	7.5	63.6	18.8	17.6
g-Ni_{2.9}Mo_{6.7}+i-Ni_{10.77}Mo_{8.3}	229.0	231.1	233.0	853.5	855.1	856.4	80.0	7.8	12.3	72.6	12.6	14.9
i-Ni_{2.9}Mo_{6.7}+i-Ni_{10.77}Mo_{8.3}	229.2	231.0	233.0	853.8	855.5	856.6	80.4	14.3	5.3	66.0	13.1	20.9

A non-boehmite derived γ -alumina and its utilization in HDS catalysis

Surface composition and oxidation degree of Mo and Ni in sulfided g- $\text{Ni}_{2.9}\text{Mo}_{6.7}$, i- $\text{Ni}_{2.9}\text{Mo}_{6.7}$, g- $\text{Ni}_{2.9}\text{Mo}_{6.7}$ +i- $\text{Ni}_{0.77}\text{Mo}_{8.3}$, and i- $\text{Ni}_{2.9}\text{Mo}_{6.7}$ +i- $\text{Ni}_{0.77}\text{Mo}_{8.3}$ are determined by means of XPS. Figure 6.9a shows the Mo 3d core-level spectra of these four samples, where three doublets related to different Mo oxidation states, together with one S 2s signal characteristic of S^{2-} can be identified. Three Mo 3d_{5/2} doublets are assigned to Mo^{6+} in MoO_3 (B.E. = 232.9 ± 0.4 eV), Mo^{5+} in oxysulfide species (B.E. = 230.9 ± 0.6 eV) and Mo^{4+} in MoS_2 (B.E. = 229.0 ± 0.5 eV) [48, 49]. Figure 6.9b shows the corresponding Ni 2p core-level spectra, and it can be deconvoluted into three components: oxidic Ni (B.E. = 856.3 ± 0.5 eV), NiMoS species (B.E. = 854.8 ± 0.6 eV) and sulfided Ni (B.E. = 853.5 ± 0.4 eV) and along with their respective satellites [50, 51]. Detailed binding energies of the main features and the atomic percentage of different Mo and Ni species based on the contributions are summarized in Table 6.4.

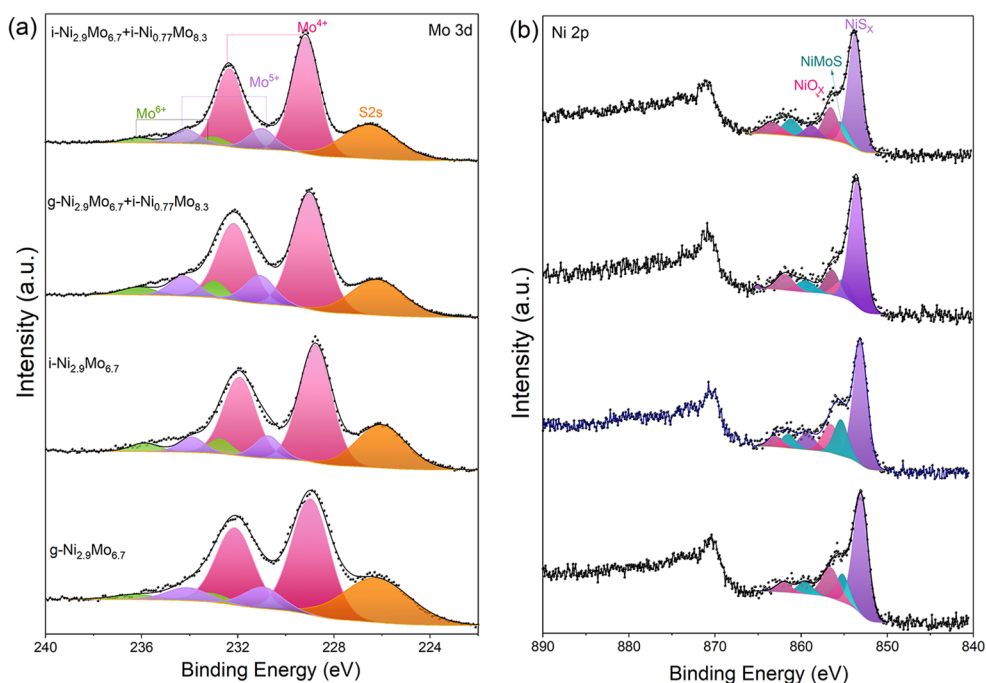


Figure 6.9. XPS spectra showing Mo 3d, S 2s and Ni 2p regions of sulfided g- $\text{Ni}_{2.9}\text{Mo}_{6.7}$, i- $\text{Ni}_{2.9}\text{Mo}_{6.7}$, g- $\text{Ni}_{2.9}\text{Mo}_{6.7}$ +i- $\text{Ni}_{0.77}\text{Mo}_{8.3}$, and i- $\text{Ni}_{2.9}\text{Mo}_{6.7}$ +i- $\text{Ni}_{0.77}\text{Mo}_{8.3}$. Experimental data are presented by black dots and fit by a black curve. The fits are composed of Mo^{4+} (pink), Mo^{5+} (purple), Mo^{6+} (green), S^{2-} (orange), NiO_x (pink), NiMoS (blue), and NiS_x (violet).

Table 6.5. XPS fit results of prepared catalysts.

Sample	S/(Ni+Mo)	Ni/Mo	Mo/Al ^a	Ni/Al ^a	(Ni/Mo) _{lab} ^b	(Ni/Mo) _{edge} ^c	Effective amount (wt.%) of Ni in NiMoS ^d
g-Ni_{2.9}Mo_{6.7}	1.54	0.72	4.6	3.4	0.31	0.42	0.15
i-Ni_{2.9}Mo_{6.7}	1.54	0.72	3.4	2.5	0.45	0.36	0.15
g-Ni_{2.9}Mo_{6.7}+i-Ni_{0.77}Mo_{8.3}	1.55	0.21	10.2	3.1	0.34	0.15	0.12
i-Ni_{2.9}Mo_{6.7}+i-Ni_{0.77}Mo_{8.3}	1.63	0.40	6.8	3.2	0.31	0.26	0.14

^a Mo(Ni)/Al (%) ratio was calculated from XPS results via equations 3, 4; ^b Ni/Mo ratio in the NiMoS slabs calculated via equation 7.

^c Ni/Mo ratio in the NiMoS edges calculated via equation 8; ^d Effective Ni content in total NiMoS species from XPS results via equation 6.

Table 6.6. Thiophene and DBT HDS results.

Catalyst	Thiophene			DBT					
	Reaction rates (mol mol _{Mo} ⁻¹ h ⁻¹)	Reaction temperature	Reaction rates (mol mol _{Mo} ⁻¹ h ⁻¹)	Selectivity			Conversion X (%)	TOF _{edge} (s ⁻¹)	
				k _{HDS}	BP	CHB			DDS : HYD
g-Ni_{2.9}Mo_{6.7}	5.5	250 °C	5.2	94.2	5.8	16.2	6.6	0.025	
		270 °C	15.4	93.3	6.7	13.9	18.3	--	
		300 °C	58.0	90.0	10.0	9.0	53.3	--	
i-Ni_{2.9}Mo_{6.7}	26.4	250 °C	16.6	93.8	6.2	15.1	18.3	0.060	
		270 °C	49.0	93.6	6.4	14.6	44.9	--	
		300 °C	182.8	91.2	8.8	10.4	89.2	--	
g-Ni_{2.9}Mo_{6.7}+i-Ni_{0.77}Mo_{8.3}	21.2	250 °C	12.7	91.6	8.4	10.9	15.4	0.025	
		270 °C	27.3	90.7	9.3	9.8	30.1	--	
		300 °C	81.0	88.5	11.5	7.7	66.8	--	
i-Ni_{2.9}Mo_{6.7}+i-Ni_{0.77}Mo_{8.3}	33.6	250 °C	10.2	87.9	12.1	7.3	21.3	0.051	
		270 °C	27.1	87.3	12.7	6.9	47.2	--	
		300 °C	124.1	84.0	16.0	5.3	94.6	--	

A non-boehmite derived γ -alumina and its utilization in HDS catalysis

Mo is predominantly present in the form of Mo(IV) (~80 %) in these four sulfided catalysts, indicating that surface Mo(VI) of the oxidic precursors is well sulfided during activation. The sulfur-to-metal (S/(Mo+Ni)) ratios reported in Table 6.5 are the complementary evidence for that, as the full conversion to MoS₂ and NiS yield S/(Mo+Ni) = 1.59 and 1.71 for two sets of catalysts with different metal loadings (2.9 wt% Ni, 6.7 wt% Mo and 3.67 wt% Ni, 15 wt% Mo). g-Ni_{2.9}Mo_{6.7} and i-Ni_{2.9}Mo_{6.7} have a comparable sulfidation degree of Mo and Ni. Even though the effective amount of Ni in NiMoS is comparable (0.15 wt%) in these two catalysts, a relative 18.8 % of Ni participates in the formation of the active NiMoS phase in i-Ni_{2.9}Mo_{6.7}, while in g-Ni_{2.9}Mo_{6.7}, this value is 14.0 %. Besides, i-Ni_{2.9}Mo_{6.7} shows a lower Mo/Al and Ni/Al value than g-Ni_{2.9}Mo_{6.7} (Table 6.5), suggesting a higher Ni and Mo dispersion in i-Ni_{2.9}Mo_{6.7}, which is consistent with TEM data. The sulfidation degree of Mo and Ni in g-Ni_{2.9}Mo_{6.7}+i-Ni_{0.77}Mo_{8.3} and i-Ni_{2.9}Mo_{6.7}+i-Ni_{0.77}Mo_{8.3} are comparable, and a higher metal dispersion was observed in i-Ni_{2.9}Mo_{6.7}+i-Ni_{0.77}Mo_{8.3}.

The results of thiophene HDS and DBT HDS are listed in Table 6.6. g-Ni_{2.9}Mo_{6.7} is the least active in thiophene HDS. i-Ni_{2.9}Mo_{6.7}, g-Ni_{2.9}Mo_{6.7}+i-Ni_{0.77}Mo_{8.3}, and i-Ni_{2.9}Mo_{6.7}+i-Ni_{0.77}Mo_{8.3} are separately 4.8, 3.9, and 5.1 times more active than g-Ni_{2.9}Mo_{6.7}. In DBT HDS, the main reaction pathway for these catalysts is DDS, with BP as the main product. With reaction temperature increases, the content of cyclohexylbenzene (CHB), main product of hydrogenation (HYD) pathway, increases. g-Ni_{2.9}Mo_{6.7} shows a 6.6 %, 18.3 %, and 53.3 % DBT conversion at 250 °C, 270 °C, and 300 °C, the conversion for i-Ni_{2.9}Mo_{6.7} is 18.3 %, 44.9 %, and 89.2 %, which is 2.8, 2.5, and 1.7 times higher than that of g-Ni_{2.9}Mo_{6.7}. The higher HDS activity in i-Ni_{2.9}Mo_{6.7} is due to the higher efficiency of the formed active NiMoS phase, as TOF_{edge} value of i-Ni_{2.9}Mo_{6.7} (0.060 s⁻¹) is almost 3 times as higher as that of g-Ni_{2.9}Mo_{6.7} (0.025 s⁻¹). Since there is a similar amount of NiMoS particles in these two catalysts (Table 6.5), the influence of NiMoS content can be ignored. Combing all structural information, we infer that the high reducibility in the oxidic precursors caused by the weak metal-support interaction promotes the formation of sulfided catalyst with highly metal dispersion and active NiMoS phase during sulfidation [52].

With extra metal loading, varying degrees of activity improvement are observed; g-Ni_{2.9}Mo_{6.7}+i-Ni_{0.77}Mo_{8.3} presents a 15.4 %, 30.1 %, and 66.8 % DBT conversion at 250 °C, 270 °C, and 300 °C, which is a 130 %, 64 %, and 25 % activity increase compared to g-Ni_{2.9}Mo_{6.7}. Compared to i-Ni_{2.9}Mo_{6.7}, a slightly activity increase (16 %, 5 %, and 6 %) is observed in i-Ni_{2.9}Mo_{6.7}+i-Ni_{0.77}Mo_{8.3} with a DBT conversion of 21.3 %, 47.2 %, and 94.6 % at 250 °C, 270 °C, and 300 °C. i-Ni_{2.9}Mo_{6.7}+i-Ni_{0.77}Mo_{8.3} exhibits 1.4, 1.6, and 1.4 times the activity of g-Ni_{2.9}Mo_{6.7}+i-Ni_{0.77}Mo_{8.3} in DBT HDS. The higher intrinsic activity of the active phase in i-Ni_{2.9}Mo_{6.7}+i-Ni_{0.77}Mo_{8.3} is one of the reasons for the higher activity, as the TOF_{edge}

Chapter 6

value of $i\text{-Ni}_{2.9}\text{Mo}_{6.7}+i\text{-Ni}_{0.77}\text{Mo}_{8.3}$ (0.051 s^{-1}) is higher than that of $g\text{-Ni}_{2.9}\text{Mo}_{6.7}+i\text{-Ni}_{0.77}\text{Mo}_{8.3}$ (0.025 s^{-1}). Besides, the higher content of the active NiMoS phase in $i\text{-Ni}_{2.9}\text{Mo}_{6.7}+i\text{-Ni}_{0.77}\text{Mo}_{8.3}$, suggested by ICP and XPS data, is also a part of the reason. Based on the data we had, the influence of second-step impregnation on $g\text{-Ni}_{2.9}\text{Mo}_{6.7}$ and $i\text{-Ni}_{2.9}\text{Mo}_{6.7}$ cannot be evaluated, since along with the increase of metal loading, the metal redispersion and structure change also occur, we cannot ideally separate these two parts of metals and ensure their contributions to catalysts' activity. TOF_{edge} value shows that the second-step impregnation does not always have a positive effect in our case.

6.4 Conclusion

A self-made alumina ($\text{Al}_2\text{O}_3(\text{self-made})$) was synthesized via a one-step preparation route, in which the solid compounds $\text{NH}_4\text{AlO}(\text{OH})\text{HCO}_3$ and NH_4HCO_3 were mechanically mixed in a mortar, dried and calcined. Catalysts with same formulation prepared with $\text{Al}_2\text{O}_3(\text{self-made})$ and $\text{Al}_2\text{O}_3(\text{commercial})$ as support present comparable performance. The same preparation route was used to prepare alumina-supported NiMo catalysts ($g\text{-Ni}_{2.9}\text{Mo}_{6.7}$) by co-mixing the metals with the alumina precursor compounds. For comparison, $i\text{-Ni}_{2.9}\text{Mo}_{6.7}$ with the same formulation was prepared by incipient wetness impregnation with $\text{Al}_2\text{O}_3(\text{self-made})$ as support. The results show that $i\text{-Ni}_{2.9}\text{Mo}_{6.7}$ has a weaker metal-support interaction and a higher reducibility in its oxidic precursor compared to $g\text{-Ni}_{2.9}\text{Mo}_{6.7}$. This high reducibility promotes the formation of sulfided catalyst with high metal dispersion and high content of active NiMoS phase during the sulfidation, which further leads to higher HDS activity in $i\text{-Ni}_{2.9}\text{Mo}_{6.7}$. With extra metals deposition by a second-step impregnation, $g\text{-Ni}_{2.9}\text{Mo}_{6.7}+i\text{-Ni}_{0.77}\text{Mo}_{8.3}$ and $i\text{-Ni}_{2.9}\text{Mo}_{6.7}+i\text{-Ni}_{0.77}\text{Mo}_{8.3}$ were prepared. By comparing the metal-support interactions and crystallinity in catalysts, we noticed that a metal redispersion occurred during the second-step impregnation. Though the DBT conversion of these two catalysts increased, the corresponding TOF_{edge} values did not show the same trend. $g\text{-Ni}_{2.9}\text{Mo}_{6.7}+i\text{-Ni}_{0.77}\text{Mo}_{8.3}$ has the same TOF_{edge} as $g\text{-Ni}_{2.9}\text{Mo}_{6.7}$ (0.025 s^{-1}), while $i\text{-Ni}_{2.9}\text{Mo}_{6.7}+i\text{-Ni}_{0.77}\text{Mo}_{8.3}$ (0.051 s^{-1}) has a lower TOF_{edge} than $i\text{-Ni}_{2.9}\text{Mo}_{6.7}$ (0.060 s^{-1}). The higher intrinsic activity of the active sites results in the promoted catalytic performance of $i\text{-Ni}_{2.9}\text{Mo}_{6.7}+i\text{-Ni}_{0.77}\text{Mo}_{8.3}$. However, the role of the second-step impregnation in our system still needs to be further investigated.

6.5. Reference

- [1] D.A. Dalrymple, T.W. Trofe, J.M. Evans, An overview of liquid redox sulfur recovery, Chem. Eng. Prog.:(United States), 85 (1989).
- [2] C. Song, X. Ma, New design approaches to ultra-clean diesel fuels by deep desulfurization and deep dearomatization, Appl. Catal., B, 41 (2003) 207-238.

A non-boehmite derived γ -alumina and its utilization in HDS catalysis

- [3] H. Cölfen, S. Mann, Higher-order organization by mesoscale self-assembly and transformation of hybrid nanostructures, *Angew. Chem. Int. Ed.*, 42 (2003) 2350-2365.
- [4] Z. Zhang, T.J. Pinnavaia, Mesostructured γ -Al₂O₃ with a lathlike framework morphology, *J. Am. Chem. Soc.*, 124 (2002) 12294-12301.
- [5] P. Rayo, J. Ramírez, P. Torres-Mancera, G. Marroquín, S.K. Maity, J. Ancheyta, Hydrodesulfurization and hydrocracking of Maya crude with P-modified NiMo/Al₂O₃ catalysts, *Fuel*, 100 (2012) 34-42.
- [6] A.A. Asadi, S.M. Alavi, S.J. Royae, M. Bazmi, Ultradeep hydrodesulfurization of feedstock containing cracked gasoil through NiMo/ γ -Al₂O₃ catalyst pore size optimization, *Energy & fuels*, 32 (2018) 2203-2212.
- [7] S.J. Wilson, The dehydration of boehmite, γ -AlOOH, to γ -Al₂O₃, *J. Solid State Chem.*, 30 (1979) 247-255.
- [8] P. Bai, P. Wu, Z. Yan, X. Zhao, A reverse cation–anion double hydrolysis approach to the synthesis of mesoporous γ -Al₂O₃ with a bimodal pore size distribution, *Microporous Mesoporous Mater.*, 118 (2009) 288-295.
- [9] D.J. Suh, T.-J. Park, J.-H. Kim, K.-L. Kim, Fast sol–gel synthetic route to high-surface-area alumina aerogels, *Chem. Mater.*, 9 (1997) 1903-1905.
- [10] B.E. Yoldas, Alumina gels that form porous transparent Al₂O₃, *J. Mater. Sci.*, 10 (1975) 1856-1860.
- [11] P. Yang, T. Deng, D. Zhao, P. Feng, D. Pine, B.F. Chmelka, G.M. Whitesides, G.D. Stucky, Hierarchically ordered oxides, *Science*, 282 (1998) 2244-2246.
- [12] R.A. Caruso, M. Giersig, F. Willig, M. Antonietti, Porous “coral-like” TiO₂ structures produced by templating polymer gels, *Langmuir*, 14 (1998) 6333-6336.
- [13] M. Yada, M. Machida, T. Kijima, Synthesis and deorganization of an aluminium–based dodecyl sulfate mesophase with a hexagonal structure, *Chem. Commun.*, (1996) 769-770.
- [14] S. Cabrera, J.E. Haskouri, J. Alamo, A. Beltrán, D. Beltrán, S. Mendioroz, M.D. Marcos, P. Amorós, Surfactant-assisted synthesis of mesoporous alumina showing continuously adjustable pore sizes, *Adv. Mater.*, 11 (1999) 379-381.
- [15] L. Ji, J. Lin, K. Tan, H. Zeng, Synthesis of high-surface-area alumina using aluminum tri-sec-butoxide – 2, 4-pentanedione – 2-propanol – nitric acid precursors, *Chem. Mater.*, 12 (2000) 931-939.
- [16] F. Vaudry, S. Khodabandeh, M.E. Davis, Synthesis of pure alumina mesoporous materials, *Chem. Mater.*, 8 (1996) 1451-1464.
- [17] Y. Kim, C. Kim, I. Choi, S. Rengaraj, J. Yi, Arsenic removal using mesoporous alumina prepared via a templating method, *Environ. Sci. Technol.*, 38 (2004) 924-931.
- [18] X. Hu, Y. Liu, Z. Tang, G. Li, R. Zhao, C. Liu, Fabrication of high-surface-area γ -alumina by thermal decomposition of AACH precursor using low-temperature solid-state reaction, *Mater. Res. Bull.*, 47 (2012) 4271-4277.
- [19] T.E. Klimova, D. Valencia, J.A. Mendoza-Nieto, P. Hernández-Hipólito, Behavior of NiMo/SBA-15 catalysts prepared with citric acid in simultaneous hydrodesulfurization of dibenzothiophene and 4, 6-dimethyldibenzothiophene, *J. Catal.*, 304 (2013) 29-46.
- [20] D. Valencia, T. Klimova, Citric acid loading for MoS₂-based catalysts supported on SBA-15. New catalytic materials with high hydrogenolysis ability in hydrodesulfurization, *Appl. Catal. B: Environ.*, 129 (2013) 137-145.

Chapter 6

- [21] L. Peña, D. Valencia, T. Klimova, CoMo/SBA-15 catalysts prepared with EDTA and citric acid and their performance in hydrodesulfurization of dibenzothiophene, *Appl. Catal. B: Environ.*, 147 (2014) 879-887.
- [22] A.J. van Dillen, R.J.A.M. Terörde, D.J. Lensveld, J.W. Geus, K.P. de Jong, Synthesis of supported catalysts by impregnation and drying using aqueous chelated metal complexes, *J. Catal.*, 216 (2003) 257-264.
- [23] Y. Fan, H. Xiao, G. Shi, H. Liu, Y. Qian, T. Wang, G. Gong, X. Bao, Citric acid-assisted hydrothermal method for preparing NiW/USY-Al₂O₃ ultradeep hydrodesulfurization catalysts, *J. Catal.*, 279 (2011) 27-35.
- [24] R. Iwamoto, J. Grimblot, Genesis, characterizations and HDS activity of Mo-P-aluminabased hydrotreating catalysts prepared by a sol-gel method, in: *Studies in Surface Science and Catalysis*, Elsevier, 1997, pp. 195-210.
- [25] F. Dumeignil, K. Sato, M. Imamura, N. Matsubayashi, E. Payen, H. Shimada, Characterization and hydrodesulfurization activity of CoMo catalysts supported on boron-doped sol-gel alumina, *Appl. Catal. A.*, 315 (2006) 18-28.
- [26] L. van Haandel, J.W. Geus, Th. Weber, Direct synthesis of TiO₂-supported MoS₂ nanoparticles by reductive coprecipitation, *ChemCatChem*, 8 (2016) 1367-1372.
- [27] W. Lai, L. Pang, J. Zheng, J. Li, Z. Wu, X. Yi, W. Fang, L. Jia, Efficient one pot synthesis of mesoporous NiMo-Al₂O₃ catalysts for dibenzothiophene hydrodesulfurization, *Fuel Process. Technol.*, 110 (2013) 8-16.
- [28] H. Liu, Y. Li, C. Yin, Y. Wu, Y. Chai, D. Dong, X. Li, C. Liu, One-pot synthesis of ordered mesoporous NiMo-Al₂O₃ catalysts for dibenzothiophene hydrodesulfurization, *Appl. Catal. B: Environ.*, 198 (2016) 493-507.
- [29] C. Tu, S. Liu, C. Liu, X. Wu, Q. Chen, W. Huang, Single-pot synthesis of NiMo-Al₂O₃ catalyst for quinoline hydrodenitrogenation, *Energy & Fuels*, 35 (2021) 1120-1128.
- [30] X. Yi, D. Guo, P. Li, X. Lian, Y. Xu, Y. Dong, W. Lai, W. Fang, One pot synthesis of NiMo-Al₂O₃ catalysts by solvent-free solid-state method for hydrodesulfurization, *RSC Adv.*, 7 (2017) 54468-54474.
- [31] X. Liu, J. Liu, L. Li, X. Zhang, H. Sun, R. Guo, S. Ren, Q. Guo, X.-D. Wen, B. Shen, Preparation of electron-rich Fe-based catalyst via electronic structure regulation and its promotion to hydrodesulfurization of dibenzothiophene, *Appl. Catal. B: Environ.*, 269 (2020) 118779.
- [32] B. Ludwig, T.T. Burke, Infrared Spectroscopy Studies of Aluminum Oxide and Metallic Aluminum Powders, Part I: Thermal Dehydration and Decomposition, *Powders*, 1 (2022) 47-61.
- [33] Y. Okamoto, T. Imanaka, Interaction chemistry between molybdena and alumina: infrared studies of surface hydroxyl groups and adsorbed carbon dioxide on aluminas modified with molybdate, sulfate, or fluorine anions, *J. Phys. Chem.*, 92 (1988) 7102-7112.
- [34] X. Liu, R.E. Truitt, DRFT-IR Studies of the Surface of γ -Alumina, *J. Am. Chem. Soc.*, 119 (1997) 9856-9860.
- [35] Z. Zhao, D. Xiao, K. Chen, R. Wang, L. Liang, Z. Liu, I. Hung, Z. Gan, G. Hou, Nature of Five-Coordinated Al in γ -Al₂O₃ Revealed by Ultra-High-Field Solid-State NMR, *ACS Cent. Sci.*, 8 (2022) 795-803.
- [36] K. Soni, B.S. Rana, A.K. Sinha, A. Bhaumik, M. Nandi, M. Kumar, G.M. Dhar, 3-D ordered mesoporous KIT-6 support for effective hydrodesulfurization catalysts, *Appl. Catal. B: Environ.*, 90 (2009) 55-63.

A non-boehmite derived γ -alumina and its utilization in HDS catalysis

- [37] A. Bhat, G.B. Megeri, C. Thomas, H. Bhargava, C. Jeevitha, S. Chandrashekar, G.M. Madhu, Adsorption and optimization studies of lead from aqueous solution using γ -Alumina, *J. Environ. Chem. Eng.*, 3 (2015) 30-39.
- [38] J.L. Brito, J. Laine, Reducibility of Ni-Mo/Al₂O₃ catalysts: a TPR study, *J. Catal.*, 139 (1993) 540-550.
- [39] B. Scheffer, P. Molhoek, J.A. Moulijn, Temperature-programmed reduction of NiO-WO₃/Al₂O₃ Hydrodesulphurization catalysts, *Appl. Catal.*, 46 (1989) 11-30.
- [40] H. Tian, C.A. Roberts, I.E. Wachs, Molecular structural determination of molybdena in different environments: Aqueous solutions, bulk mixed oxides, and supported MoO₃ catalysts, *J. Phys. Chem. C*, 114 (2010) 14110-14120.
- [41] A.G. Kalampounias, G. Tsilomelekis, R.W. Berg, S. Boghosian, Molybdenum (VI) oxosulfato complexes in MoO₃-K₂S₂O₇-K₂SO₄ molten mixtures: stoichiometry, vibrational properties, and molecular structures, *J. Phys. Chem. A*, 116 (2012) 8861-8872.
- [42] J. Zhang, J. Hu, L. Zhang, Raman studies on species in single and mixed solutions of molybdate and vanadate, *Chinese J. Chem. Phys.*, 29 (2016) 425-429.
- [43] G. Deo, I.E. Wachs, Predicting molecular structures of surface metal oxide species on oxide supports under ambient conditions, *J. Phys. Chem.*, 95 (1991) 5889-5895.
- [44] J. Moreau, O. Delpoux, E. Devers, M. Digne, S. Loridant, Impregnation of decamolybdocobaltate heteropolyanions over γ -alumina: detailed description of the physico-chemical phenomena, *Langmuir*, 29 (2013) 207-215.
- [45] V. La Parola, G. Deganello, C.R. Tewell, A.M. Venezia, Structural characterisation of silica supported CoMo catalysts by UV Raman spectroscopy, XPS and X-ray diffraction techniques, *Appl. Catal. A: Gen.*, 235 (2002) 171-180.
- [46] G. Mestl, T.K.K. Srinivasan, Raman spectroscopy of monolayer-type catalysts: supported molybdenum oxides, *Catal. Rev.*, 40 (1998) 451-570.
- [47] L. van Haandel, G.M. Bremmer, E.J.M. Hensen, Th. Weber, Influence of sulfiding agent and pressure on structure and performance of CoMo/Al₂O₃ hydrodesulfurization catalysts, *J. Catal.*, 342 (2016) 27-39.
- [48] S.J. DeCanio, M.C. Cataldo, E.C. DeCanio, D.A. Storm, Evidence from XPS for the stabilization of high-valent molybdenum by addition of potassium in Mo/Al₂O₃ catalysts, *J. Catal.*, 119 (1989) 256-260.
- [49] A. Galtayries, S. Wisniewski, J. Grimblot, Formation of thin oxide and sulphide films on polycrystalline molybdenum foils: characterization by XPS and surface potential variations, *J. Electron Spectrosc. Relat. Phenom.*, 87 (1997) 31-44.
- [50] J. Escobar, M.C. Barrera, J.A. Toledo, M.A. Cortés-Jácome, C. Angeles-Chávez, S. Núñez, V. Santes, E. Gómez, L. Díaz, E. Romero, J.G. Pacheco, Effect of ethyleneglycol addition on the properties of P-doped NiMo/Al₂O₃ HDS catalysts: Part I. Materials preparation and characterization, *Appl. Catal., B: Environ.*, 88 (2009) 564-575.
- [51] B.W. Hoffer, A.D. van Langeveld, J.-P. Janssens, R.L.C. Bonn , C.M. Lok, J.A. Moulijn, Stability of highly dispersed Ni/Al₂O₃ catalysts: effects of pretreatment, *J. Catal.*, 192 (2000) 432-440.
- [52] M. Li, J. Ihli, M.A. Verheijen, M. Holler, M. Guizar-Sicairos, J.A. van Bokhoven, E.J.M. Hensen, Th. Weber, Alumina-Supported NiMo Hydrotreating Catalysts — Aspects of 3D Structure, Synthesis, and Activity. *J. Phys. Chem. C*, 126 (2022) 18536–18549.

Chapter 6

6.6. Appendix D

Two NiMo/Al₂O₃ catalysts with target metal loadings of 15 wt% Mo, 3.67 wt% Ni, and 2 wt% P were prepared via incipient wetness impregnation of the Al₂O₃(commercial) and Al₂O₃(self-made) powder (75 – 125 μm). The impregnation solution was prepared by dissolving 0.7/0.6 mL H₃PO₄ solution (85 wt% in H₂O), 2.1/1.8 mg MoO₃, and 0.7/0.6 mg NiCO₃ in deionized water under continuous stirring. The solution was heated to 100 °C to accelerate the dissolution. The final volume of the solution was adjusted with water to the total pore volume of two used alumina carriers. After impregnation and dried overnight at 120 °C, the dried-only catalyst precursors were yielded and denoted as NiMo-PA^{dr}/Al₂O₃(commercial) and NiMo-PA^{dr}/Al₂O₃(self-made).

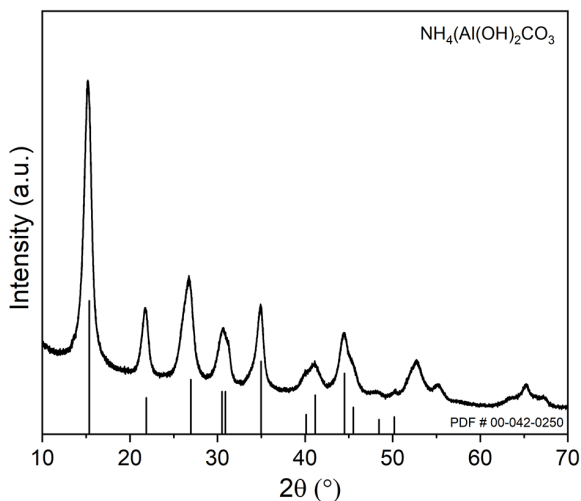


Figure D1. XRD patterns of precursor of Al₂O₃(self-made) (before calcination).

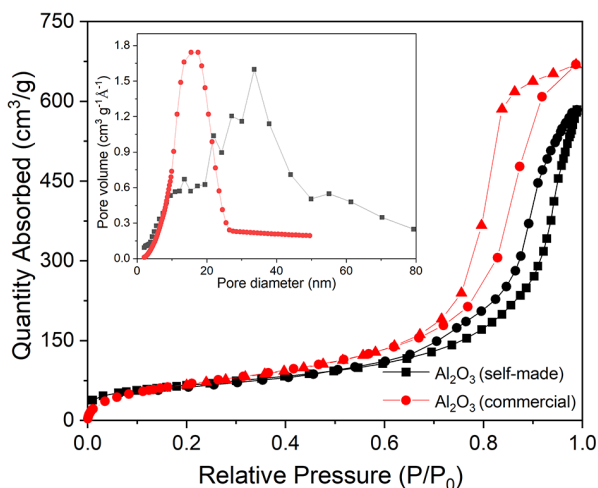


Figure D2. N₂ adsorption-desorption isotherm of Al₂O₃(commercial) and Al₂O₃(self-made). Insert is the pore size analysis results from the corresponding isotherms.

A non-boehmite derived γ -alumina and its utilization in HDS catalysis

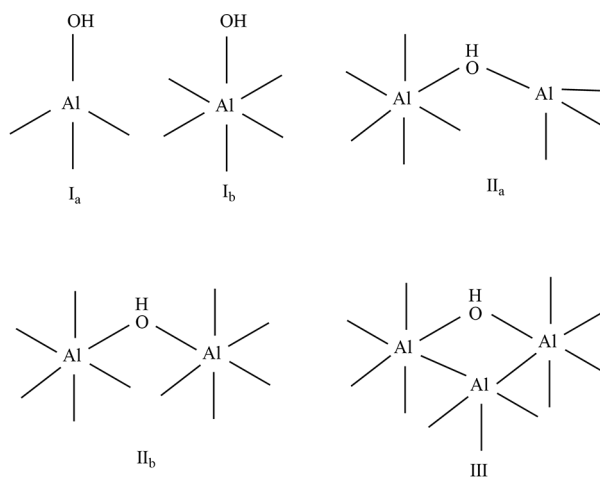


Figure D3. Structures of Al-OH groups on the surface of γ - Al_2O_3 .

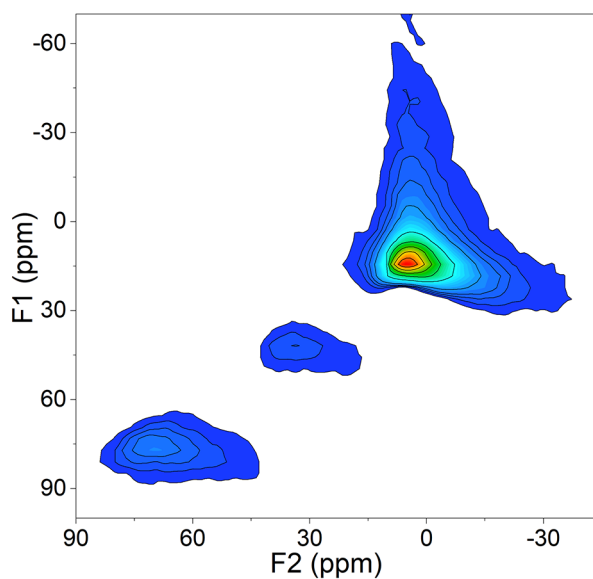


Figure D4. ^{27}Al MQ MAS NMR spectra of Al_2O_3 (self-made).

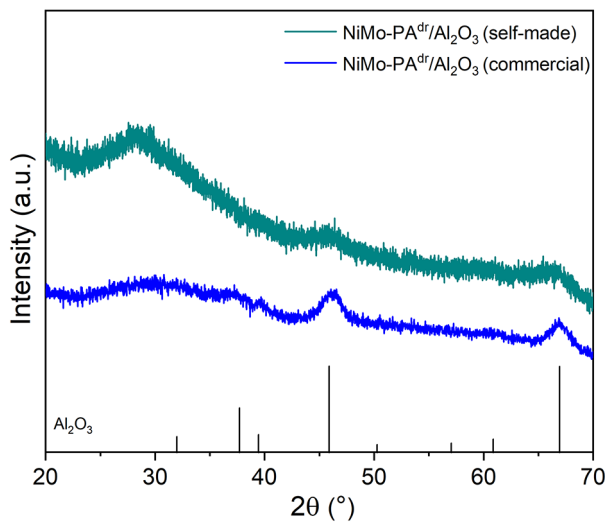


Figure D5. XRD patterns of NiMo-PA^{dr}/Al₂O₃(commercial) and NiMo-PA^{dr}/Al₂O₃(self-made).

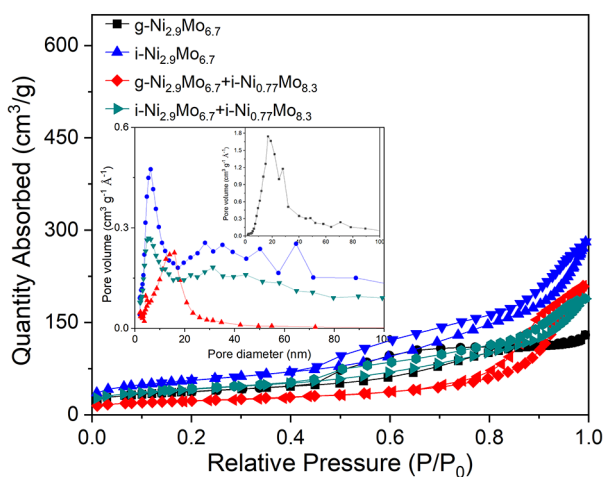


Figure D6. N₂ adsorption-desorption isotherm of g-Ni_{2.9}Mo_{6.7}, i-Ni_{2.9}Mo_{6.7}, g-Ni_{2.9}Mo_{6.7}+i-Ni_{0.77}Mo_{8.3}, and i-Ni_{2.9}Mo_{6.7}+i-Ni_{0.77}Mo_{8.3}. Insert is the pore size analysis results from the corresponding isotherms.

Chapter 7

Summary and outlook

Aspects of Synthesis, Structure, and Catalytic Performance of Alumina Supported NiMo Hydrotreating Catalysts

Hydrodesulfurization (HDS) is used worldwide to produce ultra-low sulfur fuels by removing sulfur from crude oil to meet environmental legislation. Even today, hydrodesulfurization is still one of the most extensive applications of industrial catalysis based on the amount of catalyst processed worldwide. Typical HDS catalysts consist of sulfides of molybdenum and nickel, where the concentration of the promotor nickel is only about 20 % of the molybdenum content. HDS catalysts are usually prepared in the form of oxidic precursors and converted into active sulfides in the presence of H_2/H_2S before their service in a refinery. In the commonly accepted structural model, Ni decorates the edges of MoS_2 nanoparticles under formation of the so-called NiMoS phase, which is the active phase in these catalysts. The state of the active phase results from its preparation history; it can be modified by adjusting preparation conditions, such as changing the starting material of Mo and Ni or adding different organic compounds to the metal solution. In this thesis, the relation between the oxidic precursor and the active sulfide structure of different, but consistently comparable catalyst formulations, was investigated using advanced characterization (**Chapters 3, 4, and 5**). In **Chapter 6**, the influence of two very different alumina carriers and their utilization in HDS catalysis were studied.

In **Chapter 3**, the optimum ratio of Ni/Mo was explored by comparing the catalytic activity of five NiMo/ Al_2O_3 catalysts with different Ni/Mo ratios (from 0.18 to 0.62). The activity data show that the highest performance is achieved with a Ni/Mo ratio of 0.4. Next, we systematically studied the influence of calcination and organic additives (citric acid (CA), ethylene glycol (EG), nitrilotriacetic acid (NTA), malic acid (MA)) on catalyst structure and performance. The activity data show that calcination and organic additives bring about different levels of activity (gas-phase thiophene and liquid-phase dibenzothiophene (DBT)) improvement, except for NTA. For catalysts with NTA, a different performance behavior was observed in gas-phase thiophene and liquid-phase DBT HDS, where a significant improvement in thiophene HDS was observed, while no activity enhancement or even an

Chapter 7

inhibitory effect was observed in DBT HDS. Among additives, MA(1.2)/MoO₃ (prepared from MoO₃/NiCO₃, with MA as additive and with a molar ratio of MA/Mo = 1.2) is the most active catalyst. We also studied the influence of chemical sources on catalyst performance. The catalytic activity of two series of catalysts prepared from two sets of chemical sources, i.e., (NH₄)₆Mo₇O₂₄ (AHM)/Ni(NO₃)₂ and MoO₃/NiCO₃, and in each series with the additives mentioned above, was evaluated. Thiophene HDS and DBT HDS results indicate that catalysts prepared from MoO₃/NiCO₃ show a higher activity than their counterparts prepared from AHM/Ni(NO₃)₂, and the activity difference between the pair of catalysts with additives is more evident than the pair without additives. Based on this, we infer that the complex catalyst system is more susceptible to chemical sources (preparation condition).

To better understand the reason for the activity difference caused by chemical sources, in **Chapter 4**, a detailed structural characterization of two catalysts (MA(1.2)/AHM and MA(1.2)/MoO₃) with identical formulation, same additive (MA, malic acid), but prepared respectively from (NH₄)₆Mo₇O₂₄ (AHM)/Ni(NO₃)₂ and MoO₃/NiCO₃ was conducted. The oxidic precursor, sulfided and spent states of these two samples were characterized by means of BET, temperature-programmed reduction (TPR), Raman spectroscopy, X-ray diffraction (XRD), X-ray photoelectron spectroscopy (XPS), Energy-dispersive X-ray spectroscopy (EDX), scanning transmission electron microscopy (STEM), and ptychographic X-ray computed tomography (PXCT). The results indicate that the oxidic precursor of the catalyst prepared with MoO₃/NiCO₃ (higher activity) has a higher reducibility of Mo and weaker metal-support interactions. After sulfidation, the metals are well dispersed on alumina surface and primarily exist as active NiMoS particles, which are stable during the operation and no apparent changes are observed. On the other hand, the catalyst prepared from AHM/Ni(NO₃)₂ contains limited amounts of active NiMoS particles, and the remaining metals occur as inactive, partly unsupported MoS₂ and isolated NiS_x clusters, which turned out unstable and were washed off during the operation or aggregated into larger domains. These structural differences explained the observed significant DBT HDS performance difference between MA(1.2)/AHM and MA(1.2)/MoO₃ caused by chemical sources.

The results in Chapter 4 show that the state of a sulfided active phase is distinctly determined by the structure of its oxidic precursors. This conclusion inspired us to estimate and predict catalytic activity on the basis of the oxidic state of HDS catalyst. For this purpose, in **Chapter 5** the structural properties of oxidic NiMo/Al₂O₃ catalyst precursors as obtained from UV-vis spectroscopy (absorption edge energy, E_g) and temperature-programmed reduction (temperature of main reduction peak, T_m), were correlated with their activity in DBT conversion (X). A negative linear relation between E_g and X, T_m and X was observed. This

finding implies that catalysts with lower E_g (smaller particle size) and lower T_m (higher reducibility) show a higher HDS performance.

From the above studies, we acknowledged that carriers' textural properties and stability play an essential role in supported HDS catalysts. To verify this in **Chapter 6**, we prepared two catalysts with identical compositions using two different carrier materials with comparable surface areas and pore volumes: a self-made alumina (Al_2O_3 (self-made)) prepared by decomposition of $NH_4Al(OH)_2CO_3$ and a commercial alumina (Al_2O_3 (commercial)). In a direct comparison, catalysts on the Al_2O_3 (commercial) carrier were 25 % more active. However, our self-made alumina sample did open opportunities to try alternative catalyst preparation routes. We prepared two sets of catalysts with the same metal loadings via two different methods, co-grinding and incipient wetness impregnation. While in the example above, we worked with different starting materials (chemical sources) under otherwise the same conditions; here we used the same starting materials but processed them in different preparation workflows. The DBT HDS results show that the catalyst prepared via co-grinding has a lower activity than the respective impregnated catalyst, suggesting embedding metals into the carrier has no advantage in the DBT HDS reaction.

In summary, in this study the influence of different parameters in the preparation of HDS catalysts, i.e., starting materials (chemical sources), organic additives and carrier types, on catalytic activity was investigated. We were able to explain the profound effect of chemical components in the impregnation solution on the structure and activity of resulting catalysts, and we could visualize these structural differences in the 3D space. A correlation between the structural parameters of oxidic precursors and the activity of the respective finalized sulfided catalysts was found. As we discussed the influence of chemical sources on the structure of oxidic precursors, it is still unknown what exactly happened during impregnation. Hence, it would be an interesting aspect to look into further. Real-time monitoring of the impregnation process using PXCT, STEM, X-ray fluorescence for example, allows us to further understand the core element of catalyst preparation and shed light on the improvement of catalyst. More detailed information regarding the active sites, i.e., their position (Ni especially) and morphology in catalysts and the states under HDS reaction conditions, could help us understand the catalysts better. To do that, in situ FT-IR and Raman spectroscopy are needed. In the second part of this thesis, the influence of two very different alumina carriers is discussed; an alternative catalysts preparation method (thermal decomposition of $NH_4Al(OH)_2CO_3$) was also applied, though the synthesized catalyst shows a relatively low HDS activity compared to the sample prepared via impregnation. However, this exploration provides a direction for catalyst design. We use alumina as support in this thesis, as it shows the high area surface and mechanical strength, while many other materials could also be

Chapter 7

chosen, e.g., active carbon [1], TiO₂ [2], as reported in the literature. Also, regarding the preparation method, many other methods could be used to prepare supported catalysts, such as chemical vapor deposition, ion adsorption, or deposition precipitation. Modifying MoS₂ particles to increase the proportion of active phase is another aspect we could try to move forward. As only the MoS₂ edge sites in our catalysts are active in the HDS reaction, the whole basal plane is considered inactive [3]. It would thus be groundbreaking if the basal plane could be activated. In a research of Lauritsen and Besenbacher [4], they claimed that the electronic band states near the edge of MoS₂ particles can participate in chemical bonding, which increases the conductivity of MoS₂ and makes it different from the inert MoS₂ basal plane. And this high local density of electronic states as observed even active the sulfur atom away from the edge (Figure 7.1b). This study can be considered as a theoretical basis for basal plane activation and it provides the possibility for further research.

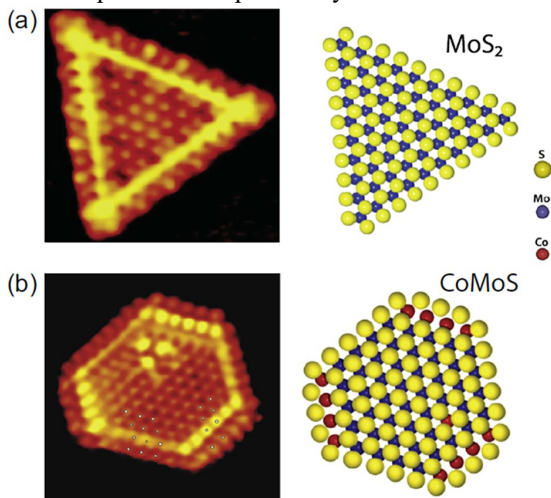


Figure 7.1. (a) Atom-resolved STM image of a triangular MoS₂ nanocrystal on Au(111) together with a ball model of the proposed edge structure reflecting (10 $\bar{1}$ 0) Mo edge with a 100% S coverage. (b) Atom resolved STM image of a truncated triangular Co-promoted nanoparticle. The interior part is MoS₂, but favorable substitution of Co is concluded to be at the ($\bar{1}$ 010) S edge. Adapted from Ref. [4]

7.1. References

- [1] Y. Sano, K.-H. Choi, Y. Korai, I. Mochida, Adsorptive removal of sulfur and nitrogen species from a straight run gas oil over activated carbons for its deep hydrodesulfurization, *Appl. Catal. B: Environ.*, 49 (2004) 219-225.
- [2] J.A. Toledo-Antonio, M.A. Cortés-Jácome, C. Angeles-Chávez, J. Escobar, M.C. Barrera, E. López-Salinas, Highly active CoMoS phase on titania nanotubes as new hydrodesulfurization catalysts, *Appl. Catal. B: Environ.*, 90 (2009) 213-223.
- [3] M. Salmeron, G.A. Somorjai, A. Wold, R. Chianelli, K.S. Liang, The adsorption and binding of thiophene, butene and H₂S on the basal plane of MoS₂ single crystals, *Chem. Phys. Lett.*, 90 (1982) 105-107.
- [4] J.V. Lauritsen, F. Besenbacher, Atom-resolved scanning tunneling microscopy investigations of molecular adsorption on MoS₂ and CoMoS hydrodesulfurization catalysts, *J. Catal.*, 328 (2015) 49-58.

Acknowledgments

The past four years of research at IMC group have been an incredible experience. This journey is full of challenges and surprises. I have learned to be an independent researcher and a better person. Part of the work presented in this thesis couldn't be done without the knowledgeable and helpful people I work with, and I would like to thank all the people who have helped me over the last four years.

First and foremost, I would like to thank my first promotor, prof. dr. Thomas Weber for giving me a chance to conduct my Ph.D. study under his supervision. Thomas, it is a great pleasure to work with you; your solid knowledge of chemistry is impressive. Your encouragement type supervision and patience are the qualities I value. Your ability to see the big picture is something I need to learn. You always ask me the right questions and tell me the importance of keeping my feet on the ground when I have whimsical ideas, which helps me a lot. The most often comment you gave me is “think logically”, which I will always keep in mind. The difficult impromptu questions you ask help me think in-depth. I have benefited greatly from all the important suggestions you have given me professionally and personally.

Emiel, thank you for allowing me to work at IMC and agreeing to be my second promotor. You said hydrodesulfurization is one of your favorite topics, and it is my favorite too. Your suggestion on medium pressure setup helped me accelerate the maintenance process. Thank you for allowing me to attend the (inter)national conferences; I enjoyed the time in Normandy!

My sincere gratitude goes to the committee members, prof. dr. E.T.C. Vogt, prof. dr. J.V. Lauritsen, prof. dr. J.A.M. Kuipers, prof. dr. J.A. van Bokhoven, and prof. dr. J. van der Schaaf for taking the time from your busy schedule to read through my thesis and evaluate my work. Your important feedbacks help me to improve it in the final stage. I would also like to thank prof. dr. D.C. Nijmeijer for attending my defense ceremony as the chairman.

My special thanks also go to our IMC staff members. Sue, it was nice to have you in our big family. It was much easier to have you helping me with the documentation work for my thesis. Emma, thank you for organizing all the “Ladies event”. Tiny, my appreciation to you for your kindness and useful suggestions is beyond words. Your help in building and maintaining my setup made my life easier. I like your positive and energetic attitude to work and life. You are always ready to help people, and you enjoy it. Adelheid, your help in ICP measurement and XRD training is highly appreciated. I am impressed with your rigorous scientific research

Acknowledgements

attitude. I hope you have a wonderful retirement life. Brahim, thank you for providing support in performing NMR experiments and being tolerant when I damaged the rotor (Sorry!). Thijs, you are always patient and modest whenever I ask for your help, so it was surprising when you told me you play in a band, but I think your hairstyle does explain that 😊.

My two paronyms are gratefully acknowledged. Siyu, we started our Ph.D. at the same time, but we only knew each other in the second year of our Ph.D. It was surprising to know that we also came from the same city. It was nice to have you around, and I enjoyed your company. Thank you for listening to my complaints and giving me helpful suggestions. It is great that you also defended your thesis this month; I wish you all the best with your future work and life. Yujie, you are the first person I knew in IMC. You introduced me to other colleagues and helped me settle down. I still remember the first time we walked to “Amazon Oriental”, it took me 1h to walk home on a cold winter evening, and this experience triggered me to buy a bike and to relocate. Thank you for inviting me over for dinners.

I want to thank the people involved in my research. Miao, as the only colleague who works with sulfide catalysts in IMC, you were my first option to turn to for help. You are always willing to help people with patience; your intelligence, modesty, and kindness are the characteristics I value most. You taught me many experimental skills, from catalyst synthesis to activity testing, which helped me become familiar with heterogeneous catalysis. Thank you for taking time to help me with my manuscript. I wish you all the best with your career. Lennart, your knowledge of hydrodesulfurization and setup design is impressive. It was nice to talk to you on some occasions, your suggestions regarding setup building and data analysis were always helpful. Arend-Jan, thank you so much for giving me the catalyst preparation training and taking care of the gas-oil HDS test for Chapters 3 and 4. It is nice to talk with you whenever I have a problem regarding catalyst preparation, your suggestions are always helpful. Johannes, you helped me with the tomography measurement and the corresponding data analysis for Chapter 4. You are so kind to answer my questions patiently; I appreciate it. I sincerely hope you can find a dream job and have a bright career. Rim, thank you for helping with the TEM measurement for Chapters 3 and 6. I know it is complicated and time-consuming to measure sulfides than the other catalyst; you need to do extra work every time. But you are always kind and willing to help me; thank you! Good luck with your final stage of Ph.D.! Janson and Marcel, thank you for taking the STEM images for me.

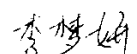
I would also like to thank other colleagues and friends in the IMC group. Songqian, I am glad you finally chose to do your “Joint Training Ph.D. program” in IMC group. I enjoyed the trip with you and all your company. We have known each other for years; you are the loveliest person I have known in my life, although sometimes I tell you that you are quite naïve

Acknowledgements

(kidding). I am grateful that you were there during my most difficult times. You entered a new stage of life last year. I wish you all the best! Lulu, your cooking skill is impressive, thank you for inviting me to nice dinners. I wish you all the best. Victor, I enjoyed our discussions about cultures and other topics. Thank you for all the chocolates and snacks! Liang, thank you for helping me with the paper waste. The trip to Greece was amazing. Tim and Yiwei, thank you for asking me out and inviting me for dinner. It was nice to hang out with you guys, and the trip to Gent with Lulu and Mingwen was amazing. I wish you great success with your studies and career. Ouyang, having you in our “gossip group” was interesting. Thank you so much for all the suggestions on job searching. I enjoyed our trip to Greece, not only because you did the most preparation work, but also the lovely pictures you took for us ☺. Tan, it was always great to chat with you. You have a kind of magic to make people feel warm. I still remember the shock of having this “iced bubble tea” with you in the winter. Hope we will meet some other day again! Lingqian, thank you for agreeing to stay overnight with me in the hotel and showing me the evening of Amsterdam. Douglas, you are the first foreign office mate I ever had. You were so kind to give me suggestions on lots of trifling matters. I wish you all the best with your career! Shiyue, thank you for the clear instructions on GC-MS and for helping me with the measurement. I enjoyed our talks during lunchtime. Anna, thank you for teaching me to measure FTIR. Sasha, thank you for helping me with GC and Raman. Valerii, thank you for measuring Raman for me; your suggestions regarding XPS peak fitting were helpful. Nikolay, thank you for taking the time to answer my question about FTIR. Younes, you spent time helping me with GC; thank you. Xianxuan, the BBQ you organized was great! Pepe, it was always good to chat with you. Good luck with your studies and future career! Dimitra, I enjoyed our conversation in the “girls night”, good luck with your last year! My gratitude also goes to other (former) IMC members: Ivo, Marta, Gabriela, Jan Philipp, Robert, Florian, Jiadong, Jérôme, Yanan, Jiachun, Xiaofeng, Geert, Zhaochun, Michael, Ferdy, Yonghui, Freddy, Angelina, Valentin, Luke, Aleksei (with beard) and Aleksei (without beard), Xiaoming, Bianca, ... It is my honor to work with you in Eindhoven.

最后谢谢爸妈一如既往的支持我的决定，过去两年对我们来说都是比较艰难的两年，但我相信一切都会好起来的！谢谢哥哥对爸妈的照顾。

Mengyan Li



01/2023, Eindhoven

List of publications

Publications within the scope of this thesis

- M. Li, J. Ihli, M.A. Verheijen, M. Holler, M. Guizar-Sicairos, J.A. van Bokhoven, E.J.M. Hensen, Th. Weber, Alumina-Supported NiMo Hydrotreating Catalysts—Aspects of 3D Structure, Synthesis, and Activity, *J. Phys. Chem. C*, 126 (2022) 18536-18549.
- M. Li, E.J.M. Hensen, Th. Weber, A Non-boehmite Derived Gamma Alumina and Its Utilization in HDS Catalysis, *in preparation*.
- M. Li, E.J.M. Hensen, Th. Weber, Predicting Catalytic Activity from Oxidic Precursor Properties, *in preparation*

Conference contributions

- M. Li, J. Ihli, M. Verheijen, E.J.M. Hensen and Th. Weber, Hierarchical structure of alumina supported catalysts, Netherlands Catalysis and Chemistry Conference (NCCC) XXIII 2022, Noordwijkerhout, The Netherlands. (oral)

Curriculum Vitae

Mengyan Li was born on October 18th, 1993 in Xi'an, Shaanxi Province, China. After finishing her high school degree in 2011, she started her bachelor study in Materials Chemistry at Shaanxi University of Science and Technology. She obtained her bachelor's degree in engineering under the supervision of Prof. Hui Liu in 2015. She continued her master's study at the same university, and in June 2018, she defended her master's thesis entitled "The synthesis and characterization of the titanium dioxide-based catalysts". Later in January 2019, she joined the Inorganic Materials and Catalysis group at Eindhoven University of Technology under the supervision of Thomas Weber and Emiel Hensen in Eindhoven; her research focuses on the alumina-supported NiMo hydrodesulfurization catalyst. The results of this work are presented in this dissertation.

